



HAL
open science

Spectroscopic study of supported MoS₂ catalysts for HER electrocatalysis in acidic media

Limor Ben Neon

► **To cite this version:**

Limor Ben Neon. Spectroscopic study of supported MoS₂ catalysts for HER electrocatalysis in acidic media. Catalysis. Normandie Université, 2023. English. NNT : 2023NORMC225 . tel-04525902

HAL Id: tel-04525902

<https://theses.hal.science/tel-04525902>

Submitted on 29 Mar 2024

HAL is a multi-disciplinary open access archive for the deposit and dissemination of scientific research documents, whether they are published or not. The documents may come from teaching and research institutions in France or abroad, or from public or private research centers.

L'archive ouverte pluridisciplinaire **HAL**, est destinée au dépôt et à la diffusion de documents scientifiques de niveau recherche, publiés ou non, émanant des établissements d'enseignement et de recherche français ou étrangers, des laboratoires publics ou privés.



Normandie Université



UNIVERSITÉ
CAEN
NORMANDIE

THÈSE

Pour obtenir le diplôme de doctorat

Spécialité CHIMIE

Préparée au sein de l'Université de Caen Normandie

Spectroscopic study of supported MoS₂ catalysts for HER electrocatalysis in acidic media

Présentée et soutenue par
LIMOR BEN NEON

Thèse soutenue le 28/09/2023
devant le jury composé de

| | | |
|-----------------------|--|-----------------------|
| M. XAVIER CARRIER | Professeur des universités, Sorbonne Université | Rapporteur du jury |
| MME DOROTHÉE LAURENTI | Directeur de recherche au CNRS, Université Lyon 1 Claude Bernard | Rapporteur du jury |
| M. PHILIPPE BAZIN | Ingénieur de recherche, Université de Caen Normandie | Membre du jury |
| M. ETIENNE GIRARD | Ingénieur de recherche, IFP Energies Nouvelles | Membre du jury |
| MME CAROLE LAMONIER | Professeur des universités, Université de Lille | Président du jury |
| MME LAETITIA OLIVIERO | Professeur des universités, Université de Caen Normandie | Directeur de thèse |
| MME FRANCOISE MAUGE | Directeur de recherche au CNRS, Université de Caen Normandie | Co-directeur de thèse |

Thèse dirigée par LAETITIA OLIVIERO (Laboratoire catalyse et spectrochimie (Caen)) et FRANCOISE MAUGE (Laboratoire catalyse et spectrochimie (Caen))



"The most important of my discoveries have been suggested to me by my failures."

Humphry Davy

Acknowledgements

I dedicate this segment to the fabulous people who have helped me and guided me through those three years of research work.

First, I would like to thank my supervisors Prof. Laetitia Oliviero and Dr. Françoise Maugé for accepting me into their team, give me the opportunity to work on this challenging research project and guiding me during these three years.

Secondly, I would like to thank Dr. Keyla Taxeiro-Santos and Dr. Laetitia Dubau from LEPMI for their expertise, guidance and cooperation during those years. I have learned a lot from you. I am also very honored to have been a research guest in your laboratory and thank you Keyla for taking the time to show me the experimental part in HER. I also thank Pascal Blanchard for his expertise in XPS spectroscopy.

Thirdly, I would like to express my gratitude to all the technicians, research engineers and fellow colleagues at the LCS who have supported me and lend me a helping hand: Valérie, Yoann, Philippe, Marie, Benjamin, Aymeric, Hamza, Mattias, Jafaar, Ludovic and Marco I thank you with all my heart.

At last, I would like to give my utmost gratitude to the most important people in my life, my family. Thank you for your unconditional love and support throughout my life. You made the difficult and stressful moments during my PhD endurable by giving me the strength to overcome any possible obstacle.

Table of contents

| | |
|---|------------|
| Chapter 1: Bibliographic study | 13 |
| Chapter 2: Experimental part | 78 |
| Chapter 3: Effect of H₃PO₄ and EDTA on MoS₂/TiO₂ and on its HER activity | 86 |
| Chapter 4: Effect of support's morphology on hydrogen evolution reaction: TiO₂ nanotubes and nanowires | 157 |
| General conclusion | 218 |
| Supplementary Chapter: Developing a new methodology to analyse carbon-based catalysts via IR-transmission | 228 |

General Introduction

The demand in energy is soaring with the economic growth and population expansion. Consequently, new pathways of sustainable energy production are needed. However, the big challenge of those technologies (e.g. wind, solar) is the storage of produced energy.

Water splitting through photo- and electrochemistry seems to be a promising solution to store the produced energy in form of dihydrogen without CO₂ emission. Indeed, hydrogen is a reliable energy vector due to his high energy density and could replace in near future fossil fuel. It is estimated that “by the year of 2050 there will be a hydrogen demand of over 45 billion gallon gasoline equivalent (GGE) in the United States of America alone which can fuel up 342 million light-duty vehicles for 82×10^{11} km travel per year.”¹ In the EU, the demand H₂ is expected to increase up to 53 Mt which is equivalent to 1.764 TWh in 2050.²

The commonly way to split water into H₂ and O₂ is water electrolysis. An electric source is connected to two electrodes (cathode, anode playing the role of a catalyst) on which two separate reactions occur either in acidic or basic media.

In acidic media, the reduction of protons into H₂ (Hydrogen evolution reaction) takes place on the cathode whereas on the anode the oxidation of water into O₂ and H⁺ occurs (Oxygen evolution reaction).³ Until today the most active electrocatalyst to produce H₂ is Pt/C due to its oxygen resistance, long stability against corrosion, hydrogen adsorption affinity and good conductivity. The precious metal platinum is itself an excellent electron conductor making this electrocatalyst highly active and subsequently considered as the benchmark catalyst for hydrogen evolution reaction. However, platinum is expensive and rare rendering cheap energy production difficult.

In order to generate low cost energy for man-kind, stable, highly active and efficient electrocatalysts need to be developed from non-precious and earth-abundant metals.

MoS₂ is a dichalcogenide which is abundant, stable, nontoxic and not expensive. The petroleum industry is already using for decades supported or non-supported MoS₂ catalysts for the elimination of sulfur and nitrogen from heavy crude oil.⁴

Interestingly, Mo atoms located on unsaturated edges of MoS₂ present a similar structure to the enzymatic catalytic centers of hydrogenase allowing to produce H₂ from protons.⁵ Herein it was assumed that MoS₂ would hold a similar HER performance and could one day replace Pt. However, its HER activity is limited by its low electrical conductivity and low edge site exposition on which HER active sites are located. As a result, different strategies were developed to overcome these issues.

Although MoS₂ is since a decade a research subject for HER electrocatalysis, the exact HER mechanism and the type of active site are still not elucidated. Hence it is difficult to engineer active MoS₂ derived catalysts for HER electrocatalysis when the exact nature and properties of the active sites on MoS₂ are unknown.

In this thesis, we tried to establish a correlation between surface characteristics of supported MoS₂ catalysts and HER activity. The main goal is to connect surface characteristics of MoS₂ with obtained HER rates in acidic media in order to determine the main key parameters influencing HER activity. Eventually these key parameters could help facilitate HER electrocatalyst engineering.

One of the most powerful tools to analyse surface characteristics of heterogenous catalysts is FTIR spectroscopy. Indeed the *Laboratoire Catalyse et Spectrochimie (LCS)* is specialized in the characterization and analysis of catalyst under controlled atmospheric conditions. Supported MoS₂ was already investigated by FTIR spectroscopy at the LCS. By coupling IR-transmission spectroscopy with CO adsorption (IR/CO) MoS₂ edge sites can be analysed quantitatively and qualitatively. For instance, edge sites can be directly probed by CO while the creation of S-vacancies and the electron density of Mo can be analysed. Herein the impact of different synthesis strategies on MoS₂ surface characteristics can be investigated and afterwards correlated to the observations made during HER activity tests. These electrocatalytic

tests will be conducted by the group of Laetitia Debau from the *Laboratoire d'Electrochimie et de Physicochimie des Matériaux et des Interfaces* (LEPMI) specialized in this field of application.

However if such an analysis method is applied, the choice of the carrier is crucial. It needs to be endowed with a good IR transparency in order to observe a signal during IR/CO analysis. Hence, the main challenge of this thesis is to find an electrically conductive, chemical stable support which is transparent for IR and allows a good Mo dispersion. Finding a carrier which is answering to all these demands is not evident.

In order to answer the main issue of this research work, the PhD thesis was divided into five parts. First, a bibliographic study will provide a general overview about HER. The main key parameters influencing this reaction will be explained as well as its general mechanism. Moreover, different promising materials for HER will be discussed which could potentially be used as carriers. Subsequently, different strategies to improve HER activity will be presented. Based on this study, we will see that the options in carriers are restricted. Subsequently TiO₂ anatase characterized by a low electrical conductivity was chosen as a carrier for MoS₂. Herein the main challenge consisted in dispersing Mo on TiO₂ and improving TiO₂ electrical conductivity in order to be able to observe a certain HER activity. For the latter two main strategies were followed to improve its conductivity. One consisted in increasing its electrical conductivity via S-doping whereas the other one involved a morphology change of TiO₂ into nanotubes and nanowires. The experimental procedures allowing to investigate their impact on MoS₂ and subsequently on HER activity are described in the second part while the followed synthesis procedures and obtained results are respectively described and treated in the third and fourth part. In these parts surface characteristics of supported MoS₂ on TiO₂ were compared with HER activity tests in order to elucidate the main key-factors influencing HER activity and kinetics. At last, these main factors will be reiterated at the end of this manuscript in order to provide a general conclusion about this research work and its envisioned perspective for the future.

Table of contents

| | |
|--|-----------|
| Chapter 1: Bibliographic study | 13 |
| 1. The half reaction of water splitting: Hydrogen evolution reaction | 13 |
| 1.1. Definition of Hydrogen Evolution Reaction (HER) | 13 |
| 1.2. Descriptors of HER | 14 |
| 1.3. Water splitting technology | 20 |
| 2. Potential electrocatalysts for HER | 23 |
| 2.1. Metal-oxide based materials | 23 |
| 2.2. Transition metal dichalcogenides | 29 |
| 2.3. Carbides | 41 |
| 2.4. Polymers | 43 |
| 2.5. Conclusion | 44 |
| 3. MoS₂/TiO₂ electrocatalyst for HER | 46 |
| 3.1. TiO ₂ : characteristics, its polymorphs and boosting its electrical conductivity | 47 |
| 3.2. MoS ₂ slab morphology on TiO ₂ | 51 |
| 3.3. DFT mechanistic study of HER on MoS ₂ | 51 |
| 4. Characterization methods | 53 |
| 4.1. Fourier Transform Infrared spectroscopy: a characterization and mechanistic study tool | 53 |
| 4.2. Raman spectroscopy | 56 |
| 4.3. UV-Vis spectroscopy | 58 |
| 5. Main conclusion about bibliographic analysis and scope of the thesis | 62 |
| Reference | 65 |

Chapter 1: Bibliographic study

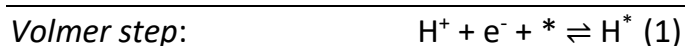
1. The half reaction of water splitting: Hydrogen evolution reaction

1.1. Definition of Hydrogen Evolution Reaction (HER)

The cathodic reaction in electrochemical water splitting, called hydrogen evolution reaction (HER: $2\text{H}^+ + 2\text{e}^- \rightarrow \text{H}_2$) is a promising solution to produce dihydrogen, a critical chemical reagent and fuel.¹ The produced hydrogen can be transported, stocked and used in fuel cells. HER became one of the most studied reactions since it offers the possibility to produce a high energetic molecule. In order to achieve high efficiency for water splitting, high active electrocatalyst requiring minimal overpotential to drive the HER are needed.⁶ Platinum is the best known HER electrocatalyst which requires a small overpotential (0.05 - 0.02 V) in acidic solutions.

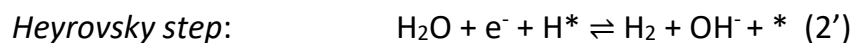
HER is characterized by multiple electron transfer steps and can be described by three steps depending on the electrolyte (acidic or alkaline).⁷

In an acidic media, the protons are immediately accessible. The reaction steps are:⁸



Where * is the active site and H* the adsorbed proton. The Heyrovsky and Tafel steps are two possible pathways after the adsorption of the proton.

In an alkaline and neutral media, the dissociation of water inducing protons needs to be reconsidered. Consequently, the elementary reaction steps of Volmer and Heyrovsky are different:



1.2. Descriptors of HER

1.2.1. Tafel slope

Usually the first step, which consist in the adsorption of a proton, is considered to be the rate determining step (RDS). However, the reaction mechanism from a kinetic perspective is not the same for every electrocatalyst. It depends strongly on the used material and its electronic properties. This is the reason why the Tafel slope is an important indicator for determining the reaction mechanism, so whether a Volmer-Heyrovsky or a Volmer-Tafel mechanism is favored and also to determine the RDS.⁹

The so called Tafel equationⁱ is a linear relation between applied overpotential η and resultant current density j_0 and can be obtained experimentally.¹⁰

$$\eta = a + b \log j_0$$

The Tafel slope b has theoretical specific values for each possible RDS step which are:

$$b_{\text{Volmer}} = 120 \text{ mV/dec}$$

$$b_{\text{Heyrovsky}} = 40 \text{ mV/dec}$$

$$b_{\text{Tafel}} = 30 \text{ mV/dec}$$

By comparing the empiric obtained slope for a certain catalyst with the theoretical values listed above, it is possible to predict the main mechanism (Volmer-Heyrovsky or

ⁱ "a" is the intercept related to the symmetry and has no electrochemical meaning.

Volmer-Tafel) and determine the RDS. For instance, if the experimental slope equals 45 mV/dec, it means that the RDS is the Heyrovsky step and a Volmer-Heyrovsky pathway is favored. An electrocatalyst is considered to have a high HER activity when b and η are low. These parameters depend strongly from the used material.

Another important parameter is the charge transfer resistance (R_{ct} in Ohm). Indeed, during the reaction electrons are transferred at the solution-electrode interface. A fast electron transfer is indicated by a low R_{ct} value which leads to higher current density and better activity. To determine its value Nyquist plot needs to be traced using electrochemical impedance spectroscopy (EIS).¹¹ This analysis tool allows to characterize the performance of an electrochemical system (e.g. electrode) by acquiring the electrical impedance Z . The latter can be defined as the resulting resistance when an alternative current is applied (i.e. the voltage U and current intensity I are not constant). The obtained plot called Nyquist plot permits the determination of R_{ct} by calculating the difference between the two intersection points on the x-axis noted R_{AB} on Figure 1.

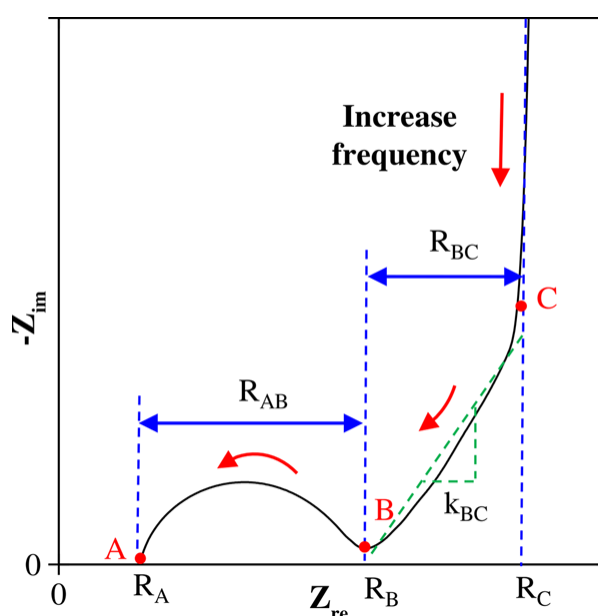


Figure 1: Schematic of Nyquist plot showing how to determine the charge transfer resistance (R_{ct}) indicated by the segment R_{AB} .¹¹

1.2.2. Hydrogen adsorption free energy

In order to develop efficient catalysts without non-precious metals, various aspects must be considered: physical and chemical properties of the material, its structural and thermodynamic properties as for instance its crystal structure, melting point, electron work function and furthermore its hydrogen adsorption free Gibbs energy (ΔG_{H^*}).

The hydrogen-metal bond is one of the most important descriptors. Indeed, the hydrogen-metal bond should neither be too strong nor too weak (Principle of Sabatier). On one hand if the bond is too strong the dissociation of the intermediates and products are difficult. On the other hand, if the bond is weak, the interaction between active site and substrate will fail. In this regard, various “volcano-plots” based on this principle and mathematical modelling were established. It was Trasatti’s predictive model for HER kinetics which allowed advances in the design of effective materials.³ He suggested that it existed a volcano-like plot correlation between the exchanged current density versus the experimentally evaluated metal-hydrogen bond strength (Figure 2). On this plot, the ascending branch of the curve indicates low proton adsorption whereas the descending branch is indicating strong proton adsorption. This empiric model was largely approved and validated. However, it needs to be pointed out that this plot is derived from experimental results and isn’t considering the electronic properties of d-orbitals.

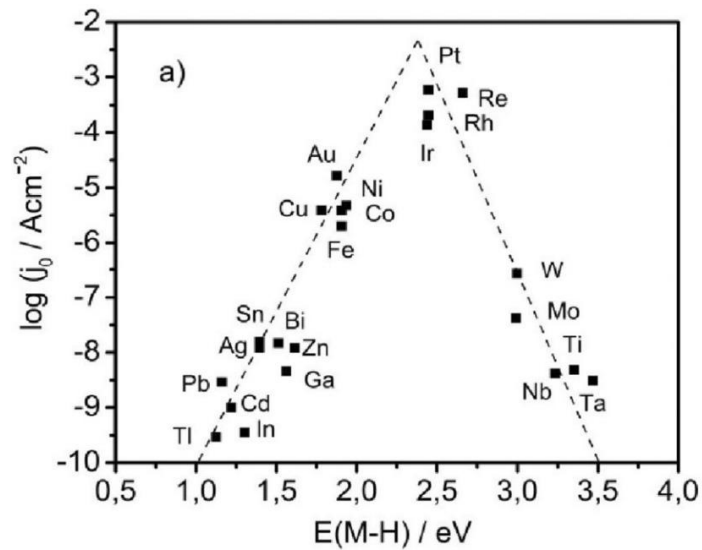


Figure 2: Trasatti's Volcano-plot based on metal-hydrogen bond strength energy.⁷

Later on, Nørskov's¹² research group identified with the help of DFT calculations and a computational approach that high rate activity in HER was achieved for materials with a Gibbs free energy of hydrogen adsorption close to zero (i.e. $\Delta G_{H^*} = 0$). This new volcano-plot (Figure 3) opened new possibilities for HER catalyst candidates because it related adsorption energy of intermediate, reaction rate and electronic property of the material (d-band theory).

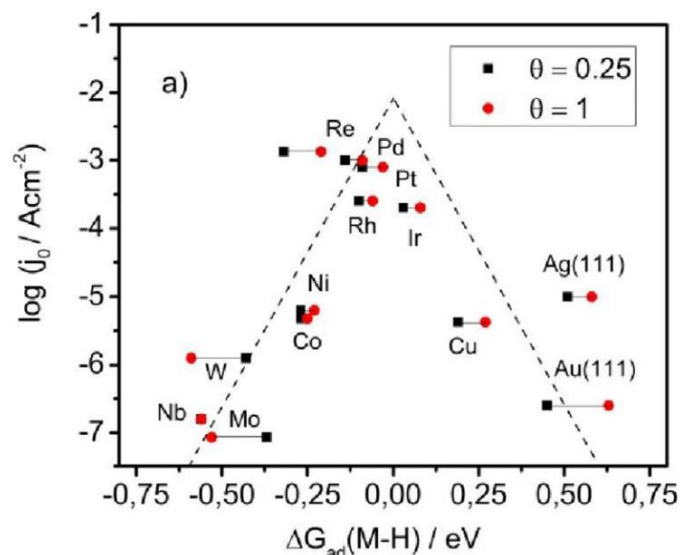


Figure 3: DFT derived "volcano"-plot for the hydrogen evolution reaction and linear dependence between exchanged current and hydrogen adsorption energy.⁷

According to this concept, the electronic structure of the metal surface is influencing the adsorption energy of an intermediate. For instance, if we look closely to the interaction between a metal and an adsorbate: the metal d-band is hybridizing with the bonding σ orbital of hydrogen forming the bonding d- σ and antibonding (d- σ)* states. The bonding state is filled while the filling of the antibonding state is influenced by the local density of states (DOS) at the metal surface. Increasing the filling of the antibonding state results in decreasing the metal-hydrogen bond. Thus, one of the biggest differences between the plots is the position of Ni and Co which have been shifted to the bottom of the volcano plot. In Trasatti's model Ni and Co are weakly adsorbing hydrogen whereas in Nørskov's model they are considered to have a strong hydrogen adsorption.

At this point it should be underlined that these volcano shaped models are based on the principle of Sabatier which applies for heterogenous gas-phase catalysis but by no means for electrocatalysis.

In electrocatalysis, the interaction between metal and electrolyte needs to be considered. The system is more complex, especially since it is influenced by the electrical field in the double layer; the so-called Helmholtz double layer.¹³ When a fluid (electrolyte) is in interaction with a solid (electronic conductor) a double layer is formed. The first layer in contact with the surface (inner layer) consists of ions adsorbed on the surface. The second layer (outer layer) contains free solvated ions attracted to the surface. The two layers are separated by an interface. This electrical field in the double layer has an effect on:

- (i) the adsorption of protons
- (ii) on the desorption of water from the metal surface
- (iii) on the solvation sphere during the process of the shift of H_3O^+ from the outer to the inner layer.⁷

This phenomenon was not incorporated into any of the previous models.

Zeradjanin et al. incorporated the interfacial interaction between metal-solvent-proton into a new model.¹³ Zeradjanin stipulated that the transition state consisted of four crucial intermediates: the metal (M), the electron (e^-), the solvent (S) and the proton H^+ who are influenced by various simultaneous process (Figure 4):

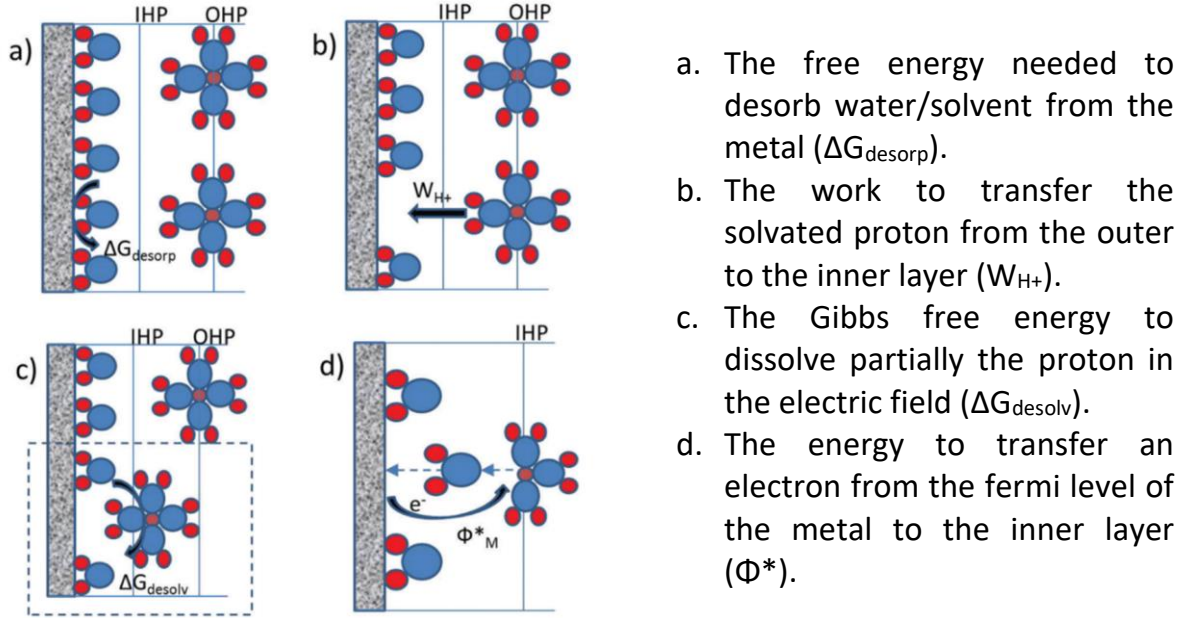


Figure 4: Illustration of the processes in the double layer necessary for the reduction of the proton. In red are hydrogen atoms, blue is oxygen atoms and smaller red circles surrounded each by four water molecules represent solvated proton ($H_3O_4^+$).¹³

Consequently, the free energy of proton adsorption is a sum of all these factors.

$$\Delta G_{H^*} = \Delta G_{\text{desorp}} + \{(W_{H^+} + \Delta G_{\text{desolv}}) + \Phi^*\}$$

The last term of the equation ($W_{H^+} + \Delta G_{\text{desolv}} + \Phi^*$) is translating basically the interaction between a proton and the electric field in the double layer. Assuming that the work function Φ^* has a strong impact on the transfer of protons and electrons, and knowing that Φ^* is proportional to the current charge density, a correlation between these two factors has been put together:

$$\log j_0 \propto \frac{\Delta G_{H^*} \beta}{k_b T} \propto \frac{\beta r \Delta \Phi}{k_b T}$$

Where j_0 – exchange current, β – symmetry factor of activation barrier, ΔG_{H^*} – change in the adsorption energy of intermediate in the rate determining step, $\Delta \Phi$ – change in

the work function upon adsorption of intermediate, r – the slope of the apparent experimental linear dependence between ΔG_{H^*} and $\Delta\Phi$. This relation implies that the stronger the hydrogen adsorption is, the larger the drop in the work function. This parameter allows to take into consideration the interfacial interaction and demonstrates its relevance for predicting the adsorption strength of protons.

1.2.3. Water splitting technology

There exist four water splitting technologies which differ by their electrolyte, operating conditions, separator and ionic agent (OH^- , H^+ , O_2).¹⁴ The most efficient and favored one is PEM (*Polymer Electrolyte Membrane*) electrolysis. The disadvantages and advantages of the other technologies are summarized in Table 1.

Table 1: Advantages and disadvantages of water splitting technologies.¹⁴

| Electrolysis process | Advantages | Disadvantages |
|--------------------------|--|--|
| Alkaline Electrolysis | Well established technology Non-noble electro catalysts Low cost technology The energy efficiency is (70–80%) Commercialized | Low current densities Formation of carbonates on the electrode decreases the performance of the electrolyser Low purity of gases Low operational pressure (3–30 bar) Low dynamic operation Laboratory stage Large system design Low durability |
| Solid Oxide Electrolysis | Higher efficiency (90–100%) Non-noble electro catalysts High working Pressure | Laboratory stage Large system design Low durability |
| Microbial Electrolysis | Used different organic waste waters | Under development Low hydrogen production rate Low purity of hydrogen |
| PEM Electrolysis | High current densities Compact system design and Quick Response Greater hydrogen production rate with High purity of gases (99.99%) Higher energy efficiency (80–90%) High dynamic operation | New and partially established High cost of components Acidic environment Low durability Commercialization is in near term |

In PEM electrolysis, the separator formed by a polysulfonated membrane (e.g. Nafion) has two major functions: firstly, to separate the produced hydrogen and oxygen during operation and secondly transfer protons from the anode to the cathode. This exchange membrane has many advantages such as lower gas permeability, high proton conductivity (0.1 ± 0.02 S/cm), lower thickness (R20–300 mm) and high pressure-operations are possible compared to other technologies listed in Table 1 . Moreover, the system exhibits a high current density (above 2 A/cm²), high efficiency, fast response, small footprint and can operate under lower temperatures (20–80 °C) to produce pure hydrogen.¹⁴

The principle of PEM electrolysis is simple (Figure 5). Two electrodes are separated by PEM in which the electrolyte diffuses. On the cathode which is usually formed by noble metals (e.g. Pt, Pd) occurs the hydrogen evolution reaction (HER) producing H_2 and on the anode formed by IrO_2 or RuO_2 the oxygen evolution reaction (OER) liberating O_2 . During OER e^- and H^+ are liberated. The PEM conducts these protons to the cathode. At the same time electrons are transferred through the external power circuit to the cathode providing the driving force (cell voltage) for the reaction (1.23V).

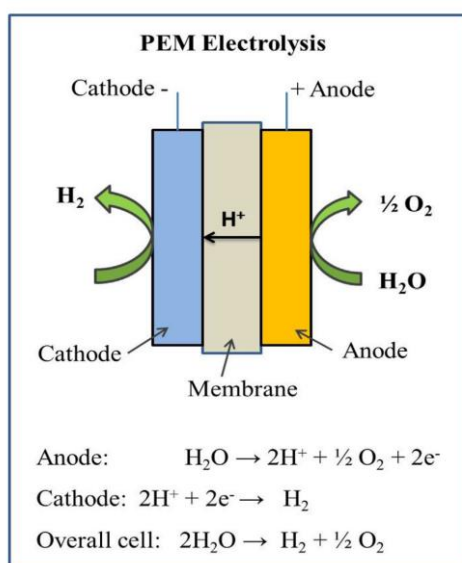


Figure 5: Schematic description of PEM electrolysis.¹⁴

The described process is for an acidic PEM. In the case of alkaline PEMs, anions are conducted by the membrane. However, their durability during water electrolysis is limited. Their lifetime is approximately close to 1000 h, whereas acidic PEMs which are more stable, are operating up to 100,000 h in water electrolysis.¹⁵ This is why acidic PEM electrolysis are favored. Furthermore, from a kinetic perspective, HER in alkaline medium is slow compared to acidic HER.¹⁶ The low concentration of protons and the additional effort to dissociate water near or on the catalyst surface are explaining it. Thus, higher overpotentials are required in alkaline electrolyte compared to acidic one.

In short acidic PEM electrolysis seems to be the most developed efficient cell, answering to the industrial demand and pushes consequently the research towards electrocatalysis in acidic media (Figure 6). However, HER in alkaline media is getting

more and more interest since it is an opening for other potential electrochemical reactions such as the chloralkali process in which Cl_2 and NaOH are produced.

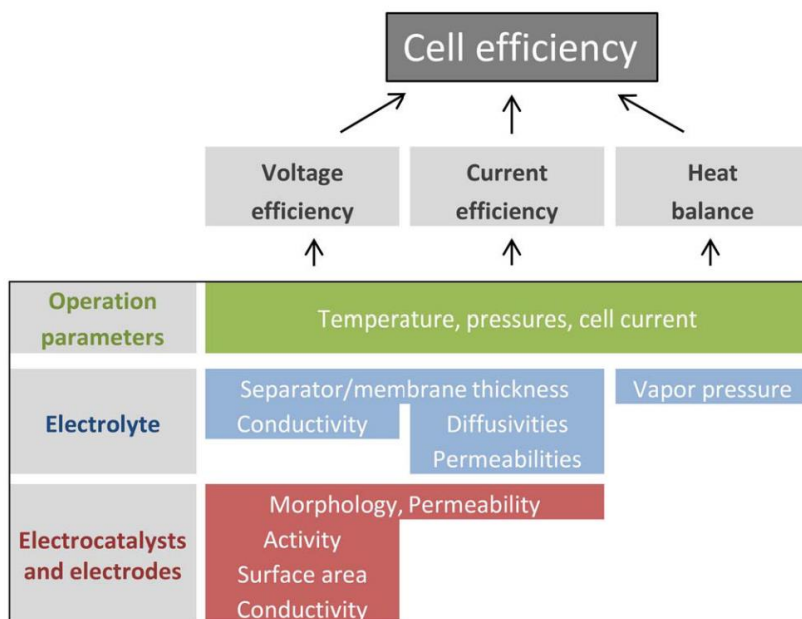


Figure 6: Schema representing the influence of the operation parameters and properties of electrolyte, electrocatalysts and electrodes on the voltage efficiency, current efficiency, heat balance and cell efficiency.¹⁵

2. Potential electrocatalysts for HER

Through the past decade efforts had been made to find new electrocatalyst for HER which consist of non-precious metals and are above all earth-abundant. Various emerging families of materials attracted particular attention due to their interesting conductive and chemical properties, low-cost production and environment friendliness. In the following we will discuss several potential material groups for HER electrocatalysis and the possible existing methods to enhance their activity.

2.1. Metal-oxide based materials

At first, metal oxides were believed to be inactive towards HER although they belong to an important family of functional materials with diverse compositions and structures. Hence, since 2015 engineered metal-oxides became promising candidates for HER.⁹

2.1.1. Simple transition metal-oxides

Transition metal-oxides composed of earth-abundant elements like Ni, Co, Ti, W are the most common in this family. TiO_2 , Ti_2O_3 , MoO_3 , NiO , WO_3 and others were intensively studied for HER. They resulted to be good candidates for HER electrocatalysts after various treatments and engineering processes. In order to increase their activity different strategies like oxygen-vacancy creation, non-metal and metal doping as well as phase structure engineering have been applied.^{9,17-21} These strategies had positive effect on the activity.

- ***Oxygen vacancy control***

Oxides of transition metals from group IV and VI (Mo, W, Ti) are especially studied since they are thermodynamically stable in acidic solutions (Pourbaix diagrams). However,

their oxide pristine forms have poor HER activity in acidic media. The breakthrough to improve their HER activity came with the idea to induce oxygen vacancies in these stoichiometric oxides. By inducing oxygen vacancies (OVs) the electronic structure, the conductivity and hydrogen adsorption energy were modulated.

One of the most remarkable examples is the nonstoichiometric oxide $WO_{2.9}$ obtained by thermal treatment which resulted to be an efficient HER catalyst whereas WO_3 was not effective (Figure 7).⁹ Moreover, DFT calculation demonstrated that the defective form of WO_3 has an optimal ΔG_{H^*} close to zero. To prepare $WO_{2.9}$, 1 g of commercial WO_3 was ground in a ball mill with the wet grinding method (ethanol, 24 h under rotation speed of 300 r.p.m.). Then the ground sample was thermally treated under reductive conditions (1 bar, under a 10% H_2 , 90% Ar flow at 100 ml/min) in a tube furnace at 500 °C for 60 min.¹⁷

Zheng et al. were inspired from this outcome and prepared conductive WO_3 nanosheets enriched with OVs (WO_{3-r} NSs).¹⁸ The activity was enhanced ($\eta_{10} = 38$ mV and Tafel slope of 38 mV/dec vs. $\eta_{10} = 70$ mV and Tafel slope of 50 mV/dec for $WO_{2.9}$) and approaching the values of commercial Pt/C (30 mV/dec). Consequently, oxygen vacancy control showed itself as an effective strategy to enhance HER activity by introducing gap states as theoretical calculation by Zheng et al. demonstrated, making WO_3 act as a degenerated semiconductor with increasing conductivity and low ΔG_{H^*} .

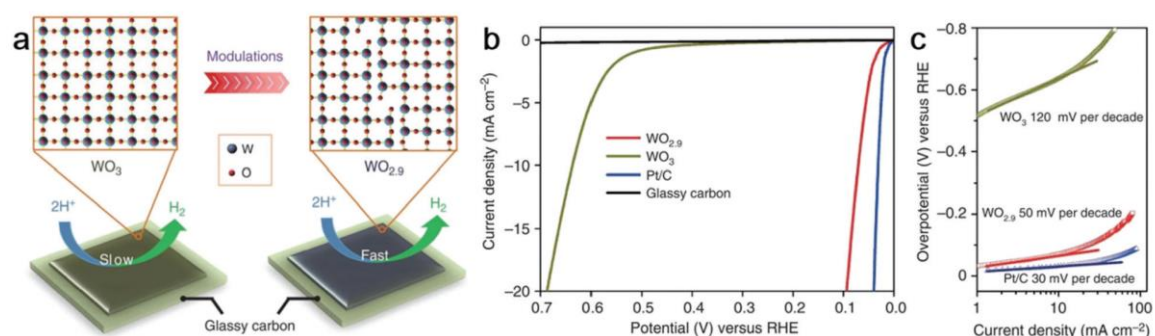


Figure 7: (a) Schematic display of HER for WO_3 and $WO_{2.9}$. (b) HER polarization curves and (c) Tafel plots of different catalysts in 0.5 M H_2SO_4 solution.⁹

In order to synthesize WO_{3-r} NSs via a liquid exfoliation method, Zheng et al. prepared tungsten oxide precursors by a solvothermal method. In ethanol 100 ml, 2 g of WCl_6

were dissolved and heated at 160 °C for 24 h. Then the precursors (1 g) were dissolved in water and ethanol solution (50 mL, 1:1) and ultrasonicated for 5 h. Finally, WO_{3-r} NSs were obtained by centrifuging the resultant dispersion to collect the supernatant.

Parallely, OVs were also reported to be generated on TiO_2 , MoO_3 and MnO_2 via thermal annealing treatment and enhanced clearly the HER activity.⁹

- ***Non-metal Doping***

Besides OVs, the addition of non-metal elements like P, S and ionic metal compounds such as Li^+ proved to be an efficient method to enhance HER activity.¹⁹

Li et al. demonstrated the boosting effect of introducing P-dopants into a reformed MoO_3 nanosheets (noted MoO_{3-x} NS).¹⁹ Li and his team link the improvement of HER activity to the creation of oxygen vacancies and the reduction of Mo^{6+} in to Mo^{5+} allowing a fast adsorption/desorption of protons.

Also, S-doping showed itself as an effective enhancement method as reported by Geng et al. for S doped MoO_2 .²⁰ Erreur ! Signet non défini. S- MoO_2 was obtained by a 2h sulfurization treatment (0.2 mmol S at the upstream side of the precursor at increasing temperature of 2 °C/min under flowing Ar). The obtained experimental results displayed the possibility to produce OVs, induce lattice defects, and regulate charge transfer via S-doping. Indeed, Geng et al. presume that the lattice defects on the basal plane have been originated by the replacement of some oxygen atoms in Mo-O by S atoms forming Mo-S under 300°C. Moreover, under reductive thermal conditions oxygen vacancies are also formed. However, by increasing the concentration of S-dopants, the amount of OVs decreases since S is slowly filling the vacancies. Furthermore, the electronic structure is optimized due to the lower electronegativity of S and Mo compared to oxygen. The electrons of S and Mo are transferred to O and are enriching its negative partial charge which facilitates hydrogen adsorption (inductive effect).²⁰

- ***Metal-doping***

Studies has shown the promoting effect on oxide of metal dopants such as Ni, Mo and Co. The obtained HER activity is superior than non-promoted catalysts.

In acidic media, HER catalyst $W_{18}O_{49}$ was promoted with Mo resulting in a significant enhancement of activity.²² It is assumed that Mo-doping can modify the electronic structure and geometry of active sites. The observed raised activity is allegedly due to the lower bond strength energy of Mo-O compared to W-O. Consequently, hydrogen adsorption is favored on Mo-O sites.²² In this same context Zeng et al. reported Ni-doping to be an effective method to modulate the electron density of MoO_2 and accelerate HER activity in acidic media.²³

- ***Phase-structure engineering***

An interesting way to boost HER activity is to modify the phase structure of the catalyst. A recent study by Li et al. demonstrated the important correlation between electronic structure and activity.²⁴ Li and his team measured electrochemical activity of recrystallized Ti_2O_3 polymorphs. There exist three different kinds, each with different crystalline structure (Figure 8b):

- α - Ti_2O_3 which is trigonal
- o - Ti_2O_3 which is orthorhombic
- γ - Ti_2O_3 which is cubic

The polymorph γ - Ti_2O_3 exhibited the highest activity (i.e. smallest overpotential) at 10 mA/cm² in acidic media. But most importantly, Li observed that the overpotential of HER decreased with smaller charge-transfer energy and strong Ti(3d)-O(2p) orbital hybridization (Figure 8 c, d). Li suggested consequently that the enhancement in HER activity is related to the electronic reconstruction during recrystallization.

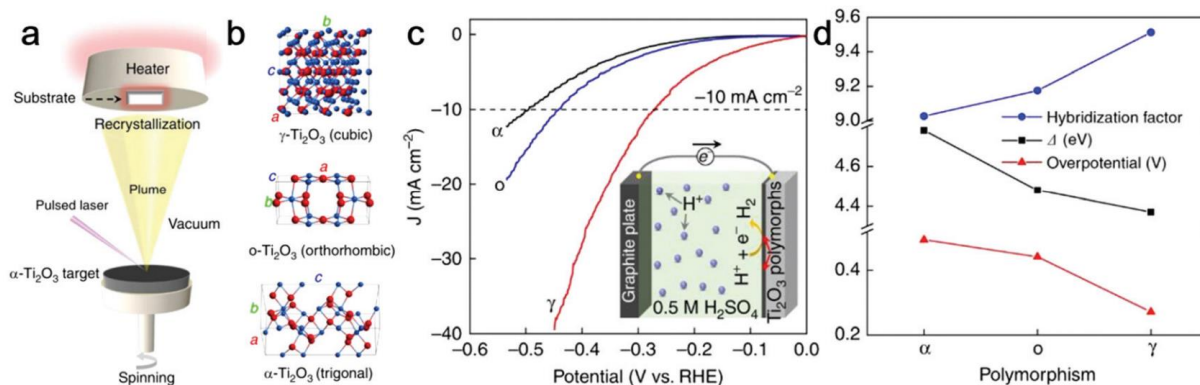


Figure 8: (a) Schematic illustration of Ti_2O_3 polymorphs synthesis in PLD chamber using the same (α - Ti_2O_3) target. (b) Crystal structure of γ - Ti_2O_3 , o - Ti_2O_3 , and α - Ti_2O_3 polymorphs. (c) HER polarization curves of polymorph catalysts in 0.5 M H_2SO_4 solution. (d) Correlation between hybridization factor, overpotential and charge transfer energy Δ .²⁴

2.1.2. Metal oxyhydroxides

Layered double hydroxides (LDHs) coupled with transition metals (e.g. $\text{NiO}(\text{OH})$) had inquired massive interest due to their low-cost production, high specific surface area, good electron distribution and alkaline stability.⁸ Metal oxyhydroxides were considered as good electrocatalysts for OER (oxygen evolution reaction) with sluggish HER activity because of inadequate hydrogen adsorption energies. Yet, it was demonstrated that water dissociation in alkaline media can be improved by adding electroactive materials and achieve consequently high HER activity.

For instance, Fe-doped VOOH was reported to be an effective HER electrocatalyst in alkaline media.⁹ It was shown via DFT calculations that Fe-sites have lower H-binding energies compared to V-sites and improved consequently the activity. Other approaches using different metal oxyhydroxides concluded to be as well efficient for HER.

Li et al. successfully increased HER activity of CoOOH via S-doping.⁹ The doping induced a decrease in barrier energy and enhanced electron conductivity. Furthermore Edvinsson et al. suggested that those kinds of S-dopants could activate inert transition-

metal (oxy)hydroxides during HER.²⁵ During one of his works, he demonstrated the synergetic effect between Ni and Fe in NiFe-LDH with the help of *in situ* Raman. During HER, water is adsorbed on NiFe-LDH. Ni is interacting with one hydrogen extremity of H₂O while Fe interacts with OH. As a result, the bond between H and OH is weakening and enables its dissociation into OH_{ads} and H_{ads} on Ni and Fe respectively (Figure 9).

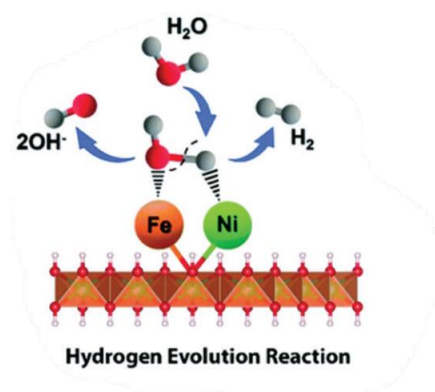


Figure 9: HER schematic step description on FeNi-LDH.²⁵

Other works demonstrated this effect on different metal hydroxides facilitating the Volmer step. This kind of materials could serve as effective promoters for H₂O dissociation for alkaline HER, especially associated with transition metal compounds such as MoS₂ (Figure 10).



Figure 10: Schematic illustration of HER on MoS₂/LDH in alkaline media showing the synergetic effect between LDH and MoS₂.²⁶

This kind of low cost electrocatalyst for alkaline HER was developed by Hu et al.²⁶ The synthesized MoS₂/NiCo-LDH exhibited higher intrinsic activity than bulk MoS₂. This result displays the promoting effect of NiCo-LDH. The binary system benefits from the good chemisorption of H on MoS₂ while OH is adsorbed on LDH. This synergetic effect allows to accelerate water dissociation and overall boost HER performance.

Other metal hydroxide catalysts based on this same synergetic effect were reported to be promising for alkaline HER such as Ni/Li_xNiO, MoNi₄/MoO₂, NiCu/NiFeO_x, Co₉S₈/TiO₂, NiS₂/Ni(OH)₂ and Cu₃N/CuO.⁹

2.2. Transition metal dichalcogenides

Transition-metal dichalcogenides (MX₂) are composed of a transition metal M (M = Mo, W) and a chalcogenide X (X = S, Se, Te). This group of promising HER catalyst is dotted with many properties such as long stability in acidic media, good electrical conductivity and low-cost synthesis.

This class of material has received a lot of attention, especially molybdenum disulfide (MoS₂), which has many interesting properties opening a vast range of application such as hydrodesulfurization catalysis, lubricant, 2D transistor, battery and recently in HER electrocatalysis. For the latter, optimal free Gibbs adsorption energy ΔG_{H^*} of 0.07 eV was determined which is close to one of Pt.²⁷

2.2.1. Structure of bulk MoS₂

Bulk MoS₂ consists of hexagonally packed layers (S-Mo-S) similar to graphite.^{28,29} Mo and S are connected by strong covalent bonds in each layer. Between two sulfur atom layers a Mo atom is sandwiched. The layers are separated by a gap of 6.5Å due to the existing weak Van der Waals bonds.

MoS₂ has different polymorph structures: the octahedral (1T phase) and trigonal prismatic (2H and 3R phases) are two possible coordination for Mo (Figure 11).

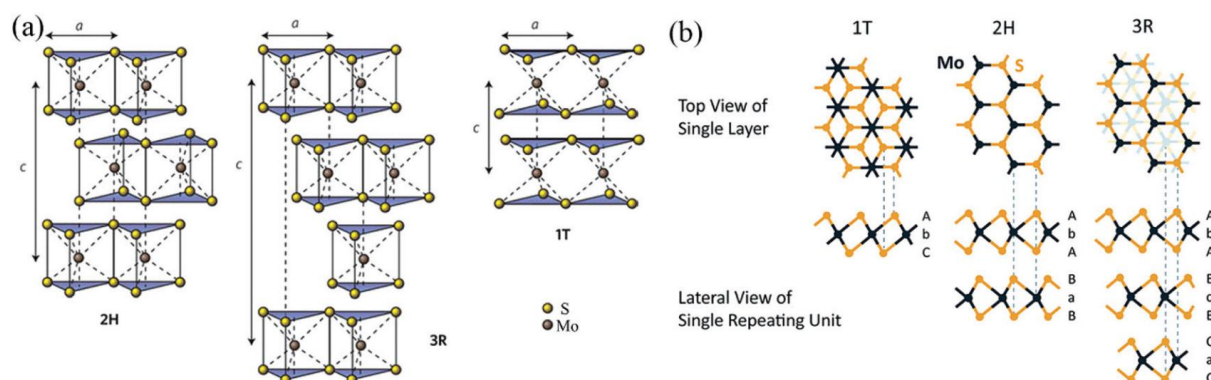


Figure 11 : crystallin structure of 2H, 3R and 1T phase-MoS₂.²⁹

The crystalline bulk MoS₂ is composed of a 2H-phase. However, it is possible to break the weak Van der Waals bonds between the S-Mo-S layers by introducing alkaline ions (e.g. Li⁺, Na⁺, K⁺) which are rendering the MoS₂ hydrophilic and also are allowing a faster electron transport by decreasing the electron diffusion energy. Consequently, the crystal is exfoliated into individual layers (1T-phase) exhibiting completely different properties than 2H-MoS₂.

For instance, the 2H-phase is semiconductor while 1T-phase MoS₂ is metallic. These variations in properties are linked to the electronic structure of Mo via its 4d-orbital.³⁰ The 4d-orbitals of 1T-phase are octahedrally coordinated and form degenerate t_{2g} and e_g orbitals. The degenerated t_{2g} state is incomplete, conferring 1T-phase its metallic characteristics but also rendering it unstable (Figure 12).³¹ Thereby 2H is thermodynamically more stable than 1T-phase.

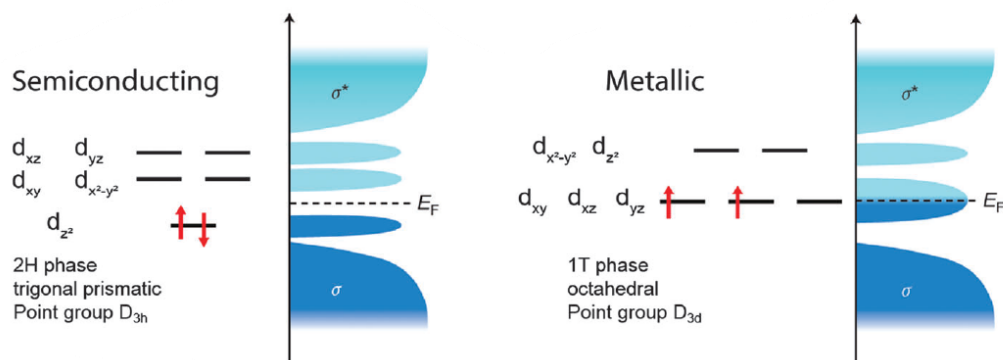


Figure 12: Electron occupation in Mo(IV) 4d orbitals for 1T and 2H phase.³¹

Based on the orbital diagram of 2H- and 1T-MoS₂ in Figure 12, it can be deduced that these two phases are dia- and paramagnetic respectively. It should also be noted that the induced phase change of 2H into 1T-MoS₂ has narrowed the band gap between the valence and conduction band reflecting an enhancement in charge transfer.

The superior HER activity of 1T-MoS₂ compared to 2H-MoS₂ was demonstrated to be mainly caused by its lower charge transfer resistance and higher amount of active sites (Table 2).³² Indeed, the active sites for HER are located for 2H-MoS₂ on its edges (Mo- and S-edges) whereas the basal plane is catalytically inactive. By changing its phase nature to 1T-MoS₂ not only its edges are active for HER but apparently also its basal plane.³³ Herein, the additional large surface plane used for HER is inducing an increase in HER activity.

Table 2: HER activity test results obtained for different solvothermal synthesized 1T/2H-MoS₂. In the table are summarized different electrochemical parameters allowing to evaluate the HER performance of prepared MoS₂ in the work of Kumar et al.³²

| catalyst | percentage of 1T phase (%) | onset overpotential (η_{onset}) (mV) | overpotential at 10 mA cm ⁻² (η_{10}) (mV) | Tafel (mV/dec) | ECSA (mF cm ⁻²) | R_{ct} (Ω) | j_0 ($\times 10^{-6}$ A cm ⁻²) | TOF ($\times 10^{-6}$ S ⁻¹) |
|---------------------------------------|----------------------------|--|--|----------------|-----------------------------|------------------------------|---|--|
| Pt | | 7 | 90 | 35 | | | 50 | 0.1042 |
| 2H-MoS ₂ | | 219 | 340 | 65 | 0.03 | 5326 | 0.03 | 0.0001 |
| 2H-MoS ₂ -H ₂ O | 48.5 | 191 | 291 | 60 | 0.06 | 2754 | 0.16 | 0.0003 |
| 2H-MoS ₂ -EtOH | 50.2 | 188 | 282 | 59 | 0.07 | 2223 | 0.2 | 0.0004 |
| 2H-MoS ₂ -DMF | 78.6 | 170 | 262 | 53 | 0.18 | 1104 | 0.7 | 0.0015 |
| 2H-MoS ₂ -Benz | | 217 | 337 | 65 | 0.03 | 4455 | 0.04 | 0.0001 |

However, although MoS₂ has a free adsorption energy close to zero, its TOF (Turn over frequency) is much smaller than Pt/C as demonstrated in Table 2. This lower activity, especially in the case for 2H-MoS₂, is linked mostly to bad edge sites exposition and low electrical conductivity. Therefore, researchers try different strategies to overcome these issues. The possible methods will be showcased at section 2.2.4.

2.2.2. MoS₂ slabs morphology

The morphology of MoS₂ catalysts was already profoundly studied for hydrodesulfurization (HDS).^{34–36} Analysis have displayed the existence of wide spread MoS₂ slabs across the catalytic surface which have a truncated triangle form. They present Mo- and S-edges (denoted M- and S-edge). DFT calculations and FTIR *in-situ* spectroscopy results proved that S-edges are highly active for HDS. By increasing the number of S-edges, meaning changing slab's morphology, the activity of HDS can be enhanced.³⁶

The morphology of MoS₂ slabs depends on several factors such as temperature and pressure of sulfidation, pH of the solution in which the catalyst was prepared and the ratio between promoter and molybdenum. Herein, promoters as Co resulted in transforming the triangular slabs into hexagonal ones causing an increase of S-edges and subsequently boosting the HDS activity (Figure 13). Furthermore, adding citric acid during catalyst preparation resulted also to be effective in changing triangular slabs into hexagonal ones with or without promoters.³⁴

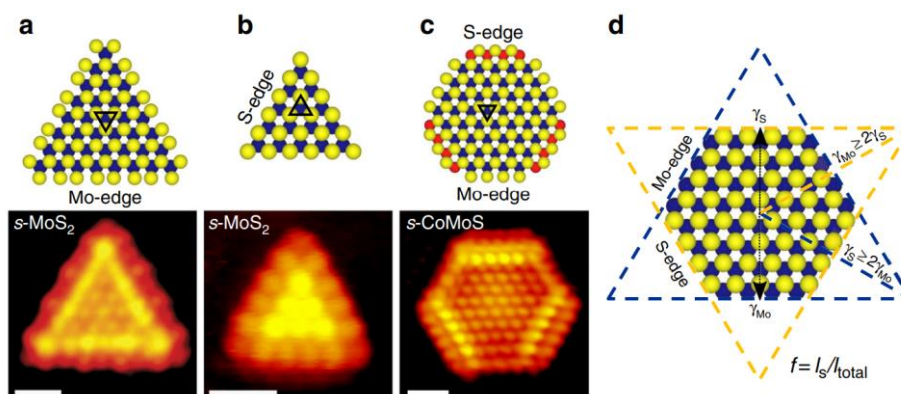


Figure 13: Top view ball models and atom-resolved STM images of fully sulfided nanoclusters (a, b, c) and two-dimensional Wulff construction representing a hypothetical hexagonal MoS₂ nanocluster together with the definition of the shape factor f where l_s is the accumulated length of the S-edges, and l_{total} is the total edge length (d).³⁷

2.2.3. Amorphous Molybdenum sulfides

This class of material was discovered to be HER active only recently and was applied in several photoelectrochemical and photocatalytic water splitting devices. They possess an important surface area due to their morphology endowing them with high electrode activity. These materials can be synthesized using wet chemical reactions with no thermal sulfurization treatment.²⁷ Interestingly, physical and chemical characterizations showed that this kind of amorphous material has close composition to MoS₃ but changes immediately its surface composition to MoS₂ when a cathodic potential is applied.^{38,39} It is assumed that the electrochemical active site reassembles to crystalline MoS₂.

Furthermore, it was reported that catalytic sites consisted of uncoordinated sulfur atoms with negative charges. As a result, proton adsorption and conversion into H₂ is facilitated. Nevertheless, one of the big disadvantages of MoS_x catalysts is their low intrinsic electrical conductivity which is retarding electron transport during HER and consequently deteriorates overall HER activity.⁴⁰

2.2.4. Methods improving MoS₂ HER-activity

- *Doping*

Small amounts of transition metals dopants as Co and Ni were established to be efficient HER promoters.⁴¹ This strategy was used for the hydrodesulfurization (HDS) reaction to increase the number of active sites and their intrinsic activity.^{37,42} STM studies revealed that these dopants are located majorly on the S-edges allowing to modify hydrogen bonding energy at the S-edges. Similar to HDS reaction, doping with Co and Ni demonstrated as well an increase of HER activity.⁴³ This beneficial effect might be correlated to a decrease in ΔG_{H^*} as demonstrated by DFT calculations.⁵

Therefore the introduction of a promoter is interesting because it allows to increase the number of active sites and to reduce ΔG_{H^*} simultaneously. Greater gains would be perhaps possible via other transition metal dopants and transition metal sulfide combination such as NiWS₂, CoWS₂, NiMoS₂.

Besides, transition metals dopants had the same beneficial effect on amorphous MoS₂. Cobalt doping was the most beneficial for boosting HER activity.⁴⁴ The Co-doped amorphous MoS₂ exhibited a larger surface area, higher H coverage causing a considerable increase in HER activity.

Heteroatoms as for instance phosphor can also act as promoter. Indeed P-dopants have been recently revealed as HER activity enhancer.⁴⁵ The introduction of P into MoS₂ may create defects and increase HER activity. Guruprasad et al. have doped MoS₂ with various NH₄H₂PO₄ concentration to obtain P-MoS₂ catalysts. They have demonstrated the beneficial effect of P-dopants in acidic and alkaline media. By increasing the concentration of P from 3% to 5% the Tafel slope was considerably lowered in acidic and alkaline media (Table 3).

Table 3: HER Electrocatalytic Performance of prepared catalysts in 0.5 M H₂SO₄ (left) and in 1 M KOH (right).⁴⁵

| catalyst | η_{10} (mV) | onset potential (mV) | Tafel slope (mV dec ⁻¹) | catalyst | η_{10} (mV) | onset potential (mV) | Tafel slope (mV dec ⁻¹) |
|--------------------------------|------------------|----------------------|-------------------------------------|--------------------------------|------------------|----------------------|-------------------------------------|
| 5% P-MoS ₂ /N,S-rGO | 94 | 88 | 47.2 | 5% P-MoS ₂ /N,S-rGO | 390 | 250 | 110 |
| 5% P-MoS ₂ /rGO | 116 | 98 | 53.6 | 5% P-MoS ₂ /rGO | 490 | 400 | 125 |
| 5% P-MoS ₂ | 133 | 101 | 59.5 | 5% P-MoS ₂ | 525 | 520 | 130 |
| 4% P-MoS ₂ | 149 | 105 | 60.7 | 4% P-MoS ₂ | 527 | 550 | 141 |
| 3% P-MoS ₂ | 170 | 120 | 71.5 | 3% P-MoS ₂ | 588 | 580 | 190 |
| MoS ₂ | 229 | 198 | 88.7 | MoS ₂ | 694 | 679 | 185 |

Lithium ions can be used as well as dopants to increase HER activity. Yet, its intercalation has three effects on molybdenum disulfide's electronic structure:²⁷

- They increase the layer spacing which changes the electronic band structure. Eventually MoS₂ is exfoliated into individual layers.
- Li changes the d-band filling and reduces the oxidation state of Mo which results in changing H-binding energy and enhancing HER activity.
- 2H semiconducting phase is transformed into 1T metallic phase at high Li content. This phase transformation can lead to an increase of conductivity and potentially activate the inert basal plane.

Indeed, the last point is easy to implement by adding n-butyllithium and water into the preparation of the catalyst. 1T-phase MoS₂ exhibited a superior HER activity than 2H-MoS₂. This observation can be explained by the fact that Li⁺ had increased not only the number of active sites but also decreased the charge transfer resistance R_{ct}.⁴⁶ The decrease in R_{ct} and electron diffusion energy allows better conductivity thanks to faster charge transport.

However 1T-MoS₂ is not only obtained by ion interaction. Bolar et al. demonstrated the possibility to synthesize a mixt 1T/2H phase via nitrogen doping.⁴⁷ Because of the π -donating character of nitrogen, the t_{2g} energy state of 1T phase can be stabilized (Figure 14).

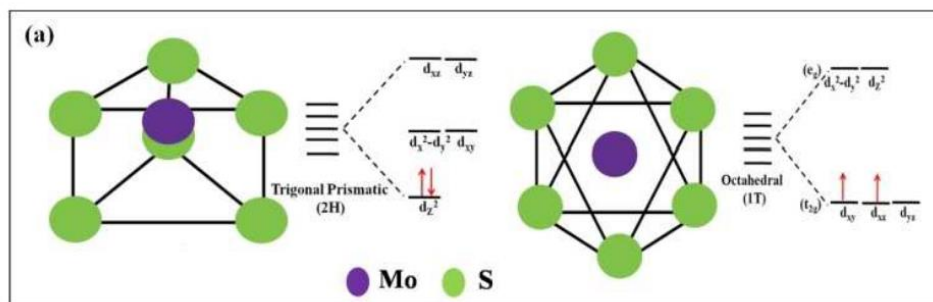


Figure 14 : *d*-Orbital splitting of Mo in trigonal prismatic (2H) and octahedral (1T) coordination environment.⁴⁸

The incorporation of N into the structure is lowering the Mo-S bond energy (due to its higher electronegativity 3.04 compared to 2.54) and consequently decreases the energy barrier of phase transition allowing this conversion. A mixture of two phases (2H/1T) was obtained resulting in an enhancement of HER activity in alkaline media. NMS2 ($x=0.0738$) revealed itself to be the most performant catalyst with the lowest band gap energy of 2.10 eV, low overpotential of 109 and 141 mV, low Tafel slope value of 37 and 44.4 mV/dec in acidic and alkaline media respectively (Figure 15).

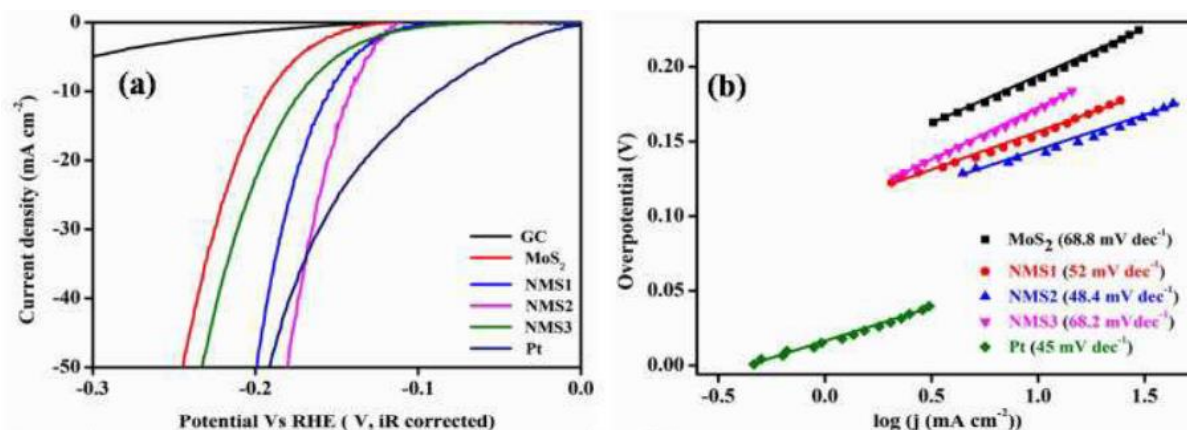


Figure 15: (a) HER polarization curves (iR corrected) of MoS₂, NMS1, NMS2, NMS3, GC, Pt/C. (b) Corresponding Tafel Plots (All the electrochemical tests were performed in 1 M KOH, NMS1, NM2, NMS3 corresponding to higher N loading in bulk 2H-MoS₂).⁴⁷

Moreover, the results show that in acidic media the rate determining step is Heyrovsky and the HER occurs under a Volmer-Heyrovsky mechanism. Meanwhile in alkaline

media the Volmer step is the rate determining step but further interpretation on the mechanism cannot be concluded.

Besides, the introduction of P-dopants is endowing MoS₂ catalyst with longer stability and durability. After 20 h, under an overpotential of 300 mV, the current density of P-MoS₂ stayed constant in acidic media.

Wang et al. have recently reported about an amorphous phosphorus-doped MoS₂ electrocatalyst (P-MoS₂ⁱⁱ) exhibiting better HER activity with a smaller Tafel slope (39 mV/dec) compared to conventional MoS₂ (50 mV/dec) catalysts and good stability in acidic media after 1000 cycle turns.⁴⁵ Wang and his team explained that the enhancement of intrinsic HER activity could be correlated to the amorphous microstructure of phosphor.

Since P-doping is a rising subject study, not many information is to be found on this issue. It would be interesting to study its effect via FTIR-spectroscopy on MoS₂, analyze the forms species and their role in HER and compare these results with N-doping.

- ***Number of MoS₂ layers***

Keeping the concept of highly catalytic active 1T-MoS₂ HER electrocatalyst, Seo et al. have established the quasi linear correlation between HER activity and the number of stacked layers of 1T-MoS₂ via TOF and DFT results.⁴⁹ The size of the basal plane was maintained constant. Seo et al. have observed that the activity increased with decreasing number of 1T-phase layers basically emphasizing the highest activity for MoS₂ monolayers. The observed enhancement of HER activity of few layered MoS₂ slabs was presumed to be originated by the formation of a high amount of edge sulfur sites and better intrinsic conductivity on monolayers compared to multilayers.

- ***Functionalizing with electron donating groups***

Benson et al. have demonstrated the beneficial effect of functionalizing 1T-phase MoS₂ with electron donating organic compounds (Figure 16).⁵⁰ Indeed by creating covalent

ⁱⁱ H₃Mo₁₂O₄₀P · xH₂O as precursor

S-C bonds, the metastable 1T phase is stabilized and leads to long term HER activity. Moreover, functionalizing with Et₂NPh prevents the transformation of metallic 1T phase into thermodynamic stable, semiconductor 2H phase during HER.

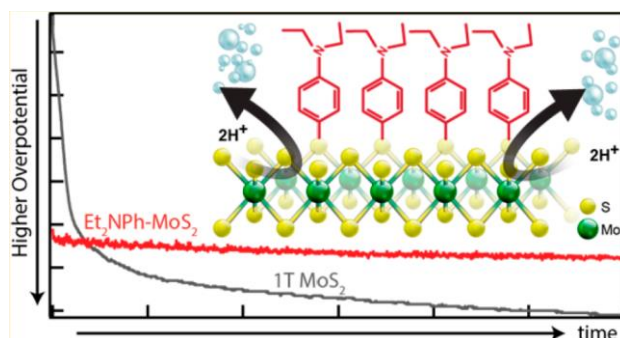


Figure 16: Impact of Et₂NPh on 1T-MoS₂ during time and HER activity.⁵⁰

- **Nanocarbon materials as catalyst carrier**

One of the main advantages of carbon is its many structure combination (graphene, nanotubes etc.) with high surface area that can be modified for high conductivity. In the following a few examples of functionalized and high conductive carbon structures will be elaborated.

One way to increase the TOF of active sites is to use reduced graphene oxide (RGO) as a support for MoS₂ nanoparticles.⁵¹

RGO is a 2D material characterized by its intrinsic high conductive properties giving rise to synergetic effect. The binary system MoS₂/RGO exhibited high HER activity with a low Tafel slope and overpotential. The enhancement in activity is due to the increase of exposed active edge sites per surface area. The RGO support enables better dispersion of MoS₂ particles, eventually leading to better active site access and probably better electron charge transfer.^{10,39,45}

Later on, new ternary systems were created like Mn/MoS₂/RGO, CoS₂@MoS₂/RGO with superior activity.

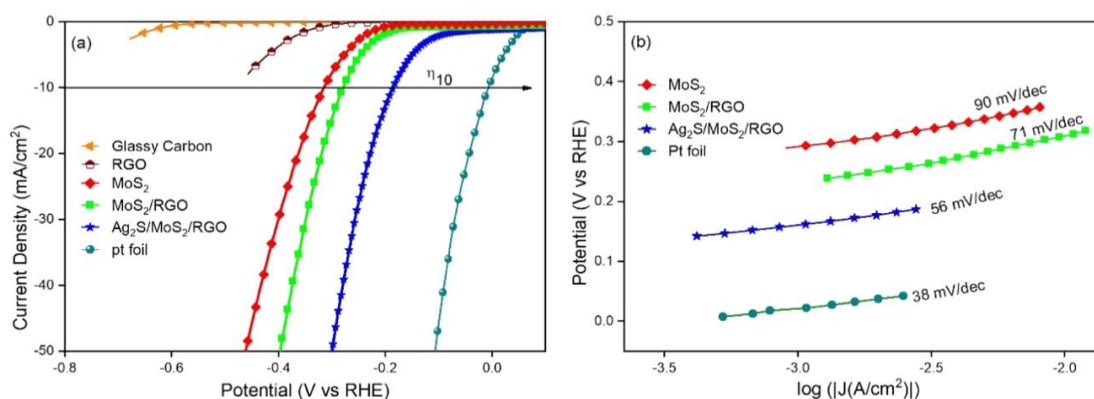


Figure 17: (a) Polarization curves of HER for various MoS₂ based catalysts up to -50 mA/cm². (b) Tafel plots of the corresponding electrocatalyst.¹⁰

Solomon et al. were successful in creating another efficient ternary system composed of Ag₂S/MoS₂/RGO via hydrothermal method.¹⁰ Compared to bare MoS₂/RGO the new catalyst exhibited higher activity (Figure 17). Solomon and co-workers explain this superior activity as a result of a synergetic effect between the two sulfides. Moreover Tafel slope values has also decreased from 71 mV/dec to 56 mV/dec indicating that the reaction between an adsorbed proton and a free one was facilitated. Another reason explaining the superior activity is the fact that the ternary system has a lower charge transfer resistance compared to the other catalyst allowing a fast electron transfer at the electrode-solution interface.

Similarly, functionalized carbon materials had been proved to be an efficient way to boost electronic charge transfer. The introduction of heteroatoms such as nitrogen, phosphor, boron, and sulfur into the structure of carbon nanotubes (CNT) and RGO increases significantly the activity.⁵²

These dopants replaced sp² carbon atoms which allowed to modify the electronic structure in carbon materials and subsequently improving the adsorption/desorption of hydrogen.

Doping of carbon carrier can also increase its electrical conductivity. D. Li and his team layered amorphous molybdenum sulfide (MoS_x) on N- doped carbon nanotube (NCNT) forest surface via wet chemical process.⁴⁰ The new catalyst was more active than amorphous MoS_x. This enhancement was explained to be generated by the N-doping

of the carrier leading to a higher conductivity. Moreover the particular morphology of the carrier has contributed to the improvement of charge transfer. Lis' work shows a great example of amorphous materials application in HER catalysis and the importance of surface engineering.

Another carbon support that could be promising is graphitic carbon nitride $g\text{-C}_3\text{N}_4$ who is endowed with HER activity.⁵³ Graphitic carbon nitride is composed of tri-s-triazine units (Figure 18). The polymorph has received particular interest for its electronic structure with medium band gap and thermal stability (up to 600°C) that can be used as photo- and electrocatalyst. Its electronic structure can be modulated via doping, functionalizing etc. and this process can be easily industrialized. For instance, S-doping can be realized under H_2S atmosphere at 450°C . Moreover, $g\text{-C}_3\text{N}_4$ compared to other carbon materials is not black and consequently could be studied by FTIR spectroscopy. Yet, his many functions could complicate FTIR analysis.

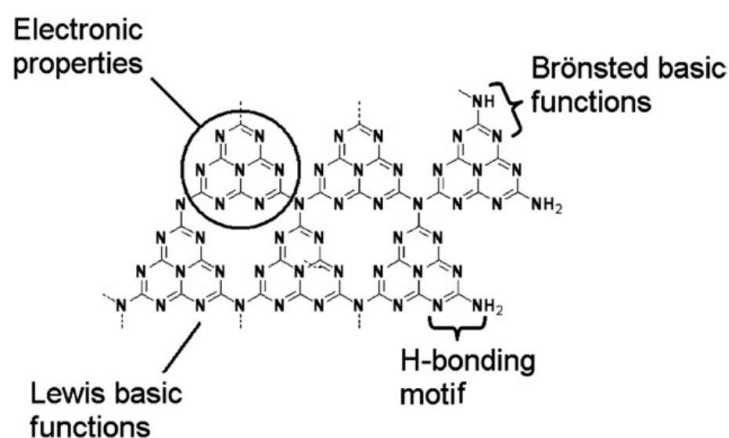


Figure 18: Multiple functionalities of $g\text{-C}_3\text{N}_4$ as a catalyst.⁵⁴

Synthesis of this semiconductor support is also easier and less time expensive than other nanocarbon materials. Niu et al. developed a simple environment friendly method to synthesize $g\text{-C}_3\text{N}_4$ nanosheets.⁵⁵ The bulk $g\text{-C}_3\text{N}_4$ was heated at 500°C for 2 h with a ramp rate of $5^\circ\text{C}/\text{min}$ in an open ceramic container. The modified support possessed larger surface area and small sheet thickness, enhanced electron mobility meaning better conductivity and also improved photocatalytic activity compared to

the bulk one. Later on, the improvement of HER activity of g-C₃N₄ nanosheets based electrocatalysts compared to the bulk one was demonstrated.⁵⁵

Iqbal et al. were also successful in synthesizing highly electroconductive g-C₃N₄ nanosheets by calcining a solution of melamine and ammonium sulphate in equal amount (Figure 19).⁵⁶

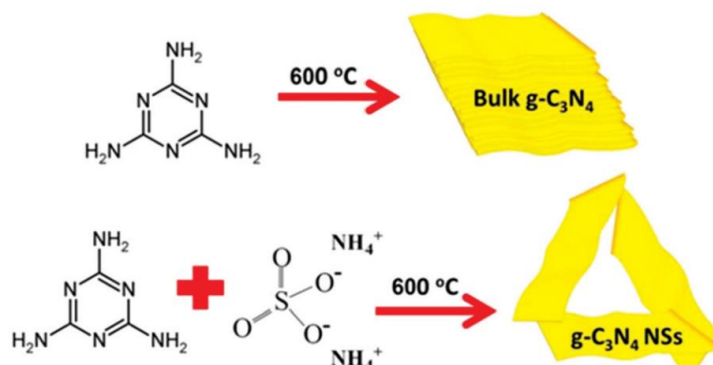


Figure 19: Schematic illustration of g-C₃N₄ synthesis.⁵⁵

2.3. Carbides

Carbides are also known as promising HER catalysts due to their interesting conductivity and stability in alkaline media.

One of the most active carbide is molybdenum carbide (Mo₂C). Hu et al. reported in 2012 that Mo₂C was showing good electrocatalytic performance for HER in acidic and alkaline media.⁵⁷ As a matter of fact Mo₂C is corrosion resistant, high electric conductive and present a Pt-like d-orbital electronic structure. Many efforts had been made to improve HER activity of this transition-metal carbide. However, one drawback of Mo₂C is the high quantity of empty d-orbitals in its structure creating negative-hydrogen binding energy and restricting the desorption of adsorbed hydrogen. In order to overcome this drawback, the amount of unoccupied d-orbitals needs to be reduced by introducing electronic rich transition metals (e.g. Co, Ni).⁵⁸ This kind of strategy allows to optimize the binding energy and thereby the activity.^{58,59} By doping Mo₂C

with Co HER activity was boosted because d-orbitals were effectively occupied. Ni exhibited same beneficial impact.

To boost electrical conductivity and consequently HER activity of Mo_2C , it is possible to use nitrogen doped carbon matrix.⁶⁰ The metal free anions are optimizing the electronic structure of Mo_2C via the hybridization between the electronic-rich p-band of N and other anions (e.g. S, P) and the d-band of Mo_2C . While N-doping resulted in increasing the number of active sites,⁶¹ P was speculated to improve HER kinetics due to his lower electronegativity. Z. Li et al. demonstrated with the help of DFT calculations that P and Ni co-doping and P-doping can synergistically optimize the hydrogen-binding energy of Mo_2C and HER performance.⁵⁸ The obtained activity increased as followed with lower Tafel slopes: Ni/NC, $\text{Mo}_2\text{C}@NC$, Ni- $\text{Mo}_2\text{C}@NC$, P- $\text{Mo}_2\text{C}@NC$, P/Ni- $\text{Mo}_2\text{C}@NC$.

One remarkable way to enhance HER activity is to couple molybdenum carbide with carbon materials having high conductivity, surface area or doped by heteroatoms as specified before. However, this kind of catalyst are synthesized in form of powder and need to undergo coating or casting process with the help of additives and polymeric binders in order to construct a working electrode. Those process are time consuming and relatively expensive. Consequently, self-supported electrocatalysts forming for example free-standing films or growing on conductive layers would be more advantageous since no additives or binders are required and less time-consuming.

Usually this new class of HER catalyst has excellent mechanical stability, good electrical conductivity and large surface area. However, there are only a few self-supported HER catalysts.⁶² In this context Xiao et al. were successful in proposing a simple and cost-efficient synthesis process for biocarbon fiber (BCF) on Mo_2C via an annealing treatment on cotton T-shirt.⁶³ BCF/ Mo_2C exhibited high activity and long stability in acidic and alkaline media due to the presence of Mo_2C . Xiao's work demonstrated also the good activity of other carbides such as VC and W_2C .

2.4. Polymers

High active acidic HER catalysts were also obtained via polyaniline $[C_6H_4NH]_n$. Polyaniline (PANI) is an organic polymer known for its conductive properties and good stability in contact with water and oxygen.⁶⁴ As a result PANI received more and more interest in heterogeneous catalysis (e.g. supercapacitors, HER catalysis) for its application as a support and also as a source of nitrogen doping after a well-controlled calcination phase.⁶⁵

The heterostructured catalyst WO_3 /polyaniline (PANI) synthesized by Wang's work exhibited superb HER activity with low overpotential and small Tafel slope close to Pt/C.⁶⁶ This excellent activity is due to the d- π interfacial electronic coupling between WO_3 and PANI optimizing the electronic structure of PANI surface. DFT calculations have shown that the antibonding state is lowered with higher electron occupation and as a result leads to a weaker interaction between catalytic surface and adsorbed proton. Thereby the activity of HER is triggered on inert PANI surface. In short, the active phase is WO_3 while PANI pumps electrons into the active phase allowing higher conductivity and fast kinetics.

Djara et al. synthesized an efficient alkaline HER catalyst by polymerizing aniline into polyaniline (PANI) in the presence of Ni(II) and Co(II) followed by calcination in air at 550°C.⁶⁵ **Erreur ! Signet non défini.** A mesoporous heterogeneous catalytic material which is self-supported onto a matrix made of C, N, S, Ni and Co was obtained. SEM images show clearly the presence of truncated octahedron particles corresponding to $NiCo_2O_4$.

It would be interesting to synthesize such a catalyst based on a conductive polymer (PANI or other polymers) with MoS_2 as active site which was shown to be also very active.^{29,67} However, one massive drawback of PANI is its thermal stability (Figure 20). Wang et al. have demonstrated that pure PANI is decomposed at 250°C.²⁹ By adding for example MoS_2 , the thermal stability can be slightly improved.

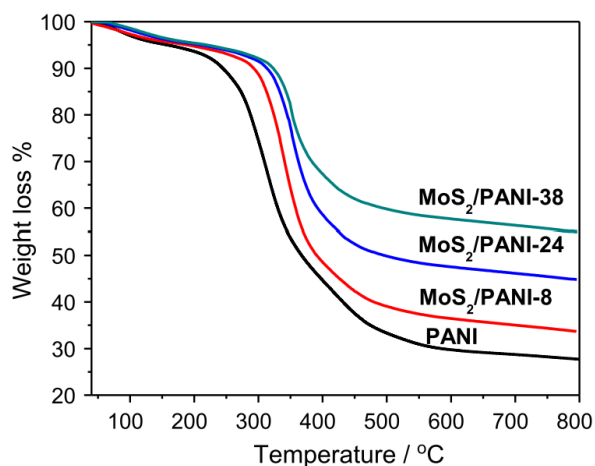


Figure 20: TGA of 8, 24, 38%wt MoS₂/PANI and pure PANI.²⁹

2.5. Conclusion

To conclude, there exist many potential HER electrocatalysts. Each group has its advantages and disadvantages as summarized in Table 4. After this profound study of possible candidates, MoS₂ is for the moment the best HER electrocatalyst considering its performance, durability, comparable free Gibbs proton adsorption energy to Pt and easy affordable synthesis. Since IR analysis should be conducted, the transparency of the carrier has to be considered. As a result, carbon supports cannot be studied as well as carbides due to transparency issues. The synthesis of PANI is time consuming and overall MoS₂-PANI isn't stable at high temperature. Consequently, a conductive metal-oxide needs to be a carrier.

Table 4: An overview of potential HER catalysts with their advantages and disadvantages, synthesis method and activity.

| Advantage/disadvantage | Methods to increase activity | Synthesis | Example | electrolyte | η_{10} (mV) | Tafel slope (mV/dec) | |
|---|--|--|---|-------------------------------------|------------------|----------------------|----|
| Metal oxide | | | | | | | |
| ✓ Optimal hydrogen adsorption energy | OVs control | Thermal treatment under Argon | WO _{2.9} | 0.5M H ₂ SO ₄ | 70 | 50 | 18 |
| ✓ High electron conductivity | | | WO _{3-r} NSs | | 38 | 38 | 18 |
| ✓ Degenerated semiconductor independent of T° via OVs control | Doping (S, P, metal...) | Hydrothermal sulfidation | S-MoO ₂ -NS | | 176 | 57 | 20 |
| ✓ Stability in acidic media | | Solvothermal | P-MoO _{3-x} -NS | | 166 | 42 | 20 |
| ✓ Stability in alkaline media in presence of Ni, Fe. | | | 10%MoW ₁₈ O ₄₉ | | 23 | 54 | 22 |
| ✓ Oxidation resistant | | Hydrothermal treatment | | | | | |
| ✓ Long durability 10-12h | | | | | | | |
| ✓ Easy synthesis | | | | | | | |
| Oxyhydroxide LDH | | | | | | | |
| ✓ Alkaline stability | Metal doping | Solvothermal | VOOH-3Fe | 1M KOH | 90 | 38 | 26 |
| ✓ Synergetic effect allowing adsorption of H and OH | | | MoS ₂ /NiCo-LDH | 1M KOH | 78 | 77 | 68 |
| ⊖ Multiply step synthesis | Combination with other active structures | | | | | | |
| Transition metal dichalcogenides | | | | | | | |
| ✓ Acidic stability | Doping | Solvothermal or sulfidation | MoS ₂ | 0.5M H ₂ SO ₄ | 400 | 149 | 69 |
| ✓ Thermodynamically stable | | | MoS ₂ /g-C ₃ N ₄ | | 260 | 63 | 69 |
| ✓ Easy synthesis | Intercalation with Li, K, Na | Solvothermal/solvation | 1T-MoS ₂ | | 230 | 45 | 70 |
| ✓ Earth transition metals abundant | | | Ca/1T-MoS ₂ | | 190 | 46 | 70 |
| | | | Ni/1T-MoS ₂ | | 191 | 47 | 70 |
| Carbides | | | | | | | |
| ✓ Alkaline and acidic stability | Deposition | Solvothermal synthesis and calcination | BCF/Mo ₂ C | 0.5M H ₂ SO ₄ | - | 84.8 | 63 |
| ✓ Corrosion resistant | on | | | 1M KOH | 71 | 52.4 | |
| ✓ High electron conductivity | conductive support | | | | | | |
| ✓ Long durability | Doping | | P/Ni-Mo ₂ C@N C | 1M KOH | | 53.61 | 58 |
| PANI | | | | | | | |
| ✓ Acidic and alkaline stability | | Polymerization | W ₁₈ O ₄₉ /PANI | 0.5M H ₂ SO ₄ | 74 | 46 | 65 |
| ✓ Organic | | | | | | | |
| ✓ Highly conductive | | | PANI-NiCo | 1M KOH | 180 | 79 | 65 |
| ⊖ Low thermal stability | | | | | | | |

3. MoS₂/TiO₂ electrocatalyst for HER

Based on the bibliographic analysis, MoS₂ will be the studied active phase for HER electrocatalysis. Transition metal dichalcogenides as mentioned before could one day render low-cost and high scale production of dihydrogen feasible. Moreover MoS₂ presents a wide range of possible applications such as in battery, transistors and fuel cells. Consequently, understanding its surface behavior and characteristics is crucial. They are easy to synthesize, environment friendly, abundant and stable in acidic and alkaline media.

Although they present comparable ΔG_{H^*} to Pt, they present low HER activity due to low edge exposition and electrical conductivity. In order to increase the edge's exposition a carrier with high BET surface should be used. Based on our bibliographic study, the carrier should be stable in acidic media, electrically conductive and be transparent in IR. These conditions are limiting the choices and a compromise needs to be made. Therefore, the transparency, high BET surface and stability were prioritized leading to choose TiO₂ as a carrier. Indeed, TiO₂ is stable in acidic media, presents high BET surface but is a semiconductor with quasi inexistent conductivity at room temperature ($\sim 10^{-10}$ S/m).⁷¹ In order to observe a certain activity in HER its electrical conductivity needs to be enhanced. Moreover when MoS₂ is dispersed on TiO₂, the creation of large slabs is favored due to strong Van der Waals interactions between those two layers,⁷² consequently rendering MoS₂ dispersion low.

In the following, several possible strategies are summarized in order to enhance the electrical conductivity of TiO₂. Moreover, we will try to obtain a better overview on MoS₂/TiO₂ characteristics as described in the literature and discuss the possible HER mechanism on active phase MoS₂. It should be noted that MoS₂/TiO₂ was already a subject for few photocatalytic HER studies exhibiting good activity (Tafel slope around 95 mV/dec depending on synthesis method and used polymorph), stability and durability.⁷³ Yet, due to the low electrical conductivity of TiO₂, it was never a subject of

research for electrocatalytic HER. Moreover MoS₂/TiO₂ has never undergone a profound FTIR-spectroscopy analysis for explaining HER activity.

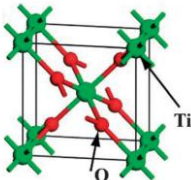
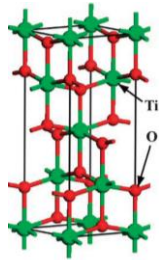
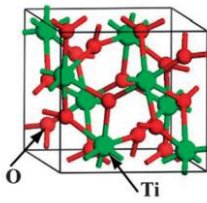
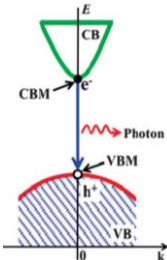
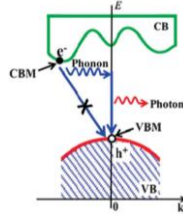
3.1. TiO₂: characteristics, its polymorphs and boosting its electrical conductivity

3.1.1. TiO₂ polymorphs

The metal oxide TiO₂ had been studied for a long time for its photo- and electrocatalytic properties especially for water splitting in both alkaline and acidic media. Its low cost and easy preparation, environment friendliness and stability make large-scale hydrogen production feasible. However to induce the hydrogen evolution reaction, TiO₂ needs to be irradiated with UV which corresponds only to 8% of the sunlight spectrum and the conductivity must be enhanced to increase HER activity.

Many researches aimed to increase the adsorption spectrum of TiO₂ in to higher wavelengths. Creating defaults on the catalytic surface such as oxygen vacancies and doping resulted to be an efficient method to increase the adsorption wavelength (i.e. including the visible spectrum making 45% of sunlight rage) and electron mobility. Besides, TiO₂ has three polymorphs (Rutile, Anatase, Brookite) endowed with different HER activity. This fact offers a variety of potential carriers. The conductive and structural characteristics are summarized in Table 5. Based on those characteristics TiO₂ anatase is the most adequate polymorph as a carrier. Indeed, compared to rutile, anatase is endowed with a larger specific surface allowing a better dispersion of Mo. Besides due to its mall effective mass indicating a faster transfer rate of holes and electrons, an easier charge transfer under photoexcitation can be expected. However, it should be emphasized that we are working under non-photoelectrical conditions and such effective charge transfer might not be observed under electrical tension.

Table 5: Comparison between the three polymorph forms of TiO₂.⁷⁴

| Polymorph | Rutile | Anatase | Brookite |
|--|--|--|---|
| Structure | Quadratic P  | Quadratic I  | Orthorhombic  |
| Thermodynamic stability | Stable phase | Metastable phase (< 500°C) | Metastable phase (at room temperature) |
| Synthesis | Hydrothermal | Hydrothermal TiCl ₃ precursor | Difficult synthesis |
| Characteristics | <ul style="list-style-type: none"> - Larger grain size - lower specific surface areas - lower surface adsorption capacity | <ul style="list-style-type: none"> - higher surface adsorption capacity due to OH groups and lower charge carrier recombination rate. - Lifetime of photogenerated electrons and holes is larger → enhancing the chance of photoexciting and holes participating in reactions | - |
| Band gap | 3.0 eV | 3.2 eV | 3.3 eV |
| Effective mass of electrons (m_e/m₀) via DFT | 0.0949 | 0.0948 | 1.4610 |
| Effective mass of holes (m_h/m₀) via DFT | 0.5620 | 0.1995 | 0.4345 |
| Consequence of effective mass | <p>small effective mass indicating the transfer rate of holes and electrons in anatase is the fastest among the three materials.</p> <p>⇒ Photoexcited charge carriers of anatase migrate and transfer easily to the surface from its interior to participate in photocatalytic reactions.</p> | | |
| Type of semiconductor | <p><i>Direct band semiconductor</i></p> <p>k is the electron wave vector and its momentum is conserved in CB and VB:</p> $k_{e(\text{VBM})} = k_{e(\text{CBM})}$  | <p><i>Indirect band semiconductor</i></p> <p>recombination of photoexcited electrons and holes is assisted by phonon:</p> $k_{e(\text{VBM})} \neq k_{e(\text{CBM})}$  | <p><i>Direct band semiconductor</i></p> $k_{e(\text{VBM})} = k_{e(\text{CBM})}$ |
| | | <p>diffusion length and reaction time of the electron and hole excited increases. => better photocatalytic performance than direct semiconductor.</p> | |

It was also reported that the activity of TiO₂ can be enhanced via doping, self-doping (Ti³⁺) and oxygen vacancies.^{75,76} Combining these findings with the active phase MoS₂ could have an effect on activity and slab morphology.

3.1.2. Methods increasing TiO₂ conductivity

3.1.2.1. Oxygen vacancies and Ti(III) self-doping

The creation of oxygen vacancies is an easy and efficient way to increase HER activity.⁷⁷ The electron transfer is facilitated by reducing the band gap from 3.2 eV to 2.02 eV and renders also the metal oxide more stable to oxidation. In order to convert pristine TiO₂ into TiO_{2-x} a simple hydrothermal process is sufficient (Figure 21). At 400°C for 5h under H₂/Ar atmosphere (5 and 95%vol respectively) oxygen vacancies are created. Above 450°C, parallelly to the formation of oxygen vacancies, Ti⁴⁺ is reduced to Ti³⁺ which are mostly considered to be Ti (III) interstitials in TiO₂ matrix resulting in the reduction of optical band gap.

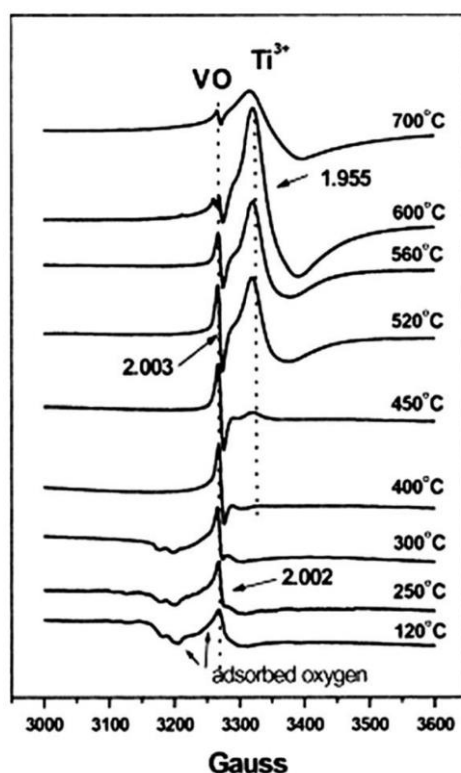


Figure 21: Electron spin resonance spectra of oxygen vacancies (VO) and trivalent titanium (Ti³⁺) in TiO₂ during the H₂ treatment.⁷⁷

Furthermore, it was observed that oxygen vacancies are more likely to be formed in anatase than in rutile whereas Ti-interstitials are favored in rutile under oxygen poor conditions and

high temperature. It was shown that the creation of oxygen vacancies and low coordinated Ti ions (Ti³⁺) on rutile TiO₂ dominated HER activity.⁷⁸ They allowed to achieve higher conductivity by modulating electron mobility, facilitating charge transfer and water adsorption in alkaline media. Moreover, the obtained catalyst had high stability and durability.

Another way to create oxygen vacancies (OVs) is doping with nitrogen. DFT calculation had demonstrated that N-doping reduces the formation energy of OVs in bulk TiO₂.⁷⁷ Consequently photogenerated electron holes are formed which are reducing band gap, improving conductivity and enhancing HER activity. In order to dope TiO₂ with N (TiO_{2-x}N_x), TiO₂ is either mixed with N-precursors such as urea during preparation followed by a calcination step or TiO₂ can be heated at 450°C for 2h under gaseous NH₃ (100ml/min).⁴⁸

3.1.2.2. *Magnéli phase Ti₄O₇*

The Magnéli phase Ti_nO_{2n-1} (3 < n < 10) is a reduced form of TiO₂ characterized by a high amount of oxygen vacancies favoring the formation coordinatively unsaturated Ti centers. The Magnéli form Ti₄O₇ has attracted in recent years a lot of attention especially in the field of Li-batteries due to its high electrical conductivity 1500 S/cm and fast charge transfer.^{71,79} However its synthesis is for the moment the most difficult to put into practice. In order to form a pure and homogenous Magnéli phase Ti₄O₇ high temperatures (1000-1300°C) under Ar/H₂ flow must be used. Several research works have tried to synthesize this phase in milder inert conditions (900-1000°C) via carbothermal or metal-reduction.^{79,80} Yet, those methods were time consuming, energy consuming and did not allow the formation of pure Magnéli phase. Moreover those kind of materials are metals and subsequently present a very low specific surface below 5 m²/g. A few research groups have tried to improve the BET surface but still either remaining below 50 m²/g or they were enhanced but by using exhaustively long steps.^{79,81}

3.1.2.3. *TiO₂ nanotube arrays -TiNTA*

By chemically anodizing Ti-foil ordered, one-directional aligned nanotube arrays (TiNTA) can be synthesized (Figure 22).^{82,83} During the electrochemical process, Ti is oxidized at the surface forming TiO₂ nanotubes which are endowed with higher charge transfers due to the ordered structure. Presenting a good stability in acidic media, TiNTA were used as HER electrocatalyst carriers.⁸⁴⁻⁸⁵ Low overpotential at 10 mA/cm², were obtained on different TiNTA derived

catalysts. Dispersing MoS₂ on those kinds of carriers would be interesting for HER application and IR-analysis.

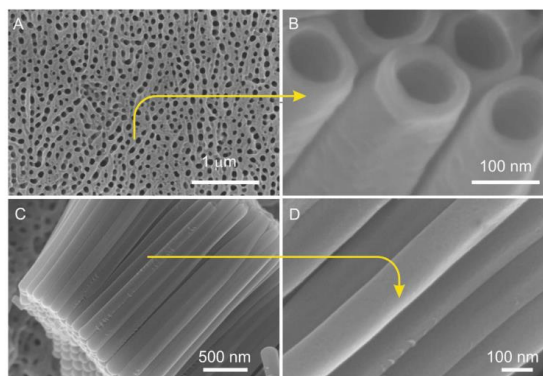


Figure 22: SEM images of TiO₂ nanotube arrays under different resolution.⁸²

3.2. MoS₂ slab morphology on TiO₂

The slab's morphology of impregnated MoS₂ on TiO₂ was already studied at the LCS in the context of HDS reactions. It was demonstrated that between MoS₂ and TiO₂ exists a strong interaction which maintains the triangular shape of MoS₂ slabs.⁷² The strong interaction is due to the forming bond (Ti-O-Mo) during impregnation between oxomolybdate and Ti⁴⁺ located at the support's surface. Because of these strong interaction large slabs with an average length of 6.8 nm are formed and stacked forming mostly bilayers.³⁵ They have a triangular shape due to the solemn presence of M-edge sites. Herein in order to increase edge site exposition the strong interaction between support and MoS₂ needs to be weakened.

3.3. DFT mechanistic study of HER on MoS₂

Understanding HER activity of MoS₂ electrocatalyst means also understanding its HER mechanism. DFT calculations allow to conduct a theoretical mechanistic study and thereby establish an idea of what to expect during operando studies.

W.Li et al. proposed a mechanism via DFT calculations for HER on 2H-MoS₂.³³ The surfaces of the most exposed edges which are (100) and (103) were (Figure 23). On the edges (100) and

(103) both Mo- and S-atom sites are accessible. The solvent effect of H₃O⁺ was incorporated into the DFT calculations since the proton has to be separated from the hydronium complex (H₂O-H-H₂O).

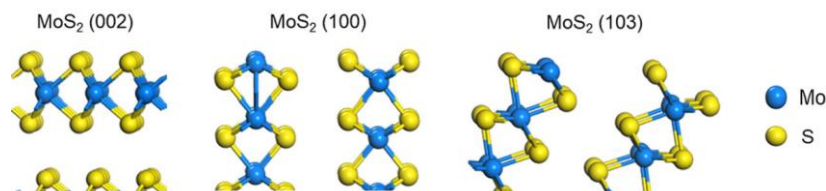
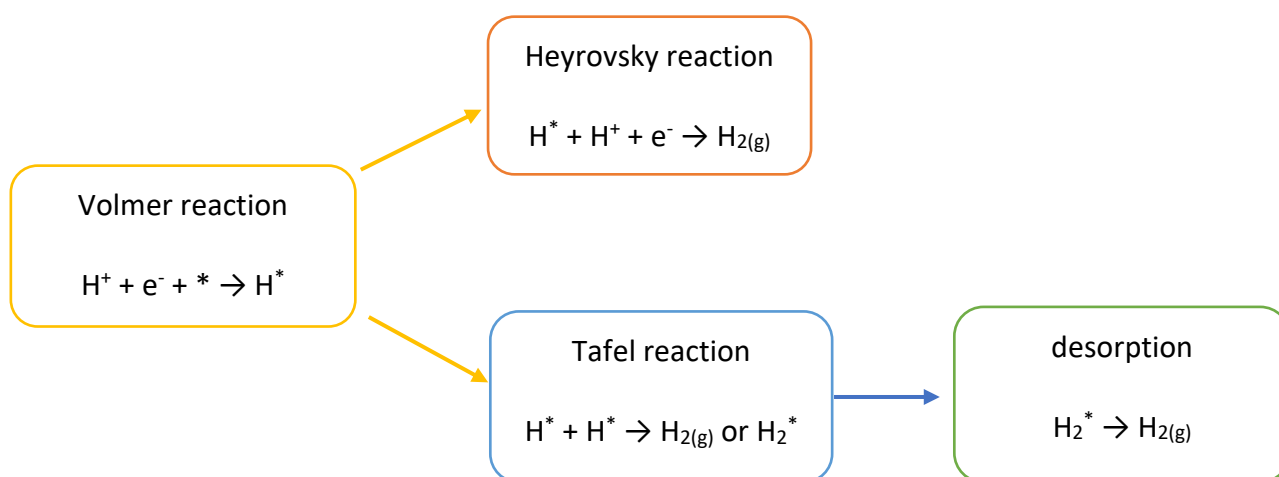


Figure 23: Slab model of 2H-MoS₂ of basal plane (002) and edges (100) (103).³³

As a reminder the global mechanism of HER is composed of several steps (after proton dissociation from H₃O⁺) where two pathways are possible; the Volmer-Heyrovsky or Volmer-Tafel pathway:



W.Li's team analyzed each step separately and proposed the following mechanism. On the edges located on (100) and (103) proton adsorption is favorable on both Mo- and S-atom sites (noted H^{*}-Mo and H^{*}-S respectively). After the proton adsorption on these sites, the hydrogen adsorbed on S-sites migrates to adjacent protonated Mo-sites (H^{*}-Mo). This step is showed to be thermodynamically and kinetically favorable for Volmer-Heyrovsky and Volmer-Tafel pathway. Eventually the migrated hydrogen and H^{*}-Mo will react to form adsorbed H₂ on Mo-site (H₂^{*}-Mo). The desorption of H₂ was determined to be more difficult on Mo-edges which could determine the overall HER reaction rate.

Soriaga and co-workers conducted also mechanistic studies via DFT calculation and consent with the assumption that the production of H₂ via Volmer-Tafel pathway is produced on Mo-

edge sites via the interaction between two adjacent H^* -Mo and H^* -S located on Mo-edges (Figure 24).⁸⁶ The recombination of two adsorbed protons on S-atom sites resulted to be thermodynamically unfavorable.

Soriaga and co. argue also that the Volmer-Heyrovsky pathway seems to be favored on Mo-edges. In contrast to W. Li et al., Soriaga et al. stipulate that H_3O^+ is favorably adsorbed on Mo-atom sites adjacent or not to a protonated S-atom site since electrons are easier transferred from the Mo-H bond to form H_2 (Figure 24).

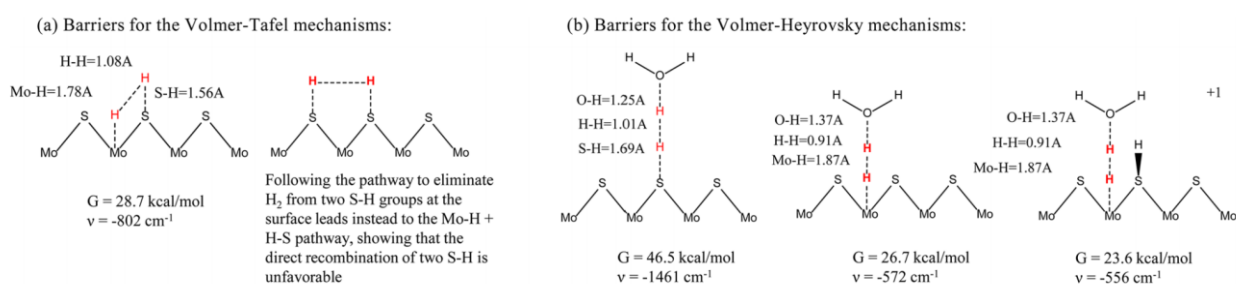


Figure 24 : Schematics of the transition state structures considered for H_2 formation with respective bond lengths, free Gibbs energy and calculated frequencies.⁸⁶

4. Characterization methods

4.1. Fourier Transform Infrared spectroscopy: a characterization and mechanistic study tool

4.1.1. FTIR in-situ spectroscopy

Fourier transform infra-red spectroscopy (FTIR) is an effective and powerful tool to analyze and characterize heterogeneous catalysts surface in particular with the help of probe molecules.

By sending probes such as CO, NO and pyridine under high vacuum on heterogeneous catalysts, surface studies can be conducted. The probe will be adsorbed by the analyzed material, causing a change in its vibration under IR irradiation and give information about the surface.

Depending on the used probe it is possible to characterize the acidity/basicity of the catalyst, quantify Lewis and Bronsted sites, whether or not oxygen and lattice vacancies exist and also analyze the interaction force between adsorbent and active site. In short, this kind of analysis allows to picture the surface of the catalyst in terms of active sites.

4.1.2. Set up

The used FTIR spectroscopy is built of three parts: the evacuation system, the IR cell, and the spectrometer (Figure 25).

The evacuation system, which is connected to a pump system, enables to work under ultrahigh vacuum conditions (10^{-3} Pa) in the IR cell and to introduce and evacuate probe molecules into the cell. The IR cell is "a low temperature glass cell" rendering the sample's analysis at high and low (100K) temperature and as well at atmospheric pressure is possible. The flow of Argon, H_2 and H_2S can be controlled and changed easily via mass flow controllers. The spectrometer is a Fourier Transform IR spectrometer from Nicolet, with a MCT (Mercury Cadmium Telluride) detector. At the LCS, the IR set-up was innovated. The new set-up called the PELICAEN allows a better temperature control of the sample essential for approaching real conditions. Moreover the sample holder build of platinum is moved up and down automatically.

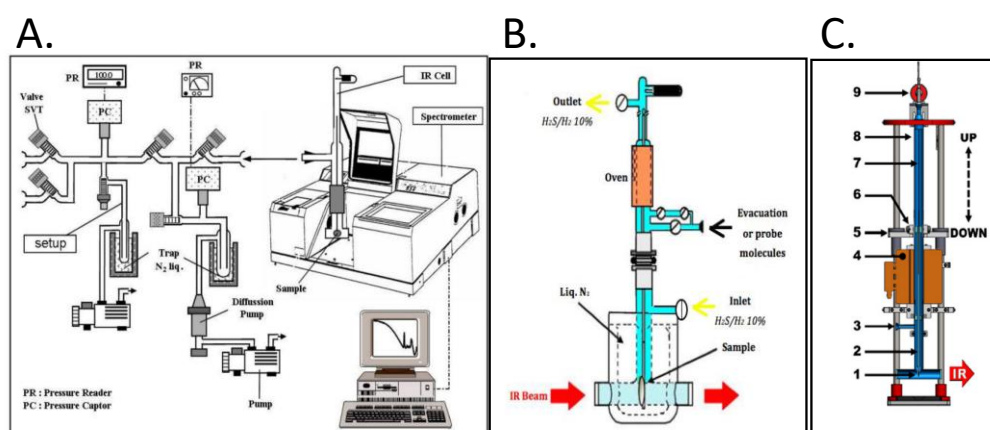


Figure 25 : Set up of FTIR spectroscopy (A.) and of IR-cell showcasing the older version (B) with the new version, the PELICAEN (C).⁸⁷

4.1.3. IR/CO study of MoS₂

CO is a universal probe molecule allowing quantitative and qualitative analysis. During the adsorption of CO by a metal atom, the 5 σ orbital of CO is hybridizing with the unoccupied state of the metal by transferring part of its electrons. Afterwards the electrons from the metal d-orbital can be transferred back to the lowest occupied orbital of CO 2 π^* via hybridizing. This process is called π back-donation (M \rightarrow CO) and is translated on the FTIR spectra by a downward shift. The stronger the back donation is, the more the stretching frequency of C-O is decreasing. Vis versa the σ donation (CO \rightarrow M) is demonstrated via an upward shift (Figure 26).

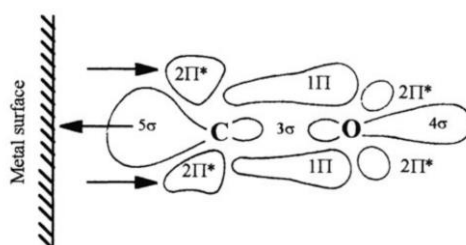


Figure 26 : π back-donation and σ -donation between metal and CO probe molecule.⁸⁸

The morphology of the MoS₂ slab was already studied profoundly with CO. The probe molecule permits to differentiate M- and S-edges from each other. As explained before, the HER active sites on 2H-MoS₂ are located on the edges whereas on 1T-MoS₂ the main active sites are believed to be located on the basal plane. Consequently, being able to distinguish active sites on the edges and basal plane is crucial.

In the literature, several empiric and theoretical studies were conducted by IR/CO on unpromoted MoS₂/Al₂O₃.^{35,89,90} The obtained frequencies for each vibration band are reported in Table 6.

Table 6 : CO/IR Vibration frequencies for unpromoted MoS₂.^{90,91}

| v (CO) experimental (cm⁻¹) | v (CO) DFT calculated (cm⁻¹) | assignment |
|--|--|--|
| 2130 | - | Partially sulfided |
| 2110 | 2110 | M-edge (50% sulfur coverage) |
| 2098 | 2087 | M-edge (37.5% sulfur coverage) |
| 2065 | 2078 | S-edge (100% sulfur coverage) |
| 2040 | - | S-edge (sulfur coverage between 75-100%) |
| 2020 | 1989 | S-edge (75% sulfur coverage) |
| 1995 | - | Metallic Mo (Mo ⁰) |

4.2. Raman spectroscopy

Raman spectroscopy is a powerful tool to analyze metal oxides and their coordination since their absorption range is below 1000 cm⁻¹, a region hard to interpret in FTIR due to cell window absorption. Depending on the coordination of the metal with oxygen, the Raman band position is different. Moreover Raman allows to distinguish 1T-MoS₂ from 2H-MoS₂ and verify the presence of molybdenum oxide and sulfide salt. The different attributions reported in the literature for heteropolymolybdate ions and MoS₂ polytypes are summarized in Table 7 and in Table 8. Based on the reported Raman modes of 1T-MoS₂ and 2H-MoS₂ it might be difficult to interpret Raman spectra of MoS₂ supported on TiO₂. In fact Raman modes of TiO₂ E_g(1) and B_{1g}(1) located at 157 and 397 cm⁻¹ respectively are overlapping with the acoustic phonon mode J₁ of 1T-MoS₂ and the out-of-plane vibration E_{2g} of 2H-MoS₂. Herein it might be more challenging to discriminate the formation of these two phases and other characterization tools will be needed in order to confirm their presence.

Table 7: Raman vibration attributions for different molybdenum oxide and sulfide salt and polymolybdates.⁹²⁻⁹⁴

| Compound | Vibration band (cm ⁻¹) |
|--|------------------------------------|
| MoO ₄ ²⁻ | 916, 897 |
| Mo ₇ O ₂₄ ⁶⁻ | 940 |
| Mo ₁₂ O ₃₇ ²⁻ | 955 |
| Mo ₆ O ₁₉ ²⁻ | 980 |
| P ₂ Mo ₅ O ₂₃ ⁶⁻ | 945 |
| PMo ₁₁ O ₃₇ ³⁻ | 970 (pH = 2.5), 963 (pH=3.4) |
| PMo ₁₂ O ₄₀ ³⁻ | 995, 987 |
| Na ₂ MoO ₄ | 890, 808, 380, 322, 305 |
| K ₂ MoS ₄ | 482, 468, 456 |
| Mo-S or Mo-O | 250-400, 500-560, 908 |

Table 8: Raman modes of MoS₂ and MoO₃.²⁸

| 1T-[MoS ₂] ^{nb} | | 2H-MoS ₂ ^c | | MoO ₃ ^d | |
|--------------------------------------|-----------------|----------------------------------|-----------------|-------------------------------|----------------------|
| | | | | 116 | B _{1g} , m |
| | | | | 128 | B _{2g} , m |
| 147 | | | | | |
| 151 | J ₁ | | | 156 | B _{1g} , s |
| 226 | J ₂ | | | 228 | B _{3u} , w |
| 286 | E _{1g} | | | 286 | B _{2g} , m |
| 333 | J ₃ | | | 338 | B _{1g} , m |
| | | 380 | E _{2g} | | |
| 412 | A _{1g} | 407 | A _{1g} | | |
| | | | | 603 | B _{1u} , vs |
| | | | | 876 | B _{3u} , vs |

4.3. UV-Vis spectroscopy

4.3.1. Electron transitions

UV-Vis-NIR spectroscopy allows to investigate electron transfers between orbitals or bands of atoms, ions, and molecules in the gas phase as well as in liquids and solids.⁹⁵ Its large spectral range from 200 nm to 2500 nm is of special interest in heterogeneous catalysis. In situ investigations of optical properties, energy gaps, support interactions and modification of the catalyst during calcination and poisoning are possible. Moreover, transition metal ion (TMI) centers, especially 3d ions, rare earth metal ions (e.g. lanthanoids), adsorbed molecules, molecular ions and radicals are the most suitable to be studied.⁹⁵

During UV-Vis-NIR analysis, the UV (200 – 400 nm), visible (400 – 800 nm) and NIR (800 – 2500 nm) irradiation are interacting with the matter, causing the promotion of electrons to higher energy states. Several electronic transitions are possible (Figure 27):

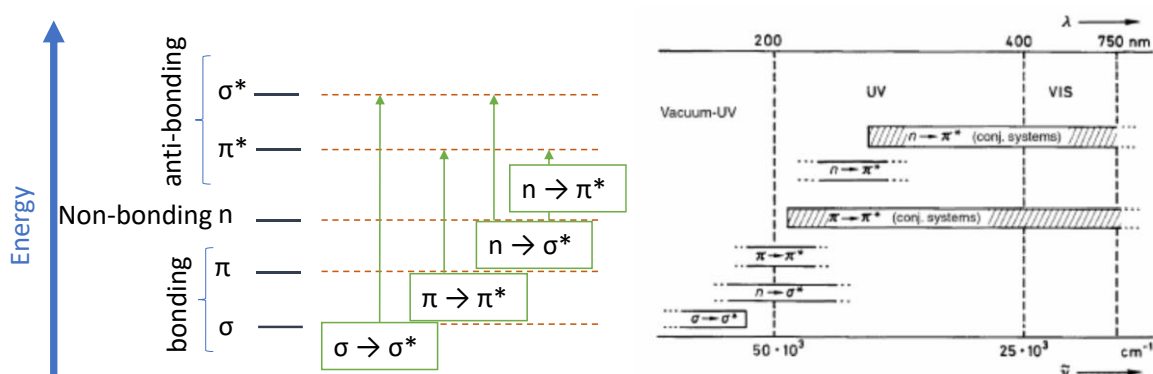


Figure 27 : Energy diagram of possible electron transition in a molecule (left). Absorption range of possible electron transitions under UV-vis irradiation (right).

The transition state $\sigma \rightarrow \sigma^*$ requires high transition energy which means low absorption wavelength (< 190 nm) and is consequently invisible on the UV-vis-NIR spectra unless the analysis is conducted under high vacuum. However, the transition states π to π^* and n to π^* are visible. This kind of transition are characteristic for organic compounds such as aromatics and conjugated systems with functional groups (e.g. N=N, C=O). Other transitions as d-d or metal to ligand charge transfer and vis versa are also possible to be observed. A charge transfer results from the exchange of charge between two molecular entities in which one is

the electron donor and the other the acceptor. For example, CdS is yellow due to the transition from $S^{2-}(\pi) \rightarrow Cd^{2+}(5s)$. S^{2-} is the electron donor and Cd^{2+} is the acceptor.

A ligand to metal charge transfer (LMCT) arises from the transfer of electrons from molecular orbital (MO) with ligand-like character to those with metal-like character. This type of transfer is predominant if the ligand has relatively high-energy lone pairs (e.g. S or Se) or if the metal has low-lying empty orbitals (i.e. d^0).

Inversely, a metal to ligand charge transfer (MLCT) is the transfer of electrons from MO with metal like character to those with ligand like character. This kind of charge transfer is observed in complexes with ligands having low-lying π^* orbitals especially aromatic ligands. Besides, if the metal ion has low oxidation number for its d orbitals, the transition will occur at low energy.

The described possible transitions that can be observed with the respective center (i.e. TMI, support etc.) are summarized in Table 9.

Table 9: Overview of possible transitions during UV-Vis-NIR spectroscopy.⁹⁶

| Center | Transitions |
|-------------------------------------|---|
| Transition metal ion | d-d, metal-to-ligand charge transfer; ligand-to-metal charge transfer |
| Rare earth ion | f-f, f-d |
| Molecules, radicals, molecular ions | $n \rightarrow \pi^*$; $\pi \rightarrow \pi^*$ |
| Support | Band gap, impurities, defects |

4.3.2. Energy gap determination

As mentioned in the table above, impurities and defects on the support can have an impact on the band gap (Figure 28). The determination of the band gap energy, which is the energy needed for an electron to be excited from the valence band (VB) to the conduction band (CB), is crucial for predicting photophysical and photochemical properties of semiconductors. A semiconductor such as TiO_2 has an energy gap of 3.2 eV. This energy gap can be decreased by doping or by lattice formation. The smaller the gap is, the faster is the electron transfer to the conduction band. Thus, the absorption is shifted towards higher wavelength. By introducing defects or having impurities on the support, new energy levels in-between conduction and valence band are formed. This is usually observed for supports with high surface area.

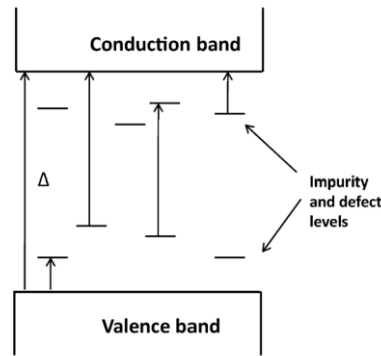


Figure 28: Energy levels of impurities and defects in the support.⁹⁶

In order to determine the energy gap E_g the Tauc plot is used:

$$(F(R_\infty) \times h\nu)^{\frac{1}{y}} = B (h\nu - E_g).$$

The plot derives from the relation between the Kubelka-Munk function (equation 1) and the postulation that the energy-dependent absorption α can be expressed by equation 2.⁹⁷

$$F(R_\infty) = \frac{K}{S} = \frac{(1 - R_\infty)^2}{2R_\infty} \text{ where } R_\infty = \frac{R_{\text{sample}}}{R_{\text{standard}}} \quad (1)$$

$$(\alpha \cdot h\nu)^{1/y} = B(h\nu - E_g) \quad (2)$$

h : Planck constant

y : constant depends on the nature of the electron transition and is equal to 1/2 or 2 for the direct and indirect transition band gaps.

ν : photon's frequency

K : absorption coefficient

S : scattering coefficient

R_∞ : reflectance of infinitely thick specimen

The determination of the energy gaps of materials composed of multiple semiconductors or dopants is however complicated and not evident since transition bands are overlapping. Moreover for such complex systems it is difficult to understand based on the literature how to determine energy gaps making it obvious that the use of UV-Vis-spectroscopy is not the most adequate tool to determine the exact energy gap.^{95,97,98} Hence it can only be regarded as an estimation. Indeed there are two methods described in the literature. The first consist

in tracing a fitted line (Tauc-plot) which passes through the slope of the curve.^{95,98} At the intersection with the x-axes (i.e. meaning the axes of energy) E_g is determined (Figure 29). Yet this method is argued to be not accurate for complex materials having several transitions. It seems that the determined energy gaps are underestimated. Based on this argument another mathematic approach was used which consist in tracing a baseline. At the intersection with the Tauc-plot E_g is found. However the described mathematic model is not compared to other determined energy gaps by other methods such as Reflection Electron Energy Loss Spectroscopy (REELS) making its accuracy doubtful. Moreover its is not clear where the baseline needs to be traced when several transitions are present. Subsequently it was decided to determine the energy gaps based on the first method which is approached by most research works in the literature in order to be able to compare the obtained values with other works. Besides the determined energy gaps are an estimation and will only indicate the trend in charge transfer knowing well that these estimations might be actually underestimated.

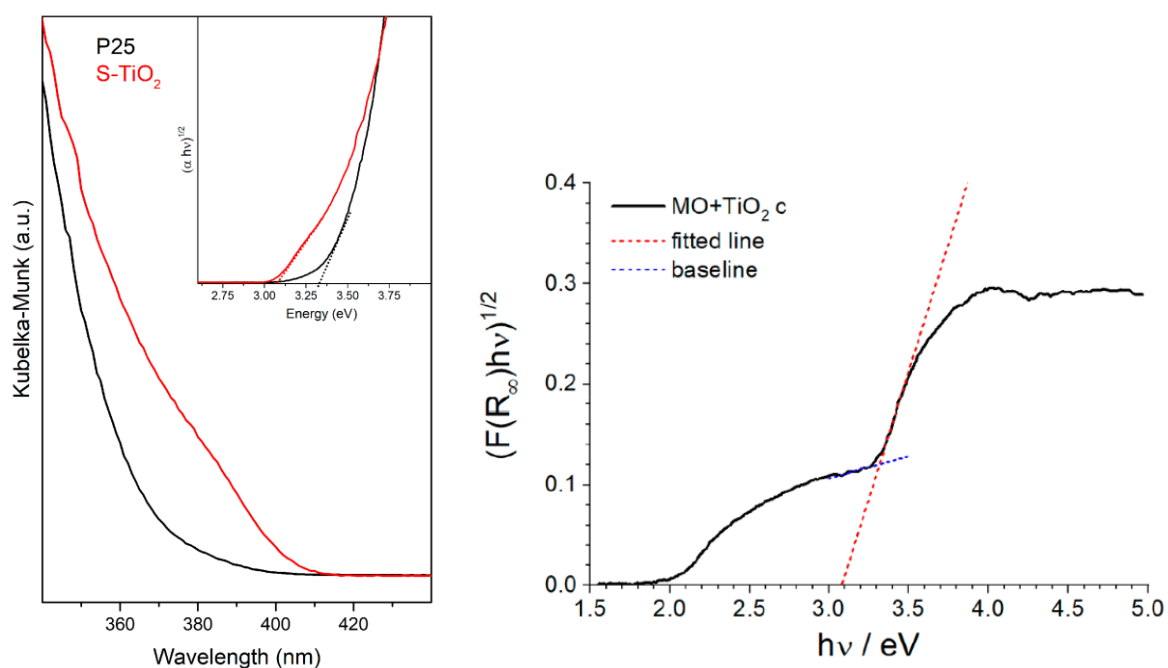


Figure 29: Determination methods of energy gap. On the left, simple conventional fitting line.⁹⁸ The E_g is determined at the intersection with the x-axes. On the right mathematical approach using a baseline.⁹⁷ Its intersection with the fitting line gives the values of the E_g .

5. Main conclusion about bibliographic analysis and scope of the thesis

The aim of this thesis is to get a better understanding about the active sites for HER by correlating surface characterization results obtained via IR/CO spectroscopy with HER activity tests in acidic media. Based on the obtained results different strategies to improve HER activity can be proposed helping in HER electrocatalyst engineering.

Based on the bibliographic analysis, MoS₂ dispersed on TiO₂ (noted: MoS₂/TiO₂) will be the studied electrocatalyst. MoS₂ was chosen as the active phase due its similar free Gibbs adsorption energy of protons to Pt and stability in acidic media. Yet, low edge sites exposition and poor electrical conductivity are limiting the activity leading to high overpotentials and high Tafel slopes as well as high energy consumption. Herein we propose in this work to increase the edge site exposition by using a carrier endowed with high BET surface which will enhance MoS₂ dispersion. However finding a carrier with optimal electrical conductivity, specific surface, stability in acidic media as well as good transparency under IR is not evident. Electrical conductivity is mostly related to metallic carriers with a compact structure leading to low BET surfaces and insufficient transparency for IR-transmission analysis. Hence, transparency of the carrier was prioritized leading to choose TiO₂ as a carrier for MoS₂. Indeed, TiO₂ is stable in acidic media, presents a high BET surface and is transparent to IR-beam. Nevertheless, TiO₂ has two drawbacks: Firstly, due to strong Van der Waals bonds between TiO₂ and MoS₂, large triangular truncated slabs are formed with exposed M-edges. As a results MoS₂ dispersion is very small. Secondly, as mentioned before TiO₂ electrical conductivity needs to be improved to observe a certain activity in HER.

In order to overcome those main issues two strategies will be followed:

- **Use of chelating agents and dopants (N, P) for MoS₂ and sulfur doping of TiO₂:**

First, we will investigate the effect of H₃PO₄ and EDTA as chelating agents on MoS₂. Herein, TiO₂ will be impregnated with a saturated solution containing Mo-precursor and various H₃PO₄ or EDTA concentrations and eventually sulfided. With the help of IR-transmission spectroscopy coupled to CO adsorption (IR/CO), a profound surface characterization of EDTA and H₃PO₄ modified MoS₂/TiO₂ will be conducted. Based on this analysis the amount of

formed M- and S-edges will be determined as well as the effect on Mo dispersion and slab size. EDTA and H_3PO_4 might as well act simultaneously as N- and P-dopants respectively and favor HER activity.

Since MoS_2 is formed under sulfidation, TiO_2 is also partially sulfided. This introduction of sulfur might be sufficient to enhance the electrical conductivity of TiO_2 to observe a certain activity in HER. Indeed, TiO_2 is a semiconductor and presents a modulable energy gap. Via S-doping, intermediate energy levels are introduced leading to a decrease in energy gap. Subsequently the semiconductor behavior of TiO_2 can approach the characteristics of a semi-metal which implies a higher conductivity. By favoring S-doping via sulfidation, initial BET surface of TiO_2 remains high whereas a solvothermal S-doping method would drastically decrease its specific surface. In order to verify the effect on the energy gap, UV-Vis spectroscopy was performed to estimate the energy gap in TiO_2 .

Since TiO_2 is not endowed with a fast charge transfer under electrical tension, it might inhibit HER activity by not providing sufficiently electrons for the Volmer and Heyrovsky steps. Electrons are essential during the adsorption of protons on MoS_2 edges ($\text{H}^+ + \text{e}^- + \text{adsorption site} \rightarrow \text{H adsorbed}$) and also during the reaction between a free and adsorbed proton to form H_2 (Heyrovsky step). As a result, the poor electrical conductivity might hide the effect of EDTA and H_3PO_4 on HER. Therefore, we will try to analyze the impact of H_3PO_4 and EDTA on MoS_2 dispersed on black carbon (MoS_2/C), an electrically conductive carrier, using Raman spectroscopy, Hydrodesulfurization (HDS) of thiophen test and HER activity tests. The obtained results will be compared with the ones obtained for H_3PO_4 and EDTA modified $\text{MoS}_2/\text{TiO}_2$ catalysts.

- **Tubular morphology change of TiO_2 :**

At last, the impact on MoS_2 by changing the morphology of TiO_2 into a tubular one will be investigated. Indeed, chemical anodization of Ti-foil has resulted in the formation of TiO_2 nanotube arrays (TiNTA) which present higher charge transfer capacities due to aligned and ordered structure of nanotubes.^{84,85} However TiNTA are reflective and cannot be analyzed by IR/CO. TiO_2 nanotubes can be synthesized via a solvothermal approach leading to the formation of disordered nanotubes. The overall enhanced charge transfer effect is significantly less pronounced than on TiNTA, yet locally on an isolated nanotube, charge transfer is still more pronounced compared to bulk TiO_2 . Thus, MoS_2 dispersed on

solvothermal synthesized nanotubes will undergo a profound study about how the carrier's morphology is impacting MoS₂ and subsequently its HER activity.

Reference

- (1) Mazloomi, K.; Gomes, C. Hydrogen as an Energy Carrier: Prospects and Challenges. *Renew. Sustain. Energy Rev.* **2012**, *16* (5), 3024–3033.
- (2) Deloitte. *Study on Hydrogen in Ports and Industrial Coastal Areas*; 2022. <https://doi.org/10.2843/90661>.
- (3) Dubouis, N.; Grimaud, A. The Hydrogen Evolution Reaction: From Material to Interfacial Descriptors. *Chem. Sci.* **2019**, *10* (40), 9165–9181.
- (4) Moses, P. G.; Hinnemann, B.; Topsøe, H.; Nørskov, J. K. The Hydrogenation and Direct Desulfurization Reaction Pathway in Thiophene Hydrodesulfurization over MoS₂ Catalysts at Realistic Conditions: A Density Functional Study. *J. Catal.* **2007**, *248* (2), 188–203.
- (5) Cao, Y. Roadmap and Direction toward High-Performance MoS₂ Hydrogen Evolution Catalysts. *ACS Nano* **2021**, *15* (7), 11014–11039.
- (6) Huang, J.; Chen, Y. Combining Theory and Experiment in Advancing Fundamental Electrocatalysis. *Curr. Opin. Electrochem.* **2019**, *14*, A4–A9.
- (7) Zeradjanin, A. R.; Grote, J. P.; Polymeros, G.; Mayrhofer, K. J. J. A Critical Review on Hydrogen Evolution Electrocatalysis: Re-Exploring the Volcano-Relationship. *Electroanalysis* **2016**, *28* (10), 2256–2269.
- (8) Li, L.; Wang, P.; Shao, Q.; Huang, X. Metallic Nanostructures with Low Dimensionality for Electrochemical Water Splitting. *Chem. Soc. Rev.* **2020**, *49* (10), 3072–3106.
- (9) Zhu, Y.; Lin, Q.; Zhong, Y.; Tahini, H. A.; Shao, Z.; Wang, H. Metal Oxide-Based Materials as an Emerging Family of Hydrogen Evolution Electrocatalysts. *Energy Environ. Sci.* **2020**, *13* (10), 3361–3392.
- (10) Solomon, G.; Mazzaro, R.; You, S.; Natile, M. M.; Morandi, V.; Concina, I.; Vomiero, A. Ag₂S/MoS₂ Nanocomposites Anchored on Reduced Graphene Oxide: Fast Interfacial Charge Transfer for Hydrogen Evolution Reaction. *ACS Appl. Mater. Interfaces* **2019**.

- (11) Mei, B. A.; Munteshari, O.; Lau, J.; Dunn, B.; Pilon, L. Physical Interpretations of Nyquist Plots for EDLC Electrodes and Devices. *J. Phys. Chem. C* **2018**, *122* (1), 194–206.
- (12) Tsai, C.; Chan, K.; Nørskov, J. K.; Abild-Pedersen, F. Theoretical Insights into the Hydrogen Evolution Activity of Layered Transition Metal Dichalcogenides. *Surf. Sci.* **2015**, *640*, 133–140. <https://doi.org/10.1016/j.susc.2015.01.019>.
- (13) Zeradjanin, A. R.; Vimalanandan, A.; Polymeros, G.; Topalov, A. A.; Mayrhofer, K. J. J.; Rohwerder, M. Balanced Work Function as a Driver for Facile Hydrogen Evolution Reaction - Comprehension and Experimental Assessment of Interfacial Catalytic Descriptor. *Phys. Chem. Chem. Phys.* **2017**, *19* (26), 17019–17027.
- (14) Shiva Kumar, S.; Himabindu, V. Hydrogen Production by PEM Water Electrolysis – A Review. *Mater. Sci. Energy Technol.* **2019**, *2* (3), 442–454.
- (15) Schalenbach, M.; Tjarks, G.; Carmo, M.; Lueke, W.; Mueller, M.; Stolten, D. Acidic or Alkaline? Towards a New Perspective on the Efficiency of Water Electrolysis. *J. Electrochem. Soc.* **2016**, *163* (11), F3197–F3208.
- (16) Wei, J.; Zhou, M.; Long, A.; Xue, Y.; Liao, H.; Wei, C.; Xu, Z. J. Heterostructured Electrocatalysts for Hydrogen Evolution Reaction Under Alkaline Conditions. *Nano-Micro Lett.* **2018**, *10* (4), 1–15.
- (17) Li, Y. H.; Liu, P. F.; Pan, L. F.; Wang, H. F.; Yang, Z. Z.; Zheng, L. R.; Hu, P.; Zhao, H. J.; Gu, L.; Yang, H. G. Local Atomic Structure Modulations Activate Metal Oxide as Electrocatalyst for Hydrogen Evolution in Acidic Water. *Nat. Commun.* **2015**, *6* (May).
- (18) Zheng, T.; Sang, W.; He, Z.; Wei, Q.; Chen, B.; Li, H.; Cao, C.; Huang, R.; Yan, X.; Pan, B.; Zhou, S.; Zeng, J. Conductive Tungsten Oxide Nanosheets for Highly Efficient Hydrogen Evolution. *Nano Lett.* **2017**, *17* (12), 7968–7973.
- (19) Li, L.; Zhang, T.; Yan, J.; Cai, X.; Liu, S. F. P Doped MoO_{3-x} Nanosheets as Efficient and Stable Electrocatalysts for Hydrogen Evolution. *Small* **2017**, *13* (25), 2–8.
- (20) Geng, S.; Liu, Y.; Yu, Y. S.; Yang, W.; Li, H. Engineering Defects and Adjusting Electronic Structure on S Doped MoO₂ Nanosheets toward Highly Active Hydrogen Evolution Reaction. *Nano Res.* **2020**, *13* (1), 121–126.

- (21) Xia, Z.; Tao, Y.; Pan, Z.; Shen, X. Enhanced Photocatalytic Performance and Stability of 1T MoS₂ Transformed from 2H MoS₂ via Li Intercalation. *Results Phys.* **2019**, *12* (November 2018), 2218–2224.
- (22) Zhong, X.; Sun, Y.; Chen, X.; Zhuang, G.; Li, X.; Wang, J. G. Mo Doping Induced More Active Sites in Urchin-Like W₁₈O₄₉ Nanostructure with Remarkably Enhanced Performance for Hydrogen Evolution Reaction. *Adv. Funct. Mater.* **2016**, *26* (32), 5778–5786.
- (23) Zheng, G.; Wang, C.; Pei, A.; Lopez, J.; Shi, F.; Chen, Z.; Sendek, A. D.; Lee, H. W.; Lu, Z.; Schneider, H.; Safont-Sempere, M. M.; Chu, S.; Bao, Z.; Cui, Y. High-Performance Lithium Metal Negative Electrode with a Soft and Flowable Polymer Coating. *ACS Energy Lett.* **2016**, *1* (6), 1247–1255.
- (24) Li, Y.; Yu, Z. G.; Wang, L.; Weng, Y.; Tang, C. S.; Yin, X.; Han, K.; Wu, H.; Yu, X.; Wong, L. M.; Wan, D.; Wang, X. R.; Chai, J.; Zhang, Y.; Wang, S.; Wang, J.; Wee, A. T. S.; Breese, M. B. H.; Pennycook, S. J.; Venkatesan, T.; Dong, S.; Xue, J. M.; Chen, J. Electronic-Reconstruction-Enhanced Hydrogen Evolution Catalysis in Oxide Polymorphs Yangyang. *Nat. Commun.* **2019**, *10* (3149).
- (25) Qiu, Z.; Tai, C. Direct Observation of Active Catalyst Surface Phases and the Effect of Dynamic Self-Optimization in NiFe-Layered Double Hydroxides for Alkaline Water Splitting. *Energy Environ. Sci.* **2019**, No. 12, 572–581.
- (26) Hu, J.; Zhang, C.; Zhou, D.; Leung, K. H.; Yang, S.; Hu, J.; Zhang, C.; Jiang, L.; Lin, H.; An, Y.; Zhou, D.; Leung, M. K. H. Nanohybridization of MoS₂ with Layered Double Hydroxides Efficiently Synergizes the Hydrogen Evolution in Alkaline Media Nanohybridization of MoS₂ with Layered Double Hydroxides Efficiently Synergizes the Hydrogen Evolution in Alkaline Media. *Joule* **2017**, No. 1, 383–393.
- (27) Benck, J. D.; Hellstern, T. R.; Kibsgaard, J.; Chakthranont, P.; Jaramillo, T. F. Catalyzing the Hydrogen Evolution Reaction (HER) with Molybdenum Sulfide Nanomaterials. *ACS Catal.* **2014**, *4* (11), 3957–3971.
- (28) Strachan, J.; Masters, A. F.; Maschmeyer, T. Critical Review: Hydrothermal Synthesis of 1T-MoS₂- an Important Route to a Promising Material. *J. Mater. Chem. A* **2021**, *9* (15), 9451–9461.

- (29) Wang, J.; Wu, Z.; Hu, K.; Chen, X.; Yin, H. High Conductivity Graphene-like MoS₂/Polyaniline Nanocomposites and Its Application in Supercapacitor. *J. Alloys Compd.* **2015**, *619*, 38–43.
- (30) Lei, Z.; Zhan, J.; Tang, L.; Zhang, Y.; Wang, Y. Recent Development of Metallic (1T) Phase of Molybdenum Disulfide for Energy Conversion and Storage. *Adv. Energy Mater.* **2018**, *8* (19), 1–29.
- (31) Schmidt, H.; Giustiniano, F.; Eda, G. Electronic Transport Properties of Transition Metal Dichalcogenide Field-Effect Devices: Surface and Interface Effects. *Chem. Soc. Rev.* **2015**, *44* (21), 7715–7736.
- (32) Venkateshwaran, S.; Senthil Kumar, S. M. Provoking Metallic 1T Phase Conversion of 2H-MoS₂ via an Effectual Solvothermal Route for Electrocatalytic Water Reduction in Acid. *ACS Sustain. Chem. Eng.* **2022**, *10* (16), 5258–5267.
- (33) Li, W.; Liu, G.; Li, J.; Wang, Y.; Ricardez-Sandoval, L.; Zhang, Y.; Zhang, Z. Hydrogen Evolution Reaction Mechanism on 2H-MoS₂ Electrocatalyst. *Appl. Surf. Sci.* **2019**, *498* (May), 143869.
- (34) Chen, J.; Mi, J.; Li, K.; Wang, X.; Dominguez Garcia, E.; Cao, Y.; Jiang, L.; Oliviero, L.; Maugé, F. Role of Citric Acid in Preparing Highly Active CoMo/Al₂O₃ Catalyst: From Aqueous Impregnation Solution to Active Site Formation. *Ind. Eng. Chem. Res.* **2017**, *56* (48), 14172–14181.
- (35) Dominguez Garcia, E.; Chen, J.; Oliviero, E.; Oliviero, L.; Maugé, F. New Insight into the Support Effect on HDS Catalysts: Evidence for the Role of Mo-Support Interaction on the MoS₂ Slab Morphology. *Appl. Catal. B Environ.* **2020**, *260* (July 2019).
- (36) Chen, J.; Maugé, F.; El Fallah, J.; Oliviero, L. IR Spectroscopy Evidence of MoS₂ Morphology Change by Citric Acid Addition on MoS₂/Al₂O₃ Catalysts - A Step Forward to Differentiate the Reactivity of M-Edge and S-Edge. *J. Catal.* **2014**, *320* (1), 170–179.
- (37) Grønborg, S. S.; Salazar, N.; Bruix, A.; Rodríguez-Fernández, J.; Thomsen, S. D.; Hammer, B.; Lauritsen, J. V. Visualizing Hydrogen-Induced Reshaping and Edge Activation in MoS₂ and Co-Promoted MoS₂ Catalyst Clusters. *Nat. Commun.* **2018**, *9* (1).

- (38) Casalongue, H. G. S.; Benck, J. D.; Tsai, C.; Karlsson, R. K. B.; Kaya, S.; Ng, M. L.; Pettersson, L. G. M.; Abild-Pedersen, F.; Nørskov, J. K.; Ogasawara, H.; Jaramillo, T. F.; Nilsson, A. Operando Characterization of an Amorphous Molybdenum Sulfide Nanoparticle Catalyst during the Hydrogen Evolution Reaction. *J. Phys. Chem. C* **2014**, *118* (50), 29252–29259.
- (39) Merki, D.; Stéphane, F.; Heron, V.; Xile, H. Amorphous Molybdenum Sulfide Films as Catalysts for Electrochemical Hydrogen Production in Water. *Chem. Sci.* **2011**, *2*, 1262–1267.
- (40) Li, D. J.; Maiti, U. N.; Lim, J.; Choi, D. S.; Lee, W. J.; Oh, Y.; Lee, G. Y.; Kim, S. O. Molybdenum Sulfide/N-Doped CNT Forest Hybrid Catalysts for High-Performance Hydrogen Evolution Reaction. *Nano Lett.* **2014**, *14* (3), 1228–1233.
- (41) Gaur, A. P. S.; Zhang, B.; Lui, Y. H.; Tang, X.; Hu, S. Morphologically Tailored Nano-Structured MoS₂ Catalysts via Introduction of Ni and Co Ions for Enhanced HER Activity. *Appl. Surf. Sci.* **2020**, *516* (March), 146094.
- (42) Blanchard, P.; Lamonier, C.; Griboval, A.; Payen, E. New Insight in the Preparation of Alumina Supported Hydrotreatment Oxidic Precursors: A Molecular Approach. *Appl. Catal. A Gen.* **2007**, *322* (SUPPL.), 33–45.
- (43) Kibsgaard, J.; Tuxen, A.; Knudsen, K. G.; Brorson, M.; Topsøe, H.; Lægsgaard, E.; Lauritsen, J. V.; Besenbacher, F. Comparative Atomic-Scale Analysis of Promotional Effects by Late 3d-Transition Metals in MoS₂ Hydrotreating Catalysts. *J. Catal.* **2010**, *272* (2), 195–203.
- (44) Daniel, M.; Vrubel, H.; Lorenzo, R.; Stéphane, F.; Xile, H. Fe, Co, and Ni Ions Promote the Catalytic Activity of Amorphous Molybdenum Sulfide Films for Hydrogen Evolution. *Chem. Sci.* **2017**, No. 3, 2515.
- (45) Guruprasad, K.; Maiyalagan, T.; Shanmugam, S. Phosphorus Doped MoS₂ Nanosheet Promoted with Nitrogen, Sulfur Dual Doped Reduced Graphene Oxide as an Effective Electrocatalyst for Hydrogen Evolution Reaction. *ACS Appl. Energy Mater.* **2019**, *2* (9), 6184–6194.
- (46) Lukowski, M. A.; Daniel, A. S.; Meng, F.; Forticaux, A.; Li, L.; Jin, S. Enhanced Hydrogen Evolution Catalysis from Chemically Exfoliated Metallic MoS₂ Nanosheets. *J. Am. Chem. Soc.* **2013**, *135* (28), 10274–10277. <https://doi.org/10.1021/ja404523s>.

- (47) Bolar, S.; Shit, S.; Murmu, N. C.; Kuila, T. Doping-Assisted Phase Changing Effect on MoS₂ Towards Hydrogen Evolution Reaction in Acidic and Alkaline PH. *ChemElectroChem* **2020**, *7* (1), 336–346.
- (48) Kong, X.; Peng, Z.; Jiang, R.; Jia, P.; Feng, J.; Yang, P.; Chi, Q.; Ye, W.; Xu, F.; Gao, P. Nanolayered Heterostructures of N-Doped TiO₂ and N-Doped Carbon for Hydrogen Evolution. *ACS Appl. Nano Mater.* **2020**, *3* (2), 1373–1381.
- (49) Seo, B.; Jung, G. Y.; Sa, Y. J.; Jeong, H. Y.; Cheon, J. Y.; Lee, J. H.; Kim, H. Y.; Kim, J. C.; Shin, H. S.; Kwak, S. K.; Joo, S. H. Monolayer-Precision Synthesis of Molybdenum Sulfide Nanoparticles and Their Nanoscale Size Effects in the Hydrogen Evolution Reaction. *ACS Nano* **2015**, *9* (4), 3728–3739. <https://doi.org/10.1021/acsnano.5b00786>.
- (50) Benson, E. E.; Zhang, H.; Schuman, S. A.; Nanayakkara, S. U.; Bronstein, N. D.; Ferrere, S.; Blackburn, J. L.; Miller, E. M. Balancing the Hydrogen Evolution Reaction, Surface Energetics, and Stability of Metallic MoS₂ Nanosheets via Covalent Functionalization. *J. Am. Chem. Soc.* **2018**, *140* (1), 441–450.
- (51) Voiry, D.; Salehi, M.; Silva, R.; Fujita, T.; Chen, M.; Asefa, T.; Shenoy, V. B.; Eda, G.; Chhowalla, M. Conducting MoS₂ Nanosheets as Catalysts for Hydrogen Evolution Reaction. *Nano Lett.* **2013**.
- (52) Yan, Y.; Xia, B.; Xu, Z.; Wang, X. Recent Development of Molybdenum Sulfides as Advanced Electrocatalysts for Hydrogen Evolution Reaction. *ACS Catal.* **2014**, *4* (6), 1693–1705.
- (53) Dong, G.; Zhang, Y.; Pan, Q.; Qiu, J. A Fantastic Graphitic Carbon Nitride (g-C₃N₄) Material: Electronic Structure, Photocatalytic and Photoelectronic Properties. *J. Photochem. Photobiol. C Photochem. Rev.* **2014**, *20* (1), 33–50.
- (54) Thomas, A.; Fischer, A.; Goettmann, F.; Antonietti, M.; Müller, J. O.; Schlögl, R.; Carlsson, J. M. Graphitic Carbon Nitride Materials: Variation of Structure and Morphology and Their Use as Metal-Free Catalysts. *J. Mater. Chem.* **2008**, *18* (41), 4893–4908.
- (55) Niu, P.; Zhang, L.; Liu, G.; Cheng, H. M. Graphene-like Carbon Nitride Nanosheets for Improved Photocatalytic Activities. *Adv. Funct. Mater.* **2012**, *22* (22), 4763–4770.

- (56) Iqbal, W.; Qiu, B.; Lei, J.; Wang, L.; Zhang, J.; Anpo, M. One-Step Large-Scale Highly Active g-C₃N₄ Nanosheets for Efficient Sunlight-Driven Photocatalytic Hydrogen Production. *Dalt. Trans.* **2017**, *46* (32), 10678–10684.
- (57) Heron, V.; Xile, H. Molybdenum Boride and Carbide Catalyze Hydrogen Evolution in Both Acidic and Basic Solutions. *Angew. Chemie - Int. Ed.* **2012**, *51*, 12703–12706.
- (58) Li, Z.; Xu, S.; Chu, K.; Yao, G.; Xu, Y.; Niu, P.; Yang, Y.; Zheng, F. Synergistic Tuning of the Electronic Structure of Mo₂C by P and Ni Codoping for Optimizing Electrocatalytic Hydrogen Evolution. *Inorg. Chem.* **2020**, *59* (18), 13741–13748.
- (59) Wang, D.; Liu, T.; Wang, J.; Wu, Z. N, P (S) Co-Doped Mo₂C / C Hybrid Electrocatalysts for Improved Hydrogen Generation. *Carbon N. Y.* **2018**, *139*, 845–852.
- (60) Han, W.; Chen, L.; Ma, B.; Wang, J.; Song, W.; Fan, X.; Li, Y.; Zhang, F.; Peng, W. Nitrogen-Doped Porous Carbon for PH-Universal Hydrogen Evolution : Insights into the Synergistic and Structural Defects. *J. Mater. Chem. A* **2019**, No. 7, 4734–4743.
- (61) Zhang, K.; Zhao, Y.; Fu, D.; Chen, Y. Molybdenum Carbide Nanocrystal Embedded N-Doped Carbon Nanotubes as Electrocatalysts for Hydrogen Generation. *J. Mater. Chem. A* **2015**, No. 3, 5783–5788.
- (62) Xiong, K.; Li, L.; Zhang, L.; Ding, W.; Peng, L.; Wang, Y.; Chen, S.; Shiyu, T.; Zidong, W. Ni-Doped Mo₂C Nanowires Supported on Ni Foam as a Binder-Free Electrode for Enhancing the Hydrogen Evolution Performance. *J. Mater. Chem. A* **2015**, No. 3, 1863–1867.
<https://doi.org/10.1039/c4ta05686h>.
- (63) Xiao, J.; Zhang, Y.; Zhang, Z.; Lv, Q.; Jing, F.; Chi, K.; Wang, S. Self-Supported Biocarbon-Fiber Electrode Decorated with Molybdenum Carbide Nanoparticles for Highly Active Hydrogen-Evolution Reaction. *ACS Appl. Mater. Interfaces* **2017**, *9* (27), 22604–22611.
- (64) Kumar, D.; Sharma, R. C. Advances in Conductive Polymers. *Eur. Polym. J.* **1998**, *34* (8), 1053–1060.
- (65) Djara, R.; Masquelez, N.; Lacour, M. A.; Merzouki, A.; Cambedouzou, J.; Cornu, D.; Tingry, S.; Holade, Y. Self-Supported Electrocatalysts Derived from Nickel-Cobalt Modified

- Polyaniline Polymer for H₂-Evolution and O₂-Evolution Reactions. *ChemCatChem* **2020**, *12* (22), 5789–5796.
- (66) Huang, Z. F.; Song, J.; Yonghua, D.; Shuo, D.; Libo, S.; Chen, W.; Kaidi, Y.; Zhengfei, D.; Wang, X. Optimizing Interfacial Electronic Coupling with Metal Oxide to Activate Inert Polyaniline for Superior Electrocatalytic Hydrogen Generation. *Carbon Energy* **2019**, No. 1, 77–84.
- (67) Zhu, J.; Sun, W.; Yang, D.; Zhang, Y.; Hoon, H. H.; Zhang, H.; Yan, Q. Multifunctional Architectures Constructing of PANI Nanoneedle Arrays on MoS₂ Thin Nanosheets for High-Energy Supercapacitors. *Small* **2015**, *11* (33), 4123–4129.
- (68) Xu, X.; Zhong, W.; Yan, S.; Zhang, L.; Liu, G.; Du, Y. Advanced Catalysts for Hydrogen Evolution Reaction Based on MoS₂/NiCo₂S₄ Heterostructures in Alkaline Media. *Int. J. Hydrogen Energy* **2020**, *45* (3), 1759–1768.
- (69) Fageria, P.; Sudharshan, K. Y.; Nazir, R.; Basu, M.; Pande, S. Decoration of MoS₂ on G-C₃N₄ Surface for Efficient Hydrogen Evolution Reaction. *Electrochim. Acta* **2017**, *258*, 1273–1283.
- (70) Attanayake, N. H.; Thenuwara, A. C.; Patra, A.; Aulin, Y. V.; Tran, T. M.; Chakraborty, H.; Borguet, E.; Klein, M. L.; Perdew, J. P.; Strongin, D. R. Effect of Intercalated Metals on the Electrocatalytic Activity of 1T-MoS₂ for the Hydrogen Evolution Reaction. *ACS Energy Lett.* **2018**, No. 1.
- (71) Liu, M.; Jhulki, S.; Sun, Z.; Magasinski, A.; Hendrix, C. Atom-Economic Synthesis of Magnéli Phase Ti₄O₇ Microspheres for Improved Sulfur Cathodes for Li-S Batteries. 1–22.
- (72) Arrouvel, C.; Digne, M.; Breyse, M.; Toulhoat, H.; Raybaud, P. Effects of Morphology on Surface Hydroxyl Concentration: A DFT Comparison of Anatase-TiO₂ and γ -Alumina Catalytic Supports. *J. Catal.* **2004**, *222* (1), 152–166.
- (73) Paul, K. K.; Sreekanth, N.; Biroju, R. K.; Narayanan, T. N.; Giri, P. K. Solar Light Driven Photoelectrocatalytic Hydrogen Evolution and Dye Degradation by Metal-Free Few-Layer MoS₂ Nanoflower/TiO₂(B) Nanobelts Heterostructure. *Sol. Energy Mater. Sol. Cells* **2018**, *185* (April), 364–374.

- (74) Zhang, J.; Zhou, P.; Liu, J.; Yu, J. New Understanding of the Difference of Photocatalytic Activity among Anatase, Rutile and Brookite TiO₂. *Phys. Chem. Chem. Phys.* **2014**, *16* (38), 20382–20386.
- (75) Burda, C.; Lou, Y.; Chen, X.; Samia, A. C. S.; Stout, J.; Gole, J. L. Enhanced Nitrogen Doping in TiO₂ Nanoparticles. *Nano Lett.* **2003**, *3* (8), 1049–1051.
- (76) Cao, Y.; Xing, Z.; Li, Z.; Wu, X.; Hu, M.; Yan, X.; Zhu, Q.; Yang, S.; Zhou, W. Mesoporous Black TiO_{2-x}/Ag Nanospheres Coupled with g-C₃N₄ Nanosheets as 3D/2D Ternary Heterojunctions Visible Light Photocatalysts. *J. Hazard. Mater.* **2018**, *343*, 181–190.
- (77) Pan, X.; Yang, M. Q.; Fu, X.; Zhang, N.; Xu, Y. J. Defective TiO₂ with Oxygen Vacancies: Synthesis, Properties and Photocatalytic Applications. *Nanoscale* **2013**, *5* (9), 3601–3614.
- (78) Feng, H.; Xu, Z.; Ren, L.; Liu, C.; Zhuang, J.; Hu, Z.; Xu, X.; Chen, J.; Wang, J.; Hao, W.; Du, Y.; Dou, S. X. Activating Titania for Efficient Electrocatalysis by Vacancy Engineering. *ACS Catal.* **2018**, *8* (5), 4288–4293.
- (79) Kundu, D.; Black, R.; Berg, E. J.; Nazar, L. F. A Highly Active Nanostructured Metallic Oxide Cathode for Aprotic Li-O₂ Batteries. *Energy Environ. Sci.* **2015**, *8* (4), 1292–1298.
- (80) Pang, Q.; Kundu, D.; Cuisinier, M.; Nazar, L. F. Surface-Enhanced Redox Chemistry of Polysulphides on a Metallic and Polar Host for Lithium-Sulphur Batteries. *Nat. Commun.* **2014**, *5* (May), 3–10.
- (81) Mei, S.; Jafta, C. J.; Lauermann, I.; Ran, Q.; Kärgell, M.; Ballauff, M.; Lu, Y. Porous Ti₄O₇ Particles with Interconnected-Pore Structure as a High-Efficiency Polysulfide Mediator for Lithium–Sulfur Batteries. *Adv. Funct. Mater.* **2017**, *27* (26), 1–10.
- (82) Terracciano, M.; Galstyan, V.; Rea, I.; Casalino, M.; De Stefano, L.; Sberveglieri, G. Chemical Modification of TiO₂ Nanotube Arrays for Label-Free Optical Biosensing Applications. *Appl. Surf. Sci.* **2017**, *419*, 235–240.
- (83) Cao, Y.; Wu, Y.; Badie, C.; Cadot, S.; Camp, C.; Quadrelli, E. A.; Bachmann, J. Electrocatalytic Performance of Titania Nanotube Arrays Coated with MoS₂ by ALD toward the Hydrogen Evolution Reaction. *ACS Omega* **2019**, *4* (5), 8816–8823.

- (84) Lačnjevac, U.; Vasilić, R.; Dobrota, A.; Đurđić, S.; Tomanec, O.; Zbořil, R.; Mohajernia, S.; Nguyen, N. T.; Skorodumova, N.; Manojlović, D.; Elezović, N.; Pašti, I.; Schmuki, P. High-Performance Hydrogen Evolution Electrocatalysis Using Proton-Intercalated TiO₂nanotube Arrays as Interactive Supports for Ir Nanoparticles. *J. Mater. Chem. A* **2020**, *8* (43), 22773–22790.
- (85) Liu, Z.; Zhang, X.; Wang, B.; Xia, M.; Gao, S.; Liu, X.; Zavabeti, A.; Ou, J. Z.; Kalantar-Zadeh, K.; Wang, Y. Amorphous MoS_x-Coated TiO₂ Nanotube Arrays for Enhanced Electrocatalytic Hydrogen Evolution Reaction. *J. Phys. Chem. C* **2018**, *122* (24), 12589–12597.
- (86) Huang, Y.; Nielsen, R. J.; Goddard, W. A.; Soriaga, M. P. The Reaction Mechanism with Free Energy Barriers for Electrochemical Dihydrogen Evolution on MoS₂. *J. Am. Chem. Soc.* **2015**, *137* (20), 6692–6698.
- (87) Douaihy, R. Z.; Lakiss, L.; El-Roz, M.; Levaque, Y.; Vimont, A.; Bazin, P. Impact of the Si/Al Ratio on the Ethanol/Water Coadsorption on MFI Zeolites Revealed Using Original Quantitative IR Approaches. *Phys. Chem. Chem. Phys.* **2023**, 11555–11565.
<https://doi.org/10.1039/d3cp00549f>.
- (88) F. Maugé, C. Binet, J. C. L. *IR Characterization of Metal Catalysts Using CO as Probe Molecule*.
- (89) Chen, J.; Labruyere, V.; Maugé, F.; Quoineaud, A. A.; Hugon, A.; Oliviero, L. IR Spectroscopic Evidence for MoS₂ Morphology Change with Sulfidation Temperature on MoS₂/Al₂O₃ Catalyst. *J. Phys. Chem. C* **2014**, *118* (51), 30039–30044.
- (90) Travert, A.; Dujardin, C.; Maugé, F.; Cristol, S.; Paul, J. F.; Payen, E.; Bougeard, D. Parallel between Infrared Characterisation and Ab Initio Calculations of CO Adsorption on Sulphided Mo Catalysts. *Catal. Today* **2001**, *70* (1–3), 255–269.
- (91) Decanio, E. C.; Storm, D. A. Determination of Zero-Valent Molybdenum after Moderate Temperature Reduction of Alumina-Supported Catalysts. *J. Catal.* **1991**, *130* (2), 653–656.
- (92) Cordova, A.; Blanchard, P.; Lancelot, C.; Frémy, G.; Lamonier, C. Probing the Nature of the Active Phase of Molybdenum-Supported Catalysts for the Direct Synthesis of Methylmercaptan from Syngas and H₂S. *ACS Catal.* **2015**, *5* (5), 2966–2981.

- (93) Van Veen, J. A. R.; Sudmeijer, O.; Emeis, C. A.; De Wit, H. On the Identification of Molybdophosphate Complexes in Aqueous Solution. *J. Chem. Soc. Dalt. Trans.* **1986**, No. 9, 1825–1831.
- (94) Murata, K.; Ikeda, S. Studies on Molybdophosphates Containing a Group 4A Metal Ion by Laser Raman Spectroscopy. Interference of Group 4A Metal Ions in the Determination of Phosphorus. *Anal. Chim. Acta* **1983**, 151 (C), 29–38.
- (95) Hunger, M.; Weitkamp, J. In Situ IR, NMR, EPR, and UV/Vis Spectroscopy: Tools for New Insight into the Mechanisms of Heterogeneous Catalysis. *Angew. Chemie - Int. Ed.* **2001**, 40 (16), 2954–2971.
- (96) Specac. The Specac Quest: How the ATR Accessory Works. **2016**.
- (97) Makuła, P.; Pacia, M.; Macyk, W. How To Correctly Determine the Band Gap Energy of Modified Semiconductor Photocatalysts Based on UV-Vis Spectra. *J. Phys. Chem. Lett.* **2018**, 9 (23), 6814–6817.
- (98) Cravanzola, S; Cesano, F.; Gaziano, F.; Scarano, D. Sulfur-Doped TiO₂: Structure and Surface Properties. *Catalysts* **2017**, 7(7), 214

Table of contents

| | |
|-------------------------------------|-----------|
| Chapter 2: Experimental part | 78 |
| 2.1 Characterization tools | 78 |
| 2.2 Activity tests | 82 |
| Reference | 84 |

Chapter 2: Experimental part

In this following chapter all characterization methods and procedures are detailed. Synthesis procedures of catalysts are to be found in each chapter.

1. Characterization tools

X-ray:

XRD patterns were recorded on powder, with a PANalyticalX'Pert Pro diffractometer using Cu K α radiation ($\lambda = 1.5418 \text{ \AA}$, 45 kV, 40 mA). This analysis was conducted in order to validate the preservation of the anatase phase as well as the formation of nanotubes and nanowires.

BET-measurements:

At -196°C nitrogen adsorption/desorption isotherms were measured using Micrometrics Model ASAP 2020 volumetric adsorption analyzer. Samples were degassed at 300°C under vacuum. With the help of the BET equation the specific surface area (S_{BET}) was determined and the total volume was calculated from the volume adsorbed at $P/P_0 = 0.95$.

Inductively coupled plasma mass spectrometry (ICP-MS):

50 mg of each sample were mixed with 3 ml aqua regia, 3 ml HF, 2 g boric acid and 94 ml DI water at room temperature. Before ICP analysis the mixture was diluted 10 times in 0.5% aqua regia. Analyses were performed in order to determine the amount of Na, K, P, S, Ti and Mo on samples and estimate the S/Mo ratio and Mo dispersion which were calculated by using the equations:

$$\frac{S}{Mo} = \frac{n(S)_{tot\ of\ catalyst} - n(S)_{support}}{n(Mo)}$$

$$Mo\ dispersion = \frac{probed\ concentration\ of\ M - edge\ sites\ (\mu mol. g^{-1})}{n(Mo)_{ICP}(\mu mol. g^{-1}) \times \left(\frac{S}{Mo}\ ratio\right)}$$

If $S/Mo < 2$, its calculated value was inserted into the equation. Otherwise, if $S/Mo \geq 2$ the value of 2 is used meaning that all Mo is considered under the MoS_2 form.

For carbon-based materials, a demineralization process of carbon was conducted before dilution. Herein, 50 mg of each sample were solubilized in 8 ml HNO_3 and heated in a microwave oven (Anton Paar Multiwave eco, rotor HVT50-T8) at 600W and 200°C. Afterwards the same amount of aqua regia, HF and boric acid were added to the solution and filled with 86 ml DI water. All sulfided catalysts were conditioned under argon to avoid the destruction of the sulfide phase.

Microscopic characterization SEM-EDX and TEM:

Scanning Electron Microscopy (SEM) images of TiNT, TiNW and TiNT(9%- MoS_2) sulfided at 335°C and 350°C were taken using a Tescan Mira I LMH under 20kV. Energy Dispersive X-Ray (EDX) measurements were recorded using two Bruker XFLASH 6/30 EDX cameras. Transmission electron microscope (TEM) analysis was conducted on sulfided samples to evaluate slab length and stacking number. MoS_2/TiO_2 prepared with EDTA was analyzed at CRISMAT by Xavier Portier. To do so samples were deposited on a copper mesh laying on a carbon film after being dispersed in ethanol.

Catalysts which underwent a morphology change were analyzed at LEPMI by Laetitia Dubau. TEM images were obtained on a JEOL 2010 TEM apparatus equipped with a LaB_6 filament operating at 200 kV (point-to-point resolution = 0.19 Å). For the statistical analysis in both cases a population of 500 slabs in average was probed.

IR/CO-spectroscopy:

IR/CO analysis for performed in order to establish a relationship between structure and HER activity. Herein catalysts were analyzed in order to determine the concentration of active sites, the impact on Mo electron density and its dispersion as well as investigate the impact of sulfidation and morphology change on the support TiO_2 anatase. Herein, pellets with a diameter of 16 mm of 12 mg were pressed and placed in a platin sample holder which levitates automatically up and down from IR cell to oven. This in-situ IR cell called PELICAEN is the latest version developed by the LCS laboratory allowing a better sample temperature control. CO adsorptions were performed under liquid nitrogen (-173°C) in an adapted quartz cell. Samples were sulfided in-situ (10% H_2S/H_2 , 30ml/min) at 300°C - 400°C for 2h (3°C/min). After

activation controlled small doses of CO were introduced under liquid nitrogen into the cell and each time a spectrum was taken from 4000 to 650 cm^{-1} (256 scans; resolution is 4 cm^{-1}) with a NICOLET 5700 equipped with a MCT detector. Spectra were normalized to 10 mg and treated with OMNIC for band decomposition (Voigt function) and subtraction (Spectrum of small CO doses minus spectrum before CO adsorption). M-edge sites concentration was calculated using the equation:

$$n_{M-edge} = \frac{S \times A_{CO-Medge}}{m \times \epsilon}$$

Where S is the surface of the pellet (2.01 cm^2), $A_{CO-Medge}$ is the integrated air of $\nu(\text{CO}/\text{M-edge})$ when saturation is reached, m the weight of the pellet normalized to 10 mg and ϵ the molar extinction coefficient for CO/M-edge on TiO_2 (15.3 $\text{cm}/\mu\text{mol}$).¹

Raman Spectroscopy:

Jobin Yvon Labram 300 Raman spectrometer was used equipped with a confocal microscope, an Nd-YAG laser (frequency doubled, 532 nm) and a CCD detector. Spectra of sulfided and non sulfided samples were recorded at room temperature under air in the region between 50 – 1200 cm^{-1} . Liquid samples were analyzed via a sensor which was submerged in the analyzed solution. The gap between sensor and flask bottom was maintained constant. Prior to analysis, spectrometer was calibrated using a silicone plate. The intensity of beam was maintained below 10 mW (scan rate 300 seconds, accumulation of spectra 4) with the help of a filter in order to avoid oxidation of the sample, especially of polymolybdate and MoS_2 . In order to preserve the sulfided phase, samples analyzed by IR/CO which were sulfided in-situ under vacuum and conditioned in form of a pellet were immediately analyzed by Raman. This method was applied in order to avoid the complete deterioration of the sulfided phase. The pellet was divided into five zones. For each zone a Raman spectrum was taken. The aim of the analysis was to investigate the nature of the formed polymolybdate and validate the presence of MoS_2 as well as determining its phase nature. Spectra were analyzed with the software LabSpec6 d'HORIBA Scientific.

UV-Vis spectroscopy:

To determine the variation of energy gap in function of doping concentration on sulfided and non sulfided samples, a UV-Vis analysis was conducted with Varian Cary-4000 UV-Vis

spectroscopy in the region between 200 – 800 nm. For this analysis diffused attenuation was used. Background was taken with MgO powder for each lamp change at 300, 350 and 400 nm. Energy gaps of TiO₂ and MoS₂ were determined by Tauc-Plot as described in Chapter 1 section 4.3.2. For TiO₂ the function $(F(R)\times E)^{0.5} = f(E)$ was traced and for MoS₂ $(F(R)\times E)^2 = f(E)$ since the first is an indirect semiconductor and the latter a direct semiconductor.

X-ray photoelectron spectrometry (XPS):

XPS was employed to determine the chemical state of TiNT(9%-MoS₂) sulfided at 335°C under 10% H₂S/H₂ 30mL/min and its composition. XPS characterization was conducted with a Kratos AXIS Ultra DLD with a monochromatized X-ray source Al K α (1486.6 eV) (180 W, 12 mA, 15 kV). The pressure inside the analysis room was below 5.0x10⁻⁹ torr during analysis. The extraction function of the spectrometer was calibrated with the help of a gold slab to the binding energy (BE) of its pic Au 4f_{7/2} at 83.96 eV. The dispersion of the spectrometer was calibrated with copper to its binding energy of its pic Cu 2p_{3/2} at 932.62 eV.

A survey spectrum of the sample was taken in the range of 1200 to 5 eV with an energy of 160 eV at an acquisition time of 1 s per 1eV.

During analysis the compensation of surface charge Kratos was employed. The analysis was conducted on an oval zone of 700 x 300 μ m.

The obtained spectrum was treated with CASA XPS. Herein the spectrum's binding energies were corrected taking the pic of C_{1s} (284.8 eV) as a reference, the baseline of the type Shirley was used and spectrum was decomposed using a mixt Gaussian-Lorentzian function (G/L=30%). The decomposing of Mo 3d XPS signals was carried out using the oxide and sulfide references as reported by P. Blanchard et al.²⁻⁴ The atomic concentrations were obtained by determining the respective areas of the corresponding peaks corrected with respect to the sensitivity factors.

2. Activity tests

HDS-Thiophen test:

Catalysts were activated in a fixed quartz reactor at 335-400°C under 10% H₂S/H₂ flow (30 ml/min) for 4h with a ramp of 3°C/min. Afterwards H₂S/H₂ was evacuated by N₂ (20 ml/min) for 10 minutes. The set-up is schematized in Figure 1.

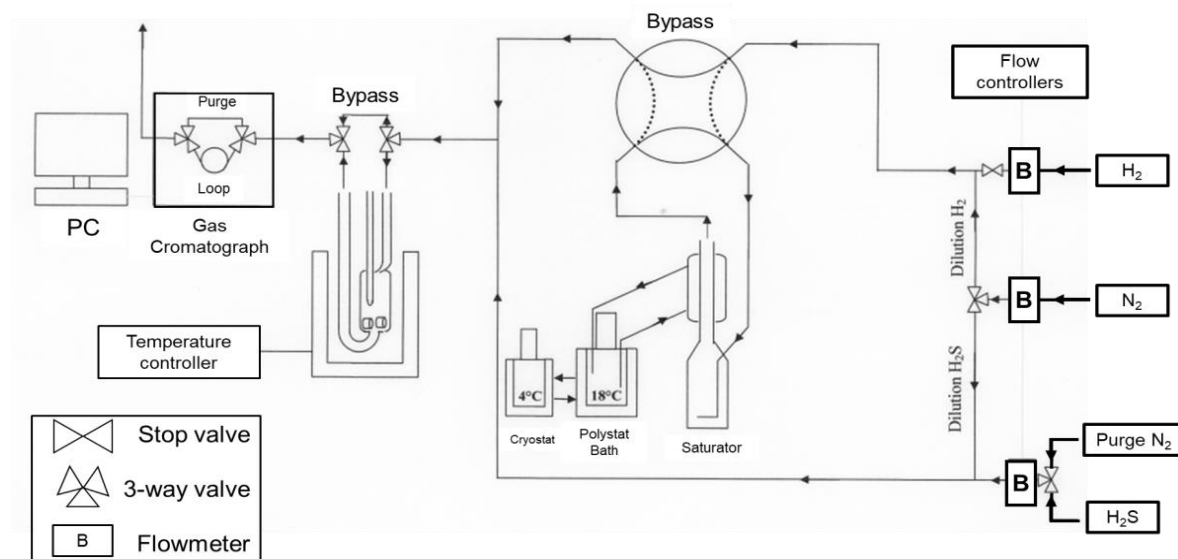


Figure 1: Schematic representation of HDS-thiophen set-up.

Catalytic tests were performed for 6h at 335°C and 350°C ($P_{\text{reactor}} = 0.1 \text{ MPa}$). The catalytic test was conducted under a feed flow of thiophene (90 ml/min, 8 kPa), pure H₂ (72 ml/min, 91.2 kPa) and H₂S/H₂ 10% (20 ml/min, 2.1 kPa). A saturator was used in order to convert the liquid thiophen into gas. The outlet gas from the reactor was analyzed with a Varian 3900 gas chromatograph equipped with flam ionization detector. Herein a silica fused column with low polarity was used (J&W VF-1ms GC Column, 15 m, 0.25 mm, 0.25 μm). Every 11 minutes a chromatogram was acquired. The heating program of the column was adjusted to a starting temperature of 50°C which increased to a final temperature of 100°C (13.6°C/min). The conversion of thiophene was controlled below 10% to operate in differential conditions. Concentrations of butane, 1-butene, trans-2-butene, cis-2-butene, tetrahydrothiophene (THT) and thiophene were recorded and treated with GALAXIE. Specific rate r_s (mol/h.kg) was calculated based on the formula:

$$r_s = \frac{X \times F}{m_{\text{cat sulf}}}$$

where X is thiophene conversion (%), F the molar flow rate of thiophene ($\text{mol}\cdot\text{h}^{-1}$) and $m_{\text{cat sulf}}$ is the weight of the sample after sulfidation. In order to calculate the intrinsic activity, r_s was divided by the probed amount of M-edge sites with CO during IR analysis.

HER-test:

HER activity tests were performed at LEPMI (*Laboratoire d'Electrochimie et de Physicochimie des Matériaux et des Interfaces*, Grenoble). In short, homogenous catalytic inks were prepared by mixing grinded electrocatalyst powder in a Nafion[®] suspension (5 wt. % in *n*-propanol) and isopropanol. An aliquot of this ink was then deposited onto the working electrode, a glassy carbon disk of 5 mm diameter which was afterwards dried under air using a heat gun to evaporate the Nafion[®] solvents, isopropanol and the water. The catalyst loading was $300 \mu\text{g}_{\text{powder}} \text{cm}^{-2}$ for the electrochemical characterizations. All electrochemical measurements were carried out using a bi-potentiostat (Autolab PGSTAT302N) operated with NOVA 2.0 software. The totality of the glassware used in this work was cleaned using a $\text{H}_2\text{SO}_4/\text{H}_2\text{O}_2$ (50 % v/v) solution before use. A four-electrode electrochemical cell thermostated at $T = 25^\circ\text{C}$ was used. A carbon plate and a freshly prepared home-made reversible hydrogen electrode (RHE) were used as counter-electrode and reference electrode, respectively. The electrochemical experiments were carried out using a rotating disk electrode. For each sample, 10 HER cyclic voltammograms (CVs) were recorded between 0.1 and -0.4 V vs. RHE at $v = 10 \text{ mV s}^{-1}$ in Ar-saturated 0.5 M H_2SO_4 electrolyte at $T = 25^\circ\text{C}$ and at 1600 rpm.

Reference

- (1) Dominguez Garcia, E.; Chen, J.; Oliviero, E.; Oliviero, L.; Maugé, F. New Insight into the Support Effect on HDS Catalysts: Evidence for the Role of Mo-Support Interaction on the MoS₂ Slab Morphology. *Appl. Catal. B Environ.* **2020**, *260* (July 2019).
- (2) Cordova, A.; Blanchard, P.; Lancelot, C.; Frémy, G.; Lamonier, C. Probing the Nature of the Active Phase of Molybdenum-Supported Catalysts for the Direct Synthesis of Methylmercaptan from Syngas and H₂S. *ACS Catal.* **2015**, *5* (5), 2966–2981.
- (3) Palencia-Ruiz, S.; Uzio, D.; Legens, C.; Laurenti, D.; Afanasiev, P. Stability and Catalytic Properties of 1T-MoS₂ Obtained via Solvothermal Synthesis. *Appl. Catal. A Gen.* **2021**, *626* (July).
- (4) Blanchard, P.; Lamonier, C.; Griboval, A.; Payen, E. New Insight in the Preparation of Alumina Supported Hydrotreatment Oxidic Precursors: A Molecular Approach. *Appl. Catal. A Gen.* **2007**, *322* (SUPPL.), 33–45.

Table of contents

| | |
|--|------------|
| Chapter 3: Effect of H₃PO₄ and EDTA on MoS₂/TiO₂ and on its HER activity | 86 |
| 1. Introduction | 86 |
| 2. Characterization of MoS₂ supported on TiO₂ prepared with EDTA or H₃PO₄ | 89 |
| 2.1. Catalyst's preparation | 89 |
| 2.2. Elemental analysis of x-PMoS ₂ /TiO ₂ and x-NMoS ₂ /TiO ₂ | 90 |
| 2.3. IR/CO spectroscopy analysis | 91 |
| 2.4. TEM analysis of 0.5NMoS ₂ /TiO ₂ : Impact of EDTA on MoS ₂ slabs size | 106 |
| 2.5. Raman analysis of MoS ₂ /TiO ₂ prepared with EDTA or H ₃ PO ₄ | 107 |
| 2.6. UV-Vis analysis of MoS ₂ /TiO ₂ prepared with EDTA or H ₃ PO ₄ | 114 |
| 2.7. HDS and HER activity tests of MoS ₂ /TiO ₂ prepared with EDTA or H ₃ PO ₄ | 117 |
| 2.8. Discussion | 127 |
| 2.9. Conclusion | 130 |
| 3. Studying the effect of EDTA and H₃PO₄ addition during preparation of MoS₂/C on HER activity | 133 |
| 3.1. Introduction | 133 |
| 3.2. Synthesis | 135 |
| 3.3. Characterization results of EDTA and H ₃ PO ₄ prepared MoS ₂ /C | 136 |
| 4. Main conclusion | 147 |
| Reference | 148 |
| Annexe | 152 |

Chapter 3: Effect of H₃PO₄ and EDTA on MoS₂/TiO₂ and on its HER activity

1. Introduction

Scaling up production of green hydrogen via water electrolysis is of great importance today. To render the process economic, fabrication of electrocatalysts by solvent-free or solvent-low synthesis with few synthesis steps such as incipient impregnation seems to be a good strategy. The operating conditions are extremely acidic due to H₂SO₄ used as electrolyte. It implements that the cathodic material including the catalyst needs to be anti-corrosive and stable. Carbon materials such as carbon black, graphene or reduced graphite oxide (RGO) became the most promising and investigated electrocatalyst carriers. They are stable in acidic medium, endowed with interesting electrical conductivity and present a vast BET surface which is important for good active site dispersion. Furthermore these kind of supports are abundant. Electrocatalysts derived from this kind of materials present good HER activity.^{1;2} This is the reason why MoS₂ supported on carbon materials have become big research subjects. However characterization of MoS₂ supported on carbon materials via IR/CO spectroscopy is for the moment impossible from a technical operating point of view. This is why the carbon carrier will be replaced by TiO₂ presenting a good IR transparency. MoS₂ supported on TiO₂ (noted MoS₂/TiO₂) is answering to all the chemical stability conditions needed for HER electrocatalysis in acid media. However MoS₂/TiO₂ has two main drawbacks: In one hand TiO₂ has a poor electrical conductivity (< 10⁻¹⁰ S/m) which might limit HER activity by not injecting sufficiently electrons to the active phase during reaction.³ On the other hand MoS₂ edge site exposition on TiO₂ is low due to the strong interaction between MoS₂ and the support leading to small Mo dispersion.⁴ Subsequently high overpotentials are achieved (above – 0.3V at -10 mA/cm²) and high Tafel slopes.^{5;6}

In order to overcome these issues two main strategies will be applied in this chapter. First, S-doping of TiO₂ will be carried out as a means to enhance TiO₂ electrical conductivity and subsequently charge transfer. This sulfur doping will occur during sulfidation. Simultaneously, Mo impregnated on TiO₂ can be converted into MoS₂ without deteriorate the initial BET

surface of the carrier and achieve a maximum Mo-dispersion. In regards to this applied method two main questions will be investigated. (i) Is the amount of introduced sulfur into TiO₂ via sulfidation sufficient to enhance TiO₂ charge transfer? (ii) Is S-doping of TiO₂ influencing HER activity of MoS₂/TiO₂?

Herein ICP-MS will be performed to quantify the amount of introduced sulfur in TiO₂ depending different sulfidation temperatures. Moreover the impact of sulfidation temperature and time on TiO₂ will be investigated via IR/CO. Eventually UV-Vis spectroscopy will be used to determine TiO₂ energy gap which will indicate if charge transfer is improved.

The second strategy targeting an increase in MoS₂ edge site exposition will consist in adding EDTA or H₃PO₄ during catalyst's preparation. EDTA is a known chelating agent⁷ while H₃PO₄ as a phosphorous source.⁸ Subsequently we will try to use those additives introduced in different concentrations during synthesis to increase M-edge site exposition and also as a source of nitrogen and phosphorous respectively. For the latter, we will investigate whether N- and P-doping has occurred and if in this case the conductivity of MoS₂ has been improved. An increase in MoS₂ conductivity might help achieve higher HER activities and also enhance kinetics.

In order to study the impact of the addition of these additives at different amounts during preparation on MoS₂ and subsequently on HER activity, the following procedure will be applied: First ICP-MS and EDX analysis will be performed to quantify the presence of Mo, S, Ti, P and N. Based on this elemental analysis we will be able to conclude whether EDTA and H₃PO₄ act as N- and P-source respectively. Moreover S/Mo ratios can be determined and give information about the sulfidation degree of Mo. Secondly, different surface characterization technics will be applied on prepared catalysts in order to study the effect of those additives' addition on MoS₂. Precisely, IR/CO spectroscopy will permit to quantify the amount of edge sites, evaluate sulfur vacancy creation and also give us information about the electron density of Mo. By coupling ICP-MS and IR/CO results Mo dispersion can be estimated. With the help of Raman spectroscopy MoS₂ phase nature will be investigated while UV-Vis spectroscopy will be used to determine the energy gaps of MoS₂ and TiO₂. Since thiophen is more sensitive to steric hindrance than CO, HDS activity tests will be performed to evaluate the accessibility and activity of edge sites. Based on the obtained characterization results we will try to understand

the observed HER activities of analyzed catalysts and determine the impact of the addition of EDTA and H_3PO_4 during preparation on HER activity and kinetics.

Since the low electrical conductivity of TiO_2 might mask the impact of EDTA and H_3PO_4 , HER activity tests will be conducted on MoS_2 supported on carbon black and prepared with EDTA and H_3PO_4 . The obtained results will be compared to the ones of MoS_2 supported on TiO_2 in order to evaluate whether the impact of EDTA and H_3PO_4 addition was masked.

2. Characterization of MoS₂ supported on TiO₂ prepared with EDTA or H₃PO₄

2.1. Catalyst's preparation

Extrudates of TiO₂ anatase were purchased at Degussa, (NH₄)₆Mo₇O₂₄·4H₂O, EDTA (Ethylenediaminetetraacetic acid) and H₃PO₄ 0.85%_{wt} were delivered by Sigma Aldrich.

- Preparation of TiO₂ anatase as support:

Extrudates of TiO₂ anatase were sieved (0.2 < d < 0.4 mm) then calcined for 3h at 400°C with ramp of 3°C/C (S_{BET} = 143 m²/g; V_p = 0.38 ml/g).

- Synthesis Mo/TiO₂ (3 Mo/nm²):

The Mo-precursor (NH₄)₆Mo₇O₂₄·4H₂O was solubilized in DI water (V_{water} = m_{support} × 1.3V_{pore}). The obtained solution was used to impregnate the calcined TiO₂ and afterwards left for 2h maturation. Eventually the prepared catalyst was dried at 120°C for 16h.

- Synthesis of x-PMo/TiO₂ and x-NMo/TiO₂ (3 Mo/nm²):

The same procedure as for Mo/TiO₂ was used to prepare x-PMo and x-NMo/TiO₂. In short, (NH₄)₆Mo₇O₂₄·4H₂O was mixed with different amount of either H₃PO₄ or EDTA and then impregnated on TiO₂. The proportions between additives and Mo-precursor were varied so that the molar ratio between P and Mo will be x = P/Mo = 0.5; 1; 1.5; 2 and for EDTA prepared catalysts the molar ratio x = N/Mo = 0.5; 1; 1.5; 2. After 2h maturation, samples were dried at 120°C for 16h.

- Preparation of MoS₂/TiO₂, x-PMoS₂/TiO₂ and x-NMoS₂/TiO₂ (3 Mo/nm²):

In order to form MoS₂ on TiO₂ prepared with or without EDTA and H₃PO₄, dried samples Mo/TiO₂, x-PMo/TiO₂ and x-NMo/TiO₂ were sulfided under 10% H₂S/H₂ flow (30 ml/min) for 2h (3°C/min) at 400°C.

2.2. Elemental analysis of x-PMoS₂/TiO₂ and x-NMoS₂/TiO₂

ICP-MS analysis were performed on x-PMoS₂/TiO₂ and x-NMoS₂/TiO₂ to quantify the amount of P, Mo, S and Ti. EDX analysis confirmed the absence of nitrogen indicating that EDTA was completely decomposed after sulfidation at 400°C. The results are summarized in Table 1 and Table 2. Based on ICP-MS results of x-PMoS₂/TiO₂, H₃PO₄ is acting as a source of phosphorous meaning a dopant. However with its increasing concentration, a decrease in S/Mo ratio is observed up to 0.88 when P/Mo equals 2. Consequently, it can be deduced that the sulfidation degree was insufficient to transform the total amount of Mo into MoS₂ due to presence of phosphorous. Thus, it seems very possible that the proportion of oxygen in molybdenum sulfide phase is relatively high.

Table 1: ICP-MS results of x-PMoS₂/TiO₂ (x = 0; 0.5; 1; 1.5; 2) (* corresponds to the total amount of sulfure for analyzed catalyst).

| Sample | %_{wt}P | %_{wt}S* | %_{wt} Ti | %_{wt}Mo | Atomic ratio S/Mo |
|--|------------------------|-------------------------|--------------------------|-------------------------|--------------------------|
| <i>MoS₂/TiO₂</i> | 0 | 6.65 | 67.48 | 5.82 | 2.32 |
| <i>0.5PMoS₂/TiO₂</i> | 0.62 | 4.68 | 48.65 | 5.02 | 1.55 |
| <i>1PMoS₂/TiO₂</i> | 1.03 | 4.48 | 49.77 | 4.77 | 1.51 |
| <i>1.5PMoS₂/TiO₂</i> | 1.59 | 4.18 | 49.67 | 4.86 | 1.31 |
| <i>2PMoS₂/TiO₂</i> | 2.82 | 3.40 | 44.17 | 4.68 | 0.88 |

In contrary to x-PMoS₂/TiO₂, catalysts which were prepared with EDTA, present a S/Mo ratio equaling 2. Hence the sulfidation degree was sufficient to transform the total amount of Mo into MoS₂. Herein EDTA seems to act as a chelating agent but not as a N-dopant. Nevertheless, a slight decrease in S/Mo is observed. It could be related to difficulty to solubilize EDTA at high concentration during the preparation of the impregnation solution.

Table 2: ICP-MS results of $x\text{-NMoS}_2/\text{TiO}_2$ ($x= 0; 0.5; 1; 2$) (* corresponds to the total amount of sulfure for analyzed catalyst).

| Sample | %wt S* | %wt Ti | %wt Mo | Atomic ratio S/Mo |
|---------------------------------|---------------|---------------|---------------|--------------------------|
| $\text{MoS}_2/\text{TiO}_2$ | 6.65 | 67.48 | 5.82 | 2.32 |
| $0.5\text{NMoS}_2/\text{TiO}_2$ | 5.89 | 51.70 | 4.79 | 2.35 |
| $1\text{NMoS}_2/\text{TiO}_2$ | 5.91 | 54.68 | 4.96 | 2.28 |
| $1.5\text{NMoS}_2/\text{TiO}_2$ | 5.78 | 58.91 | 5.22 | 2.10 |
| $2\text{NMoS}_2/\text{TiO}_2$ | 5.78 | 49.61 | 5.22 | 2.10 |

2.3. IR/CO spectroscopy analysis

2.3.1. IR/CO analysis of TiO_2 anatase

2.3.1.1. Dehydrated TiO_2 anatase

The IR spectra of TiO_2 anatase was taken after annealing the sample in the IR cell at 300°C for 2h under Argon. Two major regions are observed: The hydroxyl region at $3750\text{-}3600\text{ cm}^{-1}$ and the structural band region related to Ti-O vibration below 1200 cm^{-1} .

Since anatase has different exposed facets mainly (001), (100), (101), (110), different absorption bands are found for each specific facet when CO adsorption occurs (Figure 1).

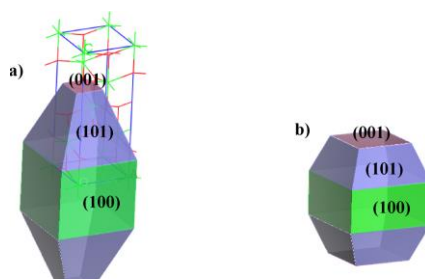


Figure 1: Representation of dehydrated TiO_2 anatase nanocrystalline facets based on the work of S. Dzwigaj et al.⁹

It was demonstrated by Arrouvel et al. via DFT calculations that titanium ions in anatase are preferentially penta or hexa coordinated (noted Ti_V , Ti_{VI} respectively) and oxygen can be monocoordinated or twofold coordinated leading to corresponding μ_1 and μ_2 hydroxyl groups.¹⁰ Non dissociated adsorbed water is noted μ_1OH_2 .

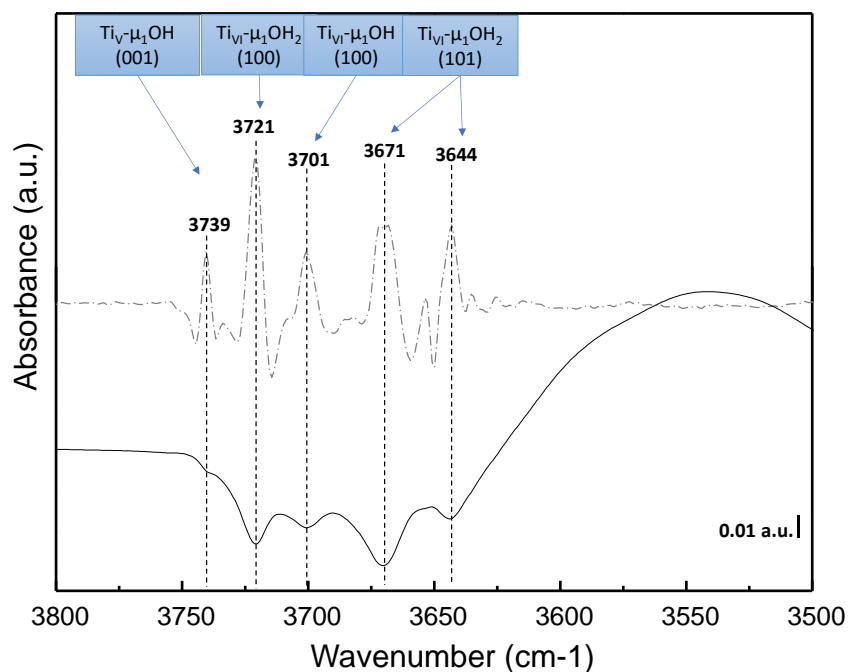


Figure 2: IR/CO spectrum of TiO_2 at 1 Torr equilibrium pressure and its second derivative showing the different interaction OH-groups on TiO_2 .

At 3739 cm^{-1} the vibration of $Ti_V-\mu_1OH$ (001) is visible followed by the vibration of $Ti_{VI}-\mu_1OH_2$ (100) at 3721 cm^{-1} (Figure 2). The vibration band with the weakest intensity at 3701 cm^{-1} belongs to $Ti_{VI}-\mu_1OH$ (100) as already described by Arrouvel et al.¹⁰ and Dufour et al.¹¹

Chemisorbed H_2O on hexacoordinated titanium ions situated on (101) is also found at 3671 and 3644 cm^{-1} noted $Ti_{VI}-\mu_1OH_2$ (101). The deformation bands of H_2O on penta or hexa coordinated titan on (101), (100) can be observed between $1610-1563\text{ cm}^{-1}$ having small intensities even after dehydration due to the strong affinity of (101) and (100) surfaces for water.

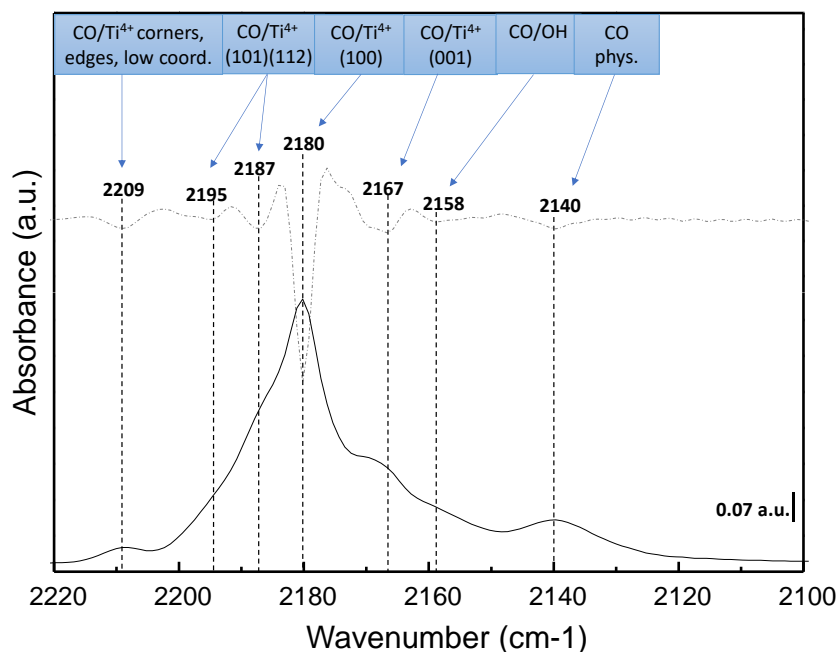


Figure 3: IR/CO spectrum at 1 Torr equilibrium pressure of TiO_2 and its second derivative showing different CO/Ti^{4+} adsorption bands.

CO adsorption on TiO_2 is giving rise to six different bands which are differentiated by tracing the second derivative of the spectrum (Figure 3). The band located at 2158 cm^{-1} is ascribed to $\nu(\text{CO}/\text{OH})$ whereas the five other bands correspond to Lewis acid sites (CO/Ti^{4+} interaction) located on different facets. The obtained spectrum is in agreement with the work of Mino et al.¹² The small intensity of the absorption band at 2209 cm^{-1} is due to the interaction of CO with low coordinated Ti^{4+} located on edges, steps and corners. At 2180 cm^{-1} the intense band is ascribed to (100) Lewis acid sites and presents two shoulders. The first one at 2187 cm^{-1} which corresponds to (101) Lewis sites and is overlapping the band at 2195 cm^{-1} related to (112) Lewis sites. The second shoulder at 2167 cm^{-1} corresponds to $\nu(\text{CO}/\text{Ti}^{4+}(\text{001}))$.

2.3.1.2. Impact of sulfidation on TiO_2 anatase

TiO_2 was sulfided at 300°C , 350°C and 400°C for one and two hours (noted S- TiO_2). Afterwards CO ($P_{\text{eq}} = 1\text{ Torr}$) adsorption spectra of sulfided supports were compared in order to analyze the effect of time and temperature of sulfidation.

In overall it was observed that sulfidation has a great impact on acid sites (Lewis and Bronsted). The intensity of these bands decreased and their band position shifted.

- *Effect of temperature:*

The intensity of Ti-OH vibration decreased clearly with higher sulfidation temperature and are very weak compared to TiO₂. On S-TiO₂ spectrum, absorption bands of Ti_{VI}-μ₁OH₂ (101) at 3644 cm⁻¹ have disappeared. Only those between 3740 and 3670 cm⁻¹ are visible (Figure 4). After H₂S treatment, bands of Ti_{VI}-μ₁OH₂ (101) and Ti_{VI}-μ₁OH (100) have shifted by 5 and 8 cm⁻¹ to higher wavenumbers reflecting an increase in acidity.

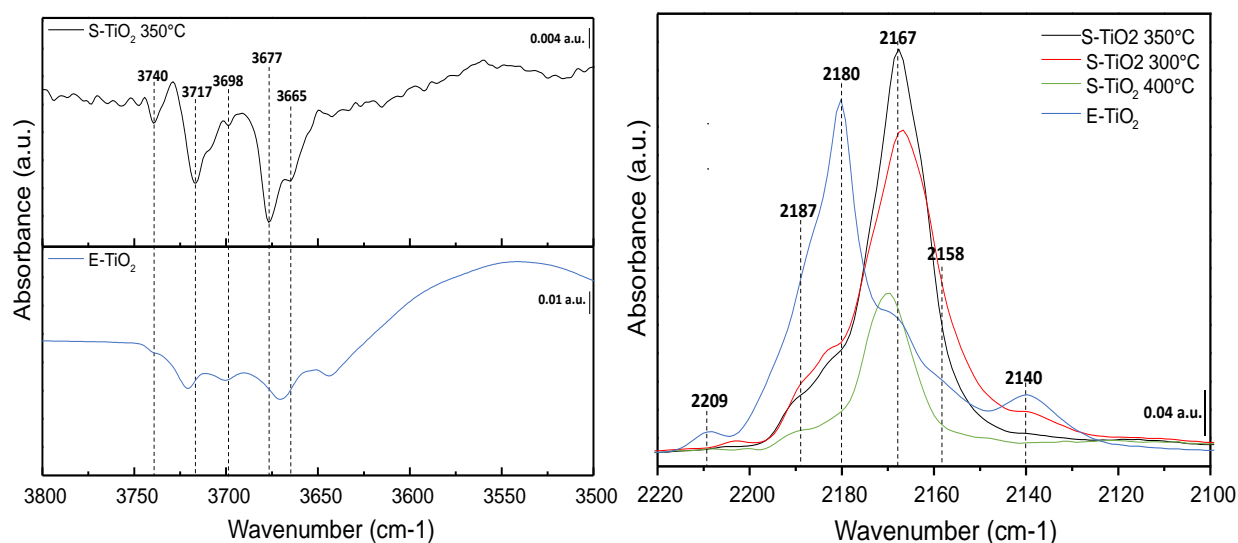


Figure 4: On the left, IR/CO spectra of TiO₂ and S-TiO₂ activated at 350°C for 2h at 1 Torr equilibrium pressure focalized on OH-region (3500-3800 cm⁻¹). On the right, comparison of IR/CO spectra (1 Torr equilibrium pressure) of TiO₂ and S-TiO₂ sulfided at 300°C, 350°C and 400°C for 2h.

This observation can be explained by the undissociative adsorption of H₂S on anatase generating new Bronsted acid sites which are in interaction (via SH) with hydroxyl groups.¹³

For the vibration band Ti_{VI}-μ₁OH₂ (100) a downward shift of 5 cm⁻¹ was observed. This result could be explained by neighboring Ti-SH sites generated by the dissociation of H₂S. Those sites are less prone to attract hydrogen compared to Ti-OH causing a decrease in acidity.

Concerning the region between 2220 cm⁻¹ and 2120 cm⁻¹, the spectrum of adsorbed CO has the same shape as IR/CO spectrum of TiO₂. The only difference is the clear backdown shift ($\Delta\nu = 2-14$ cm⁻¹) of CO/Ti⁴⁺ and CO/OH bands due to sulfur/oxygen exchange. The increase in sulfidation temperature allows to enhance this exchange. This enhancement is clearly visible by comparing the spectra of S-TiO₂ sulfided at 300°C, 350°C and 400°C at constant sulfidation

time, where a blueshift of the vibration band $\nu(\text{CO}/\text{Ti}^{4+} (100))$ is observed ($\Delta\nu = 3-4 \text{ cm}^{-1}$) (Figure 5). The increase in sulfidation temperature has also an impact on the intensity. The maximum band of intensity is reached for 350°C. It should be noted due to high scattering and transparency issues of the sample during IR analysis, the intensity at 400°C drops drastically.

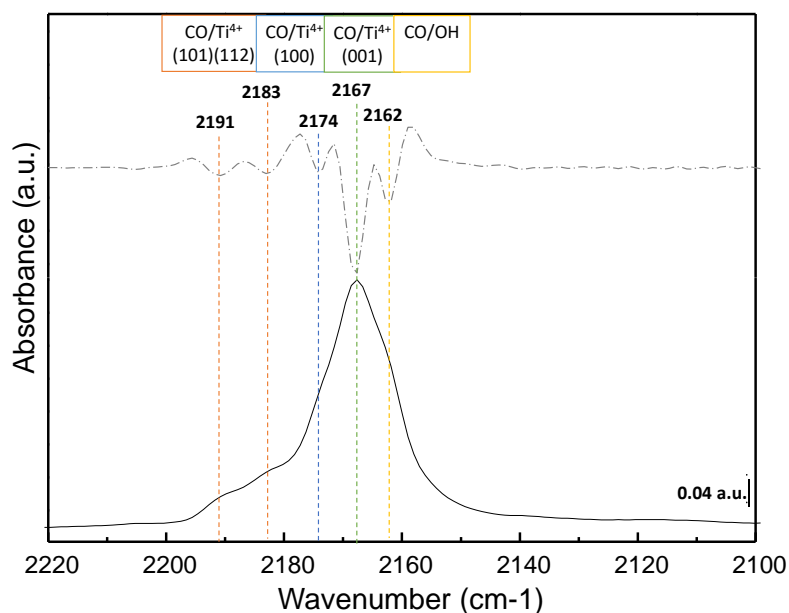


Figure 5: IR/CO spectrum of $S\text{-TiO}_2$ 350°C with its 2nd derivative (dotted gray line).

Sulfidation has also an effect on the intensity of several bands (Figure 5). For instance, $\nu(\text{Ti}^{4+}/\text{CO} (100))$ decreased in intensity after sulfidation and was shifted to 2174 cm^{-1} whereas the intensity of $\nu(\text{Ti}^{4+}/\text{CO} (001))$ has increased and was only slightly shifted to 2167 cm^{-1} . One possible explanation would be the variation in adsorption energy of anatase facets. One facet might be more prone to sulfidation than another.

- Effect of time:

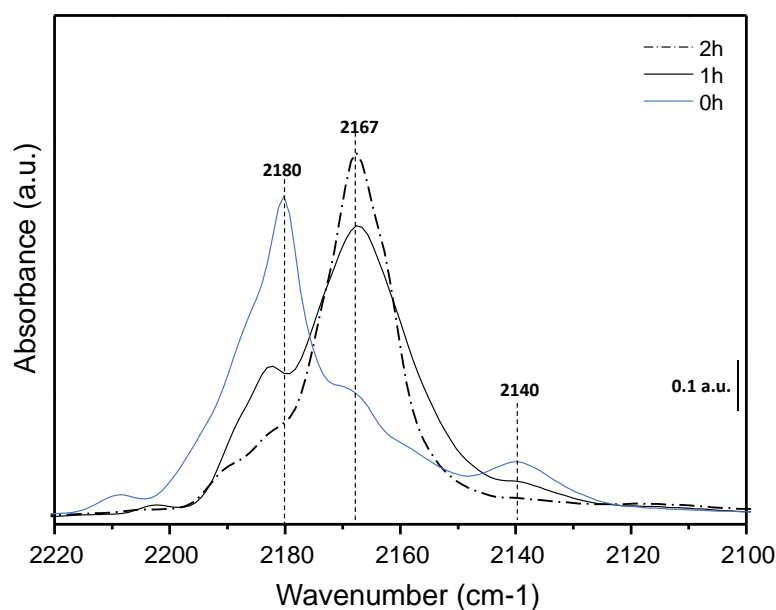


Figure 6: Evolution of IR/CO spectra of S-TiO₂ at 1 Torr equilibrium pressure depending on sulfidation time at 350°C.

Sulfidation time has the same impact on intensity and band position as described for sulfidation temperature. By increasing the time of sulfidation at constant temperature a blueshift can be observed. For instance, at 350°C after 1h sulfidation, the band of $\nu(\text{Ti}^{4+}/\text{CO}(100))$ is positioned at 2167 cm^{-1} whereas after 2h it is shifted to 2168 cm^{-1} and consequently approaching the vibration band of TiO₂ at 2180 cm^{-1} (Figure 6). Subsequently it can be deduced that the longer the sulfidation, the more oxygen atoms are replaced by sulfur. However, it should be underlined that the shifting of adsorption bands is less significant with increasing sulfidation time above 350°C.

Those described shifts concord with obtained ICP-MS results which confirm the oxygen/sulfur exchange. Indeed, with increasing temperature the weight percentage of sulfur increases up to 2.3%. Above 350°C this value remains constant (Table 3).

Table 3: ICP-MS results of sulfided TiO₂ at 300°C, 350°C and 400°C for 4h under 10% H₂S/H₂.

| Sulfidation temperature (°C) | 300 | 350 | 400 |
|--|------------|------------|------------|
| Weight percentage of sulfur (%) | 1.6 | 2.3 | 2.2 |

2.3.1.3. Conclusion about the impact of sulfidation on TiO_2

Sulfidation has an impact on the support (Figure 7). It decreases the acidity of Lewis acid sites based on the observed downward shift of $\nu(CO/Ti^{4+})$ by $10-16\text{ cm}^{-1}$. The higher the sulfidation temperature (or sulfidation time), the more vibration bands of Lewis sites detected by CO adsorption are blueshifted. This shift is reflecting a rise in the replacement of oxygen by sulfur. During this exchange, oxygen vacancies are likely to be created above 350°C since H_2 is also present and favors the creation of vacancies.¹⁴

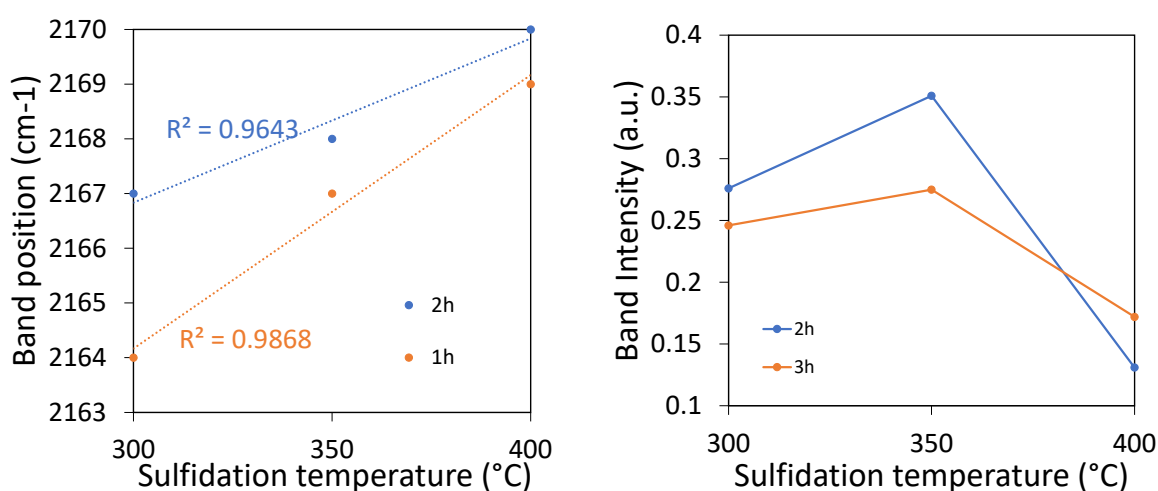


Figure 7: Effect of sulfidation temperature and time on the absorption band position of $\nu(Ti^{4+}/CO(100))$ (left) and on its intensity (right).

A maximum of intensity is detected for 350°C S- TiO_2 . The weight percentage of sulfur introduced in TiO_2 is around $2\%_{wt}$ and remains stable above 350°C . Herein, it can be presumed that during activation of HER electrocatalysts, the support will be doped with $2\%_{wt}$ S-atoms which could induce an enhancement in the electrical conductivity by decreasing the energy gap.¹⁵ Hence, based on these results, catalysts will be sulfided at 400°C in order to introduce a maximum of sulfur amount into TiO_2 framework which will be around $2.2\%_{wt}$ and achieve a high yield in MoS_2 formation.

2.3.2. IR/CO analysis of MoS₂/TiO₂ prepared or not with EDTA and H₃PO₄

2.3.2.1. IR/CO analysis of MoS₂/TiO₂

IR/CO analysis was performed on MoS₂/TiO₂ which was sulfided in-situ at 400°C for 2h. Using CO as a probe molecule, edge sites on MoS₂/TiO₂ were quantified. The molar extinction coefficient ϵ was determined by introducing small doses of CO in to IR-cell. It was hypothesized that the total amount of CO was adsorbed. The molar number of adsorbed CO can be deduced by using the "Ideal gas law" ($PV = nRT$) and a plot can be traced (Area of band = f° (amount in μmol of CO per cm^2)). The slope of this plot corresponds to the molar extinction coefficient whereas the plateau translates the saturation of free M- or S-sites. At the point where the curve is constant, the total concentration of M- or S-edges can be determined. On IR/CO spectra of MoS₂/TiO₂ only M-edges were detected at 2118 cm^{-1} due to the existing strong Van der Waals interaction between MoS₂ and TiO₂ (Figure 9). The molar extinction coefficient ($\epsilon_{\text{CO/M-edge}}$) was determined to be $15.3 \pm 0.1 \text{ cm}/\mu\text{mol}$ which is in agreement with the value obtained by Mauge et al.¹⁶ (Figure 8).

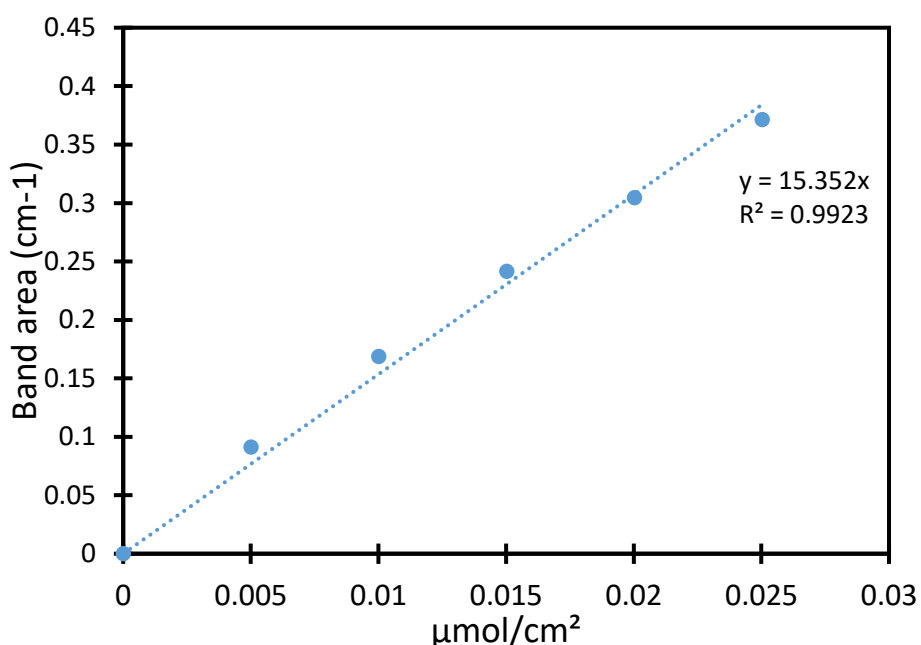


Figure 8: Integrated absorption band area of $\nu(\text{CO/M-edge})$ in function of adsorbed CO ($\mu\text{mol}/\text{cm}^2$). Band area values are related to the first five small doses at an equilibrium pressure of 0.125 Torr.

In total 84 μmol of M-edge sites per gram of sulfide catalyst sites were probed by CO. Since only M-edge sites are present, triangular, truncated shaped slabs were formed on TiO_2 . Furthermore, absorption bands of CO in interaction with TiO_2 surface sites between 2190 and 2150 cm^{-1} are found as described in section 2.3.1.2 before.

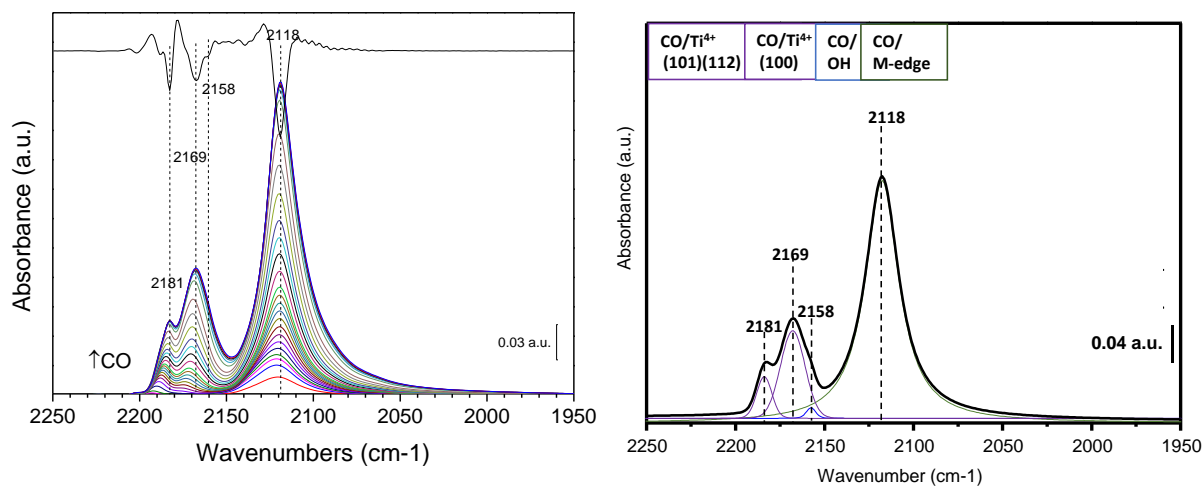


Figure 9 : On the left, IR/CO spectra of $\text{MoS}_2/\text{TiO}_2$ up to saturation at 1 Torr equilibrium pressure with its second derivative. On the right its deconvolution spectrum close to saturation.

2.3.2.2. IR/CO analysis of $x\text{-PMoS}_2/\text{TiO}_2$

After activation at 400°C , IR/CO spectra of $x\text{-PMoS}_2/\text{TiO}_2$ resemble each other ($x = \text{P}/\text{Mo} = 0.5; 1; 1.5; 2$). The spectra can be divided into four zones. The first one is the OH region where at 3670 cm^{-1} a vibration band is visible. This band is related to the OH vibration of Ti-POH which was formed during impregnation. The second zone is around 2500 cm^{-1} : Two new bands appear at 2504 and 2477 cm^{-1} (Figure 10A). The third zone is related to the structural vibration of the heteropolymolybdates (HPM) in interaction or not with anatase below 1100 cm^{-1} and the last zone corresponds to the interaction CO/Ti^{4+} and CO/MoS_2 ($2200\text{-}2050\text{ cm}^{-1}$) (Figure 10B).

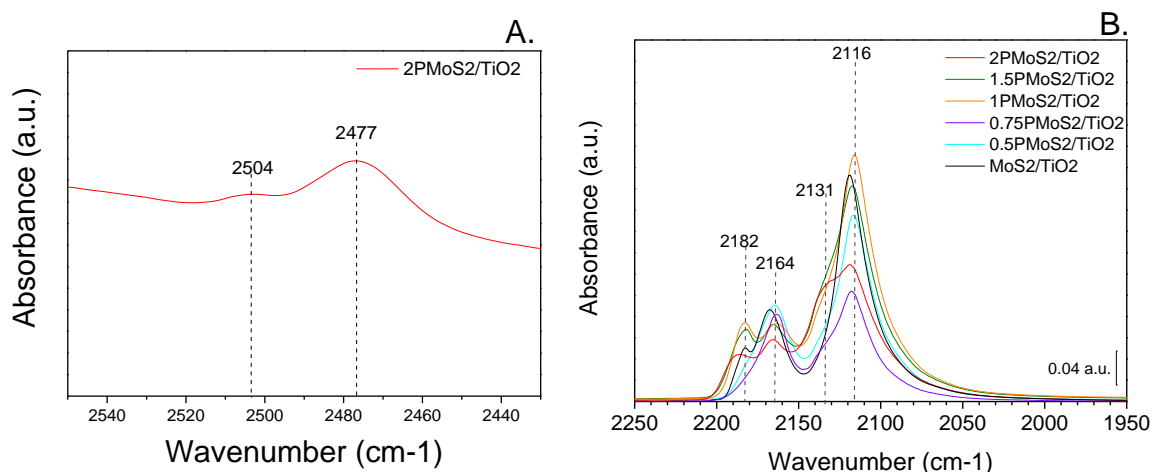


Figure 10: IR spectra of 2PMoS₂/TiO₂ showing two new absorption bands at 2504 and 2477 cm⁻¹ as also observed for other P-doped catalysts (A.) IR/CO spectra of x-PMoS₂/TiO₂ at 1 Torr equilibrium pressure (B.).

On IR/CO spectra, we observe that H₃PO₄ has little effect on $\nu(\text{CO/M-edge})$. Indeed, absorption band position of $\nu(\text{CO/M-edge})$ remain unchanged except for 0.5PMoS₂/TiO₂ where a small downward shift ($\Delta\nu = 2 \text{ cm}^{-1}$) compared to MoS₂/TiO₂ is noted. Consequently, the backdonation from Mo to CO is more pronounced which means that molybdenum's electron density was enriched. This slight increase in electron density could be linked to the formation of P-Mo bonds which are enriching Mo with electrons.

In addition, P-doping is also favoring the creation of sulfur vacancies on M-edges. Sulfur depleted M-edge sites containing a sulfur coverage of 37.5% are confirmed on x-PMoS₂/TiO₂ IR/CO spectra due to presence of the absorption band around 2100 cm⁻¹ (Figure A1).¹⁷ With increasing H₃PO₄ loading up to P/Mo = 0.75, the proportion of S-vacancies is rising (Figure 11). Above P/Mo = 0.75, the amount of S-vacancies is decreasing. The strong decrease for P/Mo = 2 might be linked to the preferred formation of MoO_xS_y at high H₃PO₄ concentrations which is detected at 2131 cm⁻¹ by IR/CO. Its band intensity is increasing with P/Mo ratio.

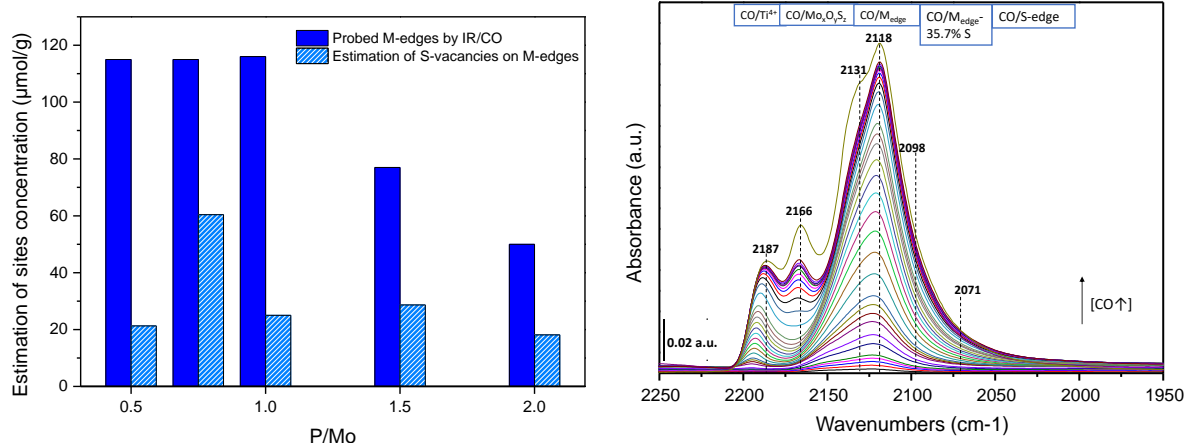


Figure 11: On the left, column diagram demonstrating the evolution of S-vacancies on M-edges depending on P/Mo molar ratio. The amount of S-vacancies was estimated by cross-multiplication of probed M-edge sites by IR/CO using the integrated area under the absorption band at 2100 cm^{-1} and 2118 cm^{-1} . It was assumed that both sites have the same molar extinction coefficient. On the right, IR/CO spectra of 2PMoS₂/TiO₂ up to saturation at 1 Torr equilibrium pressure emphasizing the high amount of formed MoOxSy visible at 2131 cm^{-1} .

We also note that at high phosphorus concentration (P/Mo = 1.5; 2) a weak contribution of $\nu(\text{CO/S-edge})$ is distinguished at 2071 cm^{-1} . By using the molar extinction coefficient of 35 $\text{cm}^2/\mu\text{mol}$,¹⁸ the amount of S-edge sites was determined to be around 1 $\mu\text{mol/g}$. This small quantification of S-edges is insignificant compared to the probed amount of M-edges and is highlighting the strong Van der Waals interaction between MoS₂ and TiO₂ preventing the formation of S-edges. Consequently, H₃PO₄ does not favor the increase of S-edge/M-edge ratio and MoS₂ slabs are having a triangular truncated shape.

Table 4: Summary of obtained M- and S-edge sites by CO adsorption on xP-MoS₂/TiO₂ (x = 0; 0.5; 0.75; 1; 1.5; 2) and variation of band position.

| Sample | % _{wt} P | $\nu(\text{CO/M-edge})$ (cm^{-1}) | S-edge sites ($\mu\text{mol/g}$) | M-edge sites ($\mu\text{mol/g}$) | Estimated Mo dispersion | Atomic ratio S/Mo |
|---|-------------------|---|---------------------------------------|---------------------------------------|-------------------------|-------------------|
| MoS ₂ /TiO ₂ | 0 | 2118 | 0 | 84 | 0.15 | 2.32 |
| 0.5PMoS ₂ /TiO ₂ | 0.62 | 2116 | 0 | 115 | 0.22 | 1.55 |
| 0.75PMoS ₂ /TiO ₂ | 0.85 | 2116 | 0 | 115 | 0.17 | 1.87 |
| 1PMoS ₂ /TiO ₂ | 1.03 | 2117 | 0 | 116 | 0.23 | 1.51 |
| 1.5PMoS ₂ /TiO ₂ | 1.59 | 2118 | 1 | 77 | 0.15 | 1.31 |
| 2PMoS ₂ /TiO ₂ | 2.82 | 2118 | 1 | 50 | 0.11 | 0.88 |

However phosphoric acid can be used to increase the concentration of M-edge sites at low P/Mo proportions as well as improve Mo dispersion (Table 4). Indeed, the highest amount of M-edge sites was probed when P/Mo = 0.5; 0.75; 1 whereas above this molar ratio the concentration of probed M-edges is strongly decreasing and is even lower than probed M-edge sites concentration for MoS₂/TiO₂. This drop in M-edge sites can be explained by the favored agglomeration of oxides at high H₃PO₄ concentration which is validated by the increase in intensity of the absorption band $\nu(\text{CO}/\text{MoOxSy})$ at 2131 cm⁻¹ and low S/Mo ratios. For the latter, a clear drop was observed up to 0.88 with higher phosphor loading.

Herein H₃PO₄ seems to be a good additive to increase Mo dispersion when used at P/Mo = 0.5 and P/Mo = 1.

However, H₃PO₄ hasn't only an effect on MoS₂ but also on the support. For P-doped MoS₂/TiO₂ the intensity of $\nu(\text{CO}/\text{OH})$ is weaker compared to the one of MoS₂/TiO₂. One possible explanation would be that during impregnation, H₃PO₄ interacts with Ti-OH favoring the creation of new Bronsted acid sites. This assumption is verified by the presence of the bands mono- and bidentate phosphate found at 2504 and 2477 cm⁻¹ (Figure 10A).¹⁹

H₃PO₄ modifies also the amount and strength of Lewis acid sites. In fact adding, H₃PO₄ increases Lewis acidity which is translated by an upward shift of $\nu(\text{CO}/\text{Ti}^{4+} (101)(112))$ to 2188 cm⁻¹ when P/Mo = 2. Moreover, its intensity is also decreasing with higher H₃PO₄ concentration. Thus, we can assume that Lewis acid sites located on (101) and (112) facets are favored for the anchoring of Mo-precursor in the presence of H₃PO₄. Especially when P/Mo = 0.5; 0.75, $\nu(\text{CO}/\text{Ti}^{4+} (101)(112))$ intensity is the lowest. Therefore, it can be deduced that MoS₂ was majorly formed on (101)(112) facets.

In contrary to the band described before, $\nu(\text{CO}/\text{Ti}^{4+} (001))$ at 2169 cm⁻¹ shifts to lower wavenumbers up to 2166 cm⁻¹. Its intensity is decreasing with higher P-concentration compared to MoS₂/TiO₂. In this case we observe that these sites are gaining in basicity. This could be related to neighboring P-OH groups which are affecting the acidity of those Lewis acid sites via H-bonding between OH and Ti⁴⁺.

2.3.2.3. IR/CO analysis of $x\text{-NMoS}_2/\text{TiO}_2$

$\text{MoS}_2/\text{TiO}_2$ catalysts prepared with EDTA were analyzed by IR/CO. The obtained spectra are presented in Figure 12.

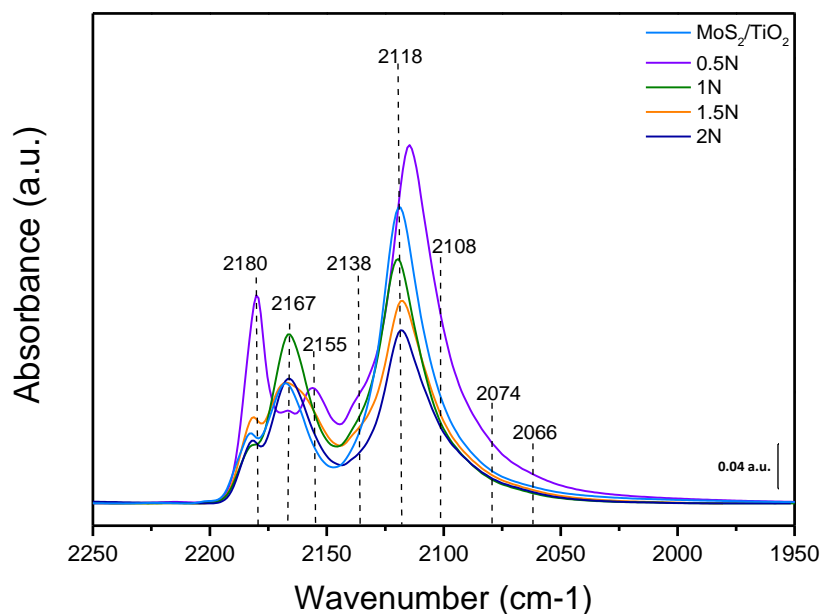


Figure 12: IR/CO adsorption spectra of $x\text{-NMoS}_2/\text{TiO}_2$ ($x= 0.5; 1; 1.5; 2$) at 1 Torr equilibrium pressure.

A shifting in the absorption band position of $\nu(\text{CO}/\text{M-edge})$ depending on the introduced amount of EDTA during preparation is noted. The most prominent shift of $\nu(\text{CO}/\text{M-edge})$ is observed when $\text{N}/\text{Mo} = 0.5$. Its downward shift to 2115 cm^{-1} indicates that the electron density of Mo has increased. IR/CO results also demonstrate that the addition of EDTA affects also the concentration of probed M-edge sites. The probed concentrations are summarized in Table 5.

Table 5: Determined number of M- and S-edges after small doses CO adsorption with the observed band position depending on N/Mo molar ratio as well as ICP-MS results to determine Mo-dispersion and S/Mo ratio.

| <i>Sample</i> | <i>$\nu(\text{CO/M-edge})$ (cm^{-1})</i> | <i>S-edge sites</i> ($\mu\text{mol/g}$) | <i>M-edge sites</i> ($\mu\text{mol/g}$) | <i>Estimated Mo dispersion</i> | <i>Atomic ratio S/Mo</i> |
|--|---|---|---|--------------------------------|--------------------------|
| <i>MoS₂/TiO₂</i> | 2118 | 0 | 84 | 0.15 | 2.32 |
| <i>0.5NMoS₂/TiO₂</i> | 2115 | 0 | 121 | 0.24 | 2.35 |
| <i>1NMoS₂/TiO₂</i> | 2119 | 0 | 78 | 0.15 | 2.28 |
| <i>1.5NMoS₂/TiO₂</i> | 2118 | 1 | 41 | 0.07 | 2.10 |
| <i>2NMoS₂/TiO₂</i> | 2118 | 0 | 38 | 0.07 | 2.10 |

Based on these results it is evident that the addition of EDTA during preparation is only beneficial when N/Mo = 0.5. Above this molar ratio the concentration of probed M-edge sites is decreasing and is even smaller than for MoS₂/TiO₂. Accordingly, Mo dispersion is following the same trend. However, the higher estimated Mo dispersion for 0.5NMoS₂/TiO₂ might indicate the formation of smaller MoS₂ slabs on this catalyst compared to MoS₂/TiO₂. Herein it might be possible that EDTA has favored the formation of small slabs when N/Mo = 0.5 by reducing the strong interaction between support and MoS₂. Yet, this reduction in interaction force was not sufficient to favor the creation of S-edges. Only for 1.5NMoS₂/TiO₂ a very weak band at 2066 cm⁻¹ was detected. Nevertheless, the determined S-edge site concentration of 1 μmol/g is insignificant compared to the amount of probed M-edge sites (41 μmol/g).

Depending the introduced amount of EDTA during preparation, specific facets are dispersed with MoS₂. In fact when N/Mo is increasing, the intensity of $\nu(\text{CO/Ti}^{4+} (001))$ is higher compared to the absorption bands of CO adsorbed on (101) (112) and (100) facets. Yet, when N/Mo = 0.5, the contrary is observed. The absorption band $\nu(\text{CO/Ti}^{4+} (001))$ presents the weakest intensity. Hence, it can be deduced that MoS₂ is dispersed preferentially on (001) facets for 0.5NMoS₂/TiO₂. For the other catalysts MoS₂ is dispersed majorly on (101) (112) and (100) facets.

At 2135 cm⁻¹ an absorption band ascribed to $\nu(\text{CO/MoOxSy})$ having a weak intensity is observed. Hence a very small amount of mixt molybdenum oxysulfide species were formed

although S/Mo ratios are above 2. Its intensity is slightly increasing with N/Mo ratio. The presence of MoOxSy might be linked to solubility issues of EDTA at high concentrations. As a result, inhomogeneous impregnation solutions are obtained leading to an uneven dispersion of MoS₂ on TiO₂.

Curve fitting allowed to distinguish a variation in sulfur coverage on M-edges depending N/Mo ratio (Figure 12 and Figure A2). The rising bands around 2106 and 2088-2074 cm⁻¹ correspond to adsorbed CO on M-edge sites with a sulfur coverage of 50% and 37.5% respectively.¹⁷ Consequently, EDTA permits the formation of S-vacancies. If we assume that $\nu(\text{CO/M-edge})$ and $\nu(\text{CO/S-vacancies on M-edges})$ have similar molar extinction coefficients, it is possible by a simple cross-multiplication between integrated area of $\nu(\text{CO/M-edge})$ and $\nu(\text{CO/S-vacancies on M-edges})$ and probed concentration of M-edges to estimate the amount of S-vacancies (Figure 13). Based on the obtained results EDTA favors the creation of sulfur depleted M-edges. The highest amount of S-vacancies is formed at N/Mo = 0.5 whereas as at N/Mo = 1 the lowest amount is formed.

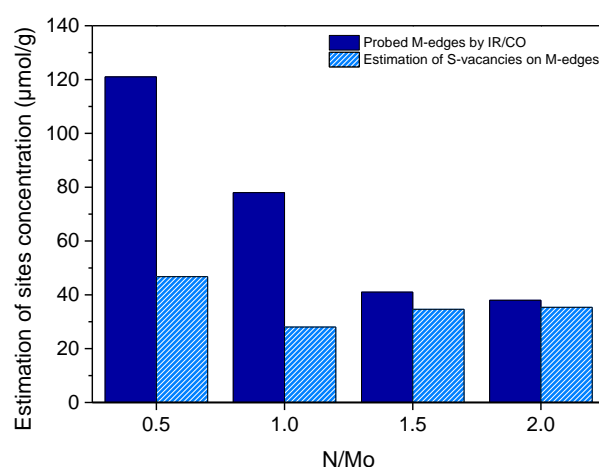


Figure 13: Evolution of M-edge sites concentration and estimated amount of formed S-vacancies on M-edges depending on N/Mo ratio by considering the molar extinction coefficient to be the same for both sites.

2.4. TEM analysis of 0.5NMoS₂/TiO₂: Impact of EDTA on MoS₂ slabs size

Estimated Mo dispersion for 0.5NMoS₂/TiO₂ are higher compared to the one for MoS₂/TiO₂. This increase in Mo dispersion might indicate a decrease in MoS₂ slab size. Herein, EDTA addition might favor a decrease in slab length. In the work of E.D. Garcia it was demonstrated that the average length of MoS₂ slabs supported on TiO₂ are large and have an average length of 6.8 ± 0.4 nm whereas the average stacking number is 2.1 ± 0.2 .⁴

In order to verify our hypothesis TEM images were taken of 0.5NMoS₂/TiO₂ to investigate the impact of EDTA on MoS₂ slab size and stacking. On the presented TEM image in Figure 14 small monolayered MoS₂ slabs visualized by the black lines are observed.

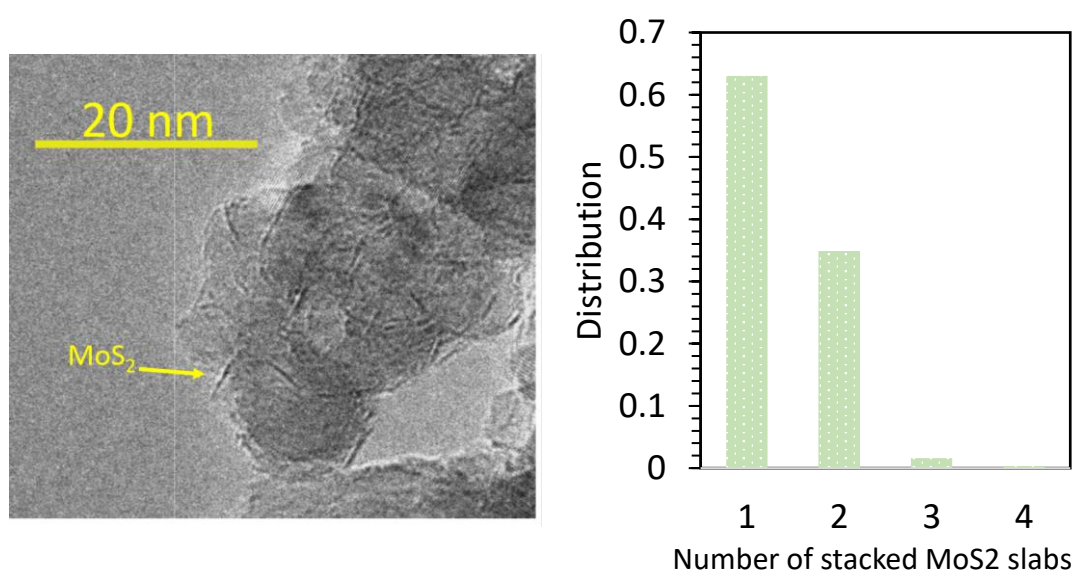


Figure 14: On the left, TEM-image of 0.5NMoS₂/TiO₂ showing small MoS₂ slab monolayers. On the right, distribution diagram of MoS₂ slabs stacking number.

Indeed, on a probed population of 547 slabs, we determine an average length of 2.0 ± 0.1 nm and an average stacking number of 1.4 ± 0.1 . Consequently, EDTA has an impact on MoS₂ stacking number and slab length which was reduced by a factor of 4 compared to the reported length on MoS₂/TiO₂. These results are explaining the higher probed concentrations of M-edge sites and the good dispersion of Mo. Hence, EDTA is also a useful chelating agent allowing the decrease in interaction between MoS₂ and TiO₂ thus avoiding the formation of large slabs.

Based on this result we can also strongly assume that H₃PO₄ has a similar effect on slab length when P/Mo = 0.5; 1 because of the strong increase of estimated Mo dispersion.

2.5. Raman analysis of MoS₂/TiO₂ prepared with EDTA or H₃PO₄

2.5.1. Raman spectra of x-PMoS₂/TiO₂

2.5.1.1. Analysis of non sulfided catalysts x-PMo/TiO₂

It is well known that in the presence of H₃PO₄, heptamolybdate is forming an organo-metallic complex.²⁰ These complexes are forming different Keggin structures depending on the pH solutions. By doping Mo/TiO₂ with various phosphoric acid amounts it can be expected that different Keggin structures were formed due to the change in acidity of the impregnation solution.²⁰

Since the pH of impregnation solution varied between 1 and 2 for P/Mo = 0.5; 1; 1.5 it is highly possible that 12 or 11-molybdophosphate was formed (PMo₁₂; PMo₁₁). These Keggin structures are composed of MoO₆ units, each one of them containing one terminal Mo-O bond and four bridging Mo-O-Mo bonds. The units share their edges forming Mo₃O₁₃ clusters in which tetrahedron PO₄ is centered. In the case of 11-molybdophosphate the missing Mo-atom deforms the Keggin structure. Different possible phosphomolybdate structures are pictured in Figure 15.

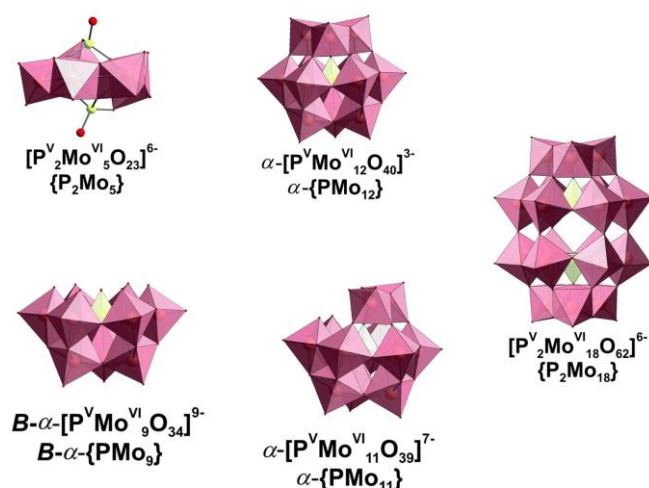


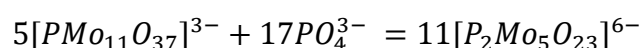
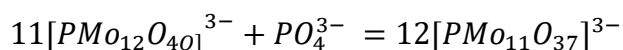
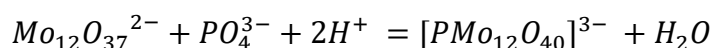
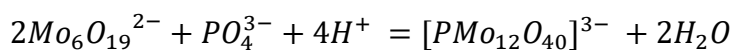
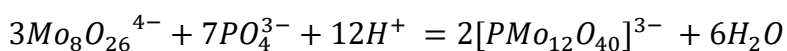
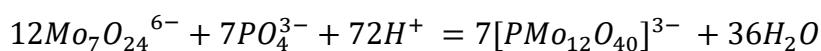
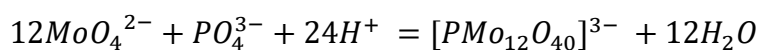
Figure 15: Representation of different Keggin structures of phosphomolybdates. MoO₆ units in pink, PO₄ center in yellow and oxygen in red.²⁰

Knowing which Keggin structure was impregnated on TiO₂ is important because it might help us better understand the low S/Mo ratios. Since impregnation solution's pH were measured we can expect to form the following heteropolyanions as described in Table 6.

Table 6: Expected phosphomolybdate complex formation related to impregnation solution's pH.

| $(X/Mo)_{mol}$ | 0.5 | 1 | 1.5 | 2 |
|--|--|--|---|---|
| pH for H ₃ PO ₄ solution | 2.13 | 1.18 | 1.04 | 0.95 |
| Stable Mo-H ₃ PO ₄ complex | [PMo ₁₂ O ₄₀] ³⁻ | [PMo ₁₂ O ₄₀] ³⁻ ↔ [PMo ₁₁ O ₃₉] ⁷⁻ | [PMo ₁₁ O ₃₉] ⁷⁻ [P ₂ Mo ₅ O ₂₃] ⁶⁻ | [P ₂ Mo ₅ O ₂₃] ⁶⁻ |

PMo₁₂ can be formed with any isopolymolybdate in the presence of H₃PO₄. Once PMo₁₂ is formed and pH = 1, it is in equilibrium with PMo₁₁. At further acidification PMo₁₁ is polymerizing to [P₂Mo₅O₂₃]⁶⁻ (noted P₂Mo₅) as long as the molar ratio P/Mo > 2.²¹ As followed the chemical equations are:



In order to validate the presence of PMo₁₂, commercial PMo₁₂ precursor was directly impregnated on TiO₂ (PMo₁₂/TiO₂) and its obtained Raman spectrum was compared to the once of dried x-PMo/TiO₂ (Table 7; Figure A4). The vibration bands of PMo₁₂ are observed at 990 and 998 cm⁻¹ for PMo₁₂/TiO₂. These exact vibrations are also visible for 0.5 and 1PMo/TiO₂. Hence, the presumption of the existence of PMo₁₂ on synthesized catalyst is confirmed.

Table 7: Observed Raman vibrations of dried x-PMo/TiO₂ and PMo₁₂/TiO₂.

| Dried Catalysts | Raman vibration band cm ⁻¹ | Attribution |
|-------------------------------------|--|--|
| PMo ₁₂ /TiO ₂ | 990 | [PMo ₁₂ O ₄₀] ³⁻ |
| | 998 | |
| Mo/TiO ₂ | 950 | [Mo ₁₂ O ₃₇] ²⁻ |
| 0.5PMo/TiO ₂ | 989 | [PMo ₁₂ O ₄₀] ³⁻ |
| 1PMo/TiO ₂ | 987 | [PMo ₁₂ O ₄₀] ³⁻ |
| | 991 | |
| 1.5PMo/TiO ₂ | 951 | [H ₂ P ₂ Mo ₅ O ₂₃] ⁴⁻ |
| 2PMo/TiO ₂ | 951 | [H ₂ P ₂ Mo ₅ O ₂₃] ⁴⁻ |

The formation of PMo₁₂ is predominant as long as P/Mo ≤ 1. Above this molar ratio we notice the formation of P₂Mo₅, the polymerized form of PMo₁₁ already described by Murata et al. who studied the formed species in function of molar ratio between H₃PO₄ and molybdenum depending pH's solution via Raman.²¹ Indeed, Murata et al. described P₂Mo₅ to be stable at a pH between 1 and 4 when P/Mo = 2. However, the ratio 1.5 was not studied by these authors and yet P₂Mo₅ is detected. Consequently, we can assume that at P/Mo > 1.5 (1 < pH < 2) during preparation, PMo₁₂ is formed.

2.5.1.2. Raman analysis of sulfided catalysts x-PMoS₂/TiO₂

Raman spectroscopy is an important analysis tool to analyze the phase nature of MoS₂. It allows to distinguish 2H-MoS₂ from its polytype 1T-MoS₂. In the literature 2H-MoS₂ was described to have two characteristic bands at 380 and 407 cm⁻¹ corresponding to E_{2g} (vibration in-plane) and A_{1g} (vibration out-of-plane) respectively. The 1T-phase is characterized by four bands J₁, J₂, J₃ (i.e. acoustic phonon modes) and A_{1g} detected at 151, 212-226, 333 and 412 cm⁻¹.²²

Raman spectra of synthesized P-doped and undoped MoS₂/TiO₂ are presented in Figure 16. For MoS₂/TiO₂ E_{2g} and A_{1g} are found at 388 and 401 cm⁻¹. The vibration bands at 397, 517, 640 cm⁻¹ belong to Ti-O structural vibrations (B_{1g}(1), B_{1g}(2) + A_{1g} and E_g(3)).²³ The Raman spectrum of TiO₂ anatase is figured in the annex (Figure A3). An intense band around 157 cm⁻¹ is also visible and refers to E_g(1) of TiO₂. The vibration bands at 517 and 640 cm⁻¹ are decreasing in intensity with higher H₃PO₄ concentration and are also shifted; especially the band B_{1g}(2)+A_{1g} at 517 cm⁻¹. For P/Mo > 1, the vibration B_{1g}(2)+A_{1g} is redshifted by 6 cm⁻¹ compared to MoS₂/TiO₂. This shift indicates that Ti-O bonds are under tensile strain. This could be linked to sulfur/oxygen exchange in TiO₂ occurring during sulfidation.

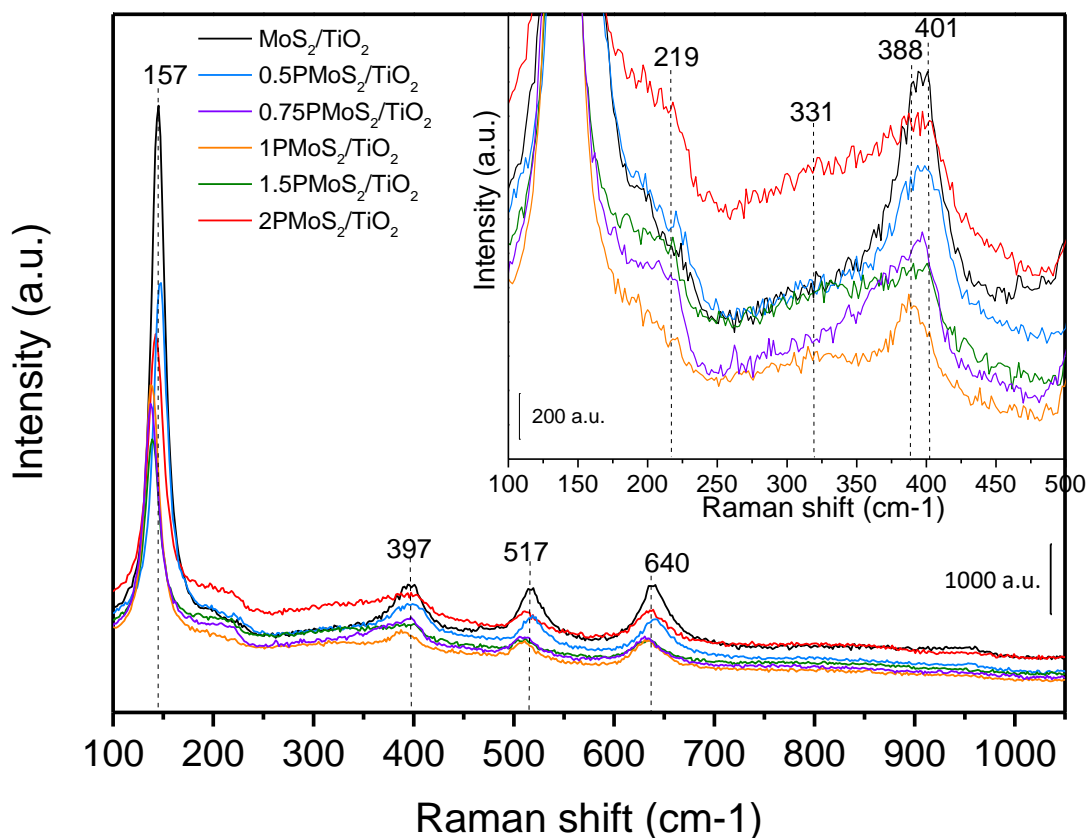


Figure 16: Raman spectra of P-doped and undoped MoS₂/TiO₂ with a zoom on MoS₂ vibration region in the capture.

We also note the appearance of a new broad band in between 321 and 331 cm⁻¹ with increasing H₃PO₄ concentration. Parallely to this contribution, a band at 219 cm⁻¹ is also appearing and rises in intensity with increasing P-loading. For both bands the maximum intensity is archived when P/Mo = 2. At first, one might confuse these two bands with J₂ and J₃ of 1T-MoS₂. However, the vibration band A_{1g} at 412 cm⁻¹ is missing. Therefore, it seems more likely that those bands are related to the structural vibration Mo-O of molybdenum oxide which is favored with higher H₃PO₄ concentrations on x-PMoS₂/TiO₂.²⁴ The presence of molybdenum oxide species in form of MoO_xS_y was confirmed by IR/CO. Hence the introduction of H₃PO₄ via incipient impregnation did not favor the formation of 1T-MoS₂.

2.5.2. Raman spectra of EDTA prepared catalysts

2.5.2.1. Raman analysis of non sulfided catalysts x-NMo/TiO₂

In the literature, not many studies have treated the complexation of EDTA with molybdenum and even less considered the system EDTA-Mo impregnated on TiO₂-anatase. As a result, it is difficult to elucidate which complex was formed based on the obtained Raman spectra of non-sulfided catalysts (Table 8). We note that the band at 950 cm⁻¹ ascribed to [Mo₁₂O₃₇]²⁻ is downward shifted to 935 cm⁻¹ with higher EDTA amounts. At N/Mo = 0.5 a new band is appearing at 924 cm⁻¹ and disappears instantly when the molar ratio surpasses 0.5. It follows that only two bands are observed at 935 cm⁻¹ and 950 cm⁻¹ which correspond to the symmetric band vibration $\nu(\text{Mo-O}_t)$ of [Mo₇O₂₄]⁶⁻ and [Mo₁₂O₃₇]²⁻.²⁵

Table 8: Observed Raman vibrations for dried and calcined x-NMo/TiO₂. Attributions were based on reported attributions.^{26;27}

| Catalyst | Dried: Raman vibration band cm⁻¹ | Attribution |
|-------------------------|--|--|
| Mo/TiO ₂ | 950 | [Mo ₁₂ O ₃₇] ²⁻ |
| 0.5NMo/TiO ₂ | 924 | |
| | 935 | (Mo-O _t) ν_{sym} [Mo ₇ O ₂₄] ⁶⁻ |
| | 950 | [Mo ₁₂ O ₃₇] ²⁻ |
| 1NMo/TiO ₂ | 935 | (Mo-O _t) ν_{sym} [Mo ₇ O ₂₄] ⁶⁻ |
| 1.5NMo/TiO ₂ | 950 | [Mo ₁₂ O ₃₇] ²⁻ |
| 2NMo/TiO ₂ | | |

Although Raman spectra of x-NMo/TiO₂ are not informative about the formed complex, which is important for this work in order to comprehend the S/Mo ratios, it is possible to assume which kind of complex was formed based on the work of Richard L. Kula.²⁸ In his analytical work about EDTA-Mo(VI) complexation, Kula describes the different formed complexes in function of pH using NMR and pH-titration. This provides important key information about the potential formed EDTA-Mo complex on x-NMoS₂/TiO₂. When the molar ratio between EDTA

and Mo is inferior to ½, dimeric [(MoO₃)₂EDTA]⁴⁻ is formed between a pH of 4 to 6. However, when this ratio is higher, monomeric [(MoO₃)EDTA]⁴⁻ is observed and furthermore above a pH of 2 polymerization occurs (Figure 17).

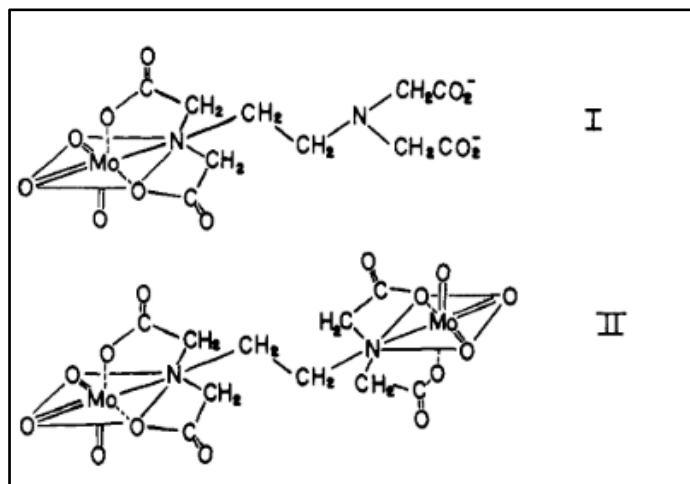


Figure 17: Complex structure of monomeric [(MoO₃)EDTA] (I) and dimeric [(MoO₃)₂EDTA] (II).²⁸

Knowing the impregnation solution's pH for each prepared catalyst (Table 9), it can be assumed that for N/Mo = 0.5 a dimeric complex was impregnated on the support. Whereas for N/Mo = 1; 1.5; 2 either a monomeric complex was formed or even polymerized since pH varies between 2 and 3.

Table 9: Expected Mo-EDTA complex depending on impregnation solution's pH.

| (X/Mo)mol | 0.5 | 1 | 1.5 | 2 |
|------------------------|---|---|---|--|
| pH for EDTA | 4 | 3 | 2-3 | 2 |
| Stable Mo-EDTA complex | [(MoO ₃) ₂ EDTA] ⁴⁻ | [(MoO ₃)EDTA] ⁴⁻ | [(MoO ₃)EDTA] ⁴⁻ | [(MoO ₃)EDTA] ⁴⁻ polymerized |

2.5.2.2. Raman analysis of sulfided catalysts x-NMoS₂/TiO₂

The obtained Raman spectra of MoS₂/TiO₂ prepared with EDTA are shown in (Figure 18). The support's vibration bands were found at 145; 395; 516 and 639 cm⁻¹ while the characteristic Raman bands of 2H-MoS₂ were detected at 383 and 404 cm⁻¹. For the latter, a blueshift with increasing EDTA concentration to 387 and 407 cm⁻¹ respectively was noticed. Moreover the

addition of EDTA improved the crystallinity of the 2H phase. This deduction can be made based on the gained band intensity of E_{2g} and A_{1g} as well as their observed blueshift.

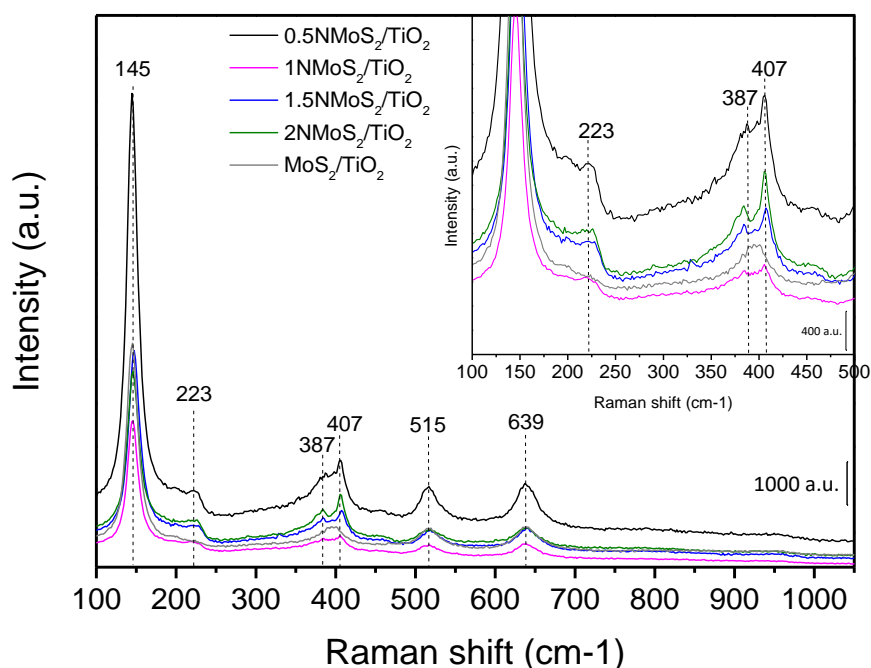


Figure 18: Raman spectra of $x\text{-NMoS}_2/\text{TiO}_2$ ($x = 0; 0.5; 1; 1.5; 2$) with a zoom on MoS₂ vibration region in the capture.

2.6. UV-Vis analysis of MoS₂/TiO₂ prepared with EDTA or H₃PO₄

In order to investigate the impact of sulfidation on TiO₂ charge transfer as well as the impact of EDTA and H₃PO₄ on MoS₂ electrical conductivity, energy gaps were determined by using Tauc-plot. Herein, UV-Vis spectra were taken of prepared sulfided and non sulfided catalysts with EDTA or with H₃PO₄. The mathematical methodology was already described in the first chapter. In overall, the smaller the energy gap, the more the material is approaching the properties of a conductor. This decrease reflects subsequently an improvement in charge transfer.

2.6.1. Effect of sulfidation on TiO₂ energy gap

Tauc-plots of sulfided and non sulfided TiO₂ were traced (Figure 19). The determined energy gap of TiO₂ ($E_g(\text{TiO}_2)$) is around 3.1 eV. The obtained value is in agreement with reported TiO₂ energy gap of around 3.2 eV.^{29,30} With a 2%wt intake in sulfur, a small decrease in energy gap was observed. It was determined to be 2.9 eV. Yet, with a difference of 0.2 eV it seems very improbable that sulfidation will induce any enhancement in TiO₂ charge transfer.

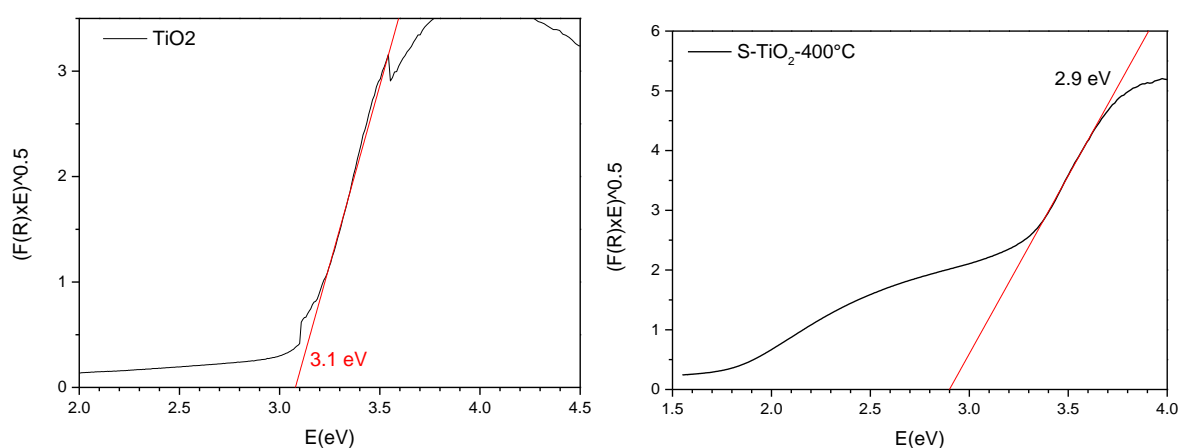


Figure 19: Tauc-plots of TiO₂ and sulfided TiO₂ (S-TiO₂) at 400°C.

2.6.2. Effect of H₃PO₄ addition during synthesis on energy gaps

Based on ICP-MS and Raman results, H₃PO₄ acts as a source of phosphorous making MoS₂ doping possible. But we also have seen that phosphoric acid has also a strong impact on TiO₂. Hence, one might expect to observe a more pronounced effect on TiO₂ and MoS₂ energy gaps compared to EDTA since it decomposed completely after sulfidation. Herein, energy gaps of TiO₂ were determined before and after sulfiding P-doped catalysts. E_g of MoS₂ were also determined using Tauc-plot to investigate the impact of H₃PO₄ addition on MoS₂ conductivity. The obtained values depending P/Mo ratio of TiO₂ and MoS₂ energy gaps are summarized in Figure 20.

First a decrease in TiO₂ energy gap was observed after Mo impregnation (Figure 20A). E_g decreased from 3.1 eV to 2.8 eV. Subsequently the impregnation of TiO₂ with Mo has narrowed the energy gap between the valence and conduction band. This observation

concorde with other research works in which different transition metals were used.³¹ After sulfiding Mo/TiO₂, $E_g(\text{TiO}_2)$ is decreasing further to 2.3 eV.

The energy gaps of TiO₂ before and after sulfidation are varying depending on the molar ratio P/Mo (Figure 20A). In both cases the lowest energy gaps are measured when P/Mo = 0.75; 1. Subsequently P-doping is affecting directly TiO₂ band gap energy probably due to the adsorption of H₃PO₄ on TiO₂ during synthesis. Yet, $E_g(\text{TiO}_2)$ of non-sulfided catalysts are higher compared to sulfided catalysts. Consequently S-doping allows to decrease considerably TiO₂ energy gap in combination with Mo and phosphorous.

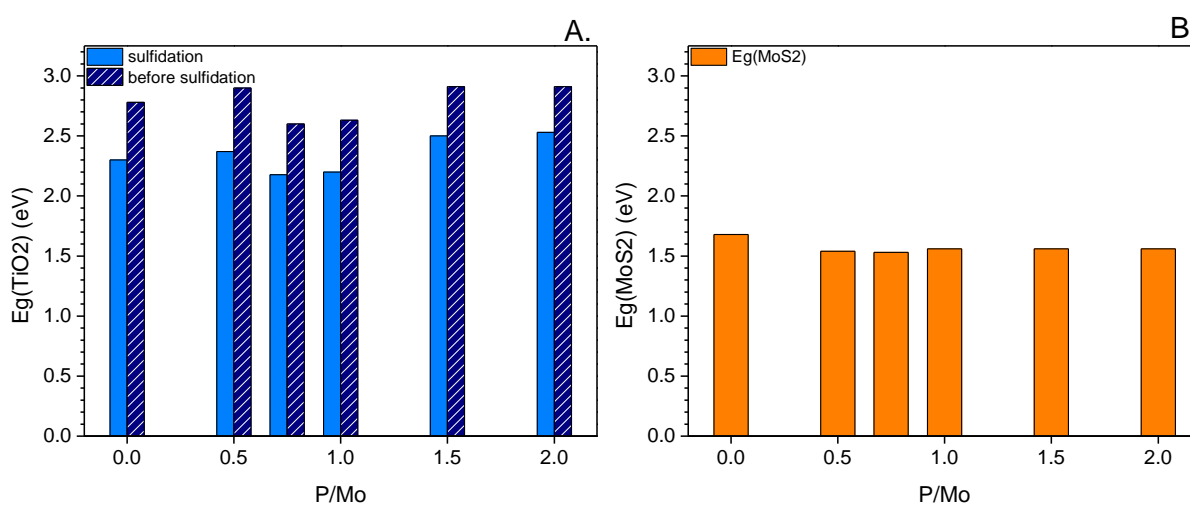


Figure 20: Estimated energy gaps by Tauc-plot in function of molar ratio P/Mo: (A.) E_g of TiO₂ before and after sulfidation; (B.) E_g of MoS₂.

In contrast to the noteworthy impact observed for $E_g(\text{TiO}_2)$, the addition of phosphoric acid is not affecting significantly the energy gap of MoS₂ (Figure 20B). A small decrease of 0.15 eV was noted by adding H₃PO₄ during preparation which could be explained by the P-doping effect of MoS₂. The smallest energy gap for MoS₂ was observed when P/Mo = 0.5; 0.75.

2.6.3. Effect of EDTA addition during synthesis on energy gaps

Exactly as for x-PMoS₂/TiO₂, energy gaps of TiO₂ and MoS₂ were determined before and after sulfiding EDTA prepared catalysts. The obtained values depending N/Mo ratio are summarized in Figure 21.

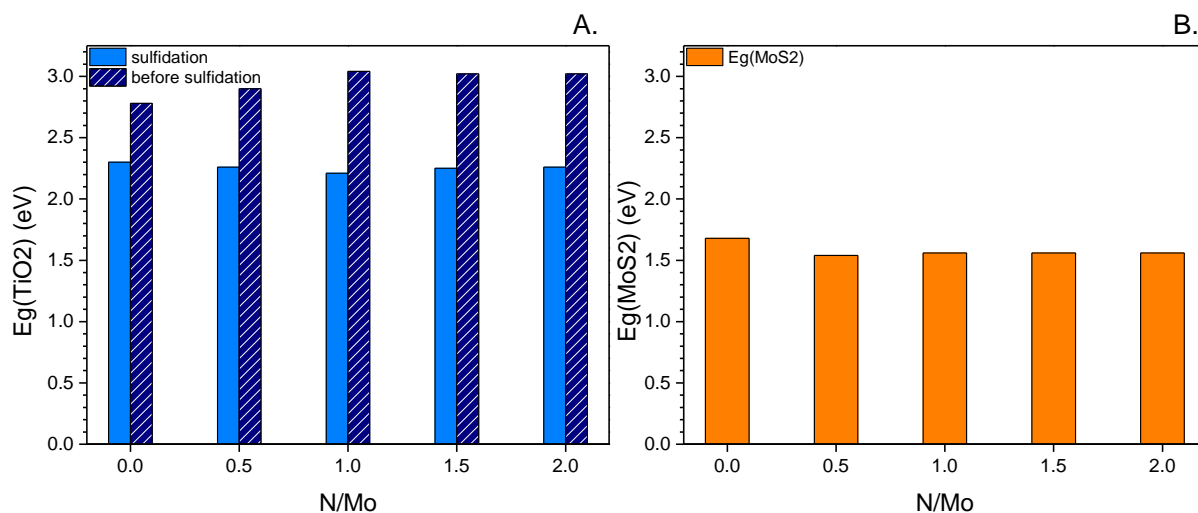


Figure 21: Estimated energy gaps by Tauc-plot in function of molar ratio N/Mo: (A.) Eg of TiO₂ before and after sulfidation; (B.) Eg of MoS₂.

However TiO₂ and MoS₂ energy gaps remain relatively constant even after the addition of EDTA during preparation. Herein EDTA has no impact on TiO₂ energy gap after sulfidation.

2.7. HDS and HER activity tests of MoS₂/TiO₂ prepared with EDTA or H₃PO₄

2.7.1. HDS activity test

2.7.1.1. HDS of thiophene with P-doped MoS₂/TiO₂

Hydrodesulfurization (HDS) of thiophene in the presence of x-PMoS₂/TiO₂ was conducted at 350°C. These catalytic tests were performed to study the accessibility of M-edge sites and investigate their activity in function of P/Mo ratio. The obtained activities are summarized in Table 10.

Table 10: HDS activity results of P-doped MoS₂/TiO₂ catalysts in function of P/Mo ratio.

| <i>ratio(P/Mo)</i> | 0 | 0.5 | 0.75 | 1 | 1.5 | 2 |
|--|------|------|------|------|------|------|
| <i>r HDS (without THT) mol/h.kg</i> | 6.3 | 1.9 | 3.9 | 3.6 | 3.5 | 1.6 |
| <i>probed M-edges μmol/g</i> | 84 | 115 | 115 | 116 | 77 | 50 |
| <i>intrinsic activity h⁻¹</i> | 74.6 | 16.8 | 33.6 | 31.1 | 45.4 | 31.6 |

Several observations were made. First the catalysts are not stable for a long time. After three hours they are deactivated. Secondly, they are selective towards the formation of butane and not but-1-ene. This observation is related to the presence of exposed M-edge sites favoring the hydrogenation pathway during HDS of thiophen. This observation is also in agreement with the work of Moses et al.³²

At last, we note that the presence of phosphor is not beneficial for HDS. The activity rates of x-PMoS₂/TiO₂ drop by 40% compared to MoS₂/TiO₂ (Table 10). Nonetheless, by comparing the effect of increasing P-loading on x-PMoS₂/TiO₂, a rise in HDS activity rates is observed up to 3.9 mol/h.kg. This activity rate remains approximatively constant for 0.5 < P/Mo < 1.5. When P/Mo = 2, the lowest activity with 1.58 mol/h.kg is achieved.

The described variation in HDS activity depending P/Mo ratio is probably linked to M-edge site concentration. Since active sites are located on M-edges, it is evident that the higher their concentration is, the more active will be the catalyst for HDS. Indeed 115 μmol/g of M-edge sites were probed by CO when P/Mo is in between 0.5 and 1 whereas the lowest amount of M-edge sites was probed when P/Mo = 2. Hence, the amount of M-edge sites was divided by three causing 2PMoS₂/TiO₂ to be the less active catalyst for HDS. However this explanation is not accurate for 0.5PMoS₂/TiO₂ and 1.5PMoS₂/TiO₂. For the first a low HDS activity was observed despite having 115 μmol/g of M-edge sites whereas the latter one is endowed with a higher HDS activity with only 77 μmol/g of probed M-edge sites. Moreover 1.5PMoS₂/TiO₂ presents the highest intrinsic activity compared to the other P-doped MoS₂ catalysts.

As a result, the number of M-edges is not the only parameter affecting HDS-activity. One possible parameter which might have influenced activity is the type of facet on which MoS₂ was dispersed. Based on IR/CO results (100) facets were majorly covered with MoS₂ when

P/Mo = 0.5. Contrarywise the dispersion of MoS₂ on (100) and (001) facets was approximatively equivalent when P/Mo was superior to 0.5. Subsequently, MoS₂ covering (001) facets could be more active for HDS of thiophen. Indeed (001) facets were reported to be more catalytically active than (100) due to their higher surface energy which is more efficient for dissociative adsorption of reactants.^{33,34} As a result, the higher surface energy of (001) facets might influence the adsorption of reactants on MoS₂ leading to higher intrinsic activities.

2.7.1.2. HDS of thiophene with EDTA prepared MoS₂/TiO₂

The catalytic test of x-NMoS₂/TiO₂ was conducted in the same conditions described above. During the catalytic test no selectivity for the formation of butane or butene was observed. Both compounds were equally formed. And it should also be emphasized that for N/Mo = 0.5; 1; 1.5; 2 no THT was detected which might be due to its fast conversion. Activity rates of sulfided catalysts are doubled when the molar ratio between N and Mo equals 0.5 and 1 (Table 11). Afterwards a decline is observed in accordance with the decrease of M-edge site concentration. But, if the concentration of active sites is included, 1.5NMoS₂/TiO₂ is presenting the highest intrinsic activity. Afterwards the intrinsic activity is decreasing in the following order: 1.5NMoS₂/TiO₂ > 1NMoS₂/TiO₂ > 2NMoS₂/TiO₂ > 0.5NMoS₂/TiO₂ > MoS₂/TiO₂.

Table 11: HDS-test results for EDTA prepared MoS₂/TiO₂ catalysts.

| <i>ratio(N/Mo)</i> | 0 | 0.5 | 1 | 1.5 | 2 |
|--|------|------|-------|-------|-------|
| <i>r HDS (without THT) mol/h.kg</i> | 6.3 | 10.4 | 13.6 | 9.7 | 3.8 |
| <i>probed M-edges μmol/g</i> | 84 | 121 | 78 | 41 | 38 |
| <i>intrinsic activity h⁻¹</i> | 74.6 | 85.7 | 173.8 | 237.8 | 101.3 |

Based on the obtained results it is surprising that 0.5NMoS₂/TiO₂ having the highest M-edge site concentration (121 μmol/g) presents a lower intrinsic activity compared to 1.5NMoS₂/TiO₂ which has 30% less M-edges. The presence of S-vacancies on M-edges doesn't give further information since 1.5NMoS₂/TiO₂ has also less probed vacancies than 0.5NMoS₂/TiO₂. At this point we cannot explain this trend of intrinsic activity.

2.7.2. HER-Test

2.7.2.1. P-doped MoS₂/TiO₂

Polarization curves of 0.75 and 2PMoS₂/TiO₂ were acquired in order to test the HER activity and determine the effect of P-doping. These catalysts were chosen because of their low energy gap, knowing that the difference in value is minimal. It was hypothesized that if the energy gap of the sulfided catalyst is low, then charge transfer might be sufficiently improved in order to observe an activity. 0.75PMoS₂/TiO₂ was chosen due to its high amount of probed M-edge sites while having a high HDS intrinsic activity in comparison to other P-doped catalysts. In contrary, 2PMoS₂/TiO₂ presented the lowest HDS intrinsic activity and M-edge sites concentration.

The HDS activity was included into the selection parameters. Since for both reactions active sites are located on the M-edges, a similar trend in activity should be observed for HDS and HER. In short, if in a batch of samples a catalyst presents a high HDS activity it will probably have a good HER activity. In Table 12 are summarized the main characterization results. Theoretically, based on the made assumptions MoS₂/TiO₂ should be the most active one for HER followed by 0.75PMoS₂/TiO₂ and 2PMoS₂/TiO₂.

Table 12: Overview on the main characterization results of x-PMoS₂/TiO₂ (x=0; 0.75; 2).

| Sample | Energy gap TiO₂ (eV) | Energy gap MoS₂ (eV) | r(HDS) mol/h.kg | Probed M-edge site concentration (μmol/g) | Estimated Mo dispersion | Atomic ratio S/Mo |
|---|--|--|------------------------|--|--------------------------------|--------------------------|
| MoS ₂ /TiO ₂ | 2.30 | 1.68 | 6.3 | 84 | 0.15 | 2.32 |
| 0.75PMoS ₂ /TiO ₂ | 2.18 | 1.53 | 3.9 | 115 | 0.17 | 1.87 |
| 2PMoS ₂ /TiO ₂ | 2.53 | 1.56 | 1.6 | 50 | 0.10 | 0.88 |

The obtained HER polarization curves and Tafel slopes are presented in Figure 22 and Figure 23 respectively. As a reminder the activity increases when overpotentials ($|η_0|$) are decreasing.

The overpotentials of analyzed catalysts are decreasing in the following order: 2PMoS₂/TiO₂ < MoS₂/TiO₂ < 0.75PMoS₂/TiO₂. Consequently, the activity is increasing in the same order.

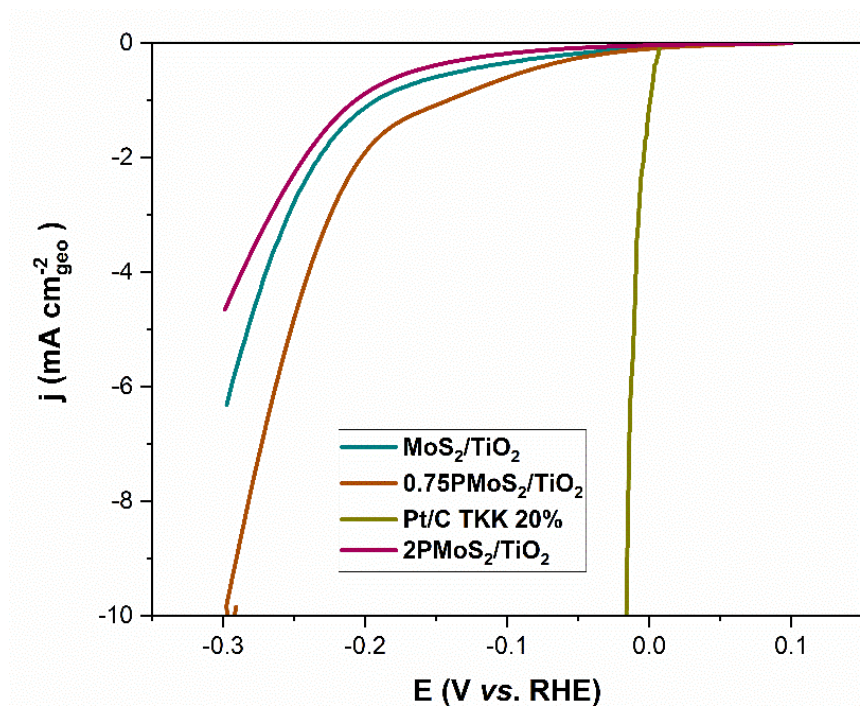


Figure 22: HER polarization curves of x -PMoS₂/TiO₂ ($x=0; 0.75; 2$) in 0.5M H₂SO₄.

This increase in activity is strongly related to the amount of M-edge sites probed by CO. Indeed, 0.75PMoS₂/TiO₂ presents the highest amount of probed M-edge sites followed by MoS₂/TiO₂ and 2PMoS₂/TiO₂. Logically, the more active sites, the higher the activity. Moreover, based on IR/CO and ICP-MS results a large amount of MoO_xS_y is to be found on 2PMoS₂/TiO₂. This phase appears to contribute barely or not at all to HER activity.

Additionally to the effect of M-edge sites concentration, charge transfer from TiO₂ to MoS₂ seems to have influenced also activity. The estimated energy gaps of TiO₂ when P/Mo = 0; 0.75; 2 are increasing in the same described order of increasing HER activity (i.e. 2PMoS₂/TiO₂ < MoS₂/TiO₂ < 0.75PMoS₂/TiO₂). Subsequently H₃PO₄ allowed to some extent enhance charge transfer of TiO₂ leading to a small improvement in activity. Nevertheless, TiO₂ is still presenting a high resistance which explains the high overpotentials at low current densities (> -300 mV). This is the reason why the range of measurements stops at -0.4 V because the measured overpotentials are superior to the ones of bulk MoS₂ reflecting the very low HER activity.⁶

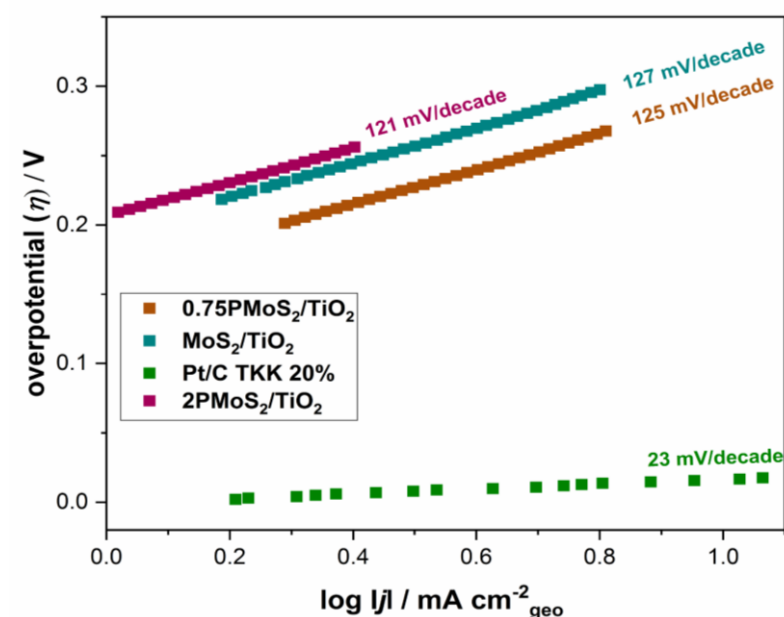


Figure 23: Tafel slopes of x -PMoS₂/TiO₂ ($x=0; 0.75; 2$).

Extrapolated Tafel slopes of analyzed catalysts are shown in Figure 23. These slopes are giving information about HER kinetics (i.e. Rate determining step and mechanism path). It should be noted that the determined slopes of these specific analyzed catalysts are not reliable because of the fast drop in current density when overpotentials are increasing. This “drop” could be related to some resistance phenomenon on the catalytic surface and/or secondary reactions in which for example molybdenum oxide species or the sulfided support are reduced. Consequently, the determined Tafel slopes are approximations but still qualitatively informative.

Based on the estimated slopes, P-doping of MoS₂/TiO₂ with H₃PO₄ did not impact Tafel slopes. They remain constant around 125 mV/dec. Therefore it can be inferred that the rate determining step is the Volmer step. Subsequently, the adsorption of protons which is the first step of HER, is very slow.

This observation could be linked to TiO₂ poor charge transfer limiting Volmer step in which electrons are involved. Additionally, energy gaps of MoS₂ remained similar after P-doping which means that the metallic character of MoS₂ was not improved and consequently proton adsorption was neither facilitated. Similarly, molybdenum’s electron density was not modified after P-doping. Thus, it can be deduced that the affinity towards protons was not improved.

At last, another parameter which could explain the high Tafel slopes is the existing strong interaction between MoS₂ and TiO₂.

Indeed F. Abild-Pedersen and co-workers have demonstrated via DFT calculations that HER activity of MoS₂ edge sites are tuned by the adhesion energy (E_{ad}) of MoS₂ onto support.³⁵ The used theoretical model for DFT calculations took into account long range Van der Waals interactions which are responsible for MoS₂ adhesion and demonstrated that the free adsorption energy of protons (ΔG_H) decreases with increasing adhesion energy leading to weaker hydrogen binding (Figure 24).

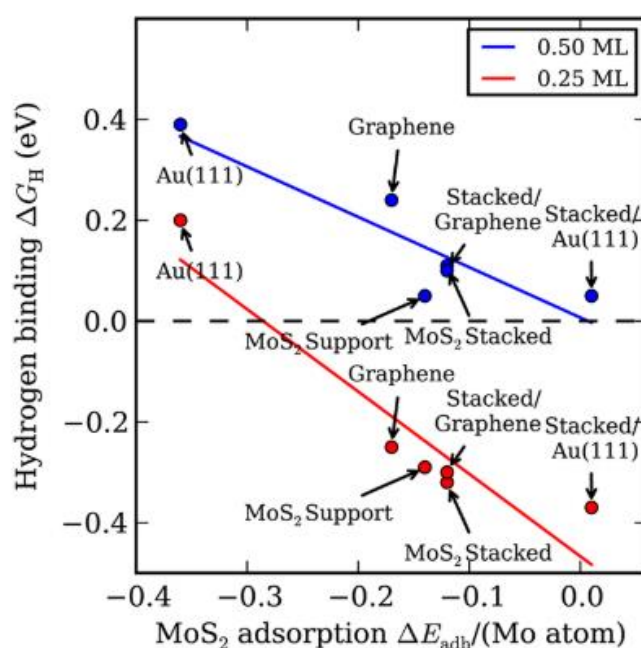


Figure 24: Results of DFT calculation made by F. Abild-Pedersen et al. representing hydrogen binding plotted in function of adhesion energy per Mo atom based on different sulfur coverage on M-edge sites (50%, 0.50 ML and 25%, 0.25 ML).³⁵

In this work two different supports were considered: graphene and Au(111) with monolayer or stacked MoS₂ layers. Considering the sulfur coverage of 50% on M-edge sites, the obtained adhesion energies for stacked MoS₂ layers on Au(111) (0.01 eV) was bigger than on graphene (-0.12 eV). Meaning that hydrogen binding is weaker for stacked M-edge sites deposited on graphene. After P. Raybaud's DFT calculation, the adhesion energy of MoS₂ on TiO₂ anatase with a sulfur coverage of 50% on M-edge sites fluctuated between -0.20 and -1.30 eV depending on formed Mo₆S_n clusters.³⁶ For 100% S-coverage on M-edge sites the adhesion energy is above -0.2 eV. If we place these values on the plot in Figure 24, ΔG_H of MoS₂/TiO₂ is in between the region of graphene and Au(111). Hereby it can be assumed that due to strong

adhesion energy of MoS₂ onto TiO₂, a decrease in hydrogen binding is induced and subsequently reducing HER activity.

Consequently it may be possible to approach thermo-neutral hydrogen binding (~ 0 eV) and preventing Volmer step to be the determining step, if S-coverage will be reduced on M-edges and strong interaction between MoS₂ and TiO₂ will be weakened.

2.7.2.2. MoS₂/TiO₂ prepared with EDTA

The HER activity tests of MoS₂/TiO₂ prepared with EDTA were also conducted. Herein all the catalysts prepared with EDTA were tested for HER due to the strong HDS activity variations. It was speculated since during both reaction hydrogen is adsorbed on M-edges where HDS and HER active sites are located, a strong variation in HER activity should also be observed. The obtained polarization curves of x-NMoS₂/TiO₂ are shown in Figure 25.

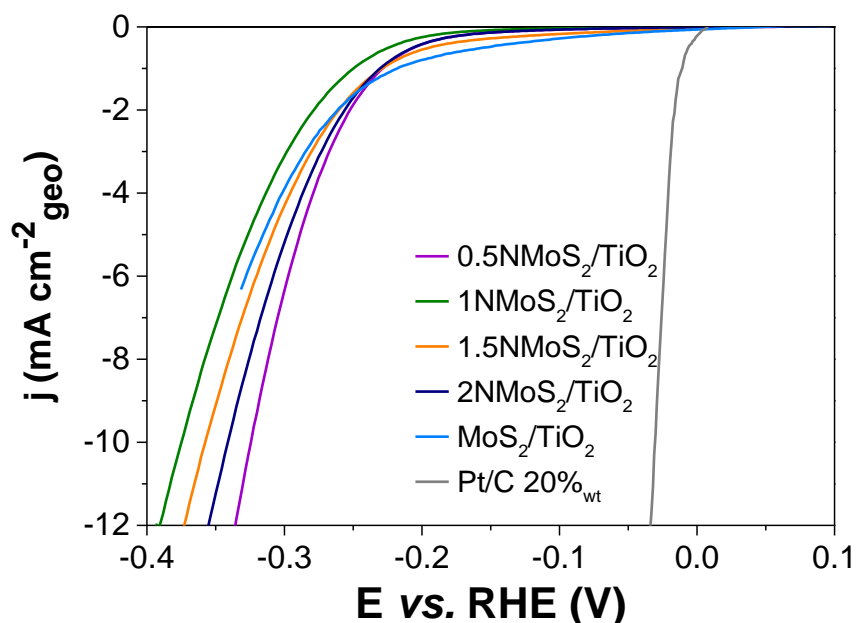


Figure 25: Polarization curves of x-NMoS₂/TiO₂ (x=0; 0.5; 1; 2) obtained during HER activity test.

The overpotentials of x-NMoS₂/TiO₂ were also below -0.3 V probably due to the low conductivity of the carrier as established for x-PMoS₂/TiO₂.

We observe that at -6 mV/cm² overpotentials are decreasing in the following order: 1NMoS₂/TiO₂ > MoS₂/TiO₂ > 1.5NMoS₂/TiO₂ > 2NMoS₂/TiO₂ > 0.5NMoS₂/TiO₂. Subsequently

HER activity increases in the same described order. However based on the surface characterization results made by IR/CO, UV-Vis spectroscopy and HDS activity tests it is not obvious to find a common explanation for this HER activity trend (Table 13).

Table 13: Overview of the main characteristics of x-NMoS₂/TiO₂.

| Sample | Atomic ratio S/Mo | Estimated energy gap TiO₂ (eV) | Estimated energy gap MoS₂ (eV) | r(HDS) mol/h.kg | Probed M-edge sites concentration (μmol/g) | Estimated Mo dispersion |
|--|--------------------------|--|--|------------------------|---|--------------------------------|
| MoS ₂ /TiO ₂ | 2.32 | 2.30 | 1.68 | 6.3 | 84 | 0.15 |
| 0.5NMoS ₂ /TiO ₂ | 2.35 | 2.31 | 1.64 | 10.4 | 121 | 0.24 |
| 1NMoS ₂ /TiO ₂ | 2.28 | 2.21 | 1.67 | 13.6 | 78 | 0.15 |
| 1.5NMoS ₂ /TiO ₂ | 2.10 | 2.22 | 1.71 | 9.7 | 41 | 0.07 |
| 2NMoS ₂ /TiO ₂ | 2.10 | 2.23 | 1.69 | 3.85 | 38 | 0.07 |

The lowest and highest HER activity rate were obtained for 1NMoS₂/TiO₂ and 0.5NMoS₂/TiO₂ respectively. This observation is certainly linked to amount of probed M-edge sites which is the highest for 0.5NMoS₂/TiO₂ as IR/CO results validate.

Surprisingly, although 1.5N and 2NMoS₂/TiO₂ present half of the amount of probed M-edge sites on 1NMoS₂/TiO₂, they are more active. Moreover, both of them present lower Mo dispersions implying larger MoS₂ slabs reflecting lower contact surface with reactants. Based on the obtained characterization results (Table 13), it is impossible to explain this trend in activity. It may be possible that the observed slight improvement in HER activity is related to the formation of S-vacancies on M-edges playing the role of additional active sites.

Another additional explanation to the observed differences in HER activity might be related to the selective dispersion of MoS₂ on (001) facets when N/Mo = 0.5. Indeed, IR/CO analysis showed that (001) facets are majorly covered with MoS₂ when N/Mo = 0.5 whereas at other N/Mo ratios, (100) facets were preferentially covered with MoS₂. As previously observed and explained for x-PMoS₂/TiO₂, MoS₂ dispersed on (001) facets might be more active for HER.³⁴

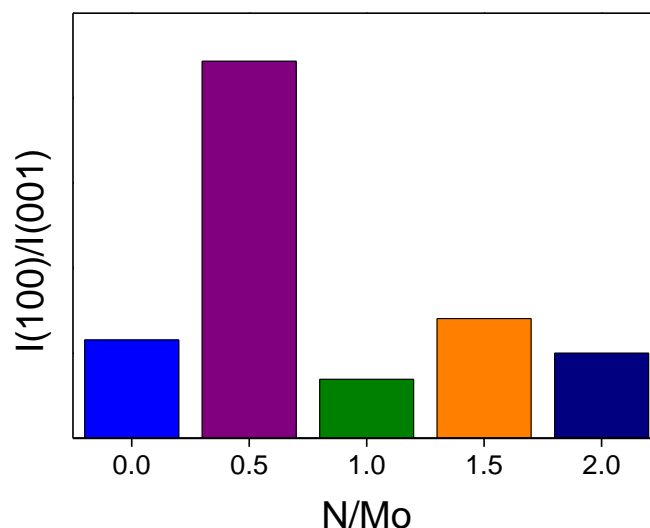


Figure 26: Evolution of the intensity ratio between $v(\text{CO}/\text{Ti}^{4+}(100))$ and $v(\text{CO}/\text{Ti}^{4+}(001))$ in function of N/Mo ratio.

In Figure 26 the presented column diagram shows the evolution of the intensity ratio between $v(\text{CO}/\text{Ti}^{4+})$ of (100) and (001) facets. The diagram makes evident that the amount of dispersed MoS₂ on (001) facets is increasing in the following order: 1NMoS₂/TiO₂ < 1NMoS₂/TiO₂ < 2NMoS₂/TiO₂ < 1.5NMoS₂/TiO₂ < 0.5NMoS₂/TiO₂. In the same order HER activity is increasing. Subsequently, it seems probable that MoS₂ dispersed on (001) facets present an enhanced HER activity compared to MoS₂ on (100) facets.

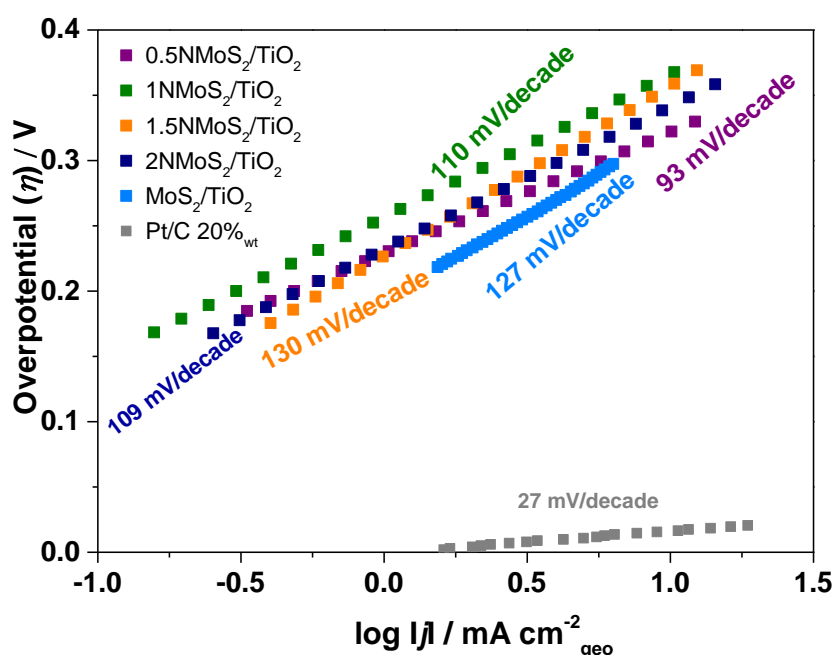


Figure 27: Determined Tafel slopes of $x\text{-NMoS}_2/\text{TiO}_2$ in comparison to the one of Pt/C.

In regards to the calculated Tafel slopes (Figure 27), their values are still high and do not change significantly with increasing N/Mo ratio. Herein EDTA had no impact on Tafel slopes. Volmer step is still the rate determining step and protons adsorption on M-edge sites are limited. The only notable decrease in Tafel slope value was when N/Mo = 0.5. Compared to MoS₂/TiO₂, Tafel slope has decreased from 127 mV/dec to 93 mV/dec which still remains very high. The only possible explanation for this decrease based on IR/CO results is the higher electron density of Mo compared to the other catalysts. Herein, the affinity towards protons might have been improved when N/Mo = 0.5.

2.8. Discussion

As expected TiO₂ - anatase is not an adequate carrier for HER electrocatalysis. S-doping of TiO₂ via sulfidation did not allow to boost the electrical conductivity sufficiently in order to improve charge transfer and subsequently decrease overpotentials. Its weak charge transfer translated by an energy gap of 2.9 eV after S-doping via sulfidation is still too high compared to graphene having a gap close to 0 eV and carbon (< 2 eV).³⁷ Hence, the generated HER activity is very low which is translated by high overpotentials at small current densities.

Based on the obtained results, Volmer step is the rate determining step after the addition or not of H₃PO₄ and EDTA during synthesis. Whether catalysts were prepared with phosphoric acid or EDTA, no obvious impact was observed on overpotentials and Tafel slopes despite their impact on MoS₂ surface characteristics. Indeed, H₃PO₄ and EDTA allowed to increase M-edge site concentrations (and Mo dispersion) when P/Mo and N/Mo ratios equaled 0.5. TEM analysis confirmed the presence of small MoS₂ slabs with an average size of 2.0 ± 0.1 nm for 0.5NMoS₂/TiO₂. Furthermore, EDTA allowed to reduce the number of stacked MoS₂ slabs to 1.4 ± 0.1. The same impact of EDTA addition on MoS₂/TiO₂ is probably also observable when H₃PO₄ is used.

Moreover, at the molar ratios of 0.5 a downward shift of 3 cm⁻¹ for ν(CO/M-edge) was observed reflecting an increase in molybdenum's electron density. Hence its affinity towards protons should have been improved. Yet, it is not reflected by the obtained Tafel slope. They

remain high in between 127 mV/dec and 100 mV/dec indicating that the rate determine step is the Volmer step.

As a result, it is questionable whether these observations are caused by the strong long ranged Van der Waals forces between MoS₂ and TiO₂ inducing weak hydrogen binding. Such weak H-binding can limit proton adsorption and consequently the production of H₂.

It should also be emphasized that EDTA addition is favoring the dispersion of MoS₂ on (001) facets when the proportion between additive and Mo is 0.5. This selectivity seems to have also an impact on HER activity.

Contrariwise to HER, these described effects on MoS₂ induced by the addition of EDTA and H₃PO₄ have a significant impact on HDS activity. While P-doping is inhibiting HDS activity, EDTA addition allows to enhance HDS activity.

Based on the obtained HER and HDS activities, MoO_xS_y seems to be not active. Indeed, the addition of H₃PO₄ or EDTA during synthesis is influencing strongly the quantity of formed mixed molybdenum sulfuroxide species visible by the absorption band $\nu(\text{CO}/\text{MoO}_x\text{S}_y)$ at 2135 cm⁻¹ which explains the low probed quantity of M-edge sites at higher P/Mo and N/Mo ratio. Indeed, with the help of Raman we have observed that with increasing P/Mo molar ratio the impregnation solution becomes more acidic and consequently has an effect on the equilibrium between heptamolybdate (i.e. Mo₇O₂₄⁴⁻) and heteropolymolybdate. The equilibrium is shifted towards the formation of phosphomolybdate-12 when pH < 3 which is the case for P/Mo inferior to 1.²⁰ Below pH of 1 the polymerization of phosphorus is favored. Species like PMo₁₂ are easier to be sulfided than P₂Mo₅. It can be assumed that at 1 < pH < 2 a maximum of PMo₁₂ was formed allowing to achieve a high coverage of M-edge sites on TiO₂. At P/Mo > 1 agglomeration of oxysulfide is favored leading to poor MoS₂ dispersion. The formation of these species explains also the drop in S/Mo ratio which is close to 1.

In contrary to H₃PO₄, EDTA stabilizes S/Mo ratio to 2 and favors a more homogeneous sulfidation of Mo-precursor into MoS₂ leading to a lower amount of MoO_xS_y. However at higher EDTA concentrations, a drop in probed M-edge sites concentration was noticed. This might be related to the type of formed EDTA-Mo complex and the solubility of EDTA at high concentration in deionized water favoring an inhomogeneous dispersion of Mo on TiO₂.

In this part, we also tried to observe a connection between HDS and HER activity. In general, the HDS activity (or HER activity) are increasing with the amount of active sites. In our case, it is the concentration of M-edge sites on which those active sites are located. Herein, HDS catalytic test is an interesting strategy to evaluate the accessibility and activity of MoS₂ edges. Yet, the trend in activity is not similar. Hence the correlation between HDS and HER activity is not obvious since other factors seems to affect reactivity such as dopant, site quality and MoS₂/support interaction.

Indeed, in the work of Palencia-Ruiz et al. the beneficial impact of alkaline ions on HER activity was demonstrated whereas in HDS they are poisonous.³⁸ For the latter, the same can be deduced for phosphorous although its addition has increased the concentration of probed M-edge sites when P/Mo is inferior to 1. HDS activity has dropped drastically for P-doped MoS₂/TiO₂ whereas P-doping did not inhibit HER activity (even though the difference between MoS₂/TiO₂ and 0.75PMoS₂/TiO₂ is around 30 mV). This slight decrease in overpotentials is linked to the increased amount in probed M-edge sites. However P-doping had no impact on Tafel slopes which contradicts the observation made by Guruprasad et al.⁸. It might be possible that the amount of phosphorous on prepared catalysts (i.e. up to 2.8%_{wt}) which is half of the amount introduced in Guruprasad's work, is not sufficient in order to affect Tafel slopes.

When EDTA is used as a chelating agent, the correlation between HDS and HER is also not verified (i.e. $r(\text{HDS})$ increases than $|\eta_{10}|$ is decreasing) (Figure 28).

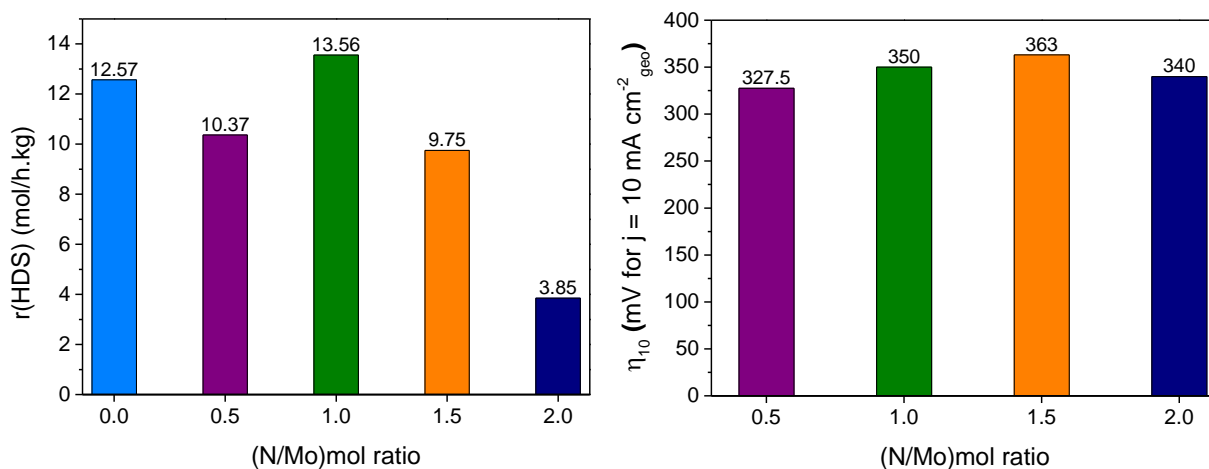


Figure 28: Comparison between obtained $r(\text{HDS})$ of $x\text{NMoS}_2/\text{TiO}_2$ ($x=0; 0.5; 1; 1.5; 2$) and their HER activity at -10 mV/cm^2 . HER activity of $\text{MoS}_2/\text{TiO}_2$ could not be measured at -10 mV/cm^2 and subsequently not included in the comparison.

In theory, $1\text{NMoS}_2/\text{TiO}_2$ should be the most active in HER while $2\text{NMoS}_2/\text{TiO}_2$ the least active one. But we do not observe it. Based on the obtained characterization results this trend cannot be explained. It can only be assumed that other parameters such as the amount of S-vacancies and MoS_2 dispersion on specific TiO_2 facets might cause this trend in HER activity. Besides the electron density of Mo for $0.5\text{NMoS}_2/\text{TiO}_2$ is the lowest as the downward shifted band of $\nu(\text{CO}/\text{M-edge})$ to 2115 cm^{-1} indicates. This increase in electron density can increase the affinity towards protons and facilitate its adsorption. This assumption is reinforced by the slight decrease in Tafel slope to 93 mV/dec .

2.9. Conclusion

The addition of EDTA and H_3PO_4 during synthesis is impacting Mo-dispersion, creation of sulfur vacancies on M-edges and the selective coverage of specific TiO_2 facets (Figure 29). However those effects on MoS_2 are only causing a significant change in activity for HDS and not for HER. Hence, it is questionable if the impact of EDTA and H_3PO_4 are truly reflected or are they masked by the low charge transfer of TiO_2 inhibiting the Volmer step. The chosen strategy to improve charge transfer via S-doping was unsuccessful. The observed decrease in energy gap

due to S-doping did not improve the conductivity of the support resulting in high overpotentials. Moreover the strong interaction between MoS₂ and TiO₂ might contribute to the determined high Tafel slopes. Such a strong interaction can cause weak H-bindings as DFT calculations of Pederson et al. demonstrate and prevent the adsorption of protons.³⁹ Herein, it might be possible to achieve lower overpotentials and Tafel slopes by decreasing the interaction MoS₂/support. Subsequently it is a strategy worth to be approached.

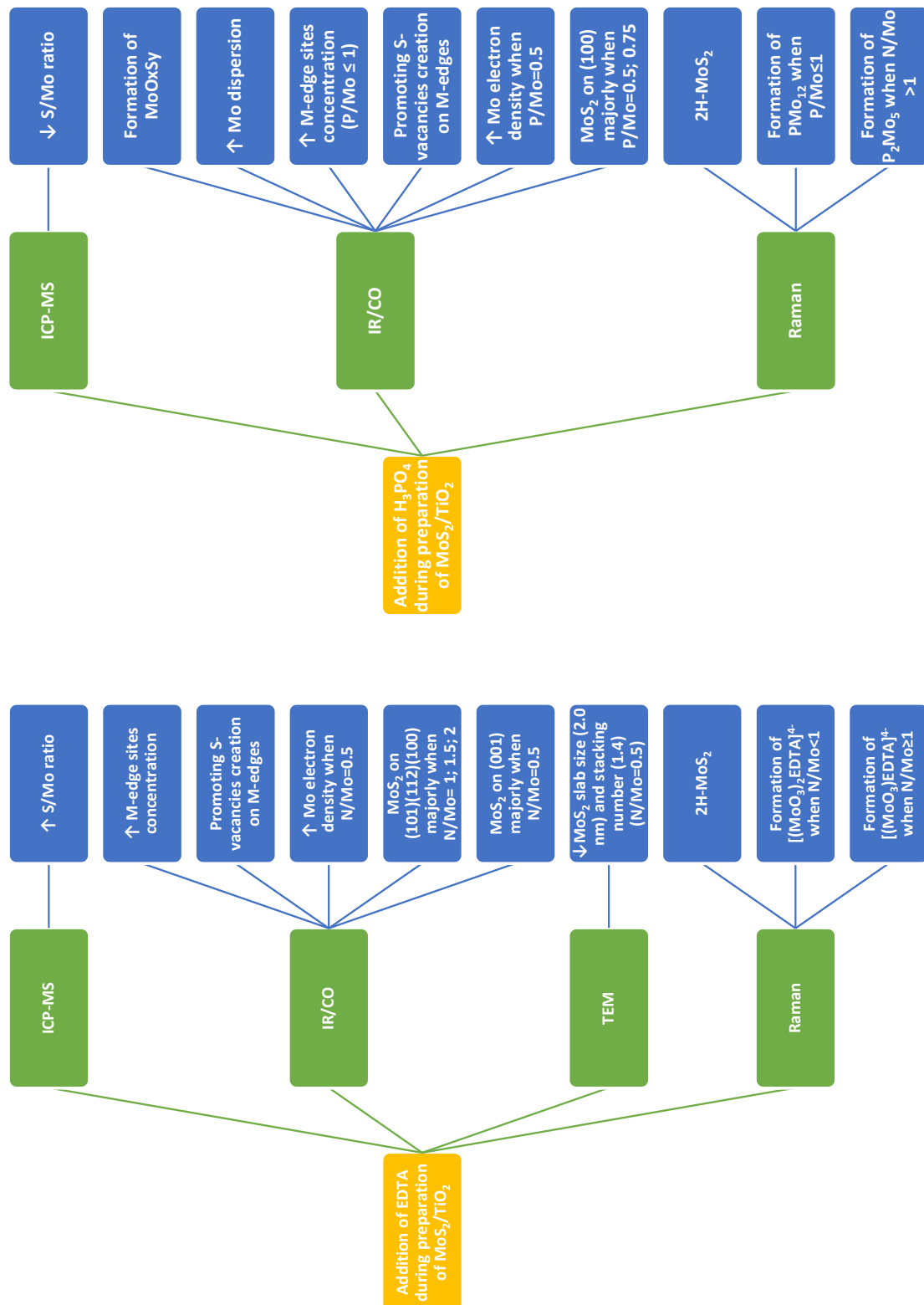


Figure 29: Overview of the impact of EDTA and H₃PO₄ on MoS₂/TiO₂. Main characterization results via IR/CO; Raman; ICP-MS and TEM are summarized for each introduced additive during incipient impregnation.

3. Studying the effect of EDTA and H₃PO₄ addition during preparation of MoS₂/C on HER activity

3.1. Introduction

In the previous part we have seen that H₃PO₄ and EDTA used at adequate molar ratios allowed to increase the concentration of M-edge sites on TiO₂. The increase of probed M-edge sites concentration was related to smaller MoS₂ slabs in the presence of EDTA (N/Mo = 0.5). We assumed H₃PO₄ has a similar effect. Moreover, catalysts which were prepared with EDTA, presented improved HDS rates compared to MoS₂/TiO₂. Yet, adding EDTA or H₃PO₄ in the impregnation solution did not induce a significant enhancement on HER activity. It was presumed that the low electrical conductivity of TiO₂ may mask the possible effect of EDTA and H₃PO₄ on HER activity. Consequently, in order to verify the effect of EDTA and H₃PO₄ addition synthesis on HER activity, a carrier endowed with higher electrical conductivity will be used which is black carbon.⁴⁰

Herein the effect of EDTA and H₃PO₄ addition in the impregnation solution during the synthesis of MoS₂ supported on black carbon (MoS₂/C) was investigated. It was also questioned whether these additives have a beneficial effect in terms of M-edge site concentration, HDS and HER activity.

However due to transparency issues of MoS₂/C towards IR, it is difficult to characterize edge sites of MoS₂/C prepared with H₃PO₄ or EDTA. Subsequently acquiring more knowledge about the concentration of edge sites, slab morphology, as well as the formation of S-vacancies on edges and molybdenum's electron density are via IR/CO to this point impossible. Consequently, it is difficult to relate surface characteristics with HER activity.

During the last decade, a discussion about the correlation between HDS and HER activity has risen. It consists in saying that if a certain catalyst presents high HDS activity rates, it will be also very active for HER. The main explanation on which this hypothesis is relying upon is that for both reactions the catalytic active sites are located on the edges of MoS₂ and play a crucial role in the adsorption of hydrogen.^{41,42} Hence it might be possible to predict the trend of HER activity of a series of catalysts based on their HDS activity. Since MoS₂/C cannot be analyzed

with IR/CO to study the surface characteristics of edge sites, it might be interesting to compare HDS and HER activity rates of MoS₂/C prepared with EDTA and H₃PO₄.

Hence in this part of this work, MoS₂/C prepared with different amount of EDTA and H₃PO₄ was analyzed using the following described method:

First, in order to investigate the effect of the addition of EDTA and H₃PO₄ on MoS₂, ICP-MS as well as SEM-EDX analysis were performed to determine the evolution of S/Mo ratio depending the introduced amount of additives in impregnation solution. This parameter will help us to reveal whether or not Mo was converted completely into MoS₂.

Secondly, with the help of Raman the impact of EDTA and H₃PO₄ on MoS₂ crystallinity, phase nature and the possible creation of other molybdenum species will be investigated.

Thirdly, HDS activity test of thiophen were conducted to observe the effect of EDTA and H₃PO₄ introduction during synthesis on activity. Generally, HDS activity is increasing with higher edge sites concentration. Subsequently a qualitative approximation of edge site concentration can be determined. Moreover, these catalytic tests might give us an insight about the presence of M- and S-edges. Indeed S-edges are favoring the direct desulfurization of thiophen into alkenes via C-S cleavage whereas M-edges are favoring the hydrogenation of thiophen into THT (tetrahydrothiophene).³² By comparing the proportions between THT, butene and butane, it might be possible to elucidate which edge was preferentially formed on MoS₂/C prepared with EDTA and H₃PO₄. At last HDS and HER activities were compared to verify if it is possible to forecast a trend in HER activity based on HDS activity rates.

3.2. Synthesis

- **Mo/C (5Mo/nm²):**

Incipient impregnation was used to synthesize supported Mo on carbon (noted: Mo/C). In short, a concentrated solution of $(\text{NH}_4)_6\text{Mo}_7\text{O}_{24} \times 4\text{H}_2\text{O}$ was prepared so that 5 Mo/nm² will be loaded on vulcan carbon (CABOT; $S_{\text{BET}}=223 \text{ m}^2/\text{g}$, $V_p=0.41 \text{ cm}^3/\text{g}$). This solution was drop wise added to carbon under mixing with a spatula until a sticky, homogenous mass was obtained. After 2h maturation, Mo/C was first dried under air at 60°C for 2h, then at 120°C for 16h (1°C/min).

- **Preparation of Mo supported on carbon with EDTA (x-NMo/C) (5Mo/nm²):**

The same procedure as for Mo/C was applied to prepare x-NMo/C only that EDTA was added to the impregnation solution. Herein, the amount of EDTA was varied so that the molar ratio (x) between nitrogen and molybdenum will equal: N/Mo = 0.5, 1; 1.5; 2. In order to obtain homogenous impregnation solution, EDTA was solubilized first in deionized water under sonication than Mo was added and further mixt for 10 minutes. Prepared catalysts were noted based on the molar ratio (x).

- **Preparation of Mo supported on carbon with H₃PO₄ (x-PMo/C) (5Mo/nm²):**

The same procedure as for x-NMo/C was applied. Instead of using EDTA, H₃PO₄ was used as an additive. H₃PO₄ was added to the impregnation solution after solubilizing $(\text{NH}_4)_6\text{Mo}_7\text{O}_{24}$ in deionized water. The molar ratio (x) of P/Mo was imposed to be 1 or 2.

- **Synthesis of sulfided phase MoS₂ supported on C (MoS₂/C; x-NMoS₂/C; x-PMoS₂/C):**

Dried synthesized samples of Mo/C; x-NMo/C; x-PMo/C were sulfided under 10% H₂S/H₂ flow (30 ml/min) for 2h at 350°C with a heating rate of 3°C/min.

3.3. Characterization results of EDTA and H₃PO₄ prepared MoS₂/C

3.3.1. ICP-MS and EDX analysis

The amount of Mo, S and P were quantified by ICP-MS on sulfided catalysts while the presence of nitrogen was verified with EDX. For the latter, no nitrogen was quantified by EDX meaning that EDTA was completely decomposed during sulfidation. The results are summarized in Table 14. The carrier carbon black was sulfided under 10% H₂S/H₂ flow at 350°C for 2h in order to determine its sulfidation degree. ICP-MS analysis allowed to determine that 4.84%_{wt} of sulfur was integrated into carbon black.

Table 14: ICP-MS results of MoS₂/C prepared with and without EDTA or H₃PO₄. The ratio between sulfur and molybdenum (S/Mo ratio) were determined by subtracting the amount of sulfur in carbon black. (corresponds to the total amount of sulfur in analyzed catalyst)*

| Sample | %_{wt} S* | %_{wt} Mo | %_{wt} P | Atomic ratio S/Mo |
|------------------------------|--------------------------|--------------------------|-------------------------|------------------------------|
| <i>C sulfided</i> | 4.84 | - | - | - |
| <i>MoS₂/C</i> | 9.45 | 11.38 | - | 1.35 |
| <i>0.5NMoS₂/C</i> | 13.15 | 11.26 | - | 2.33 |
| <i>1NMoS₂/C</i> | 12.61 | 11.73 | - | 2.11 |
| <i>1.5NMoS₂/C</i> | 14.56 | 11.17 | - | 2.73 |
| <i>2NMoS₂/C</i> | 14.54 | 10.41 | - | 2.91 |
| <i>1PMoS₂/C</i> | 7.97 | 11.23 | 3.46 | 1.40 |
| <i>2PMoS₂/C</i> | 4.12 | 11.56 | 7.97 | 1.10 |

Based on the obtained results EDTA is not a source for nitrogen due to its complete decomposition after sulfidation. Moreover, the addition of EDTA has increased S/Mo ratio. Only by increasing the concentration of EDTA in the preparation solution led to an improvement of molybdenum's sulfidation degree. At a N/Mo above 1, S/Mo ratios are clearly above 2 indicating that the sulfidation degree was overly sufficient to convert Mo in MoS₂ and apparently also to other molybdenum species.

In contrary to EDTA, H₃PO₄ is a good source to introduce phosphorous on the catalysts. The expected amount of phosphorous were quantified by ICP-MS. Yet, with increasing P-concentration, S/Mo ratio is decreasing to 1.10. This value indicates that the sulfidation degree was insufficient to transform totally Mo into MoS₂. The obtained S/Mo ratio for catalysts prepared with phosphoric acid are similar to the ones obtained for P-doped MoS₂ supported on TiO₂. We have detected on TiO₂ a high amount of MoO_xS_y which could be also the case for x-PMoS₂/C.

3.3.2. Raman analysis of x-NMoS₂/C

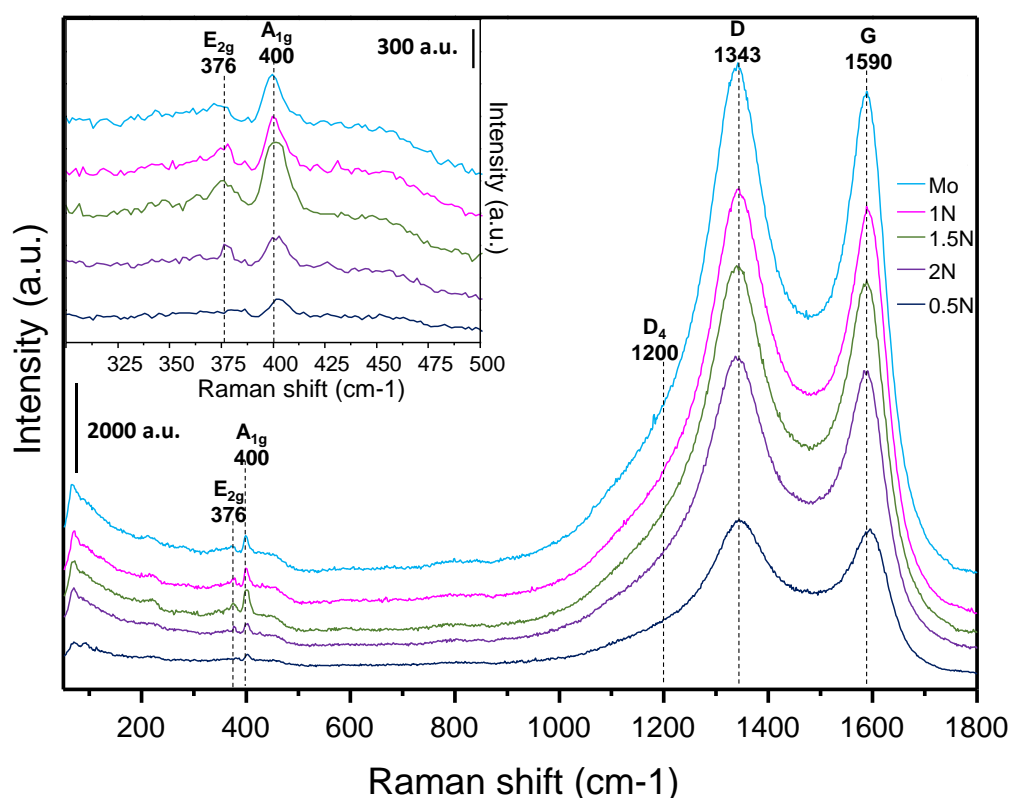


Figure 30: Raman spectra of x-NMoS₂/C (x = 0; 0.5; 1; 1.5; 2). In the capture, focus on E_{2g} and A_{1g} vibration region on x-NMoS₂/C.

Two main regions can be discerned on x-NMoS₂/C Raman spectra (Figure 30). The first one around 300-450 cm⁻¹ corresponding to ν(Mo-S) of MoS₂ and a second one around 1200-1650 cm⁻¹ corresponding to the structural vibration of carbon support.^{22,43}

On the Raman spectra of x-NMoS₂/C, in- and out-of-plane vibration, E_{2g} and A_{1g}, are detected at 376 and 400 cm⁻¹. Compared to reported structural vibrations, A_{1g} is downshifted by 7 cm⁻¹

^{1,22} This big difference indicates that Mo-S are under strong tensile strain. It is also noticed that catalysts prepared with or without EDTA present the same E_{2g} and A_{1g} band positions. Hence, black carbon might have induced the observed downward shift of A_{1g}.

At 1200, 1343, 1590 cm⁻¹ vibration modes of D₄, D and G are found.⁴³⁻⁴⁵ D₄ corresponds to the vibrations caused by hydrocarbon or aliphatic moieties connected to graphitic basic structural units.⁴⁴ The vibration modes D and G were ascribed to the vibrations along the A_{1g} and E_{2g} symmetry respectively as schematized in Figure 31.

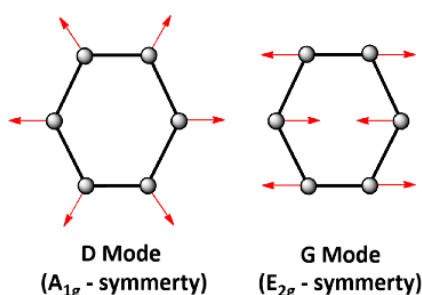


Figure 31: Representation of D and G vibration modes of carbon.⁴⁴

Although EDTA had no impact on MoS₂ structural vibrations, it seems to affect the G mode vibration. An upward shift up to 1599 cm⁻¹ is detected for 0.5NMoS₂/C. This shift reflects a lattice compression of the carbon cycle specifically for 0.5NMoS₂/C. By calculating the intensity ratio between D and G a quotient of 0.95 remaining constant for all x-NMoS₂/C was determined. It indicates a structural disorder in carbon sheets.

3.3.3. Raman analysis of x-PMoS₂/C

In Figure 32 Raman spectra of x-PMoS₂/C are presented. Surprisingly no vibration bands of MoS₂ around 376 and 400 cm⁻¹ were detected as for MoS₂/C. Only a small contribution of a broad band at 450 cm⁻¹ is discerned which is partially hidden by the background noise. The evident absence of MoS₂ might be linked to the formation of amorphous PMoO_xS_y species based on the obtained ICP-MS results validating the presence of Mo, S, P and a S/Mo ratio around 1.10.

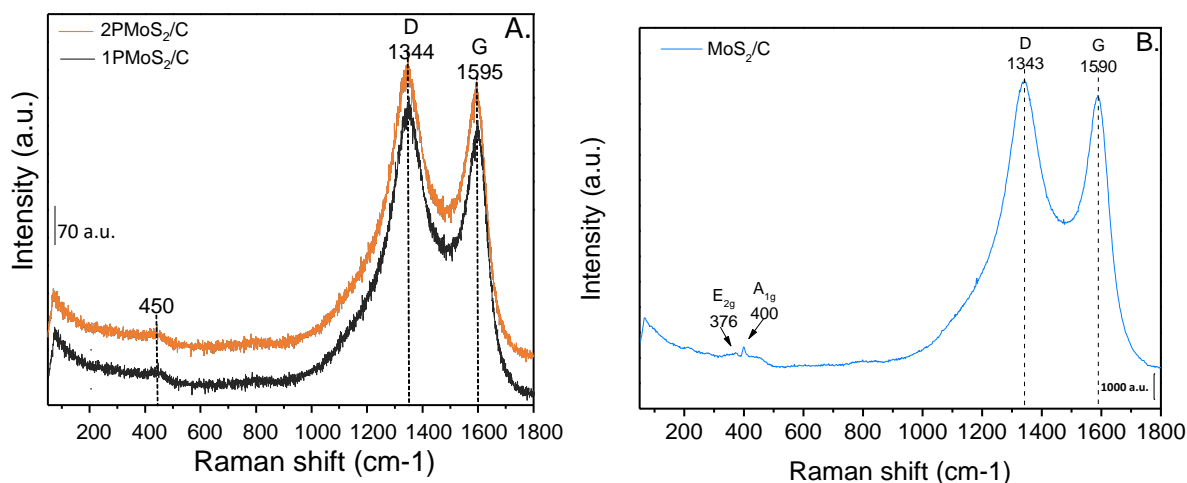


Figure 32: Raman spectra of x -PMoS₂/C ($x=P/Mo=1; 2$) (A.) and of MoS₂/C (B.).

3.3.4. HDS activity test results

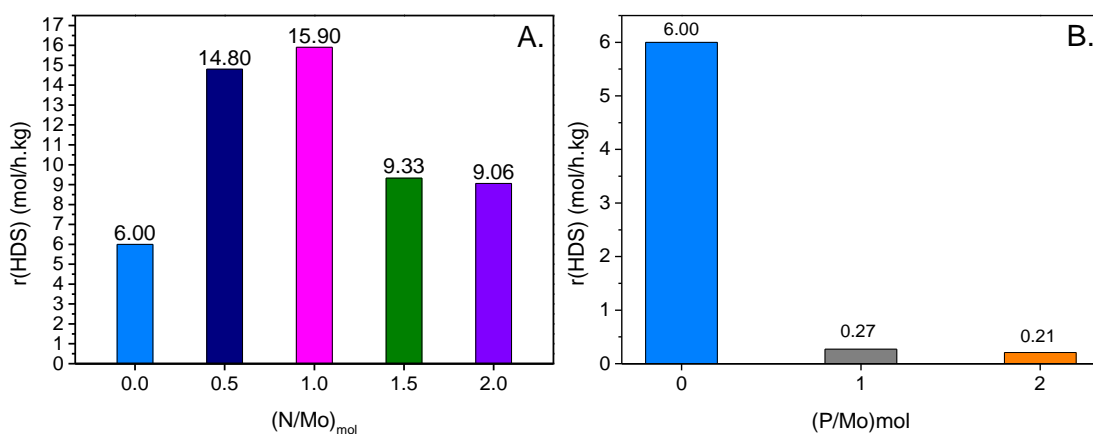


Figure 33: HDS rates of x -NMoS₂/C (A.) and x -PMoS₂/C (B.).

In Figure 33, HDS activity rates of MoS₂/C prepared with EDTA and H₃PO₄ are presented. By conducting those catalytic tests with thiophen the effect of EDTA and H₃PO₄ were investigated on HDS activity. In Figure 33A, depending on introduced EDTA concentration during catalyst's preparation, a change in HDS activity is observed. We note at a molar ratio N/Mo of 0.5 and 1, HDS activities are considerably higher than for MoS₂/C. Herein HDS activity rates for x -NMoS₂/C are increasing in the following order: MoS₂/C < 2MoS₂/C ~ 1.5NMoS₂/C < 0.5NMoS₂/C ~ 1NMoS₂/C. Contrarywise the addition of H₃PO₄ during synthesis has rendered catalysts inactive for HDS (Figure 33B). Their activity rates are close to zero.

3.3.5. Discussion and conclusion about the effect of EDTA and H₃PO₄ addition on MoS₂ and HDS activity test results

Based on Raman spectra and ICP-MS results, EDTA and H₃PO₄ do not present the same effects on MoS₂ formation. While EDTA allowed the formation of MoS₂, phosphoric acid is preventing the formation of MoS₂ as confirmed by the absence of characteristic Raman vibration bands of MoS₂ at 376 and 400 cm⁻¹. Thus explaining the absence of activity during HDS activity tests for 1PMoS₂/C and 2PMoS₂/C.

In regards to HDS activity rates of x-NMoS₂/C, different activity rates were obtained depending N/Mo ratio. Consequently the addition of EDTA during preparation had an impact on MoS₂. Yet, it is not evident how EDTA has precisely affected MoS₂. But, based on the evolution of HDS activity depending N/Mo ratio, it can be assumed that EDTA had an influence on the amount of active sites. Indeed, usually HDS activity is increasing with the number of active sites. Since HDS activity rates are increasing in the following order: MoS₂/C < 2MoS₂/C ~ 1.5NMoS₂/C < 0.5NMoS₂/C ~ 1NMoS₂/C, it can be assumed that the concentration of active sites located on the edges is increasing in the same described order. Subsequently based on this assumption when EDTA is introduced into the impregnation solution with a molar ratio N/Mo = 0.5; 1 edge sites concentration can be increased. Besides since determined S/Mo ratios of prepared catalysts are above 2, it might be highly possible that other molybdenum sulfide species were formed which could also act as additional active sites for HER. Nonetheless, 0.5NMoS₂/C is almost as active as 1NMoS₂/C which are presenting both them smaller S/Mo ratios compared to 1.5 and 2NMoS₂/C. As a result, it is questionable whether the increase in HER activity is related to the formation of specific edges (i.e. S- or M-edges) or the formation of other molybdenum sulfide species.

We have seen that due to strong interaction between TiO₂ and MoS₂, only M-edges were formed on MoS₂/TiO₂. Even in the presence of EDTA, S-edges were barely not formed due to the strong existing interaction between MoS₂ and TiO₂. However, the interaction between carbon and MoS₂ was speculated to be weaker allowing the formation of S-edges.³⁵

Depending on the presence of S- and M-edges one of the two mechanism pathways in HDS (of thiophene) can be favored. Either the direct desulfurization (DDS) of thiophene into butene

favoured on S-edges or the hydrogenation (HYD) of thiophene into tetrahydrothiophene (THT) favored by M-edges (Figure 34).^{46,47}

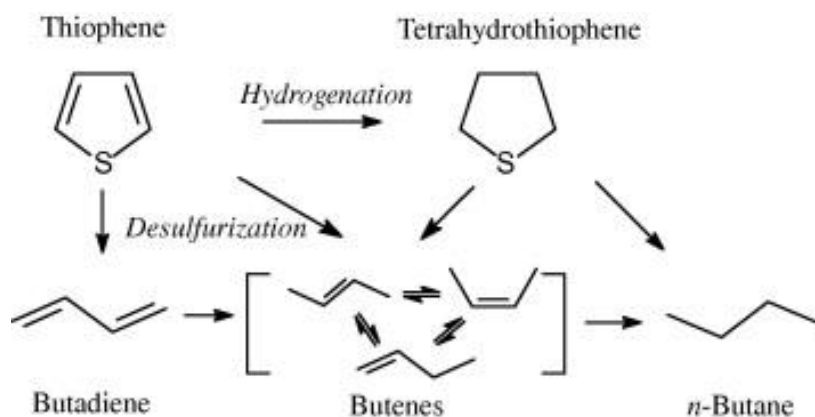


Figure 34: Mechanism of HDS test on thiophene.⁴⁸

However, HDS of thiophene is not an adequate test molecule to evaluate the selectivity of the reaction because the two paths of HDS are not strictly parallel. An approximation of the chosen selectivity towards HYD or DDS can be decided upon the formation of THT. This intermediate can only be formed via the HYD route. However, one drawback of this method is the quick transformation of this intermediate into butene and butane. As a consequence, THT is not always detected. Hence calculating and comparing the ratio between butane and butene might allow to investigate HYD selectivity for x-NMoS₂/C.

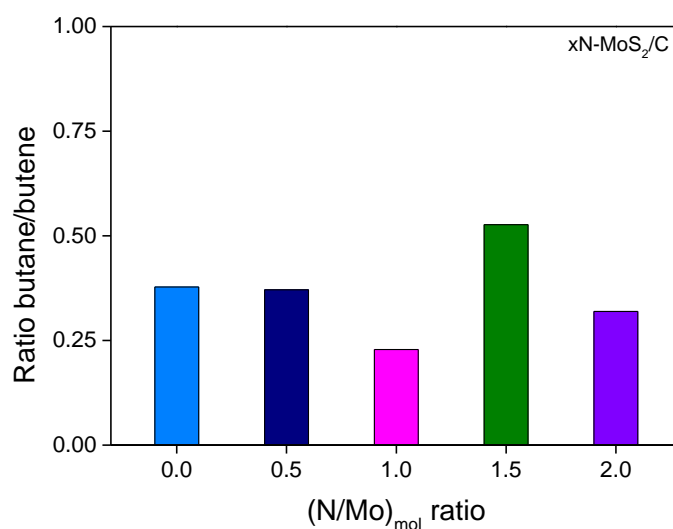


Figure 35: Comparison between butane/butene ratios in HDS of thiophen for x-NMoS₂/C.

In Figure 35 the obtained butane/butene ratios are summarized for x-NMoS₂ supported on carbon and TiO₂. For x-NMoS₂/C similar butane/butene ratios are observed for N/Mo = 0; 0.5;

2 whereas at N/Mo = 1; 1.5 ratios are differing strongly. None of the studied samples allowed to detect THT.

In the case of 1NMoS₂/C the ratio is the lowest reflecting a higher formation of butene. We remind that it was the most active catalyst. In the other case, 1.5NMoS₂/C presents the highest ratio indicating a high formation of butene. Subsequently it seems plausible that DDS was favored due to the possible presence of S-edges. For 1.5NMoS₂/C the contrary is observed. The determined butane/butene ratio is the highest leading to the conclusion that HYD was favored. Subsequently it seems very likely that M-edges are present in majority on 1.5MoS₂/C.

To conclude about this part, the addition of phosphoric acid has induced the formation of an amorphous phase and prevented the formation of MoS₂. In contrary EDTA did not prevent the formation of MoS₂. Based on determined butane/butene ratio for x-NMoS₂/C, the presence of S-edges can be assumed on 1NMoS₂/C which presents the highest HDS activity. Subsequently, the highest HER activity can be expected for this catalyst.

3.3.6. HER activity test

HER activity tests were performed on x-NMoS₂/C. Since MoS₂ was not formed on x-PMoS₂/C presenting probably instead an amorphous MoS_x phase (and should be noted accurately x-PMoS_x/C), it was decided to conduct only a HER test on 2PMoS_x/C to verify if the present amorphous phase is active. The obtained polarization curves and calculated Tafel slopes are presented in Figure 36.

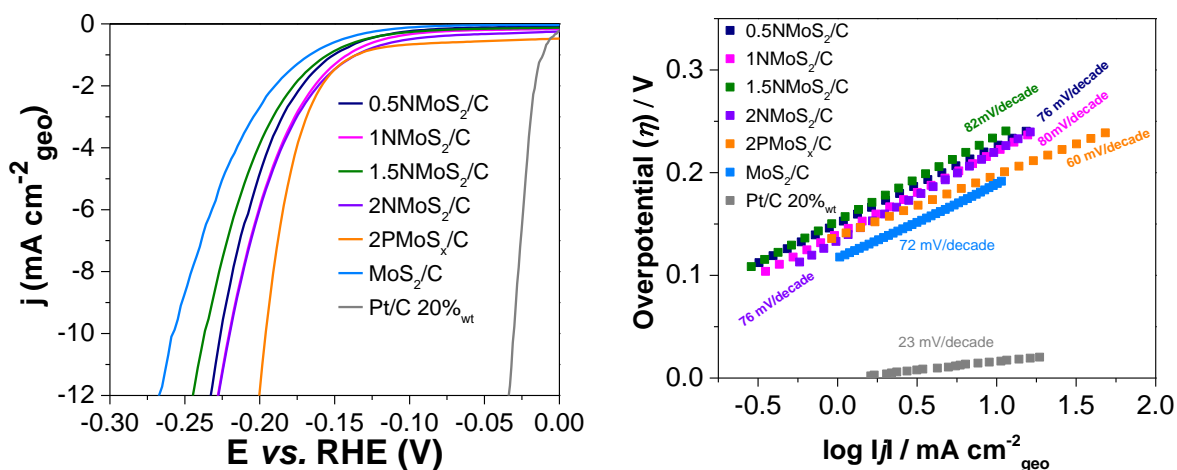


Figure 36: Polarization curves of $x\text{-NMoS}_2/\text{C}$ and $2\text{PMoS}_x/\text{C}$ in $0.5\text{M H}_2\text{SO}_4$ and their respective Tafel slope.

At -10 mA/cm^2 overpotentials (η_{10}) of $x\text{-NMoS}_2/\text{C}$ do not differ significantly. They variate minimally around -0.22 mV in the following increasing order: $\text{MoS}_2/\text{C} < 1.5\text{NMoS}_2/\text{C} < 0.5\text{NMoS}_2 < 2\text{NMoS}_2/\text{C} = 1\text{NMoS}_2/\text{C}$. Herein the addition of EDTA in various concentrations during preparation did not impact HER activity considerably. Nevertheless, its addition allowed to decrease overpotentials compared to MoS_2/C . The addition of EDTA did not affect either kinetics. Calculated Tafel slopes of $x\text{-NMoS}_2/\text{C}$ and MoS_2/C do not differ. They remain around 80 mV/dec indicating that the rate determining step seems to be the Heyrovsky step. Consequently, the reaction between a free proton and adsorbed one to form H_2 is slow. Besides the mechanism of HER is tending towards a Volmer-Heyrovsky pathway.

Surprisingly, $2\text{PMoS}_x/\text{C}$ is more active than $x\text{-NMoS}_2/\text{C}$ and presents the lowest Tafel slope. With 60 mV/dec a significant decrease compared to $x\text{-NMoS}_2/\text{C}$ is observed. The significant increase in HER activity for $2\text{PMoS}_x/\text{C}$ might be related to the formed amorphous phase which might be P-doped. Indeed, amorphous derived MoS_x species were demonstrated to be more active than MoS_2 in the work of Benck and Jaramillo et al. with an average difference of 0.1 V at -10 mA/cm^2 (Table 15).^{5,6} For instance unsupported amorphous MoS_x presents an overpotential of -0.2 V at -10 mA/cm^2 which is 0.1 V less than reported overpotentials of unsupported bulk MoS_2 (i.e. $\eta_{10} = -0.3\text{ V}$)⁴⁹.

Table 15: Comparison of reported overpotentials at - 10 mA/cm² for different MoS₂ derived HER electrocatalysts supported on carbon based carriers.⁶

| | Reference | Potential for 10 mA/cm ² _{geo} [V] vs. RHE |
|--|-----------|---|
| MoO ₃ -MoS ₂ nanowires | [54] | -0.254 |
| Electrodeposited amorp. MoS ₃ | [69] | -0.242 |
| 1T - MoS ₂ | [71] | -0.207 |
| Double gyroid MoS ₂ | [58] | -0.206 |
| Wet-chemical amorp. MoS _x | [50] | -0.200 |
| MoS _x GP | [62] | -0.194 |
| 100 μg/cm ² [Mo ₃ S ₁₃] ²⁻ GP | [96] | -0.174 |
| Li _x MoS ₂ GP | [75] | -0.168 |
| MoS ₂ RGO | [63] | -0.154 |
| MoS _x Piranha GP | [62] | -0.152 |
| [Mo ₃ S ₁₃] ²⁻ anodized GP | This work | -0.149 |
| Li-MoS ₂ CFP | [81] | -0.110 |
| MoS _x N-CNT | [126] | -0.110 |
| Polycrystalline Pt | This work | -0.021 |

The reason why amorphous MoS_x is endowed with higher activity than MoS₂ is for the moment unclear since its emerging as a potential HER electrocatalyst is relatively recent.⁶

3.3.7. Discussion and conclusion about the impact of EDTA and H₃PO₄ on HER activity

For HDS of thiophen we have observed that the addition of H₃PO₄ during synthesis is rendering the catalysts inactive due to the absence of MoS₂ whereas EDTA at adequate concentration (i.e N/Mo = 0.5; 1) allowed to enhance HDS activity. The contrary is observed for HER. The addition of H₃PO₄ during synthesis decreased overpotentials considerably and favored a decrease in Tafel slope (i.e. $\eta_{10} = -0.19$ V; 60mV/dec) while the addition of EDTA during catalyst's preparation did not instigate any significant change in overpotentials and Tafel slope. They remain approximatively around - 0.22 V at -10 mV/cm² with a Tafel slope around 80 mV/dec.

The fact that a lower Tafel slope of 60 mV/dec was obtained for 2PMoS_x/C might be related to the doping effect of phosphorous which facilitates proton adsorption by increasing molybdenum's affinity towards protons.

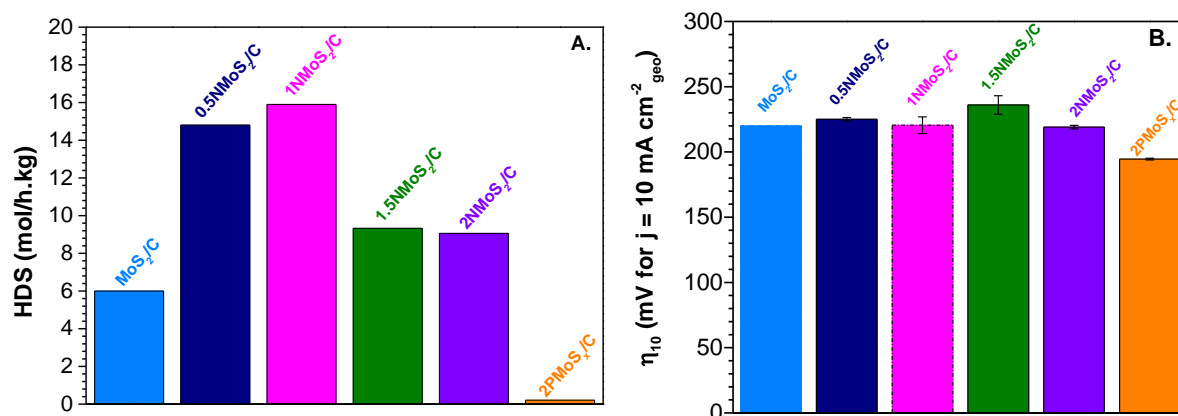


Figure 37: Comparison between HDS and HER activity of x -NMoS₂/C ($x=0; 0.5; 1; 1.5; 2$) and 2PMoS _{x} /C.

Despite the obvious impact of EDTA addition during synthesis on HDS activity which supposedly is linked to the amount of formed edges and their respective edge nature, the same impact on HER activity is not observed (Figure 37). With or without the use of EDTA during preparation overpotentials remain relatively constant. Instead of observing the highest HER activity for the most active HDS catalyst 1NMoS₂/C, we note 2NMoS₂/C to present the highest HER activity if the minimal difference between the measured overpotentials at -10 mV/cm² is neglected. Even though the difference in overpotentials is very small, it is evident that 1.5NMoS₂/C is less active than 1NMoS₂/C (Figure 37B). Due to the low butane/butene ratio for 1NMoS₂/C we assumed that this catalyst presents S-edges while 1.5NMoS₂/C having a much higher ratio presents M-edges. This speculated difference in edge nature might explain the slight difference in activity.

The correlation between HDS and HER is not verified. One would expect to have observed a similar trend between HDS and HER activity. This correlation might only be implemented for catalysts presenting MoS₂ on their surface. In our case it is highly probable that other molybdenum derived species were formed due to the variation of S/Mo ratio. Those species might be inactive for HDS but act as additional active sites for HER. This point is stressed out by 2PMoS _{x} /C being very active for HER but inactive for HDS.

To conclude, H₃PO₄ and EDTA addition have different impacts on the formation of MoS₂. Via incipient impregnation H₃PO₄ leads to an amorphous PMoO _{x} S _{y} phase and prevents the formation of 2H-MoS₂ whereas EDTA seems to increase the amount of edge sites. However similarly to MoS₂/TiO₂ prepared with EDTA, no significant impact on overpotentials and Tafel

slopes were observed whereas on HDS activity an obvious change in HDS rates was detected. Herein, the observed effects of EDTA addition during preparation on overpotentials and Tafel slopes for MoS₂ supported on TiO₂ were not masked by the low electrical conductivity of the carrier. In both cases the adsorption of protons is limiting HER.

4. Main conclusion

In this chapter we have tried to improve the conductivity of TiO₂ via S-doping in order to favor the decrease in overpotentials and enhance HER activity. This strategy resulted to be inefficient. The introduction of 2%_{wt} sulfur in TiO₂ did not allow to decrease TiO₂ energy gap sufficiently.

The other followed strategy which consisted in increasing MoS₂ conductivity and M-edge site exposition by adding EDTA and H₃PO₄ into the impregnation solution resulted to be ineffective in decreasing MoS₂ energy gaps whereas beneficial for the latter. Indeed, IR/CO results confirmed the increase in M-edge site exposition to be successful when the molar ratio between additives and molybdenum are adequate. In the case for EDTA, the molar ratio N/Mo needs to be 0.5. Only than a high Mo-dispersion is achieved. Monolayered triangular truncated small slabs of 2.0 nm length were formed as TEM analysis proves. A similar effect of H₃PO₄ can also be presumed since high Mo-dispersions were estimated. The highest probed M-edge site concentration was determined when P/Mo is in between 0.5 and 1. Moreover these additives allowed to promote the creation of S-vacancies on M-edges.

However these described effects on MoS₂ surface characteristics did not initiate a considerable decrease in overpotentials and Tafel slopes. Overpotentials still remain constant around – 0.3 V at –6 mA/cm² as well as Tafel slopes indicating Volmer step to be the rate determining step.

By changing the carrier TiO₂ with carbon black and carrying out the same synthesis procedure with EDTA, the same observations are made. Tafel slopes remain high whereas overpotentials are relatively constant. Subsequently the impact of EDTA addition is not masked by the low electrical conductivity of TiO₂. It seems more likely that the interaction force between MoS₂ and TiO₂ is limiting the adsorption of protons. Hence it might be interesting to find a method to decrease this interaction between MoS₂ and TiO₂ which might facilitate proton adsorption by strengthening H-bindings.

Reference

- (1) Li, P.; Yang, Z.; Shen, J.; Nie, H.; Cai, Q.; Li, L.; Ge, M.; Gu, C.; Chen, X.; Yang, K.; Zhang, L.; Chen, Y.; Huang, S. Subnanometer Molybdenum Sulfide on Carbon Nanotubes as a Highly Active and Stable Electrocatalyst for Hydrogen Evolution Reaction. *ACS Appl. Mater. Interfaces* **2016**, *8* (5), 3543–3550.
- (2) Dunlop, M. J.; Bissessur, R. Nanocomposites Based on Graphene Analogous Materials and Conducting Polymers: A Review. *J. Mater. Sci.* **2020**, *55* (16), 6721–6753.
- (3) Liu, M.; Jhulki, S.; Sun, Z.; Magasinski, A.; Hendrix, C. Atom-Economic Synthesis of Magnéli Phase Ti₄O₇ Microspheres for Improved Sulfur Cathodes for Li-S Batteries. 1–22.
- (4) Dominguez Garcia, E.; Chen, J.; Oliviero, E.; Oliviero, L.; Maugé, F. New Insight into the Support Effect on HDS Catalysts: Evidence for the Role of Mo-Support Interaction on the MoS₂ Slab Morphology. *Appl. Catal. B Environ.* **2020**, *260* (July 2019).
- (5) Casalongue, H. G. S.; Benck, J. D.; Tsai, C.; Karlsson, R. K. B.; Kaya, S.; Ng, M. L.; Pettersson, L. G. M.; Abild-Pedersen, F.; Nørskov, J. K.; Ogasawara, H.; Jaramillo, T. F.; Nilsson, A. Operando Characterization of an Amorphous Molybdenum Sulfide Nanoparticle Catalyst during the Hydrogen Evolution Reaction. *J. Phys. Chem. C* **2014**, *118* (50), 29252–29259.
- (6) Benck, J. D.; Hellstern, T. R.; Kibsgaard, J.; Chakthranont, P.; Jaramillo, T. F. Catalyzing the Hydrogen Evolution Reaction (HER) with Molybdenum Sulfide Nanomaterials. *ACS Catal.* **2014**, *4* (11), 3957–3971.
- (7) Ionescu, R.; Campbell, B.; Wu, R.; Aytan, E.; Patalano, A.; Ruiz, I.; Howell, S. W.; McDonald, A. E.; Beechem, T. E.; Mkhoyan, K. A.; Ozkan, M.; Ozkan, C. S. Chelant Enhanced Solution Processing for Wafer Scale Synthesis of Transition Metal Dichalcogenide Thin Films. *Sci. Rep.* **2017**, *7* (1), 1–9.
- (8) Guruprasad, K.; Maiyalagan, T.; Shanmugam, S. Phosphorus Doped MoS₂ Nanosheet Promoted with Nitrogen, Sulfur Dual Doped Reduced Graphene Oxide as an Effective Electrocatalyst for Hydrogen Evolution Reaction. *ACS Appl. Energy Mater.* **2019**, *2* (9), 6184–6194.
- (9) Dzwigaj, S.; Arrouvel, C.; Breysse, M.; Geantet, C.; Inoue, S.; Toulhoat, H.; Raybaud, P. DFT Makes the Morphologies of Anatase-TiO₂ Nanoparticles Visible to IR Spectroscopy. *J. Catal.* **2005**, *236* (2), 245–250.
- (10) Arrouvel, C.; Digne, M.; Breysse, M.; Toulhoat, H.; Raybaud, P. Effects of Morphology on Surface Hydroxyl Concentration: A DFT Comparison of Anatase-TiO₂ and γ -Alumina Catalytic Supports. *J. Catal.* **2004**, *222* (1), 152–166.
- (11) Dufour, F.; Pigeot-Remy, S.; Durupthy, O.; Cassaignon, S.; Ruaux, V.; Torelli, S.; Mariey, L.; Maugé, F.; Chanéac, C. Morphological Control of TiO₂ Anatase Nanoparticles: What Is the Good Surface Property to Obtain Efficient Photocatalysts? *Appl. Catal. B Environ.* **2015**, *174–175*, 350–360.

- (12) Mino, L.; Ferrari, A. M.; Lacivita, V.; Spoto, G.; Bordiga, S.; Zecchina, A. CO Adsorption on Anatase Nanocrystals: A Combined Experimental and Periodic DFT Study. *J. Phys. Chem. C* **2011**, *115* (15), 7694–7700.
- (13) Ziolek, M.; Kujawa, J.; Lavalley, J. C. Influence of Hydrogen Sulfide Adsorption on the Catalytic Properties of Metal Oxides. **1995**, *1169* (94).
- (14) Pan, X.; Yang, M. Q.; Fu, X.; Zhang, N.; Xu, Y. J. Defective TiO₂ with Oxygen Vacancies: Synthesis, Properties and Photocatalytic Applications. *Nanoscale* **2013**, *5* (9), 3601–3614.
- (15) Nam, S.; Kwan, T.; Boo, J. Physical Property and Photo-Catalytic Activity of Sulfur Doped TiO₂ Catalysts Responding to Visible Light. *Catal. Today* **2012**, *185* (1), 259–262.
- (16) F. Maugé, C. Binet, J. C. L. *IR Characterization of Metal Catalysts Using CO as Probe Molecule*.
- (17) Travert, A.; Dujardin, C.; Maugé, F.; Cristol, S.; Paul, J. F.; Payen, E.; Bougeard, D. Parallel between Infrared Characterisation and Ab Initio Calculations of CO Adsorption on Sulphided Mo Catalysts. *Catal. Today* **2001**, *70* (1–3), 255–269.
- (18) Chen, J.; Labruyere, V.; Maugé, F.; Quoineaud, A. A.; Hugon, A.; Oliviero, L. IR Spectroscopic Evidence for MoS₂ Morphology Change with Sulfidation Temperature on MoS₂/Al₂O₃ Catalyst. *J. Phys. Chem. C* **2014**, *118* (51), 30039–30044.
- (19) Daasch, L. W.; Smith, D. C. Infrared Spectra of Phosphorus Compounds. *Anal. Chem.* **1951**, *23* (6), 853–868.
- (20) Gumerova, N. I.; Rompel, A. Polyoxometalates in Solution: Speciation under Spotlight. *Chem. Soc. Rev.* **2020**, *49* (21), 7568–7601.
- (21) Van Veen, J. A. R.; Sudmeijer, O.; Emeis, C. A.; De Wit, H. On the Identification of Molybdophosphate Complexes in Aqueous Solution. *J. Chem. Soc. Dalt. Trans.* **1986**, No. 9, 1825–1831.
- (22) Strachan, J.; Masters, A. F.; Maschmeyer, T. Critical Review: Hydrothermal Synthesis of 1T-MoS₂- an Important Route to a Promising Material. *J. Mater. Chem. A* **2021**, *9* (15), 9451–9461.
- (23) Frank, O.; Zikalova, M.; Laskova, B.; Kürti, J.; Koltai, J.; Kavan, L. Raman Spectra of Titanium Dioxide (Anatase, Rutile) with Identified Oxygen Isotopes (16, 17, 18). *Phys. Chem. Chem. Phys.* **2012**, *14* (42), 14567–14572.
- (24) Tian, H.; Roberts, C. A.; Wachs, I. E. Molecular Structural Determination of Molybdena in Different Environments: Aqueous Solutions, Bulk Mixed Oxides, and Supported MoO₃ Catalysts. *J. Phys. Chem. C* **2010**, *114* (33), 14110–14120.
- (25) Murata, K.; Ikeda, S. Studies on Polynuclear Molybdates in the Aqueous Solution by Laser Raman Spectroscopy. *Spectrochim. Acta Part A Mol. Spectrosc.* **1983**, *39* (9), 787–794.
- (26) Krishnan, K.; Plane, R. A. Raman Spectra of Ethylenediaminetetraacetic Acid and Its Metal Complexes. *J. Am. Chem. Soc.* **1968**, *90* (12), 3195–3200.

- (27) Baran, E. J.; Wagner, C. C.; Torre, M. H. Synthesis and Characterization of EDTA Complexes Useful for Trace Elements Supplementation. *J. Braz. Chem. Soc.* **2002**, *13* (5), 576–582.
- (28) Kula, R. J. Solution Equilibria and Structures of Molybdenum(VI) Chelates (Ethylenedinitrilo)Tetraacetic Acid. *Anal. Chem.* **1966**, *38* (11), 1581–1584.
- (29) Nam, S. H.; Kim, T. K.; Boo, J. H. Physical Property and Photo-Catalytic Activity of Sulfur Doped TiO₂ Catalysts Responding to Visible Light. *Catal. Today* **2012**, *185* (1), 259–262.
- (30) Makuła, P.; Pacia, M.; Macyk, W. How To Correctly Determine the Band Gap Energy of Modified Semiconductor Photocatalysts Based on UV-Vis Spectra. *J. Phys. Chem. Lett.* **2018**, *9* (23), 6814–6817.
- (31) Lai, C. W.; Sreekantan, S. Incorporation of WO₃ Species into TiO₂ Nanotubes via Wet Impregnation and Their Water-Splitting Performance. *Electrochim. Acta* **2013**, *87*, 294–302.
- (32) Moses, P. G.; Hinnemann, B.; Topsøe, H.; Nørskov, J. K. The Hydrogenation and Direct Desulfurization Reaction Pathway in Thiophene Hydrodesulfurization over MoS₂ Catalysts at Realistic Conditions: A Density Functional Study. *J. Catal.* **2007**, *248* (2), 188–203.
- (33) Søndergaard-Pedersen, F.; Broge, N. L. N.; Yu, J.; Roelsgaard, M.; Iversen, B. B. Maximizing the Catalytically Active {001} Facets on Anatase Nanoparticles. *Chem. Mater.* **2020**, *32* (12), 5134–5141.
- (34) Ong, W.; Tan, L.; Chai, S.; Yong, S. Highly Reactive {001} Facets of TiO₂-Based Composites: Synthesis, Formation Mechanism and Characterization. *Nanoscale* **2014**, *6*, 1946–2008.
- (35) Tsai, C.; Abild-pedersen, F. Tuning the MoS₂ Edge-Site Activity for Hydrogen Evolution via Support Interactions. *Nano* **2014**, *14*, 1381–1387.
- (36) Arrouvel, C.; Breyse, M.; Toulhoat, H.; Raybaud, P. A Density Functional Theory Comparison of Anatase (TiO₂) - And. **2005**, *232*, 161–178. <https://doi.org/10.1016/j.jcat.2005.02.018>.
- (37) Lima, J. R. F. Controlling the Energy Gap of Graphene by Fermi Velocity Engineering. *Phys. Lett. Sect. A Gen. At. Solid State Phys.* **2015**, *379* (3), 179–182.
- (38) Palencia-Ruiz, S.; Uzio, D.; Legens, C.; Laurenti, D.; Afanasiev, P. Stability and Catalytic Properties of 1T-MoS₂ Obtained via Solvothermal Synthesis. *Appl. Catal. A Gen.* **2021**, *626* (July).
- (39) Tsai, C.; Chan, K.; Nørskov, J. K.; Abild-Pedersen, F. Theoretical Insights into the Hydrogen Evolution Activity of Layered Transition Metal Dichalcogenides. *Surf. Sci.* **2015**, *640*, 133–140. <https://doi.org/10.1016/j.susc.2015.01.019>.
- (40) Zhao, Q.; Zhang, K.; Zhu, S.; Xu, H.; Cao, D.; Zhao, L.; Zhang, R.; Yin, W. Review on the Electrical Resistance/Conductivity of Carbon Fiber Reinforced Polymer. *Appl. Sci.* **2019**, *9* (11).
- (41) Liu, S.; Jin, Q.; Xu, Y.; Fang, X.; Liu, N.; Zhang, J.; Liang, X.; Chen, B. The Synergistic Effect

- of Ni Promoter on Mo-S/CNT Catalyst towards Hydrodesulfurization and Hydrogen Evolution Reactions. *Fuel* **2018**, *232* (December 2017), 36–44.
- (42) Carlos G. Morales-Guio, Lucas-Alexandre Stern, and X. H. Nanostructured Hydrotreating Catalysts for Electrochemical Hydrogen Evolution. *Chem. Soc. Rev.* **2014**, *1* (3).
- (43) Bokobza, L.; Bruneel, J.-L.; Couzi, M. Raman Spectra of Carbon-Based Materials (from Graphite to Carbon Black) and of Some Silicone Composites. *C* **2015**, *1* (1), 77–94.
- (44) Rosenburg, F.; Ionescu, E.; Nicoloso, N.; Riedel, R. High-Temperature Raman Spectroscopy of Nano-Crystalline Carbon in Silicon Oxycarbide. *Materials (Basel)*. **2018**, *11* (1).
- (45) Pawlyta, M.; Rouzaud, J. N.; Duber, S. Raman Microspectroscopy Characterization of Carbon Blacks: Spectral Analysis and Structural Information. *Carbon N. Y.* **2015**, *84* (1), 479–490.
- (46) Walton, A. S.; Lauritsen, J. V.; Topsøe, H.; Besenbacher, F. MoS₂ Nanoparticle Morphologies in Hydrodesulfurization Catalysis Studied by Scanning Tunneling Microscopy. *J. Catal.* **2013**, *308*, 306–318.
- (47) Salazar, N.; Rangarajan, S.; Rodríguez-Fernández, J.; Mavrikakis, M.; Lauritsen, J. V. Site-Dependent Reactivity of MoS₂ Nanoparticles in Hydrodesulfurization of Thiophene. *Nat. Commun.* **2020**, *11* (1), 1–9.
- (48) Wang, H.; Iglesia, E. Thiophene Hydrodesulfurization Catalysis on Supported Ru Clusters: Mechanism and Site Requirements for Hydrogenation and Desulfurization Pathways. *J. Catal.* **2010**, *273* (2), 245–256.
- (49) Voiry, D.; Salehi, M.; Silva, R.; Fujita, T.; Chen, M.; Asefa, T.; Shenoy, V. B.; Eda, G.; Chhowalla, M. Conducting MoS₂ Nanosheets as Catalysts for Hydrogen Evolution Reaction. *Nano Lett.* **2013**, *13* (12), 6222–6227.

Annexe

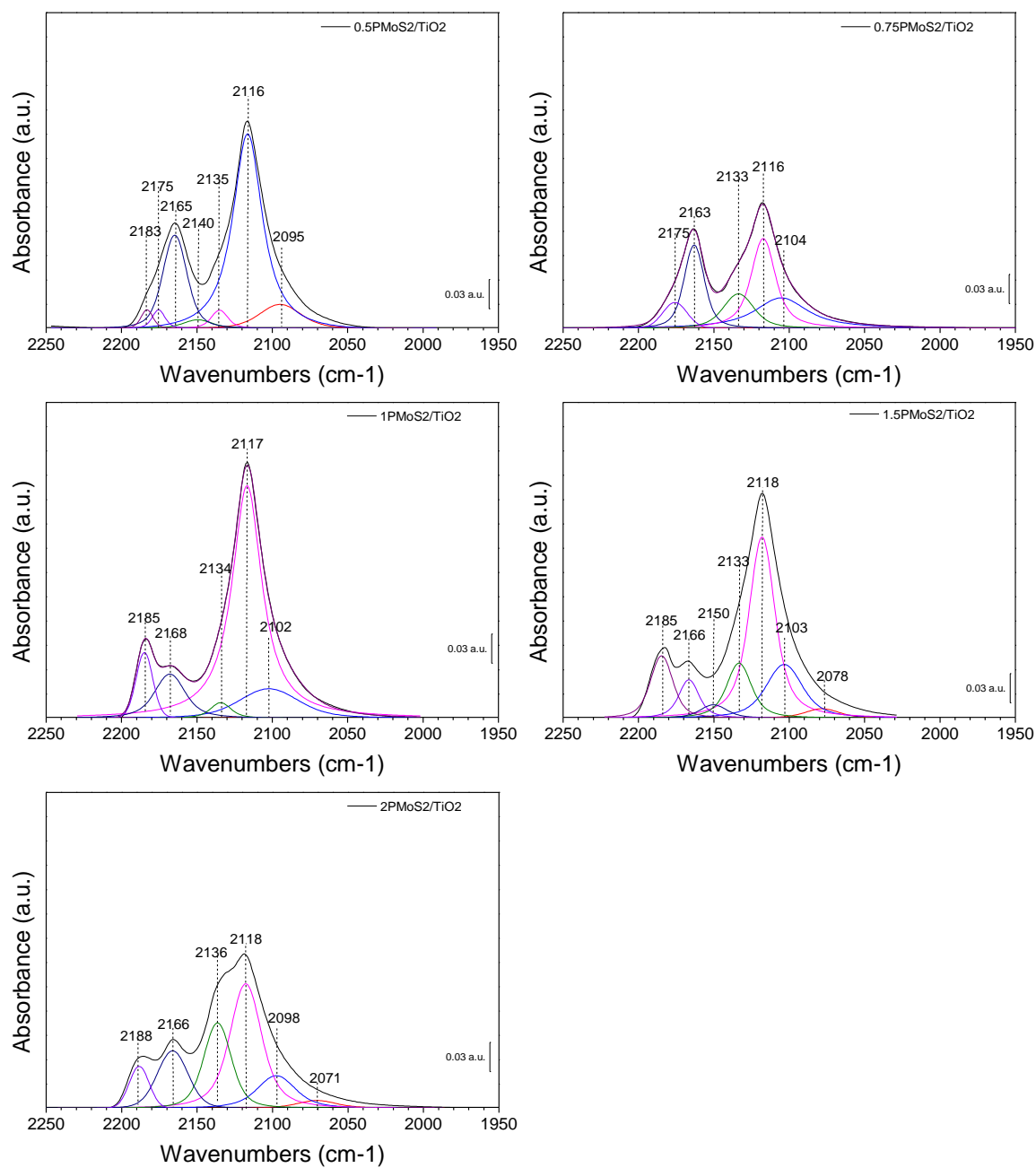


Figure A1: Curve fitting of $x\text{-PMoS}_2/\text{TiO}_2$ spectra ($x=0.5; 1; 1.5; 2$) at CO saturation.

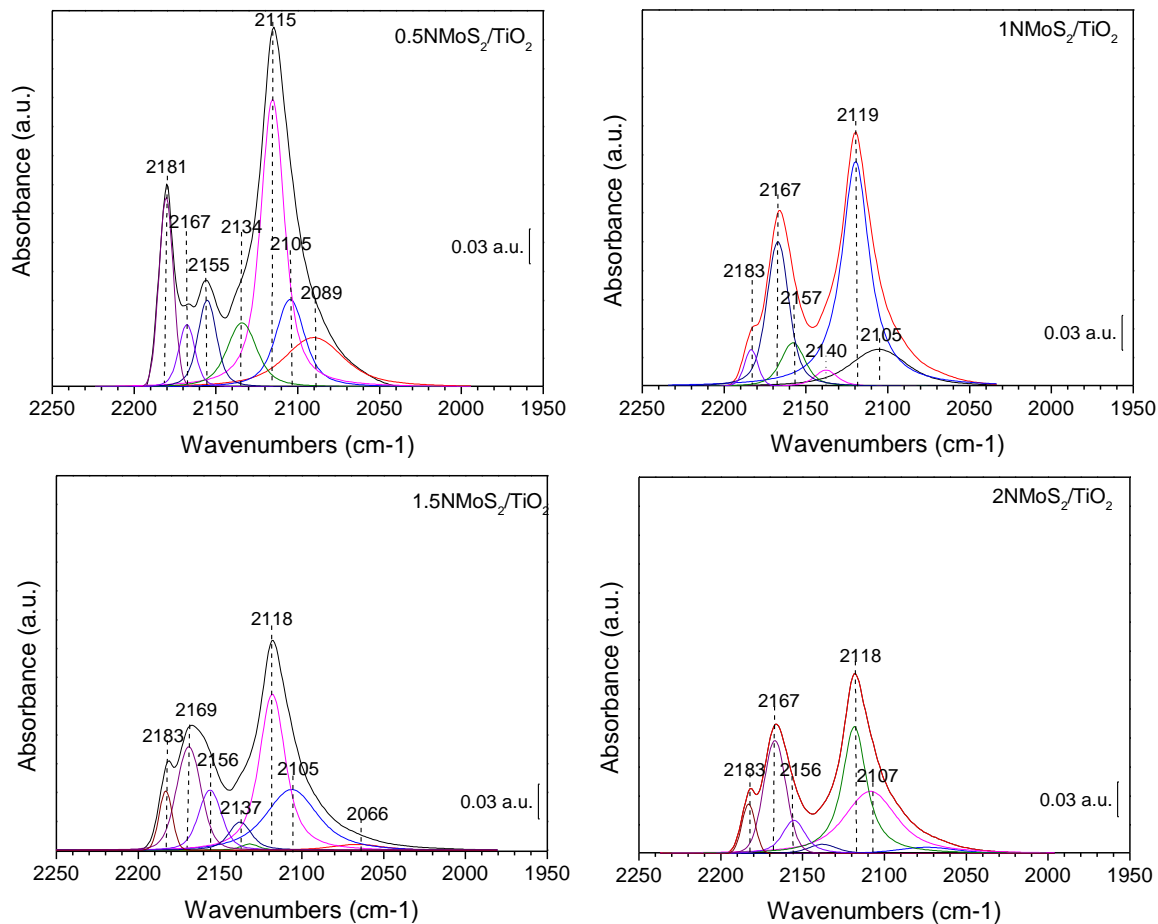


Figure A2: Curve fitting of IR/CO spectra of $x\text{-NMoS}_2/\text{TiO}_2$ at CO saturation.

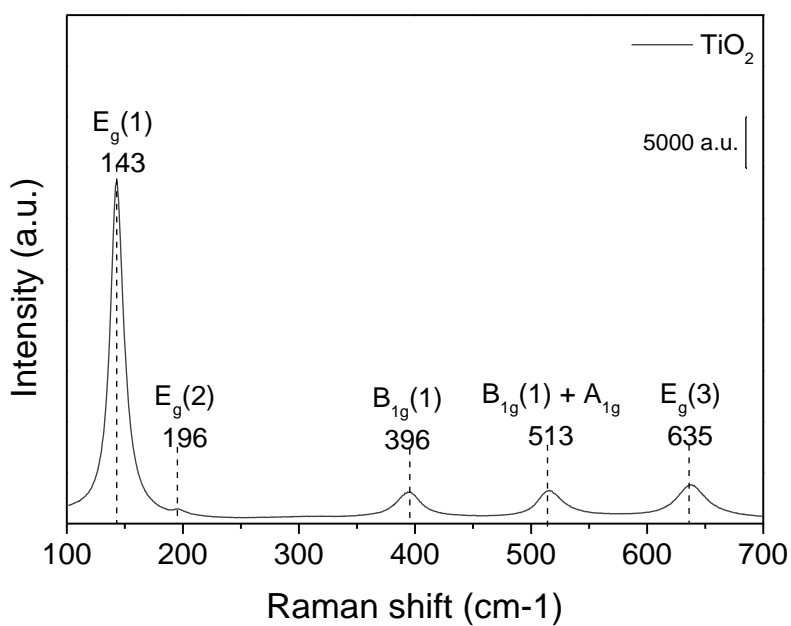


Figure A3: Raman spectra of TiO_2 anatase.

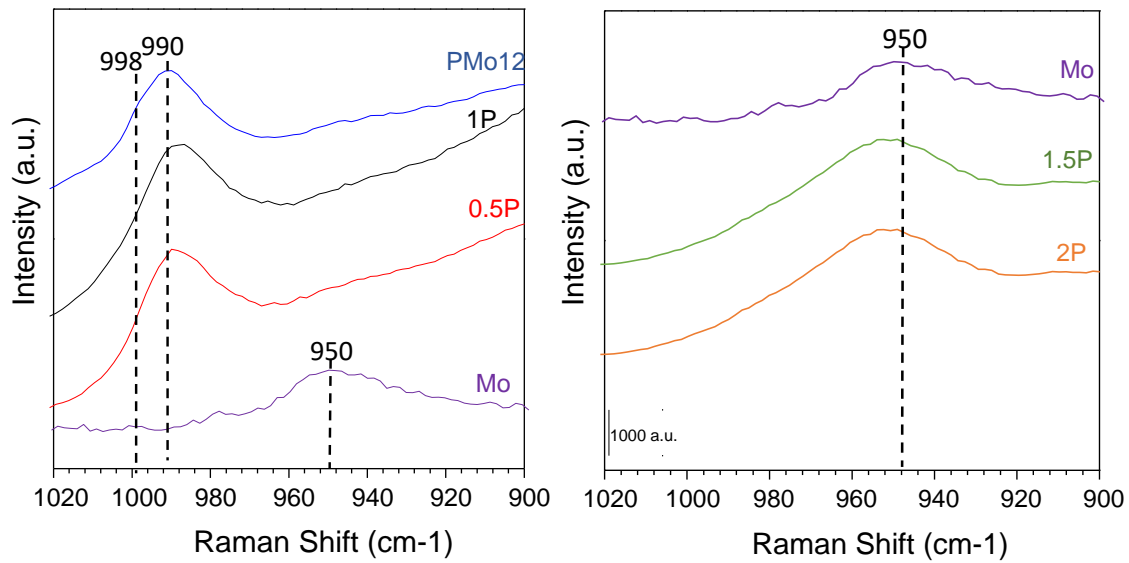


Figure A4: Raman spectra of dried PMo12/TiO₂ and x-PMo/TiO₂ focus on polymolybdate region 900-1000 cm⁻¹.

Table of contents

Chapter 4: Effect of support's morphology on hydrogen evolution reaction: TiO₂ nanotubes and nanowires **157**

1. Introduction **157**

2. Synthesis **160**

3. Study of MoS₂/TiNT prepared by incipient impregnation **162**

3.1. Characterization of sulfided and non sulfided X-Mo/TiNT 162

3.2. Discussion and conclusion about 3-MoS₂/TiNT prepared by incipient impregnation 172

4. Incorporation of molybdenum into nanotube-walls via hydrothermal synthesis **176**

4.1. Fundamental characterization (X-ray; BET and ICP) 176

4.2. IR/CO analysis of TiNT(3%; 6%; 9%-MoS₂) 179

4.3. Raman analysis of (3%; 6%; 9%) 185

4.4. XPS- analysis of TiNT(9%-MoS₂) sulfided at 335°C 187

4.5. TEM analysis of TiNT(9%-MoS₂)-335°C 188

4.6. HDS-test of TiNT (3%; 6%; 9%-MoS₂) 189

4.7. Conclusion about embedded Mo catalyst TiNT(x-MoS₂) 190

5. Impregnation of molybdenum on TiO₂ nanowires (TiNW) **192**

5.1. Fundamental characterization (X-ray; BET and ICP analysis) 192

5.2. IR/CO analysis of MoS₂ (3 Mo atoms/nm²)/TiNW 194

5.3. Raman analysis of MoS₂/TiNW before and after activation 197

5.4. TEM analysis of MoS₂/TiNW-400°C 198

5.5. HDS-test of MoS₂/TiNW 199

5.6. Conclusion about MoS₂/TiNW 199

| | |
|---|------------|
| 6. Effect of morphology change on energy gap | 200 |
| 7. HER activity test on MoS₂ dispersed on TiNT and TiNW | 202 |
| 8. Conclusion | 208 |
| Reference | 210 |
| Annex | 214 |

Chapter 4: Effect of support's morphology on hydrogen evolution reaction: TiO₂ nanotubes and nanowires

1. Introduction

As revealed in Chapter 3, doping TiO₂ anatase with heteroatoms showed itself to be insufficient in order to increase the electrical conductivity of bulk TiO₂. As a result, other supports were tried such as titanium nitride, graphitic carbon nitride (g-C₃N₄) and nickel foam (NF) based on their conductivity, optimal IR-transparency and stability in acidic media. However, titanium nitride showed poor BET surface and pellet preparation was impossible. After optimizing the BET surface of graphitic carbon nitride and impregnating it with heptamolybdate, IR spectrum showed high absorbance and overall vibration peaks related to C₃N₄ in the expected zone of CO/M-edge vibration. Consequently, analyzing this kind of material turned out to be difficult due to superposition of absorption bands. In regards to nickel foam, its BET surface resulted to be very small (4 m²/g) causing a very low amount of Mo deposition leading to the absence of CO/MoS₂ adsorption bands. Coating Ni-foam with carbon in order to increase BET surface resulted in decreasing IR signal, thus making it nearly impossible to obtain any result. Furthermore, the coating diluted itself in liquid environment which is not ideal for water electrolysis. Unfortunately, none of the above-named candidates as HER-electrocatalyst support were possible to analyze with IR-transmission spectroscopy. In addition, the reduction of TiO₂ into metallic Magnéli-phase Ti₄O₇ was tried out. However, the synthesis of a homogenous phase at 900°C resulted to be very complicated and the obtained black product was characterized by small specific surfaces and poor transparency in IR due to the reflective character of the sample.

Since the aim of this research work is to correlate HER performance and surface characteristics of HER electrocatalysts, TiO₂ was re-approached as carrier. Herein the idea was to change the morphology of bulk TiO₂ in order to improve electrical properties. As it is known in the case of carbon nanotubes (CNT), its special tube-like morphology allows to enhance fast charge transport with an electrical conductivity of 10⁴-10⁶ S/cm.¹

Matter of fact TiO₂ nanotubes exist and can be synthesized by different methods. One, a solvothermal method, consists in mixing TiO₂ with a high concentrated NaOH solution in an autoclave.^{2,3} The obtained TiO₂ nanotubes (TiNT) are disorganized while the other synthesis option creates compactly ordered, one directional aligned nanotubes. For the latter, Ti-foil undergoes electrochemical anodization^{4,5} resulting in the creation of TiO₂ nanotube arrays (TiNTA) as shown in Figure 1.

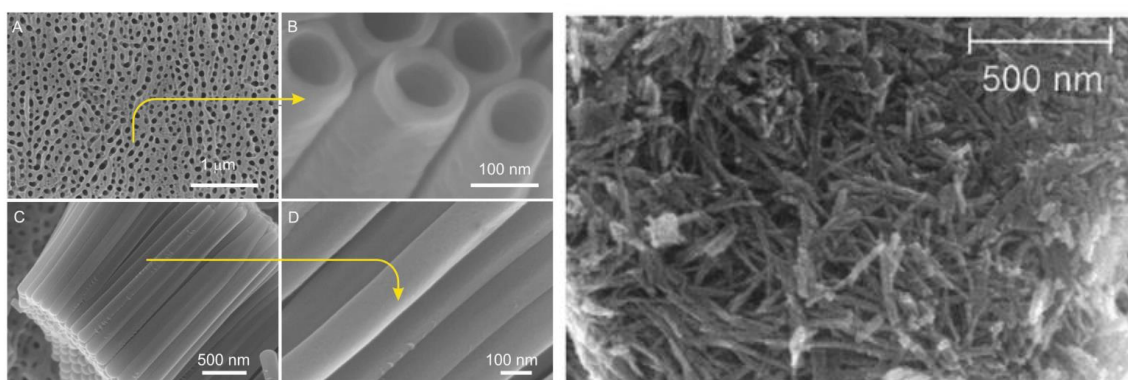


Figure 1: On the left SEM images of TiO₂ nanotube arrays under different resolution.⁴ On the right SEM image of TiO₂ nanotubes synthesized via a hydrothermal approach.³

In both methods high surface areas are obtained which is a crucial factor for high MoS₂ dispersion. In different research works TiNTA was used already as HER electrocatalyst carrier.⁶⁻⁷ Compared to TiO₂, TiNTA presents lower overpotentials at - 10 mA/cm², depending on synthesis method. A few reported results are summarized in the Table 1.

Table 1: Reported HER electrocatalyst supported on TiNTA in 0.5M H₂SO₄.

| HER catalyst | Overpotential (mV@η_{10}) | Tafel slope | Synthesis | Reference |
|------------------------------|--|--------------------|--|------------------|
| <i>Ir/TiNTA-H</i> | -46 | 36 mV/dec | Anodic anodization of Ti disk + cathodic protonation | 6 |
| <i>MoS₂/TiNTA</i> | -200 | 113 mV/dec | Anodization of Ti foil + hydrothermal approach for MoS ₂ | 8 |
| <i>MoS_x/TiNTA</i> | -157 | 53 mV/dec | Anodization of Ti foil + electrodeposition of MoS ₂ (amorphous) | 7 |
| <i>MoS₂/TiNTA</i> | -189 | - | Anodization of Ti-foil + atomic layer deposition of MoS ₂ | 5 |

As it can be seen, disordered TiO₂ nanotubes prepared by solvothermal method are not used for HER. The ordered, one directional alignment of nanotube may improve charge transfer significantly and moreover the anodized Ti-foil is used afterwards as self-supported cathode in contrary to TiNT which needs further preparation to be used as a cathode (i.e. mixing with a binder, drying etc.).

Though preparation of nanotube arrays via Ti-foil allows to achieve lower overpotentials, it is difficult to put in to practice this synthesis if IR characterization ought to be performed. Ti-foil is not transparent for FTIR-transmission spectroscopy because it reflects light. Subsequently the hydrothermal synthesis of TiNT was contemplated by knowing that the formed nanotubes

are not one directionally ordered which might affect the overall charge transfer. We put the assumption that the solvothermal synthesized TiNT will present enhanced charge transfers compared to TiO₂ but less effective than TiNTA.

Similarly to nanotubes, nanowires are also known to have better charge transfer compared to bulk materials. Hence, TiO₂ nanowires (TiNW) were also studied as potential carriers.

In the following two main questions are investigated. First, is there an effect on MoS₂ properties, charge density and HER activity by changing the carrier's morphology? Secondly, in Chapter 3 we determined that Volmer step is the rate determining step for MoS₂/TiO₂. Hence, we speculated whether or not by reducing the interaction force between Mo and TiO₂ we could actually facilitate this step by inducing stronger Mo-H interaction. Herein, we want to see if it is possible by changing the morphology of bulk TiO₂ to minimize the strong interaction between molybdenum and the support in order to facilitate Volmer step and observe smaller Tafel slopes.

2. Synthesis

TiNT: TiO₂ nanotubes were synthesized by a solvothermal approach as described already by Min Gyu Choi et al.³ In short 3 g of TiO₂ anatase (Degussa) were stirred for 20 minutes in 35 ml 10M NaOH. Afterwards the solution was sonicated for 30 minutes and put in a Teflon autoclave at 150°C for 48h. After cooling down, the solid was collected, centrifuged and washed in 0.1M HCl until pH reached 7. The excess in acid was then washed with DI water and left to dry for 24h at 100°C in oven. The white powder was calcined at 300°C for 4h with a ramp of 1°C/min.

3-Mo/TiNT: In order to form Mo/TiNT incipient impregnation was used. A concentrated solution of (NH₄)₆Mo₇O₂₄·4H₂O was prepared using DI water so that 3 Mo atoms/nm² would be dispersed on the surface. The impregnated catalysts were matured at room temperature for 1h and then dried at 110°C for 16h.

TiNT(x-Mo): Mo imbedded into TiO₂ nanotube walls were prepared with different weight percentage of Mo-precursor (3%; 6%, 9%). In short, 1 g of TiO₂-anatase powder was dissolved

in 11.6 mL 10M NaOH solution and afterwards (NH₄)₄Mo₇O₂₄·4H₂O was added with the necessary amount so that weight ratio (x) between Mo and TiO₂ equals 3%; 6%; 9%. The solution was mixed for 30 minutes and further sonicated for 20 minutes. Eventually the solution was transferred into a 20 mL Teflon autoclave and heated for 48h at 150°C. The white solid was collected by washing with 0.1M HCl until pH=7, centrifuged and washed with DI-water again. TiNT(x-Mo) were dried at 110°C overnight.

TiNW: The same synthesis protocol for TiNT with a minor change was used by replacing NaOH with KOH. In short, a solution of 10M KOH was prepared in which TiO₂-anatase and (NH₄)₆Mo₇O₂₄ were dissolved, mixed (10 minutes), sonicated (20 minutes) and heated in a Teflon autoclave for 48h at 150°C. The obtained white precipitate was washed and centrifuged with HCl until reaching a neutral pH. The white solid was dried at 110°C for 12h and then calcined for 4h at 300°C.

3-Mo/TiNW: Identically as for 3-Mo/TiNT a concentrated solution of (NH₄)₄Mo₇O₂₄·4H₂O was prepared with a Mo-loading of 3 Mo/nm².

3-MoS₂/TiNT; TiNT(x-MoS₂); 3-MoS₂/TiNW: 3-Mo/TiNT, TiNT(x-Mo), 3-Mo/TiNW underwent sulfidation (10% H₂S/H₂ 30mL/min) at 350°C for 2h (1°C/min).

3. Study of MoS₂/TiNT prepared by incipient impregnation

3.1. Characterization of sulfided and non sulfided X-Mo/TiNT

3.1.1. Fundamental characterization (DRX; SEM; BET; ICP-MS)

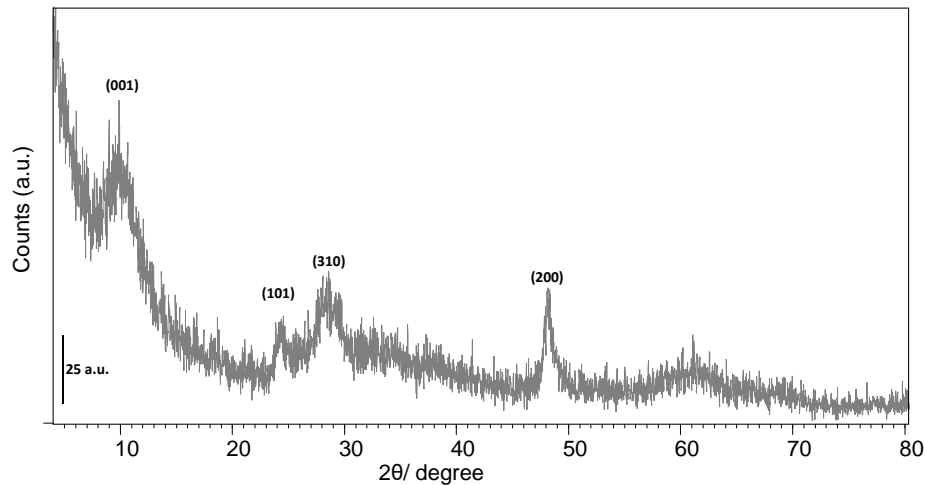


Figure 2: X-Ray diffraction patterns of synthesized TiO₂ nanotube (TiNT)

The formation of TiO₂ nanotubes (TiNT) were verified by X-ray and SEM. Indeed the formation of nanotubes was successful as results in Figure 2 and Figure 3 show. The characteristic peaks already described by M.G. Choi et al. are found at 10°, 25°, 28°, 48° corresponding to (001), (101), (310) and (200) facets respectively.³ The large peak at 60° having low intensity is probably due to the presence of bronze phase (TiO₂(B)).⁹

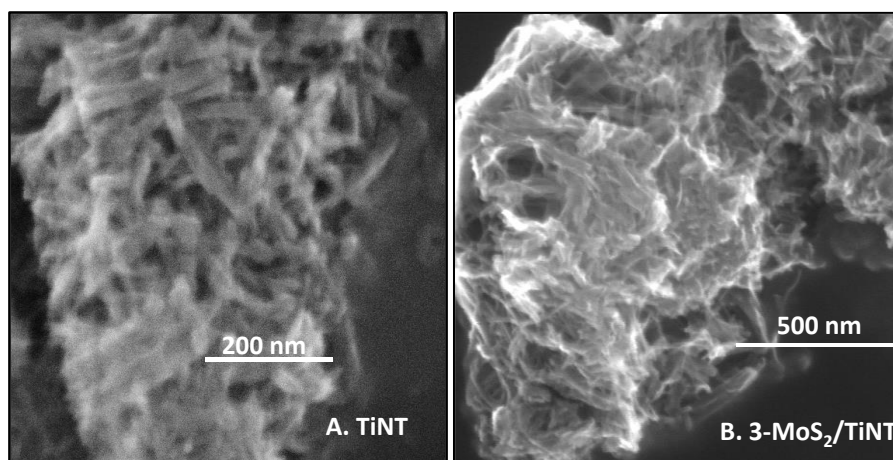


Figure 3 A. and B.: SEM-images of TiNT and 3-MoS₂/TiNT sulfided at 350°C.

SEM images (Figure 3A) show agglomerated nanotubes with an average length of 150-200 nm and a diameter of approximately 10 ± 1 nm which is confirmed by BET (Table 2). After introducing Mo and sulfiding 3-Mo/TiNT at 350°C the tubular morphology of TiO₂ remains (Figure 3B).

Table 2: BET analysis results of TiNT, S-TiNT, 3-Mo/TiNT and 3-MoS₂/TiNT.

| Sample | BET surface (m²/g) | Pore volume cm³/g | Average pore diameter (nm) | pore diameter with the highest frequency (nm) |
|--|--|---|---------------------------------------|--|
| <i>TiNT</i> | 341 | 0.724 | 9.0 | 6.4 |
| <i>S-TiNT-350°C</i> | 147 | 0.216 | 5.9 | 3.6 |
| <i>3-Mo/TiNT</i> | 255 | 0.563 | 8.8 | 6.4 |
| <i>3-MoS₂/TiNT- 350°C</i> | 29 | 0.051 | - | - |

BET analysis show that sulfidation has an impact on pore diameters, pore volume and BET surfaces. Indeed after sulfiding TiNT at 350°C (noted S-TiNT), its pore diameter is decreasing by a half as well as its BET surface. Herein, the nanotubes are unstable to applied sulfidation conditions leading to their agglomeration. Contrariwise, Mo impregnation affects only BET surface and pore volume as the results for 3-Mo/TiNT demonstrate. However, after sulfiding 3-Mo/TiNT we observe that its pore volume is close to zero as well as a strong downfall of its BET surface from 255 to 29 m²/g. Consequently, the pores are clogged, probably by the formation of MoS₂. Accordingly, this assumption is validated by the artifact of cavitation at 3.8 nm observed on pore diameter distribution graph (Figure 4). This artifact is typical for tubular pores which are obstructed at their extremities partially leaving a small narrow gap; sufficient for N₂ to fill the inside of the nanotube during adsorption.¹⁰ However, when desorption occurs N₂ is captured inside the tube inducing a delay in desorption. Subsequently the pressure inside the nanotube compared to external pressure is increasing until captured N₂ is released at once from the tube which is translated by an artifact of cavitation.

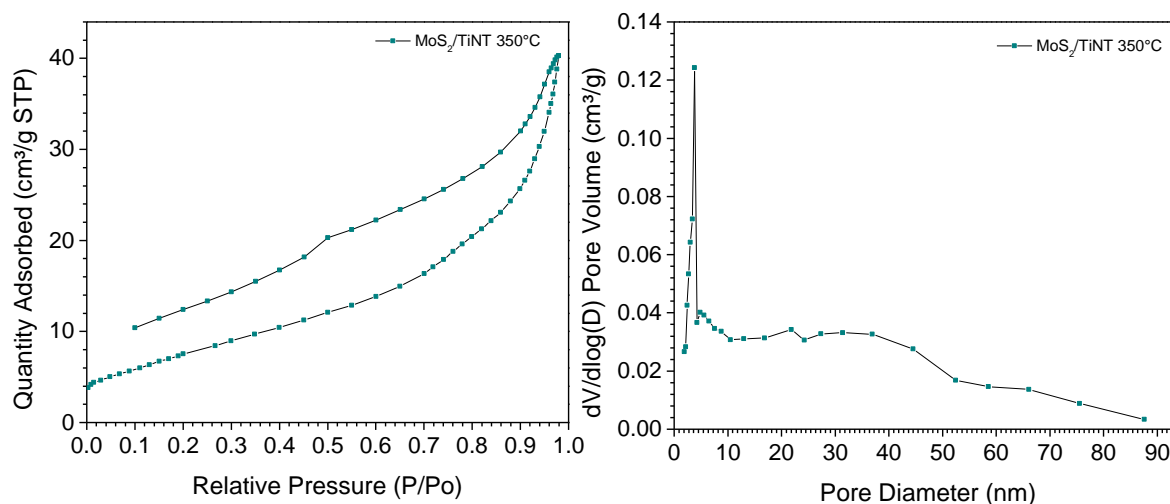


Figure 4: Hysteresis curve of N_2 adsorption and desorption of $MoS_2/TiNT-350^\circ C$ and pore diameter distribution in function of pore volume. The peak at 3.8 nm corresponds to an artifact of cavitation.

Furthermore, this phenomenon is explaining the low S/Mo ratio of 0.72 determined by ICP-MS (Table 3). Mo inside the tube was not accessible to sulfur sufficiently to be transformed into MoS_2 .

ICP-MS analysis shows also the presence of sulfur in TiNT after sulfidation at 350°C due to oxygen-sulfur exchange. The amount of sulfur (2.10%_{wt}) is similar to the one on sulfided TiO_2 at the same temperature (2.26%_{wt}). We also note a non-negligible amount of Na which is about 8%_{wt}. Herein we can conclude that a part of sodium from the basic solution NaOH used for synthesizing TiNT has been included into the nanotube structure during solvothermal synthesis.

Table 3: Overview of determined weight percentages of Na, S, Ti, Mo by ICP-MS and calculated sulfur/molybdenum ratio.

| Sample | 23 Na (%wt) | 48 Ti (%wt) | 32 S (%wt) | 95 Mo (%wt) | Molar ratio S/Mo |
|--------------------------|------------------------|------------------------|-----------------------|------------------------|-----------------------------|
| TiNT | 8.15 | 42.34 | - | - | - |
| S-TiNT-350°C | 5.91 | 32.04 | 2.10 | - | - |
| $MoS_2/TiNT-350^\circ C$ | 7.34 | 39.06 | 4.58 | 11.27 | 0.72 |

3.1.2. IR/CO analysis

CO adsorption followed by IR-transmission was performed on TiNT to analyze its surface. A band was clearly visible around 2170 cm^{-1} which shifted downwards to 2165 cm^{-1} with increasing CO pressure. After peak fitting a supplementary band at 2155 cm^{-1} was detected due to the contribution of CO/OH (Figure 5).

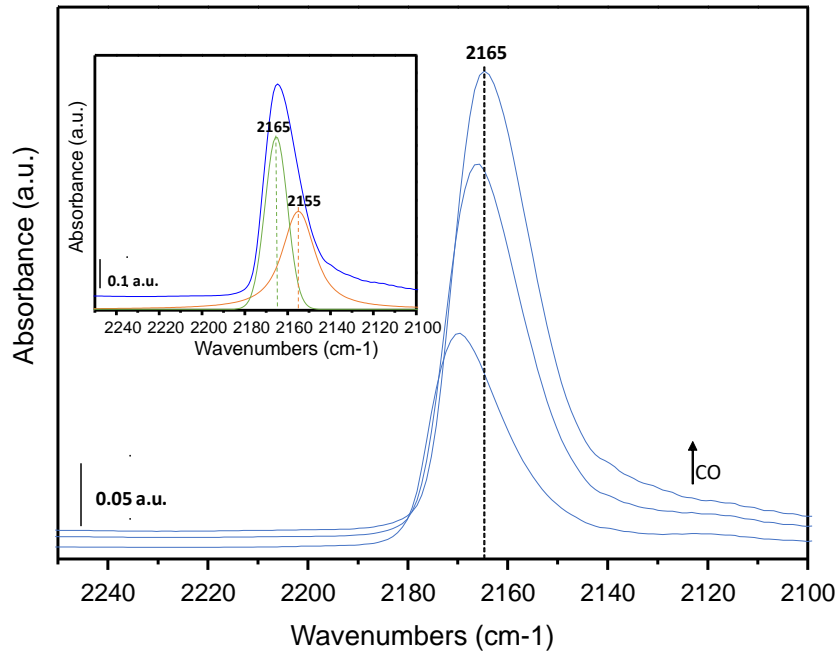


Figure 5: IR/CO spectrum of TiNT up to 1 Torr CO equilibrium pressure after annealing at 300°C under vacuum and its deconvolution spectrum presented in the small capture.

By comparing this spectrum with the spectrum of adsorbed CO on bulk TiO₂, it can be deduced that this band corresponds to $\nu(\text{CO}/\text{Ti}^{4+} (001))$ (Figure 5).¹¹ Subsequently the synthesized nanotubes are built with exposed (001) facets contrarily to bulk TiO₂ presenting mostly (100) and (101)(112) facets. By normalizing IR/CO spectra to the initial specific surface, a higher Lewis acid site density was deduced on TiO₂ compared to TiNT. Indeed, by calculating the total area of $\nu(\text{CO}/\text{Ti}^{4+})$ on both carriers, a ratio of 2.7 is determined between TiO₂ and TiNT. Hence, it can be concluded that there are 2.67 more Ti⁴⁺ sites on TiO₂ than on TiNT. Hence, TiNT presents less available impregnation sites than TiO₂ which could lead to a lower Mo dispersion.

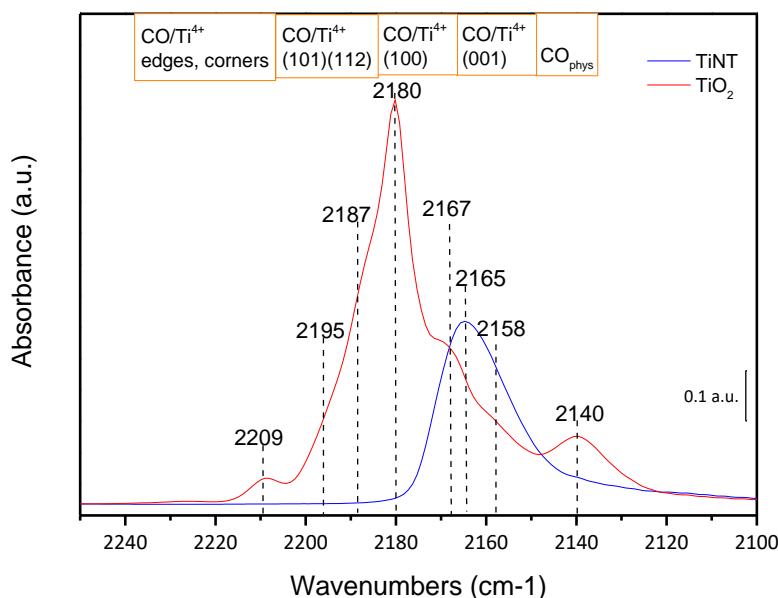


Figure 6: Comparison between IR/CO spectra of bulk TiO_2 and synthesized TiNT at 1 Torr CO equilibrium pressure normalized to same initial specific surface.

For 3- MoS_2/TiNT , the characteristic band of $\nu(\text{CO}/\text{Ti}^{4+} (001))$ was observed at 2170 cm^{-1} shifting to 2165 cm^{-1} with higher CO coverage (Figure 6). At 2155 cm^{-1} $\nu(\text{CO}/\text{OH})$ was also observed having very small intensity. The absorption band $\nu(\text{CO}/\text{M-edge})$ is downward shifted by 3 cm^{-1} compared to $\text{MoS}_2/\text{TiO}_2$ and is detected at 2115 cm^{-1} . Furthermore, curve fitting shows the presence of a new band at 2101 cm^{-1} . This band is strongly downward shifted compared to $\nu(\text{CO}/\text{M-edge})$ at 2115 cm^{-1} . The newly observed band could be related to CO adsorbed on highly sulfur depleted lacunary M-edge sites which were reported to be around 2098 cm^{-1} .¹²

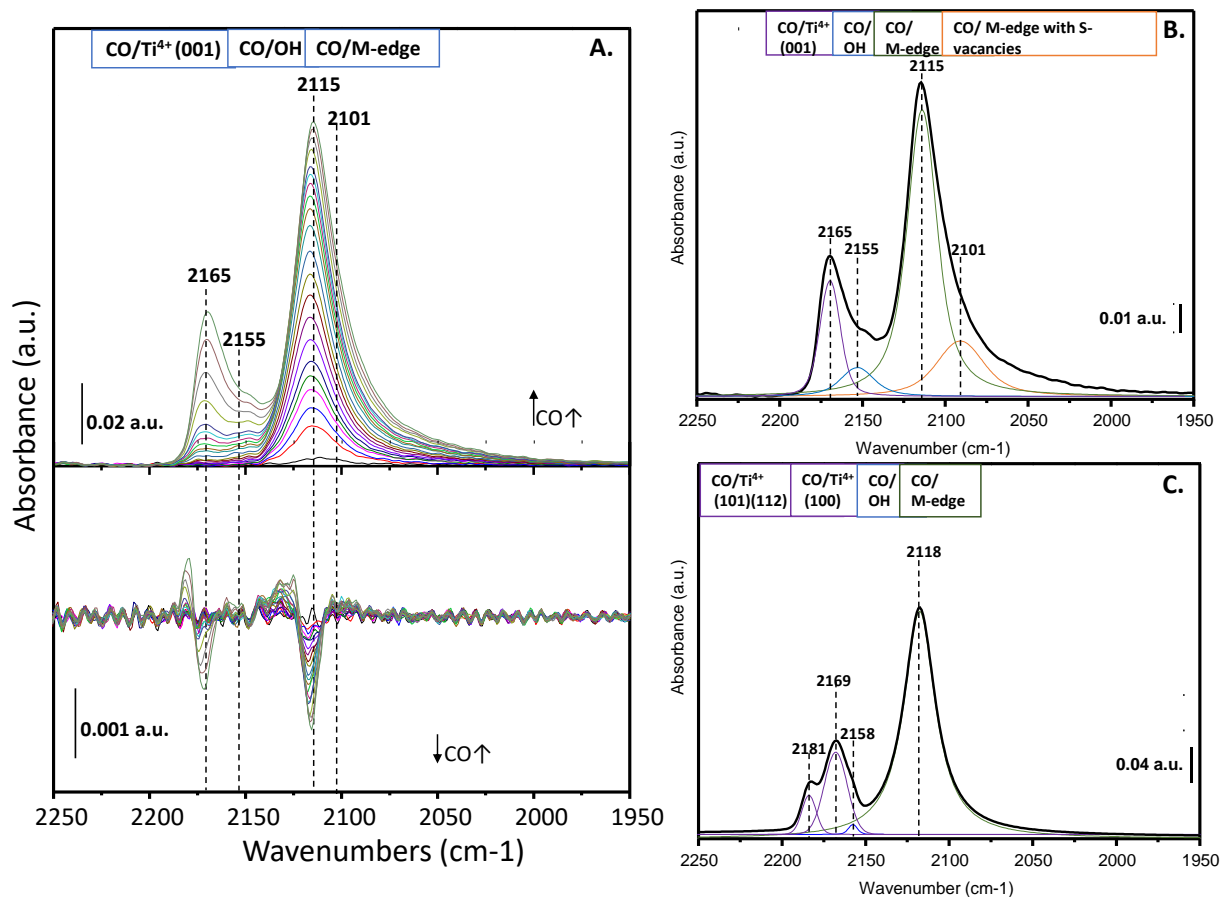


Figure 7: IR/CO spectra of 3-MoS₂/TiNT up to 1 Torr equilibrium pressure and their respective 2nd derivative (A). Deconvolution spectrum at saturation of 3-MoS₂/TiNT (B) as well as of MoS₂/TiO₂ (C).

It should also be noted that the intensity of $\nu(\text{CO}/\text{Ti}^{4+})$ at 2165 cm⁻¹ has strongly decreased after MoS₂ formation. Still, $\nu(\text{CO}/\text{Ti}^{4+})$ remains intense. Thus, we can deduce that not all Lewis acid sites are impregnated with molybdenum. The proportion of not occupied Lewis sites on 3-MoS₂/TiNT is about 43% (Figure 8). The concentration of probed M-edges sites was determined to be 29 $\mu\text{mol/g}$ which is a third of MoS₂/TiO₂ M-edge site's concentration (84 $\mu\text{mol/g}$).

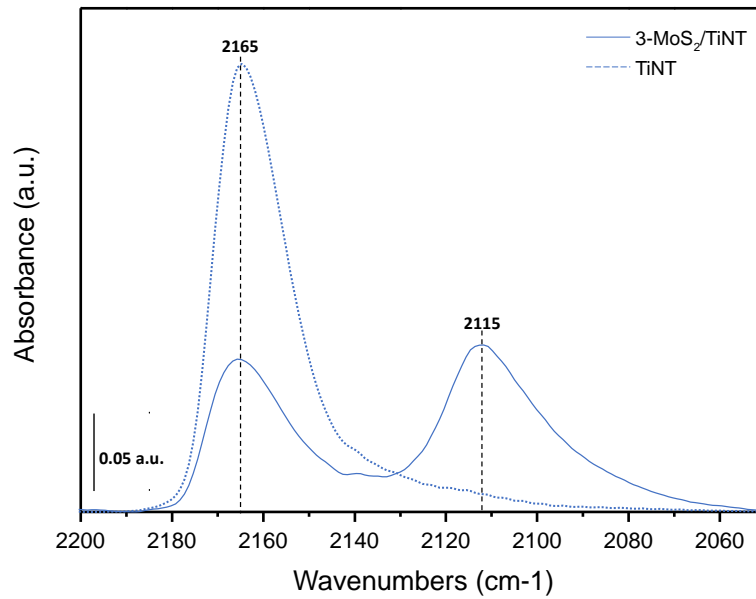


Figure 8: Comparison of IR/CO spectra between 3-MoS₂/TiNT and TiNT at 1 Torr equilibrium pressure.

3.1.3. Raman analysis

Raman analysis shows inhomogeneous distribution of MoS₂ on TiNT (conditioned in form of a pellet with a diameter of 16 mm). Depending on the analyzed region different spectra were obtained for 3-MoS₂/TiNT (Figure 9). We also detect the presence of Na₂MoS₄ (468 and 1030 cm⁻¹) as well as the vibration band at 620 cm⁻¹ which could be related to the vibration of ν(Mo-O) of sodium molybdenum oxysulfide salt.^{13,14}

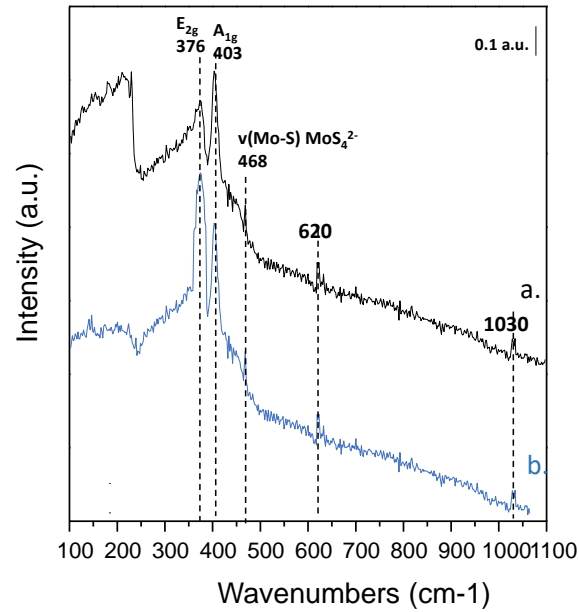


Figure 9: Raman spectra of 3-MoS₂/TiNT on different zones of analyzed pellet.

Indeed, the in- and out-of-plane vibrations of 2H-MoS₂ are found at 376 cm⁻¹ and 403 cm⁻¹ respectively (curve a, Figure 9). Compared to the reported values of E_{2g} (380 cm⁻¹) and A_{1g} (407 cm⁻¹) the in- and out vibrations of Mo-S are redshifted.^{15;16} The observed redshift implies a tensile strain on Mo-S bonds. On other regions, the same vibrations were also found but with a different intensity ratio between E_{2g} and A_{1g} (spectrum b, Figure 9). By calculating the intensity proportion $I(E_{2g})/I(A_{1g})$ the significant difference is emphasized: For the spectrum (a) the ratio $I(E_{2g})/I(A_{1g}) = 0.89$ whereas for spectrum (b) $I(E_{2g})/I(A_{1g}) = 1.2$. This difference in intensity could be related to the stacking number of MoS₂ slabs. Indeed, with raising stacking number the out-of-plane vibration A_{1g} is decreasing in intensity while E_{2g} is increasing.¹⁸ Hence, spectrum (a) is probably due to a few layered MoS₂ slabs whereas spectrum (b) represents higher number of stacking.

3.1.4. TEM-analysis of MoS₂/TiNT-350°C

Based on IR/CO and Raman results, MoS₂ was formed in small amounts on TiNT via incipient impregnation compared to MoS₂/TiO₂ and is not homogeneously dispersed. Indeed, two different Raman spectra were obtained for the same analyzed sample where the difference in intensity of E_{2g} and A_{1g} was completely different. On one spectrum in- and out-of-plane vibrations have similar intensities on the other spectrum the in-of-plane vibration was almost twice more intense than the out-of-plane vibration. Moreover, it is unclear how MoS₂ slabs are oriented on TiNT as well as their size. No information was reported about these two questions in the literature. It is only known that due to the epitaxial growth of MoS₂ on TiO₂, slabs are perpendicular to the support. Yet Arrouvel et al. have demonstrated that MoS₂ slabs can also be tilted on (001) facets of TiO₂ anatase.¹⁹ The catalyst which was synthesized (i.e. MoS₂/TiNT-350°C) is exhibiting only (001) facets as confirmed by IR/CO. Subsequently, MoS₂ slabs on TiNT could be tilted and/or perpendicular to the nanotube. In order to answer those questions TEM analysis of MoS₂/TiNT-350°C was performed. Obtained TEM images are represented in Figure 10A and 10B. Entangled nanotubes are observed. Their diameter is fluctuating around 6 ± 3 nm. By zooming further on the tubes, MoS₂ slabs are visible. The black, thin lines reflecting their presence are mostly parallelly directed to the nanotube and are anchored perpendicularly to the tube (Figure 10B). Yet, it is difficult from the projection views to infer whether MoS₂ sheets are also located inside the nanotube. Their average length was estimated to be around 1.7 ± 0.2 nm (Figure 10C). Note, that this determined slab size is much smaller than the ones on bulk TiO₂ (i.e. 6.8 nm). As a result, estimated Mo dispersion of 0.07 is not reflecting this slab size average. Herein, Mo dispersion was underestimated since its value is based on the concentration of probed M-edge sites by CO which may not have access to all possibly formed MoS₂ due to the validated clogging of nanotubes. In this regard, TEM analysis shows that there are sufficiently large slabs in between 4.0 and 7.0 nm capable to obstruct nanotubes.

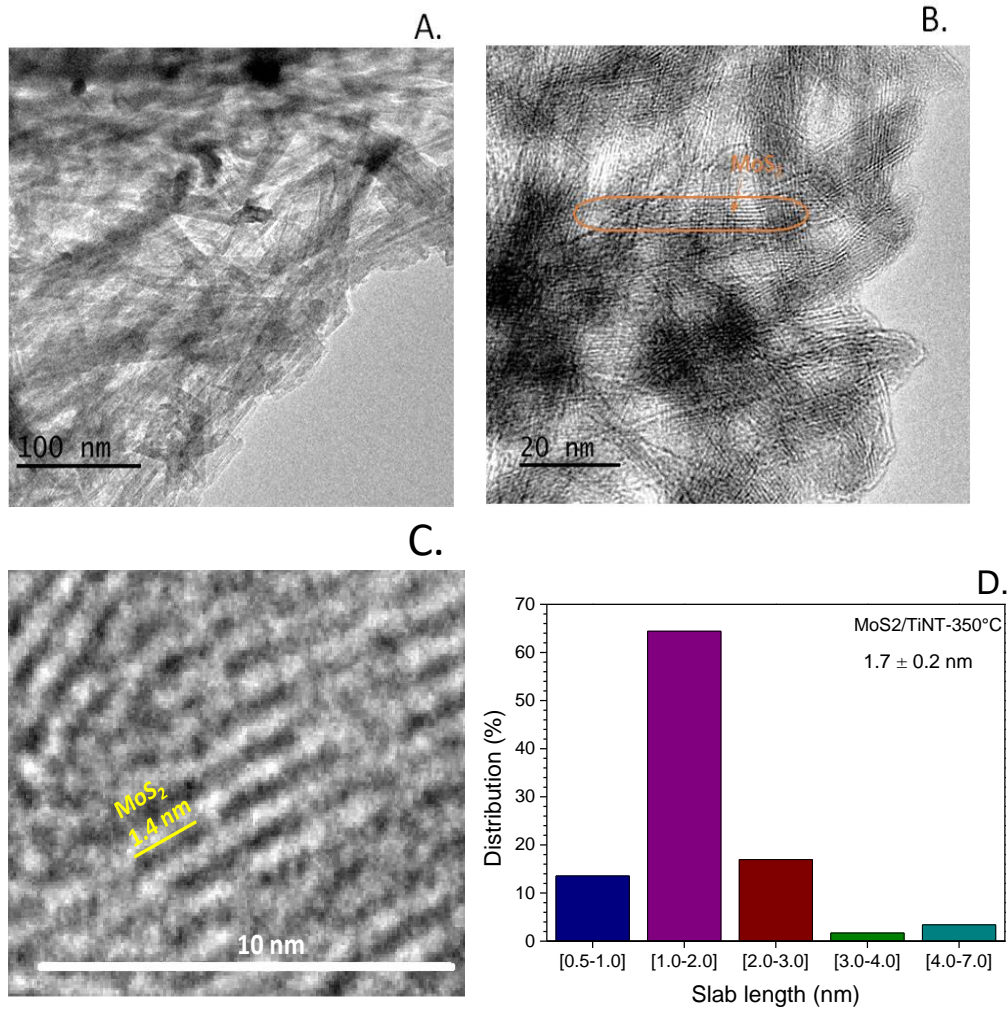


Figure 10: A, B and C. TEM images of MoS₂/TiNT-350°C at different resolutions. D. Statistical distribution of MoS₂ slab length on TiNT.

On TEM images, MoS₂ slabs are creating a sort of repeating pattern on nanotubes: slabs are aligned in a row forming a piling striped pattern seemingly as a multiple of stacked slabs. Based on these observations, the different intensity ratios between in- and out-of-plane vibrations of Mo-S on MoS₂/TiNT-350°C Raman spectra can be better explained. The repeating pattern of piled, aligned slabs seems to have a similar effect as stacking. Thus, affecting the intensity of out-of-plane vibrations of MoS₂ basal plane.

3.1.5. HDS of thiophene

As shown in previous chapters HDS catalytic test is a good way to analyze the accessibility of M- and S-edges. Results of HDS-test with thiophene are reported in Table 4 below.

Table 4: Obtained HDS activity rates for TiNT, 3-MoS₂/TiNT and MoS₂/TiO₂ sulfided at 350°C and 400°C respectively and their respective activity rates per active site in which only M-edges were considered.

| Sample | M-edge site concentration (μmol/g) | Activity rate (mol/h.kg) | Activity rate per active site (h⁻¹) |
|---|---|---------------------------------|---|
| <i>S-TiNT-350°C</i> | 0 | 0 | 0 |
| <i>3-MoS₂/TiNT-350°C (11%_{wt} Mo)</i> | 29 | 6.95 | 240 |
| <i>MoS₂/TiO₂-400°C (6%_{wt} Mo)</i> | 84 | 6.27 | 75 |

The obtained activity rates are similar with a slight increase for 3-MoS₂/TiNT. But by including the concentration of M-edge sites, 3-MoS₂/TiNT presents three times a higher activity rate per active site. Sulfided TiNT is not active for HDS.

3.1.6. Discussion and conclusion about 3-MoS₂/TiNT prepared by incipient impregnation

IR/CO results show a downwards shift of $\nu(\text{CO/M-edge})$ compared to MoS₂/TiO₂ ($\Delta\nu = 3 \text{ cm}^{-1}$). This shift indicates an increase in electronic charge density due to a pronounced backdonation from Mo to CO. As a result, the change in morphology allowed to enrich Mo with electrons. This increase in electron density could be originated by the enhancement of charge transfer due to the tubular morphology of TiO₂.

The change in morphology favored also the creation of S-vacancies on M-edges as confirmed by the presence of the absorption band at 2101 cm^{-1} . Although a much smaller concentration

of M-edge sites was probed compared to MoS₂/TiO₂, 3-MoS₂/TiNT presented similar HDS activity rates. However, if we consider the amount of active sites, M-edge sites formed on TiNT are more active. This evident increase in intrinsic activity might be related to TiO₂ facets exposition. On IR/CO spectra of 3-MoS₂/TiNT only (001) facets were detected which is in agreement with X-ray diffractogram. In the case of MoS₂/TiO₂ we observed that bulk TiO₂ was majorly presenting (100) facets and few (001) exposed facets. The fact that MoS₂ was formed solely on exposed (001) facets might greatly contribute to the observed enhancement in reactivity. (001) facets are endowed with higher surface energies which are facilitating dissociative adsorption of reactants.²⁰⁻²² The higher energy surface on (001) could impact the interaction between MoS₂ and support and subsequently influence activity.

Nevertheless, the low concentration of M-edge sites is surprising since TiNT specific surface is twice as large as bulk TiO₂. Moreover both carriers are loaded with the same amount of Mo leading to an introduced Mo concentration of 1174 μmol/g_{cata} for 3-MoS₂/TiNT and 612 μmol/g_{cata} for MoS₂/TiO₂.

Table 5: Comparison between probed M-edge sites on MoS₂/TiO₂ and 3-MoS₂/TiNT and their respective ratio between initial amount of Mo determined by ICP-MS and M-edge site concentration.

| Sample | %wt Mo (ICP-MS) | %wt S (ICP-MS) | M-edge sites (μmol/g) | Estimated Mo dispersion | Atomic ratio S/M |
|---|----------------------------|---------------------------|----------------------------------|------------------------------------|---------------------------------|
| MoS ₂ /TiNT-350°C | 11.27 | 4.58 | 29 | 0.07 | 0.72 |
| MoS ₂ /TiO ₂ -400°C | 5.82 | 6.64 | 84 | 0.15 | 2.32 |

This difference in M-edge sites concentration can be related to several factors. First, TiNT presents less Lewis acid site on area basis compared TiO₂ as demonstrated by IR/CO. Since on these site Mo-precursor adsorption occurs during synthesis, their lower amount would lead to lower Mo dispersions and subsequently lower MoS₂ formation. This assumption seems to be confirmed by the estimated Mo dispersion of 0.07 (Table 5). Note, that the value of Mo dispersion is underestimated as previously explained because CO is probably not probing all M-edge sites due to the nanotubes clogging. Herein it leads us to the second factor: the obstruction of nanotubes which was proved by BET analysis. The low determined S/Mo ratio of 0.72 for MoS₂/TiNT-350°C indicating an insufficient sulfidation rate concurs with this

assumption. Based on TEM and ICP-MS analysis it is very probable that nanotubes are obstructed by MoS₂ slabs and also sodium. The distribution of slab sizes shows the presence of sufficient large slabs (4.0 - 7.0 nm) capable to obstruct nanotubes having a diameter of 6 nm while the weight percentage of Na is 8%_w. Consequently, only MoS₂ at the tube's extremities and on the outer walls were probed by CO and are accessible for reactants. This clogging phenomenon explains also the presence of Na₂MoS₄ which is possibly imprisoned in nanotubes and is probably also contributing to the obstruction of TiNT.²³

By calculating the theoretical amount of M-edge sites which should have been formed if the total amount of 1174 μmol/g of Mo was sulfided into MoS₂ on TiNT was determined to be around 805 μmol/g (see Annex for calculation). This amount of M-edge sites is excessively higher than the probed concentration of 29 μmol/g. This discrepancy between probed concentration and theoretical one is accentuating this phenomenon of clogging. However based on the obtained results it cannot be deduced whether MoS₂ is also present inside the nanotubes. The determined S/Mo ratio of 0.72 can include various proportions of sulfur provided by MoS₄²⁻, MoO_xS_y and MoS₂.

The morphology change of TiO₂ into TiNT has also favored the formation of small slabs (1.7 ± 0.2 nm) in the absence of chelating agents. Their size is much smaller than the one reported for MoS₂/TiO₂ (i.e. 6.8 nm).²⁴ The large slab size of MoS₂ on TiO₂ was explained to be caused by the existing strong Van der Waals bonds between MoS₂ and TiO₂.²⁵ This strong decrease in slab size may indicate a weakening of those Van der Waals bonds between MoS₂ and TiNT.

To conclude, based on these results, 2H-MoS₂ was formed on exposed (001) facets. TiNT allowed to increase the electron density of Mo and significantly enhance the intrinsic activity. However, incipient impregnation of molybdenum-precursors on TiNT seems not to be a suitable strategy to achieve high and homogeneous MoS₂ dispersion on TiNT (Figure 11) since clogging occurs and prevents the formation of MoS₂ in high concentrations.

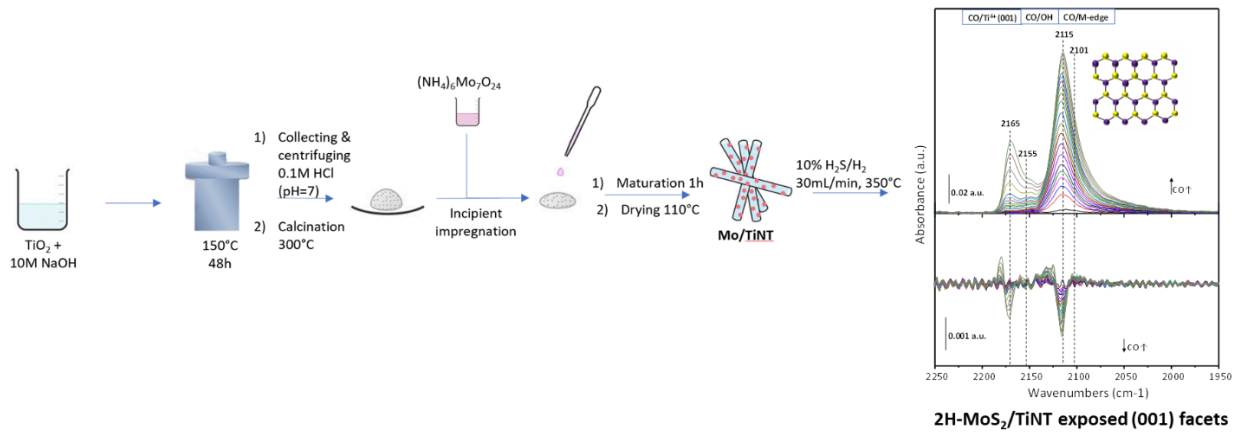


Figure 11: Overview of synthesis method to obtain 2H-MoS₂/TiNT with M-edge sites enriched with electron density and dispersed on (001) facets.

4. Incorporation of molybdenum into nanotube-walls via hydrothermal synthesis

As we have seen, incipient impregnation is not an adequate strategy to disperse molybdenum homogeneously on nanotubes. To favor a good dispersion of MoS₂ slabs, integrating molybdenum into the nanotube wall seems to be a good alternative. The possibility to integrate metallic dopants into the wall by a one-pot hydrothermal synthesis was demonstrated to be possible already with Sn and Si precursors.^{26,27} Based on these reported procedures Mo was integrated into the nanotube wall of TiO₂ anatase.

4.1. Fundamental characterization (X-ray; BET and ICP)

XRD pattern of TiNT(x-Mo) presented the same characteristic peaks as TiNT ($2\theta = 10^\circ, 25^\circ, 28^\circ, 48^\circ$). Subsequently the incorporation of Mo into the wall did not affect the formation of nanotubes during synthesis (Figure 12). However, a slight upward shift of 0.5° for (101) and (200) is observed as well as a decrease in the intensity of diffraction peaks at 10° and 28° corresponding to (001) and (310) facets. This could be related to the insertion of Mo into TiNT framework. With increasing molybdenum concentration, the peak at 10° becomes less intense. We note a complete disappearance of the peak at 10° when the weight percentage of Mo is above 3%.

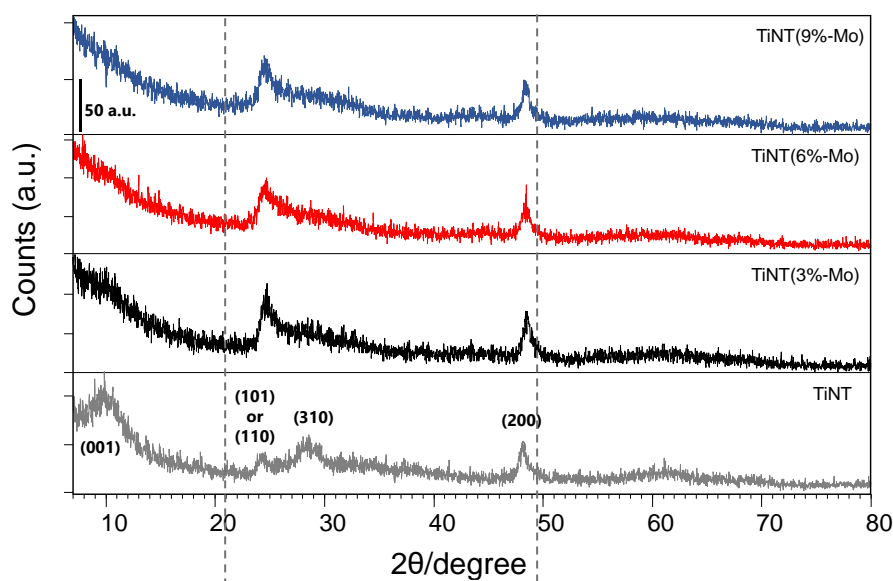


Figure 12: X-ray diffraction patterns of TiNT and TiNT (3%; 6%, 9%-Mo).

BET-analysis of dried catalysts show a slight increase in BET surface after molybdenum introduction compared to TiNT whereas pore diameters are decreasing (Table 6). We also note that after sulfidation pore volumes and diameters are slightly increasing.

Table 6: Results of BET analysis of sulfided and non-sulfided catalysts: TiNT; TiNT(3%; 6%; 9%-Mo) and S-TiNT-350°C; TiNT(3%; 9%-MoS₂)-350°C.

| <i>Sample</i> | <i>S_{BET} (m²/g)</i> | <i>V_{pore} (cm³/g)</i> | <i>Average pore diam. (nm)</i> | <i>pore diam. (nm) with highest frequency</i> |
|----------------------------------|--|--|--------------------------------|---|
| TiNT | 341 | 0.724 | 9.0 | 6.4 |
| S-TiNT-350°C | 147 | 0.216 | 5.9 | 3.6 |
| TiNT(3%-Mo) | 360 | 0.524 | 6.0 | 4.3 |
| TiNT(6%-Mo) | 372 | 0.530 | 5.7 | 4.9 |
| TiNT(9%-Mo) | 366 | 0.614 | 6.7 | 3.9 |
| TiNT(3%-MoS ₂)-350°C | 344 | 0.648 | 7.5 | 5.4 |
| TiNT(9%-MoS ₂)-350°C | 421 | 0.933 | 8.4 | 5.5 |

In contrary to TiNT containing 8%_{wt} Na, TiNT (x-Mo) presented smaller weight percentages (i.e. < 4%_{wt}) (Table 7). Indeed TiNT(3%-Mo) is presenting the highest amount of Na, whereas TiNT(6%-; 9%-Mo) are presenting a Na concentration close to zero. It seems that Na is preferentially inserted into the framework of TiNT when Mo-loading is low. In addition, ICP-MS results also show smaller Mo concentrations compared to the ones introduced during synthesis. For instance, TiNT(3%-Mo) should theoretically present a weight percentage around 3%, yet only 0.36%_{wt} of Mo are quantified on analyzed samples. Herein, a considerable gap between introduced amount of Mo and the final weight percentage of Mo is to be noticed. This difference could be related to the formation of molybdenum salt Na₂MoO₄ solubilized in the aqueous phase during synthesis which is eventually evacuated by several washing step with HCl.

After sulfidation at 350°C, we observe a high S/Mo ratio superior to 2, indicating that the sulfidation rate is overly sufficient to form MoS₂.

Table 7: Weight percentages of Na, Ti, S and Mo measured by ICP-MS analysis of sulfide and non-sulfided TiNT and TiNT(x-Mo) and the determined S/Mo ratio.

| Sample | %wt Na | %wt Ti | %wt S | %wt Mo | Atomic ratio S/Mo |
|---------------------------------------|---------------|---------------|--------------|---------------|--------------------------|
| <i>TiNT</i> | 8.15 | 42.34 | - | - | - |
| <i>S-TiNT-350°C</i> | 5.91 | 32.04 | 2.10 | - | - |
| <i>TiNT(9%-Mo)</i> | 0.53 | 43.42 | - | 4.33 | - |
| <i>TiNT(6%-Mo)</i> | 0.37 | 46.15 | - | 1.43 | - |
| <i>TiNT(3%-Mo)</i> | 3.96 | 43.08 | - | 0.36 | - |
| <i>TiNT(9%-MoS₂)-350°C</i> | 2.85 | 49.31 | 5.64 | 4.40 | 3.80 |
| <i>TiNT(9%-MoS₂)-335°C</i> | 2.66 | 47.06 | 5.61 | 4.19 | 3.97 |
| <i>TiNT(3%-MoS₂)-350°C</i> | 3.32 | 51.31 | 3.72 | 1.23 | 8.98 |

4.2. IR/CO analysis of TiNT(3%; 6%; 9%-MoS₂)

- Effect on M-edges sites and their respective sulfur coverage

IR/CO spectra of TiNT(3% and 6%-MoS₂) show similar spectra while on the one of TiNT(9%-MoS₂) $\nu(\text{CO}/\text{M-edge})$ was not observed. Only CO adsorbed on Lewis acid sites and in interaction with Ti-OH were detected (Figure 13).

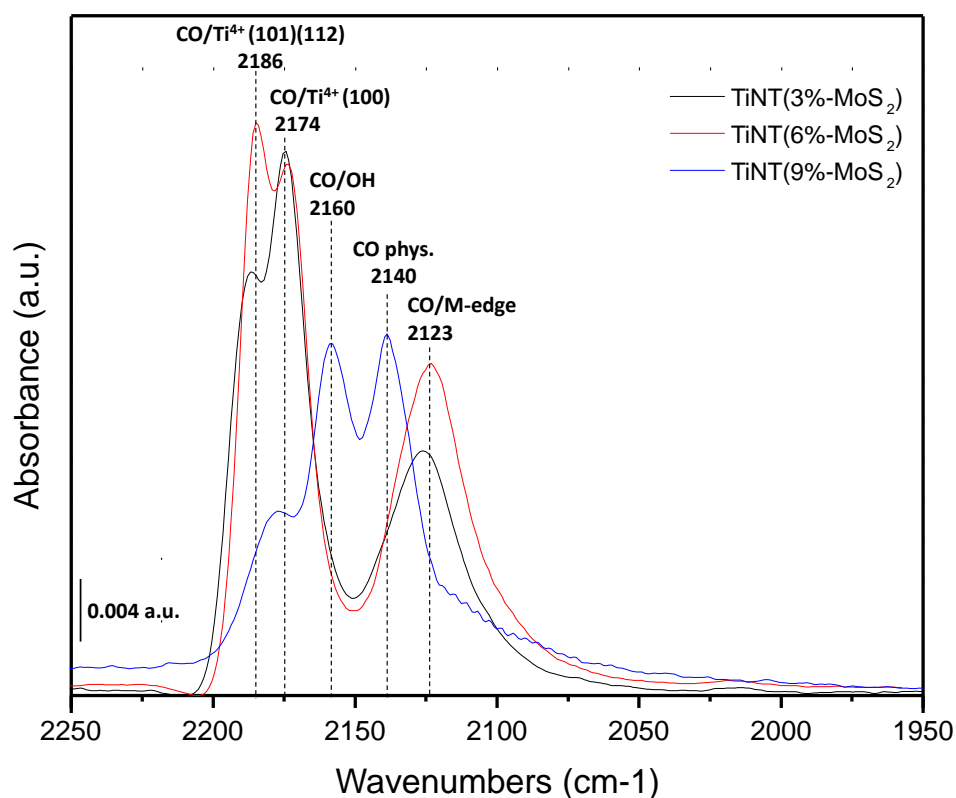


Figure 13: Comparison of obtained TiNT(x-MoS₂) IR/CO spectra at 1 Torr equilibrium pressure.

Compared to 3-MoS₂/TiNT exposing only (001) facets visible at 2165 cm⁻¹, TiNT(x-MoS₂) have (101)(112) and (100) exposed facets. Their respective characteristic absorption bands are observed at 2189 and 2174 cm⁻¹ respectively.¹¹ This means either Mo was preferentially incorporated into the walls on (001) facets or nanotubes with exposed (101) (112) and (100) facets were formed.

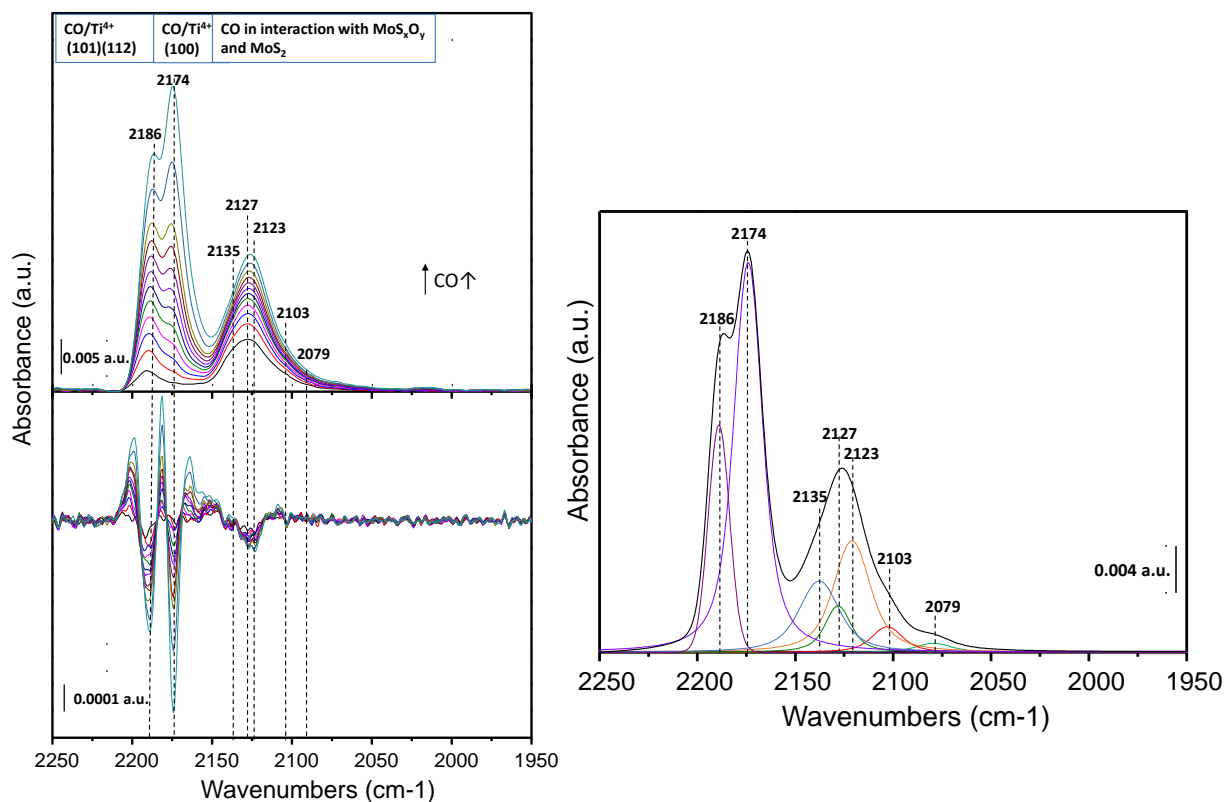


Figure 14: IR/CO spectra up to saturation at 1 Torr of TiNT(3%-MoS₂) with its second derivative and deconvolution spectrum.

On the IR/CO spectrum of TiNT(3%-MoS₂), in the region 2150–2070 cm⁻¹, a large band rises up with increasing CO concentration. With help of deconvolution and tracing the second derivative of the obtained spectra four different bands can be distinguished (Figure 14). First one at 2135 cm⁻¹ corresponding to molybdenum sulfur oxides (MoS_xO_y). The second one with a shoulder is corresponding to two different M-edge sites having different charge densities. They are observed at 2127 and 2123 cm⁻¹. The third band is located at 2103 cm⁻¹ and can be ascribed to $\nu(\text{CO}/\text{M-edge})$ with lower sulfur coverage leading to a more pronounced backdonation from Mo to CO.

At 2079 cm⁻¹ a very small band was detected. This band can either be a low sulfur covered M-edge site or a M-edge site promoted by titanium. However due to the co-presence of the CO-adsorption band at 2103 cm⁻¹ another interpretation can be proposed. Based on DFT calculations of T. Zeng et al. the absorption bands at 2079 and 2103 cm⁻¹ can be ascribed respectively to symmetric and asymmetric coupled stretching vibrations of adsorbed CO on corners of triangular MoS₂ slabs as presented in Figure 15.²⁸ Hence, the insertion of Mo

precursor into the nanotube wall followed by sulfidation might have favored the creation of sulfur vacancies on MoS₂ corners.

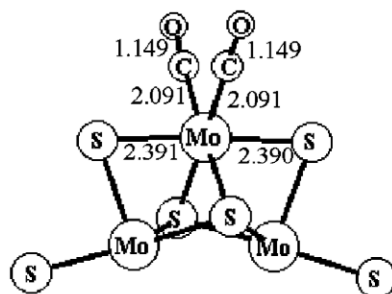


Figure 15: Representation of CO adsorption mode on MoS₂ corner.²⁸

Quantitative analysis points out a very low concentration of M-edge sites when Mo is incorporated into TiNT framework. With 5-6 $\mu\text{mol/g}$ it is evident that TiNT(3%; 6%-MoS₂) do not present MoS₂ abundantly. There are 14-times less M-edge sites compared to MoS₂/TiO₂ and 5-times less compared to 3-MoS₂/TiNT (Table 8).

Table 8: Overview of samples characteristics (MoS₂/TiO₂, 3-MoS₂/TiNT and TiNT(3% and 6%-MoS₂) in terms of Mo dispersion and density, S/Mo ratio, concentration of M-edges determined by IR/CO as well as the amount of Mo and S based on ICP-MS results.

| Sample | atoms of Mo per nm ² | %wt Mo | %wt S | M-edge sites($\mu\text{mol/g}$) | Estimated dispersion of Mo | Atomic ratio S/Mo |
|---|---------------------------------|--------|-------|-----------------------------------|----------------------------|-------------------|
| TiNT(6%-MoS ₂)-350°C | 0.3 | 1.43 | 3.90 | 6 | 0.04 | 8.09 |
| TiNT(3%-MoS ₂)-350°C | 0.2 | 1.23 | 3.72 | 5 | 0.04 | 8.98 |
| MoS ₂ /TiNT-350°C | 3.0 | 11.27 | 4.58 | 29 | 0.07 | 0.72 |
| MoS ₂ /TiO ₂ -400°C | 3.0 | 5.82 | 6.64 | 84 | 0.15 | 2.32 |

It is obvious that the difference in M-edge sites concentration is primarily related to Mo-loading which is also affecting the density of Mo on TiNT(x-MoS₂). However, there are additional reasons for this low probed concentration.

Indeed we note a smaller dispersion of Mo on TiNT(3%, 6%-MoS₂)-350°C compared to incipient impregnated samples. Subsequently, larger MoS₂ slabs can be expected on TiNT(x-MoS₂) compared to MoS₂/TiO₂-400°C. We also observe a S/Mo ratio above 2 for TiNT(3%; 6%-MoS₂)-350°C. Hence there is enough sulfur to form MoS₂ but also other molybdenum sulfide species such as MoO_xS_y, which is detected at 2135 cm⁻¹ on IR/CO spectra. Herein the formation of other molybdenum-sulfide species could explain the low concentration of M-edge sites. Besides, one cannot exclude the insertion of Mo into TiO₂ framework which is not participating in the formation of MoS₂ slabs. It should be noted that the determined S/Mo ratio is overestimated since the amount of sulfided TiO₂ cannot be subtracted. Subsequently, it might be possible, that the estimated Mo dispersion is not reflecting the reality as in the case of MoS₂/TiNT-350°C.

- *Effect of sulfidation temperature on TiNT(9%-MoS₂)*

The absence of MoS₂ on TiNT(9%-MoS₂) is questionable. The most plausible reason would be the destruction of nanotubes during sulfidation at 350°C due to high Mo-precursor loading. On SEM images (Figure 16) of TiNT(9%-MoS₂)-335°C thin entangled nanotubes are visible whereas at higher sulfidation temperatures we find agglomerated particles.

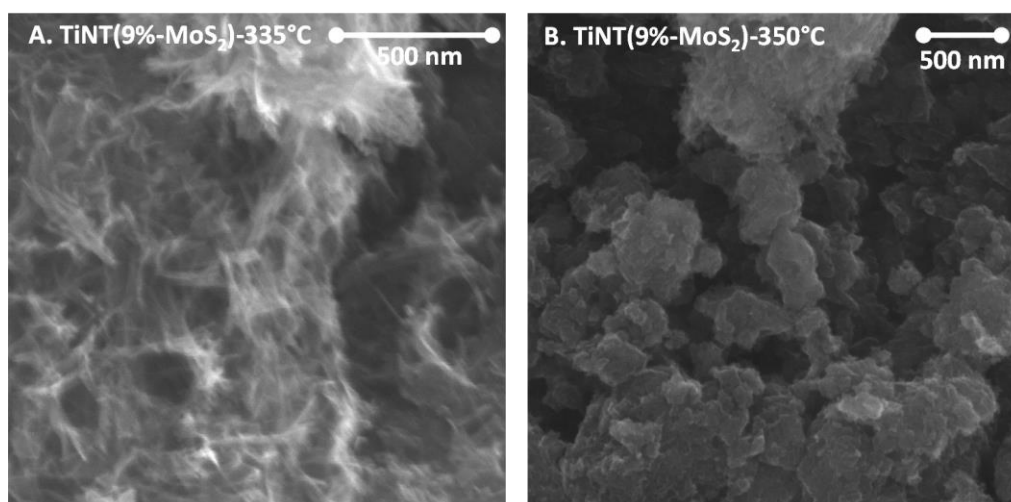


Figure 16: SEM images of TiNT(9%-MoS₂) sulfided at 335°C (A.) and 350°C (B.).

Hence this observation is tending towards our hypothesis. To verify it, IR/CO spectra were taken after sulfiding the catalyst at lower temperatures (i.e. 335°C, 320°C and 300°C).

At the lowest sulfidation temperature of 300°C, $\nu(\text{CO}/\text{M-edge})$ reappeared around 2123 cm⁻¹ testifying the presence of MoS₂ (Figure 17). With increasing sulfidation temperature, $\nu(\text{CO}/\text{M-edge})$ becomes more intense and reaches its maximum at 335°C.

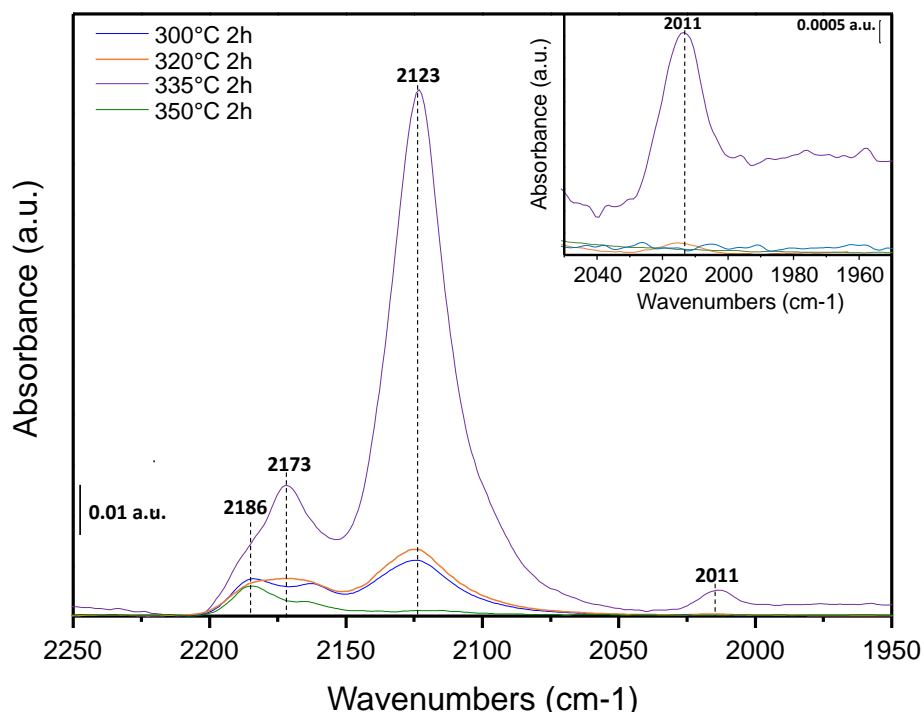


Figure 17: Comparison of TiNT(9%-MoS₂) IR/CO spectra close to CO saturation at different sulfidation temperatures.

33 $\mu\text{mol/g}$ of M-edge sites were probed via CO which is slightly higher than the detected concentration of M-edge sites on 3-MoS₂/TiNT. Furthermore, both catalysts have equal Mo dispersion indicating similar MoS₂ slab sizes (Table 9). Herein, these results confirm the low stability of TiNT when Mo is introduced in high amounts.

Table 9: Comparison between TiNT(9%-MoS₂) sulfided at 335°C and 350°C and MoS₂/TiNT-350°C based on Mo dispersion, density, M-edge sites and S/Mo ratio.

| Sample | Atoms of Mo per nm² | %wt Mo | %wt S | M-edge sites (μmol/g) | Estimated Mo dispersion | Atomic ratio S/Mo |
|----------------------------------|---------------------------------------|---------------|--------------|------------------------------|--------------------------------|--------------------------|
| TiNT(9%-MoS ₂)-335°C | 0.7 | 4.40 | 5.61 | 33 | 0.07 | 3.97 |
| TiNT(9%-MoS ₂)-350°C | 0.7 | 4.19 | 5.64 | 0 | 0 | 3.80 |
| MoS ₂ /TiNT-350°C | 3 | 11.27 | 4.58 | 29 | 0.07 | 0.72 |

On IR/CO spectra of TiNT(9%-MoS₂)-335°C, a new band with small intensity at 2011 cm⁻¹ is detected from 320°C up to 335°C and is rising with intensity.

Until now, such a downshifted band around 2011 cm⁻¹ has not been reported in the literature. By comparing this wavenumber with DFT calculations of CO adsorption on MoS₂, this band is located in the range between CO/Mo⁽⁰⁾ and S-edge sites with a sulfur coverage of 75% (Table 10).²⁹

Table 10: Experimental and theoretical CO stretching vibration assignments for non-promoted MoS₂.²⁹

| v(CO) band Experimental (cm⁻¹) | v(CO) band calculated by DFT (cm⁻¹) | Band assignment |
|--|---|----------------------------------|
| 2130 | - | Partially sulfide |
| 2110 | 2110 | M-edge (50% sulfur coverage) |
| 2098 | 2087 | M-edge (37.5% sulfur coverage) |
| 2065 | 2078 | S-edge (100% sulfur coverage) |
| 2040 | - | S-edge (75-100% sulfur coverage) |
| 2020 | 1989 | S-edge (75% sulfur coverage) |
| 1995 | - | Metallic Mo |

Based on those assignments it is highly probable that the band at 2011 cm^{-1} corresponds to CO/1T-MoS₂. Indeed, 1T-MoS₂ is metallic and consequently CO/1T-MoS₂ should theoretically appear near CO/Mo⁽⁰⁾. Moreover the temperature range in which the band at 2011 cm^{-1} is visible, was reported to be in the stability zone of 1T-MoS₂.³⁰

4.3. Raman analysis of (3%; 6%; 9%)

- Analysis of activated samples at 350°C

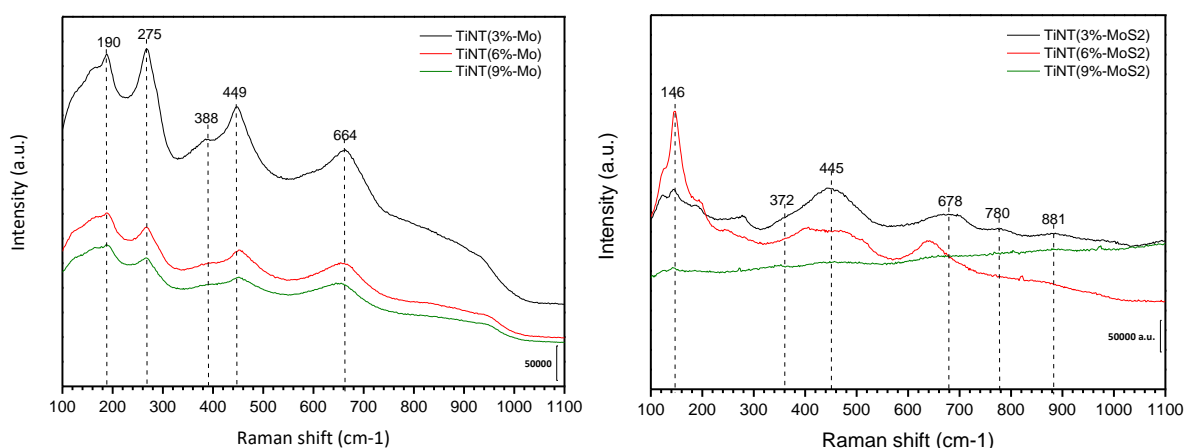


Figure 18: Raman spectra of dried TiNT(x -Mo) and TiNT(x -MoS₂). On the left: Dried TiNT(x -Mo). On the right: TiNT(x -MoS₂) sulfidated at 350°C .

Raman spectra of dried TiNT(x -Mo) show a large, weak band between $800\text{--}980\text{ cm}^{-1}$ (Figure 18). In this zone Raman vibrations related to Mo-O bonds of Mo-precursor are to be found.^{31,32} The weak and broaden band is due to the insertion of Mo-precursor into TiNT walls. Consequently, Mo was successfully embedded.

After sulfidation at 350°C , the typical discernable bands of 2H-MoS₂ (E_{2g} and A_{1g}) at 380 and 407 cm^{-1} are not detected (Figure 18).¹⁵ It seems they are included in the broad band between 300 and 500 cm^{-1} . In this observed overlapping band region, the characteristic vibration of $\nu(\text{MoS}_4^{2-})$ is also included. It was reported to be around 456 cm^{-1} .²³ With higher Mo concentration the band in between $300\text{--}500\text{ cm}^{-1}$ is becoming broader. When the concentration of Mo equals 9%, vibration bands of MoS₂ are absent. Only weak contributions

of the support are visible at 146 cm^{-1} . Thus, it demonstrates the feeble stability of TiNT at higher Mo-loading favoring their destruction at 350°C .

For TiNT(3%- MoS_2) additionally to the described vibration bands, weak vibration bands at 780 and 881 cm^{-1} are to be noticed. They can be attributed to the vibrations between Mo-O and Mo-S in Na_2MoO_4 and Na_2MoS_4 .^{23,33}

- Analysis of TiNT(9%- MoS_2) activated 300-350°C

Several Raman spectra were taken on different sample zones of TiNT(9%- MoS_2) sulfided at 335°C . Different spectra were observed for each zone. The characteristic peaks of the acoustic phonon modes J_2 (229 cm^{-1}) and J_3 (330 cm^{-1}) belonging to 1T- MoS_2 were detected (Figure 19). The formation of this metallic phase is also confirmed by the absence of in-plane vibration E_{2g} which is only detectable in the case of 2H- MoS_2 . Yet the band at 412 cm^{-1} corresponding to A_{1g} of 1T- MoS_2 is as well missing.¹⁵ It could be that the out-of-plane vibrations are restricted as already assumed for impregnated MoS_2/TiNT catalysts in 3.1.3.

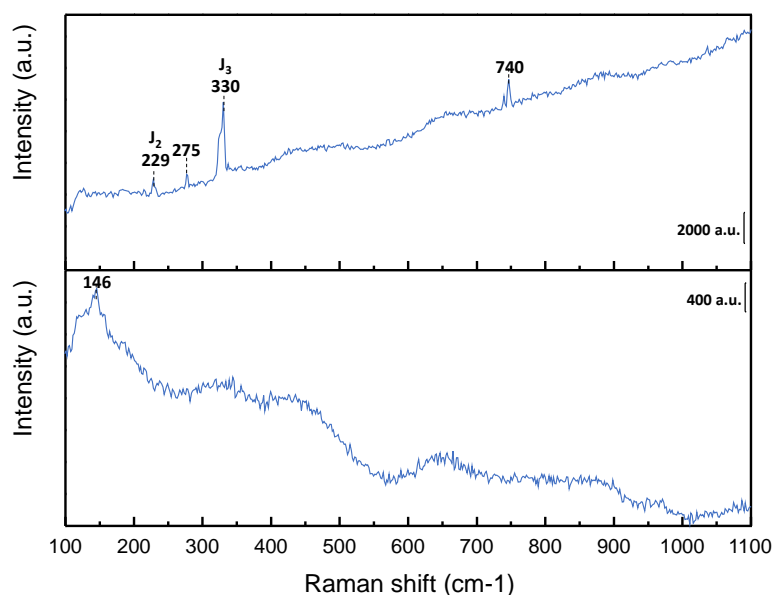


Figure 19: Raman spectrum of TiNT(9%- MoS_2) sulfided at 335°C on different sample zones.

On other zones, we can observe slight contributions of $\nu(\text{Mo-S})$ belonging either to MoS_4^{2-} and/or 2H- MoS_2 .³⁴ However the strong noise to signal ratio and the effect of fluorescence does not allow to make any clear conclusion. Consequently, based on this analysis, it seems

highly possible that 1T-MoS₂ was formed on TiNT(9%-MoS₂)-335°C. In order to validate the presence of 1T-MoS₂ other characterization tools need to be implemented as for instance XPS.

4.4. XPS- analysis of TiNT(9%-MoS₂) sulfided at 335°C

In regard to the obtained Raman and IR/CO results, to avoid speculation about the attribution of the band around 2011 cm⁻¹, XPS of TiNT(9%-MoS₂)-335°C was conducted to confirm or not the formation of 1T-phase.

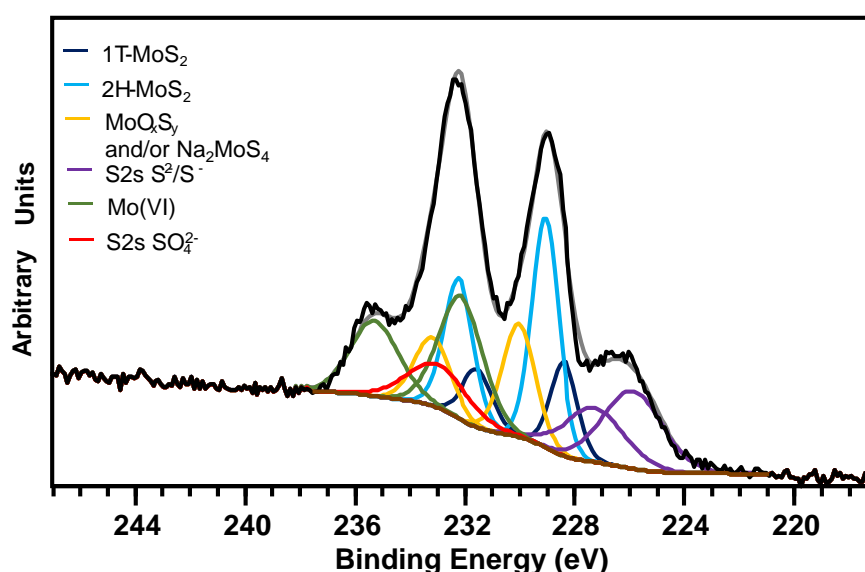


Figure 20: XPS spectrum of TiNT(9%-MoS₂) sulfided at 335°C.

On XPS spectrum of TiNT(9%-MoS₂)-335°C, both 2H and 1T-MoS₂ are detected (Figure 20). 2H-MoS₂ are characterized by Mo⁴⁺ 3d_{3/2} and 3d_{5/2} having binding energies of 232.2 eV and 229.1 eV respectively.²³ 1T-MoS₂ is reported to have lower binding energies which are approximately around 231.7eV and 228.1eV.^{35;36} After decomposition, their bands are found at 231.5 eV and 228.4 eV close to the reported values. The peak at 225.9 eV is attributed to S²⁻ 2s whereas its neighboring peak was reported to be S⁻ 2s. Sulfates were also detected around 233.0 eV. Furthermore, different molybdenum oxide species are detected. Indeed, at 235.29 eV and 232.1 eV Mo(VI) is detected which is often ascribed to MoO₃. However, Raman spectrum of TiNT(9%-MoS₂)-335°C does not present a strong band at 995-1000 cm⁻¹ corresponding to Molybdenum oxide. Thus, the observed binding energies might correspond

to Mo(VI) in a strong oxidative environment. At last, two peaks around 233.2 eV and 230.0 eV can be ascribed either to Na₂MoS₄ and/or MoO_xS_y. Accordingly, molybdenum oxysulfide species were detected by IR/CO ($\sim 2133 \text{ cm}^{-1}$). Yet, Na₂MoS₄ presence could not be confirmed by Raman. However, the intense peak of Na 1s at 1071 eV also confirmed by ICP-MS suggests the potential formation of Na₂MoS₄. Indeed, it is highly probable that Na⁺ interacted with molybdate precursor via NH₄⁺ exchange forming sodium molybdate which was subsequently during sulfidation transformed into Na₂MoS₄. Hence, the observed binding energies at 233.2 eV and 230.0 eV are probably a mix of both components. Herein via XPS deconvolution, the overall percentage of each component can be determined. TiNT(9%-MoS₂)-335°C has 15% 1T- and 34% 2H-MoS₂; 20% Na₂MoS₄ and/or Mo(V) and 31% Mo(VI). Subsequently a mixture of 1T and 2H phases with a ratio of 1: 2.5 respectively is confirmed.

4.5. TEM analysis of TiNT(9%-MoS₂)-335°C

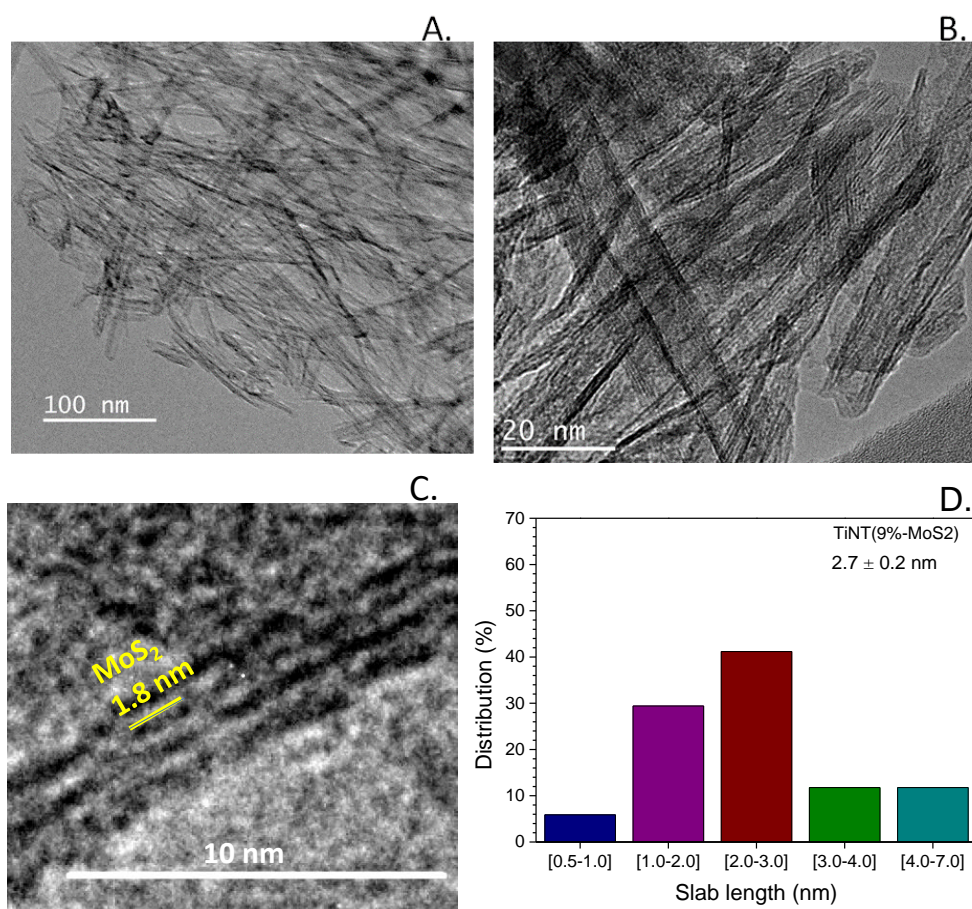


Figure 21: A, B, C. TEM images of TiNT(9%-MoS₂)-335°C with different resolutions. D. Distribution of MoS₂ slab length on TiNT(9%-MoS₂)-335°C.

Imbedding Mo into TiNT-framework did not prevent the formation of MoS₂ after sulfidation. Yet the location of MoS₂ was questionable. Is MoS₂ formed in the nanotube or on the nanotube? And how large are the formed slabs? Hence, TEM analysis was performed.

In Figure 21A and B, we confirm via TEM the presence of nanotubes on which MoS₂ slabs are spread with an average length of 2.7 ± 0.2 nm. Exactly as for MoS₂/TiNT-350°C, slabs are perpendicular to the tube and aligned to each other. However, it cannot be elucidated whether slabs are integrated into the wall or covering the wall. We also note that the distribution in slab length is broader compared to MoS₂/TiNT-350°C.

4.6. HDS-test of TiNT (3%; 6%; 9%-MoS₂)

After sulfidation at 350°C of TiNT(x-Mo), thiophene tests of TiNT(x-MoS₂) show a decrease in HDS-activity when Mo-loading is increasing (Table 11). TiNT(3%-MoS₂)-350°C is more active than TiNT(6%-MoS₂)-350°C whereas TiNT(9%-MoS₂)-350°C is almost inactive. It should be emphasized that TiNT(3%-MoS₂) presents a higher HDS rate than 3-MoS₂/TiNT while containing much smaller Mo weight percentages. Consequently, by calculating the activity depending on the number of probed active sites, active sites of TiNT(3%-MoS₂)-350°C are much more active than the ones on impregnated TiNT.

Table 11: HDS activity rates of TiNT(3%; 6%; 9%-MoS₂) in comparison to 3-MoS₂/TiNT and MoS₂/TiO₂. In (*) HDS test was performed at 335°C for TiNT(9%-MoS₂)-335°C and MoS₂/TiO₂ in order to preserve the stability of the catalyst.

| Sample | Activity rate (mol/h.kg) | Activity rate per active site (h⁻¹) |
|--|-------------------------------------|---|
| MoS ₂ /TiO ₂ -400°C | 6.27 | 75 |
| 3-MoS ₂ /TiNT-350°C | 6.95 | 240 |
| TiNT(3%-MoS ₂)-350°C | 8.18 | 1636 |
| TiNT(6%-MoS ₂)-350°C | 3.41 | 568 |
| TiNT(9%-MoS ₂)-350°C | 0.69 | Indeterminable |
| S-TiNT-350°C | 0 | 0 |
| *TiNT(9%-MoS ₂)-335°C | 1.32 | 40 |
| *MoS ₂ /TiO ₂ -400°C | 4.23 | 50 |

In order to investigate the intrinsic activity of TiNT(9%-MoS₂)-335°C, HDS activity test was performed at 335°C to preserve its stability and avoid its agglomeration. Compared to the activity test performed at 350°C, a higher activity is observed at 335°C. Hence, active sites are accessible. However, its activity as well as intrinsic activity are inferior to the ones of MoS₂/TiO₂ tested at 335°C.

4.7. Conclusion about embedded Mo catalyst TiNT(x-MoS₂)

In this work, Mo was incorporated successfully into TiNT without destroying its cylindrical structure as DRX analysis show due to the observed slight shifts of diffraction peaks. Using this strategy allowed to overcome the obstruction phenomenon of nanotubes observed when incipient impregnation was applied. However, Mo-loading are limited to 0.74 Mo/nm² due to the instability of the material leading to small edge site concentration.

Depending on sulfidation temperature and Mo-loading MoS₂ phase nature can be modified (Figure 22). Indeed, at 350°C when Mo-loading is below 0.74 Mo/nm², the formation of 2H-MoS₂ was favored. Also, IR/CO of TiNT(3%, 6%-MoS₂)-350°C provided evidence of the formation of MoS₂ presenting only M-edge sites with different sulfur coverages.

At lower sulfidation temperature of 335°C and at a Mo-loading of 0.74 Mo/nm², a mixt 1T/2H-MoS₂ phase was formed as validated by XPS. In addition, the presence of 1T-MoS₂ seems to be also confirmed by the presence of CO absorption band at 2011 cm⁻¹. A pronounced downward shift of 100 cm⁻¹ compared to $\nu(\text{CO}/\text{M-edge})$ of 2H-MoS₂ is observed which is close to CO/Mo⁽⁰⁾. However, this attribution needs be validated by DFT calculation concerning CO adsorption on 1T-MoS₂. Also, we cannot certainly confirm whether the observed band is due to the adsorption of CO on 1T-MoS₂ basal plane or on its distorted form 1T'. Although its basal plane was reported to be active and being capable of adsorbing protons, it is not evident if it is possible for CO.³⁷ D.B Putungan et al. have reported about one specific adsorption site of atomic carbon on 1T'-MoS₂ basal plane via DFT calculations.³⁸ Hypothetically the adsorption of CO should be than possible. Yet, the observed band could as well be related to the adsorption of CO on 1T-edge sites.

TEM analysis allowed to determine an average MoS₂ slab size of 2.7 ± 0.2 nm without using any chelating agents. However, although TiNT(9%-MoS₂) presents of 1T phase and small MoS₂ slabs leading to higher surface contact with reactants, a significant impact on HDS rates was not noticed. MoS₂/TiO₂-400°C is still more active than TiNT(9%-MoS₂) probably because of its higher amount in M-edges.

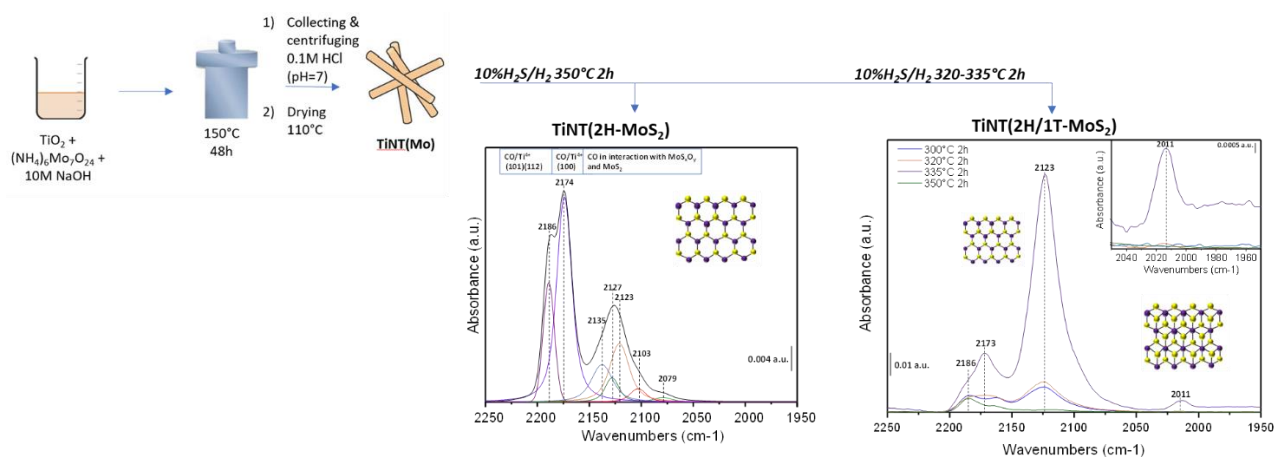


Figure 22: Overview of the synthesis method to obtain TiNT(1T-/2H-MoS₂) or TiNT(2H-MoS₂) depending on activation conditions.

5. Impregnation of molybdenum on TiO₂ nanowires (TiNW)

5.1. Fundamental characterization (X-ray; BET and ICP analysis)

TiNW were successfully synthesized as X-ray analysis demonstrates.⁹ XRD patterns of TiNT and TiNW are similar except that synthesized TiNW presents an additional peak at 43° corresponding to (003) facet (Figure 23). Moreover a TiO₂-bronze phase as in the case of TiNT at 48° and 60° was detected.³⁹

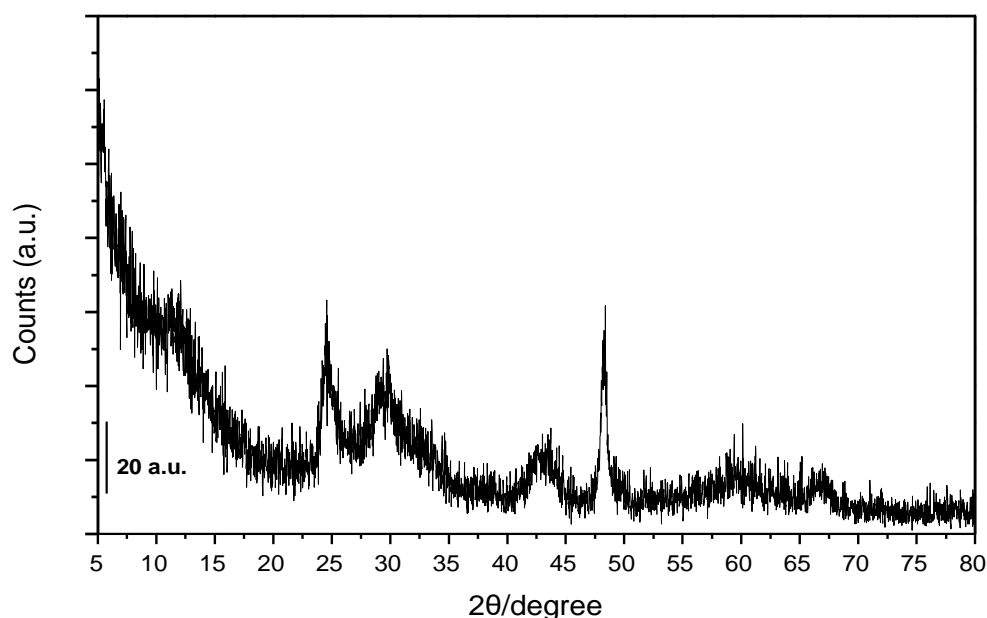


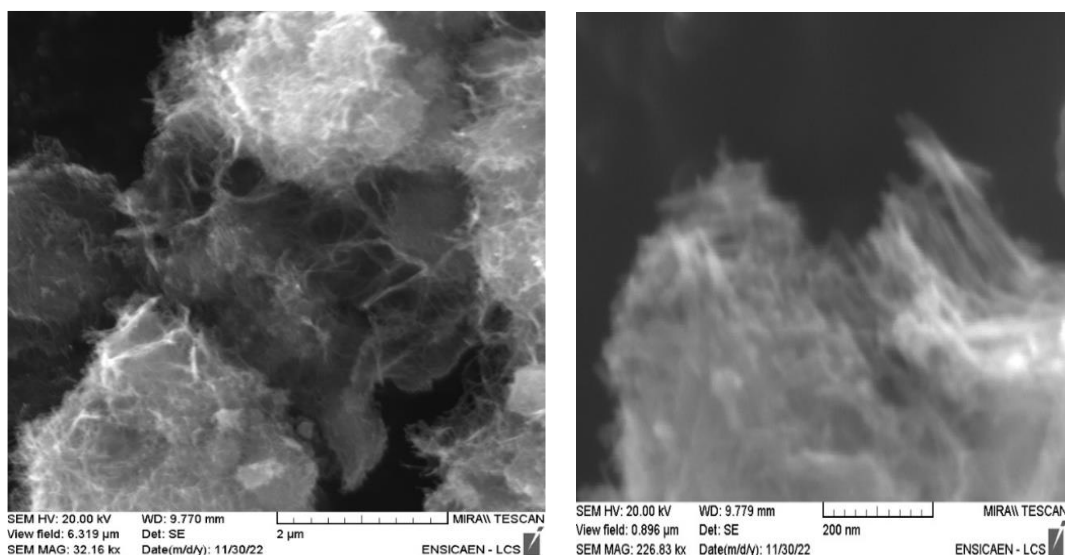
Figure 23: X-ray diffraction pattern of TiNW.

TiO₂ nanowires are characterized by a large BET surface of 332 m²/g and a pore volume of 0.714 cm³/g (Table 12). After impregnation and sulfidation we observe similar pore diameters and a slight decrease in BET surface and pore volumes which is caused by the impregnation of Mo into TiNW pores.

Table 12: BET results of TiNW and MoS₂/TiNW sulfided at 400°C.

| Sample | S_{BET} (m²/g) | Pore volume (cm³/g) | Pore diam with highest frequency (nm) | average pore diam. (nm) |
|------------------------------|--|---|--|------------------------------------|
| TiNW | 332 | 0.714 | 7.6 | 8.6 |
| MoS ₂ /TiNW-400°C | 288 | 0.668 | 7.5 | 9.3 |

On TiNW SEM images thin, entangled nanofibers are visible even after sulfidation at 350°C (Figure 24). The average diameter of these fibers is approximately 7 nm.

**Figure 24: SEM images of TiNW sulfided at 350°C.**

ICP-MS analysis allowed to quantify a non-neglectable weight percentage of 4%_{wt} potassium (Table 13). After impregnation and sulfidation, a S/Mo ratio above 2 was determined. Herein, the sulfidation rate was sufficient to form MoS₂.

Table 13: ICP-MS results of TiNW and MoS₂/TiNW-400°C.

| Sample | %wt K | %wt Ti | %wt S | %wt Mo | Atomic ratio S/Mo |
|------------------------------|--------------|---------------|--------------|---------------|--------------------------|
| TiNW | 4.14 | 52.02 | - | - | - |
| MoS ₂ /TiNW-400°C | 3.64 | 42.04 | 12.61 | 12.88 | 2.31 |

5.2. IR/CO analysis of MoS₂ (3 Mo atoms/nm²)/TiNW

By comparing the IR/CO spectra of TiNW, TiNT and TiO₂ we observe strong decrease of available Ti⁴⁺ adsorption sites for TiNW (Figure 25). Hence, it can be deduced that TiNW possess less Lewis acid sites in comparison to TiNT and TiO₂. Moreover, we observe only $\nu(\text{CO}/\text{Ti}^{4+}(100))$ at 2176 cm⁻¹, indicating that TiNW with exposed (100) facets was synthesized in the presence of KOH.

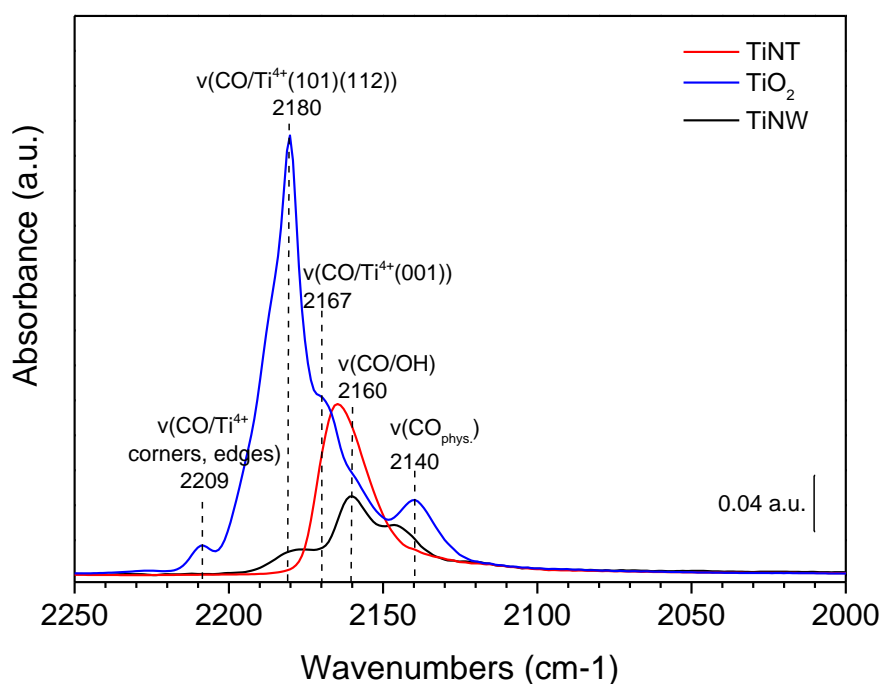


Figure 25 : Comparison of IR/CO spectra of TiNW, TiNT and TiO₂ at 1 Torr CO equilibrium pressure normalized to same initial specific surface.

On IR/CO spectra of MoS₂/TiNW three main regions are distinguished: CO in interaction with Lewis acid sites; CO in interaction with Ti-OH and MoS₂ (Figure 26).

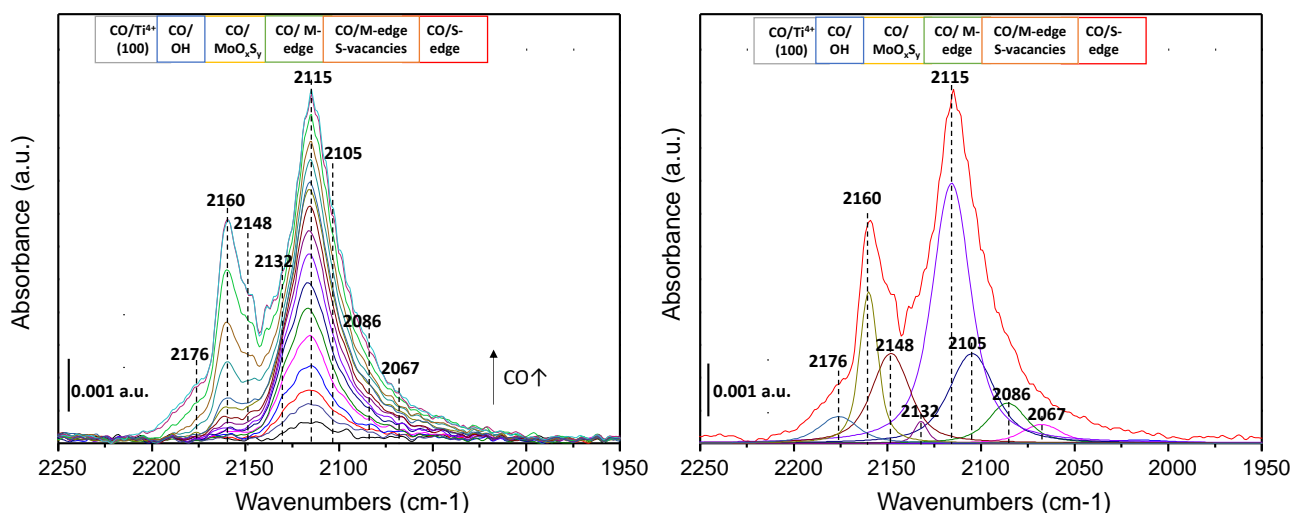


Figure 26: On the left, IR/CO spectra of MoS₂/TiNW sulfided at 350°C up to CO saturation. On the right, deconvolution of MoS₂/TiNW at saturation.

At 2176 cm⁻¹ $\nu(\text{CO}/\text{Ti}^{4+} (100))$ is detected as on the IR/CO spectrum of TiNW. Its intensity is low and allows to conclude that (100) is partially covered with MoS₂. In regards of the interaction between CO and MoS₂, two different bands can be discerned. At 2115 cm⁻¹ $\nu(\text{CO}/\text{M-edge})$ is detected which was downshifted by 3 cm⁻¹ compared to MoS₂/TiO₂. Subsequently the backdonation from Mo to CO is more pronounced and demonstrates higher electron density comparable to 3-MoS₂/TiNT. Thus, it can be concluded that the morphology change into nanowires also improves electron transfer which also enriches the metallic character of molybdenum.

The change in morphology allowed to create many sulfur vacancies on M-edge sites. Indeed, M-edges of MoS₂/TiNW are characterized by different sulfur coverages attributed to the bands at 2105 cm⁻¹ (S-coverage of 37.5%) and 2086 cm⁻¹ (S-coverage < 37.5%).^{12,40} Moreover at 2067 cm⁻¹ $\nu(\text{CO}/\text{S-edge})$ was detected having low intensity.²⁴ Yet the concentration of MoS₂ is very poor. Only 2 $\mu\text{mol/g}$ of M-edge sites were quantified which explains the scrambled spectrum.

Herein, a further increase in the activation temperature to favor sulfidation was tried on MoS₂/TiNW in order to evaluate whether or not an increase in M-edge site concentration will occur. In Figure 27 results of CO small doses adsorption are shown after activating the catalyst at 400°C. Compared to MoS₂/TiNW-350°C, the intensity of $\nu(\text{CO}/\text{M-edge})$ is higher and no absorption band of $\nu(\text{CO}/\text{Ti}^{4+})$ was observed. Consequently, nanowire sites are completely

covered with MoS₂. However, the number of M-edge sites is still very small (3 μmol/g) and did not differ extremely from MoS₂/TiNW-350°C.

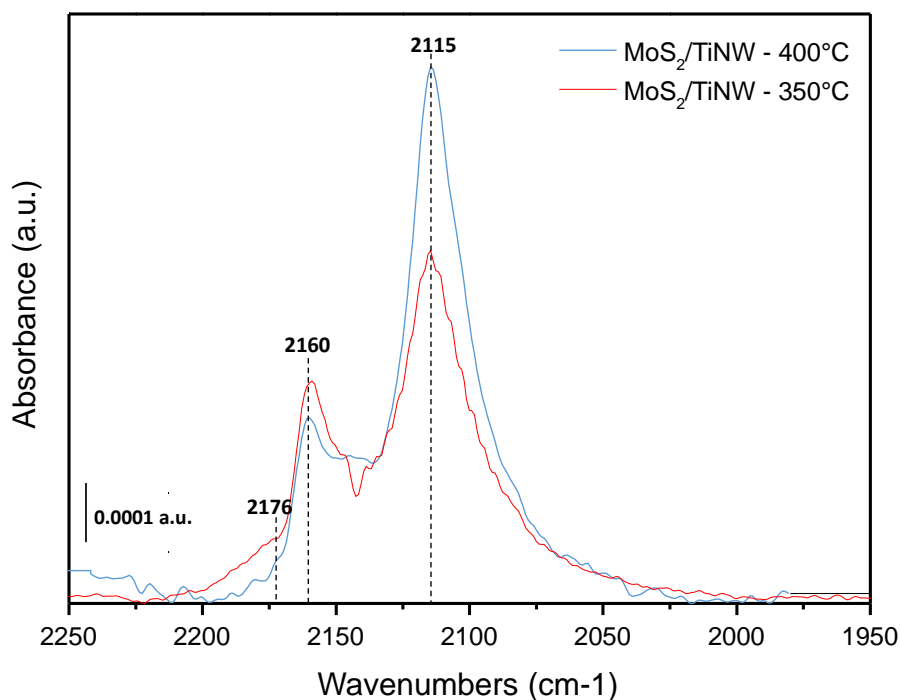


Figure 27: Comparison between IR/CO spectra of MoS₂/TiNW sulfided at 350°C and 400°C at 1 Torr equilibrium pressure of CO.

The low probed concentration could be related to an already reduced number of Ti⁴⁺ adsorption sites on TiNW compared to TiNT and TiO₂. Moreover, based on the calculated Mo dispersion which is 0.002 MoS₂ slabs seems to be very large (Table 14). This could be linked to strong Mo-TiNW interactions.

Table 14: Overview on determined S/Mo ratio, Mo dispersion and M-edge site concentration of MoS₂/TiNT-350°C, MoS₂/TiO₂-400°C, MoS₂/TiNW-400°C.

| Sample | %wt Mo | %wt S | M-edge sites (μmol/g) | Mo dispersion | Atomic ratio S/Mo |
|---|--------|-------|--------------------------|---------------|-------------------|
| MoS ₂ /TiO ₂ -400°C | 5.82 | 6.64 | 84 | 0.15 | 2.32 |
| MoS ₂ /TiNT-350°C | 11.27 | 4.58 | 29 | 0.07 | 0.72 |
| MoS ₂ /TiNW-400°C | 12.88 | 12.61 | 3 | 0.002 | 2.31 |

5.3. Raman analysis of MoS₂/TiNW before and after activation

On dried Mo/TiNW, Raman spectrum (Figure 28) shows the characteristic band of Mo-precursor at 957 cm⁻¹ corresponding to dodecamolybdate (Mo₁₂O₃₇²⁻).⁴¹

Though after sulfidation at 350°C not all of the molybdenum precursor was sulfided into MoS₂. The band at 957 cm⁻¹ remains still visible. At 380 cm⁻¹ and 407 cm⁻¹ the in- and out-of-plane vibrations of MoS₂ E_{2g} and A_{1g} are to be found, confirming the presence of 2H-MoS₂.¹⁵ The band at 352 cm⁻¹ should also be noted with the detection of two bands located at 152 and 224 cm⁻¹. The last two bands are usually ascribed to J₁ and J₂ of metastable polytype 1T-MoS₂. J₃ should be around 333 cm⁻¹, yet a large shoulder between 300 and 380 cm⁻¹ is observed making it impossible to conclude whether 1T was formed or not.

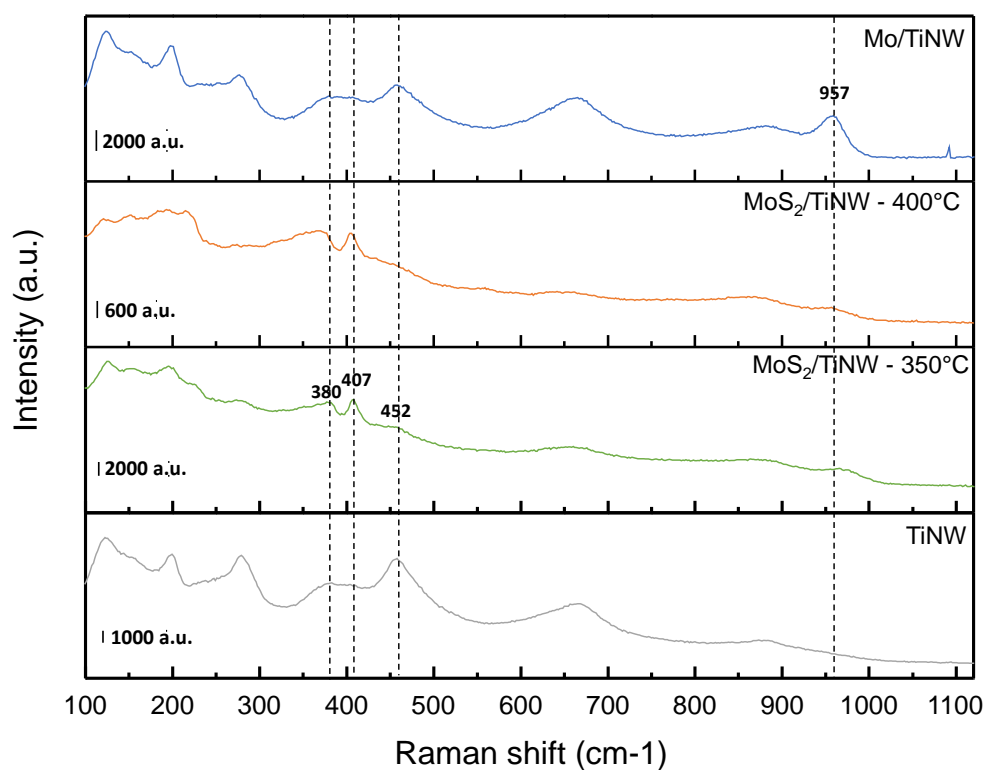


Figure 28: Raman spectra of TiNW, Mo/TiNW, MoS₂/TiNW activated at 350°C and 400°C.

The decrease in intensity of the vibration band at 452 cm⁻¹ corresponding to $\nu_{\text{sym}}(\text{Mo-S})$ of MoS₄²⁻ depending on sulfidation temperature should also be underlined. Even after sulfiding above 350°C the vibration band of MoS₄²⁻ is still visible at 452 cm⁻¹ even though its intensity decreased.

5.4. TEM analysis of MoS₂/TiNW-400°C

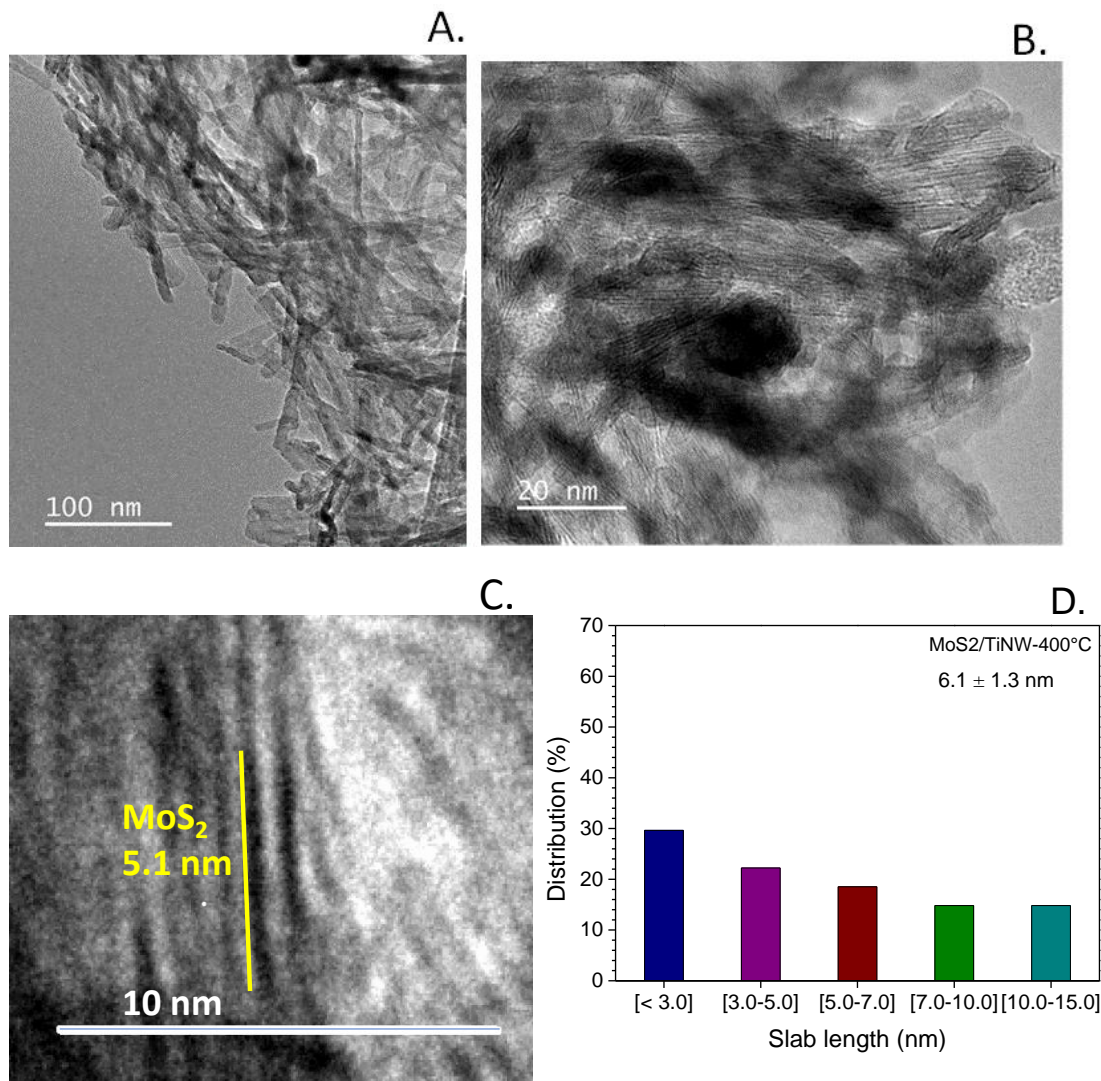


Figure 29: A, B, C. TEM images of MoS₂/TiNW-400°C in different resolutions. D. Distribution of MoS₂ slab length.

In Figure 29A and B TEM images of MoS₂/TiNW-400°C are presented. With a lower coverage of MoS₂ slabs, thin and entangled nanowires are observed with an average diameter of 6.4 ± 0.9 nm. MoS₂ slabs are large (6.1 ± 1.3 nm) but distributed in the same pattern as described previously for MoS₂/TiNT-350°C and TiNT(9%-MoS₂)-335°C. Between each MoS₂ slab an interspace of 0.5 ± 0.1 nm was measured. It should also be emphasized that the distribution of slab size is very broad. There are small slabs (i.e. below 3 nm) as well as very large slabs. Indeed, around 30% of the slabs presented a slab length in between 7 and 15 nm. This increase in slab size compared to the other analyzed samples with a nanotubular morphology, reflects

the strong existing interaction between MoS₂ and TiNW which seems to be more pronounced compared to TiNT but comparable to the one for bulk TiO₂.

5.5. HDS-test of MoS₂/TiNW

HDS-test of MoS₂/TiNW was performed. The obtained HDS rates and intrinsic activity are summarized in Table 15.

Table 15: Results of HDS test of thiophene obtained for MoS₂ supported on TiNW, TiNT and TiO₂.

| Sample | Activity rate (mol/h.kg) | Activity rate per active site (h⁻¹) |
|---|-------------------------------------|---|
| MoS ₂ /TiO ₂ -400°C | 6.27 | 75 |
| 3-MoS ₂ /TiNT-350°C | 6.95 | 240 |
| 3-MoS ₂ /TiNW-400°C | 5.13 | 1710 |

Although on MoS₂/TiNW only 3 μmol/g of M-edge sites were probed, HDS activity rates are comparable to the ones obtained for MoS₂ supported on bulk TiO₂ and TiNT. As a result, the intrinsic activity of MoS₂/TiNW is 7 times higher than MoS₂/TiNT and 22 times higher compared to MoS₂/TiO₂. This result is extremely surprising. One might have expected the contrary due to the very low Mo dispersion on MoS₂/TiNW. In contrast to MoS₂ supported on bulk TiO₂ and TiNT, MoS₂/TiNW has only exposed (100) facets which are covered with MoS₂. It might be possible that (100) TiO₂ anatase facets are influencing active sites located on M-edges inducing higher intrinsic activity.

5.6. Conclusion about MoS₂/TiNW

TiNW was easily synthesized by changing NaOH with KOH and allowed to obtain a carrier with high BET surface of 331 m²/g and thin nanowires with an average diameter of 6.4 ± 0.9 nm. M-edges are presents higher electronic densities than those of MoS₂/TiO₂ as IR/CO demonstrates ($\Delta\nu = 3 \text{ cm}^{-1}$) and the morphology of nanowires had a beneficial effect on

creating S-vacancies on M-edge sites. However, the concentration of M-edge sites is meager even when sulfidation temperature was increased to 400°C in order to sulfide the remaining Mo-precursor. The low concentration of MoS₂ is related to the formation of large MoS₂ slabs of 6.1 ± 1.3 nm as determined by TEM. Herein, the adhesion energy between Mo and TiO₂ seems to have been increased by a simple change in morphology limiting the concentration of M-edges and favoring the formation of large slabs. Nonetheless this low Mo dispersion is not impacting HDS activity. Instead comparable HDS activities to MoS₂ supported on bulk TiO₂ and TiNT were determined. Herein it is questionable whether the selective MoS₂ dispersion on TiO₂ anatase facets is generating higher activity rates or is it related to the creation of S-vacancies on M-edges.

6. Effect of morphology change on energy gap

By estimating the energy gap of TiNT, TiNW and TiO₂ before and after sulfidation with the help of UV-Vis spectroscopy, the effect of morphology change and S-doping can be investigated. Usually, the energy gap indicates whether a material is metallic, semiconductor or insulator. The lower the energy gap, the more electrons are easily transferred from the valance band to the conduction band and approaching the character of a conductor/metal.

In Figure 30 UV-Vis spectra of TiNT, TiNW and TiO₂ are traced. The maximum absorption is located in the UV-region at 318 nm for TiO₂ and is shifting downwards to 314 nm for TiNW and 298 nm for TiNT.

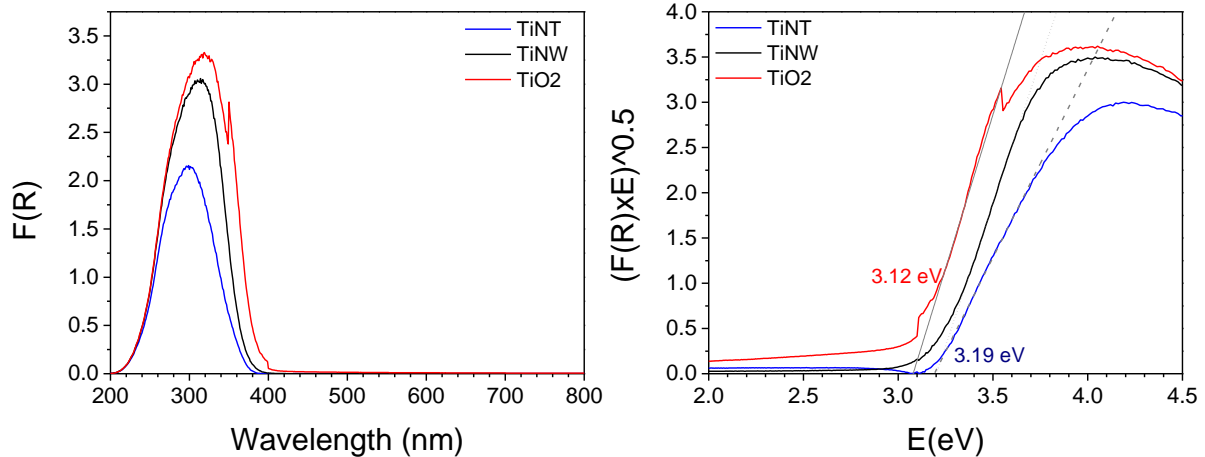


Figure 30: UV-Vis spectra and Tauc-plot tracing of TiNT, TiNW and TiO₂.

With the help of Tauc-plot the energy gaps of TiO₂, TiNT and TiNW were determined to be 3.12 eV and 3.19 eV respectively where TiNT and TiNW presented equal energy gaps. Herein we can deduce that the morphology change did not have a significant impact on the energy gap. Moreover, based on those estimations it seems that the conductivity was not improved either. However, when TiNT and TiNW are sulfided, a considerable change in energy gap was observed (Figure 31).

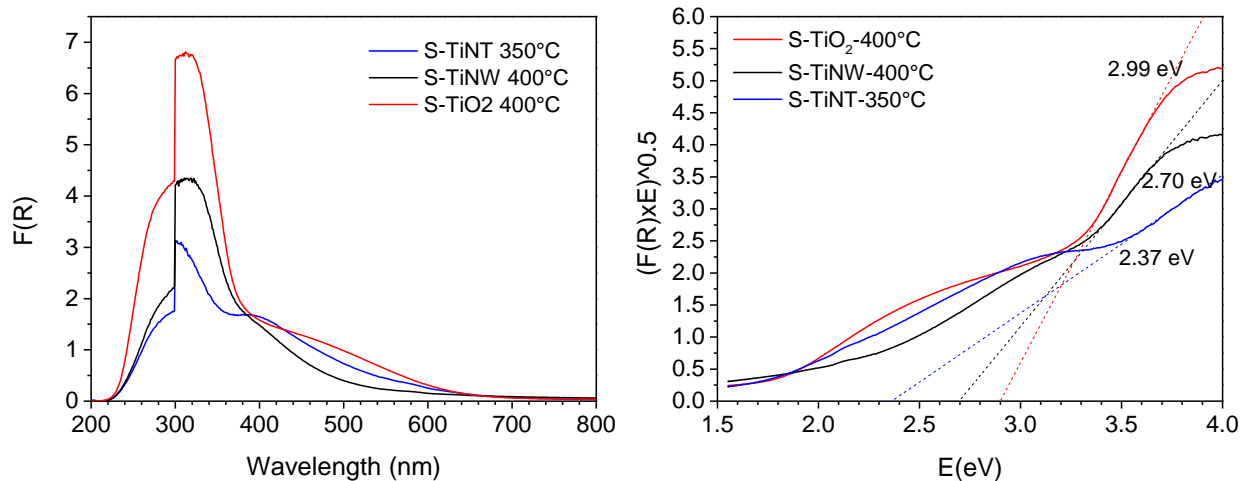


Figure 31: UV-Vis spectra and traced Tauc-plots of sulfided TiNT, TiNW and TiO₂. On the UV-Vis spectra the change of UV lamp during analysis is visible at 300 nm.

Indeed, the energy gaps of sulfided TiNW and TiNT (noted S-TiNT; S-TiNW) are considerably smaller than before sulfidation. The gap between valance band and conduction band has been narrowed by 15% and 25% for S-TiNW and S-TiNT respectively. Hence, S-doping which occurs during sulfidation via oxygen-sulfur exchange is favoring the decrease in E_g . Compared to S-

TiO₂ with $E_g = 2.99$ eV, S-TiNW presents an E_g of 2.70 eV whereas S-TiNT has an E_g of 2.37 eV. Herein, by combining morphology change and S-doping, S-TiNT is characterized with the smallest E_g followed by S-TiNW. Subsequently it can be expected that faster charge transfer will occur on S-TiNT compared to S-TiO₂.

It should be emphasized that the amount of introduced sulfur into the carriers during sulfidation is similar for TiO₂, TiNT and TiNW (around 2% based on ICP-MS) which is highlighting the combined effect of S-doping and morphology change.

7. HER activity test on MoS₂ dispersed on TiNT and TiNW

Based on IR/CO and Raman characterization results, four candidates for HER activity tests were chosen. The first one, MoS₂/TiNT activated at 350°C, due to molybdenum's enriched metallic character. Secondly, TiNT(9% and 3%-MoS₂) activated respectively at 335°C and 350°C because of the formation of 1T-MoS₂ and large amount of sulfur vacancies on M-edge sites respectively. At last MoS₂/TiNW activated at 400°C to compare the difference between nanowires and nanotubes. The main characteristics of each sample are summarized in Table 16.

Table 16: Overview on obtained IR/CO results of different samples for HER activity tests.

| Sample | M-edges sites ($\mu\text{mol/g}$) | CO/M-edge wavenumber (cm^{-1}) | S-coverage on M-edges with sulfur vacancies | Presence of 1T-MoS₂ | Synthesis method |
|--|---|---|--|---------------------------------------|---|
| <i>MoS₂/TiNT-350°C</i> | 29 | 2115 | 37.5% | no | Incipient impregnation (3 atm. Mo/nm ²) + sulfidation |
| <i>TiNT(9%-MoS₂)-335°C</i> | 33 | 2123 | $\leq 37.5\%$ | yes | Hydrothermal + sulfidation |
| <i>TiNT(3%-MoS₂)-350°C</i> | 5 | 2123 | $\leq 37.5\%$ | no | Hydrothermal + sulfidation |
| <i>MoS₂/TiNW-400°C</i> | 3 | 2115 | $\leq 37.5\%$ | no | Incipient impregnation (3 atm. Mo/nm ²) + sulfidation |
| <i>MoS₂/TiO₂-400°C</i> | 84 | 2120 | - | no | Incipient impregnation (3 atm. Mo/nm ²) + sulfidation |

Polarization curves of these four samples show high overpotentials (< -0.28 V at 1 mA/cm^2) as awaited since the support's resistance is high. In addition, exchange current densities are very low. The reference value of -10 mA/cm^2 was not reached, making it impossible to compare these results with the ones reported in the literature. However, a trend between the samples can be noticed. At -1 mA/cm^2 the overpotentials are increasing in the following order: $\text{MoS}_2/\text{TiNW-400}^\circ\text{C} < \text{TiNT}(3\%-\text{MoS}_2) < \text{MoS}_2/\text{TiNT-350}^\circ\text{C} < \text{TiNT}(9\%-\text{MoS}_2) < \text{MoS}_2/\text{TiO}_2$. Consequently, HER activity is increasing in the described order (Figure 32).

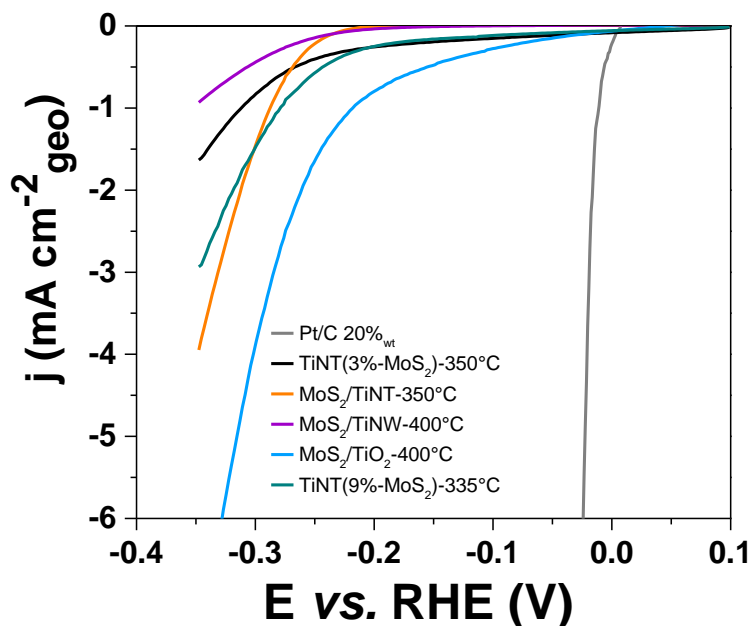


Figure 32: Polarization curves of MoS₂/TiNW 400°C; MoS₂/TiNT 350°C; TiNT(9%-MoS₂); TiNT(3%-MoS₂) and MoS₂/TiO₂.

Indeed, the first factor influencing HER activity is the concentration of active sites. The number of M-edge sites is increasing in the order: MoS₂/TiNW-400°C < TiNT(3%-MoS₂)-350°C < MoS₂/TiNT-350°C < TiNT(9%-MoS₂)-335°C < MoS₂/TiO₂. The decrease in overpotentials at -1 mA/cm² is following the same order. Consequently, HER activity increases with higher M-edge sites concentration.

However, by comparing precisely the samples with each other additional observations are to be concluded.

By comparing MoS₂/TiNT-350°C and MoS₂/TiNW-400°C prepared by incipient impregnation, we observe lower overpotentials for MoS₂/TiNT-350°C. Indeed, the gap in activity is primarily due to the number of active sites as noted before. But this difference might also be caused by the formation of MoS₂ on different TiO₂ facets. As we have seen on IR/CO spectra, MoS₂/TiNW-400°C presented (100) facets covered with MoS₂ whereas MoS₂/TiNT-350°C presented only (001) facets which are endowed with higher surface energies and could influence the activity of M-edges.^{20,21}

In regards to the presence of 1T-phase on TiNT(9%-MoS₂)-335°C, the beneficial impact on activity due to the presence of this metallic polytype is not evident. Although XPS validated

the presence of a mixt 1T/2H-MoS₂ phase, overpotentials are not significantly decreasing. It might be related to the small proportion of created 1T-phase which is metastable and transforms quickly into stable phase 2H-MoS₂. IR/CO results have demonstrated a less pronounced electron density of Mo compared to the one on TiNT. Therefore it is highly probable that hydrogen is bounded weakly to Mo on TiNT(9%-MoS₂)-335°C leading to smaller activity rates compared to MoS₂/TiNT-350°C.

Regarding the comparison between TiNT(3%-MoS₂)-350°C and MoS₂/TiNW-400°C, which have approximatively the same concentration of M-edge sites, we would expect MoS₂/TiNW-400°C to be more active because its Mo electron density is higher. However, this is not the case. It may be possible due to higher charge transfer that nanotubes of TiO₂ are more electrically conductive than TiNW. Moreover, by introducing S and Mo into the nanotube structure, defects favorable for higher electron mobility might have been created during synthesis. Furthermore, MoS₂ slab size might also influence activity. Indeed, on TiNW, large slabs were observed leading to small surface contact with reactants. In contrary, slab size on TiNT(9%-MoS₂)-335°C was demonstrated to be smaller (i.e. 2.7 ± 0.2 nm) MoS_x species are present. It was demonstrated by Jaramillo et al. that those compounds are active in HER.^{42,43} Hence, they could act as additional active sites.

Concerning the impact of carrier's morphology and Mo-introduction pathway on the rate determining step (RDS), Tafel slopes of analyzed samples were determined (Figure 33). Indeed, Tafel slopes provide an inside into HER kinetic mechanism. In short, it is possible to determine whether the mechanism pathway was Volmer-Heyrovsky or Volmer-Tafel. As a reminder, in acidic media protons are immediately accessible leading to the reaction steps:⁴⁴

| | | |
|------------------------|--|------------|
| <i>Volmer step:</i> | $H^+ + e^- + * \rightleftharpoons H^*$ (1) | 120 mV/dec |
| <i>Heyrovsky step:</i> | $H^+ + e^- + H^* \rightleftharpoons H_2 + *$ (2) | 40 mV/dec |
| <i>Tafel step:</i> | $H^* + H^* \rightleftharpoons H_2 + 2*$ (3) | 30 mV/dec |

Where * is the active site and H* the adsorbed proton.

It should be underlined that the calculated Tafel slopes (Figure 33) of TiNT(9%-MoS₂)-335°C; TiNT(3%-MoS₂)-350°C and MoS₂/TiO₂-400°C are not reliable because of the fast drop in overpotentials when current density is increasing. Herein, Tafel slopes were approximatively calculated. This fast drop in overpotential can be related to several factors:

- Poor solubilization of sample in the prepared dispersion.
- Resistance phenomena caused by the sample
- Secondary reactions occur during HER (i.e. possible reduction of molybdenum oxide).

Yet, those approximations are allowing to observe a general trend. In the case of MoS₂/TiNT-350°C and MoS₂/TiNT-400°C Tafel slopes are reliable.

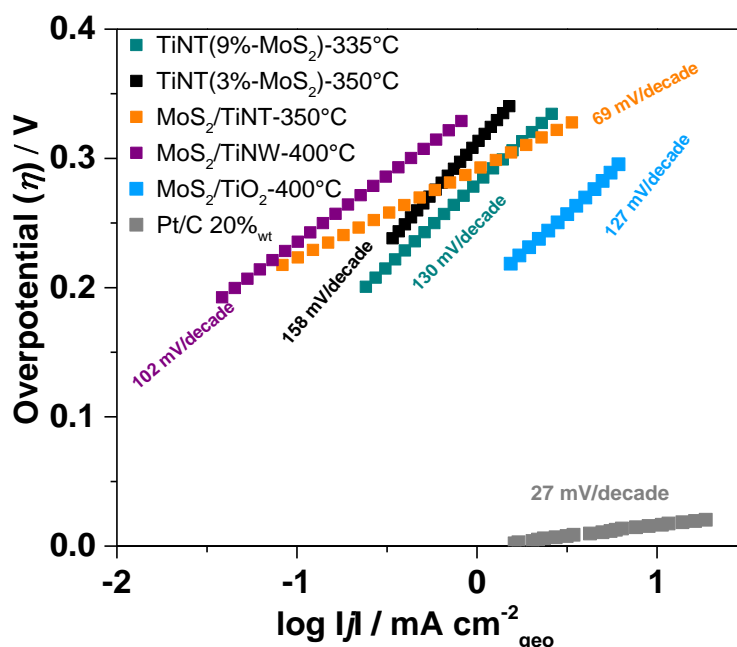


Figure 33: Calculated Tafel slopes of analyzed samples.

Based on Figure 33, we can see that MoS₂/TiNT-350°C has the lowest Tafel slope with 69 mV/dec. Hence, we can deduce that the Volmer-Heyrovsky pathway was favored and the RDS is tending towards Heyrovsky step (i.e. formation of H₂ via the reaction between a proton and an adsorbed one). Indeed, via incipient impregnation of Mo on TiNT we were able to increase molybdenum's metallic character as proved by IR/CO and facilitate the adsorption of protons. Moreover, the E_g of sulfided TiO₂ in MoS₂/TiNT-350°C is the smallest one with 2.37 eV indicating an enhanced charge transfer based on UV-Vis spectroscopy compared to TiO₂ and

TiNW. Consequently, by boosting considerably the charge transfer more electrons are available during reaction.

By comparing Mo impregnated on TiNW with those on TiNT, we observed with the help of IR/CO that both of them present similar electron density. Based on this observation, one might expect to observe similar slope values. Yet, a higher Tafel slope (102 mV/dec) was determined for MoS₂/TiNW-400°C. The fact that larger MoS₂ slabs were formed on TiNW compared to the ones on TiNT, suggests a stronger interaction between MoS₂ and TiNW compared to MoS₂-TiNT. Subsequently, we can assume based on the work of Tsai et al.⁴⁵, that the weakening of MoS₂-TiNT interaction is leading to stronger hydrogen bonds between Mo and protons. As a result, adsorption of protons is facilitated (Volmer) yet might be too strong and therefore limiting the reaction between adsorbed proton and a free one.

Imbedding Mo into the nanotube wall resulted in higher Tafel slopes compared to MoS₂/TiO₂-400°C indicating that the RDS is the Volmer step. Subsequently the insertion of Mo had no beneficial effect on proton adsorption.

8. Conclusion

HER activity tests of MoS₂ dispersed on TiNT and TiNW synthesized via either incipient impregnation or one-pot solvothermal synthesis followed by sulfidation demonstrated the importance of different factors influencing HER activity rates. Indeed, concentration of M-edge sites, phase nature of MoS₂, electronic density of molybdenum, the carrier's electronic transfer capability and distribution of MoS₂ on different TiO₂ facets are all parameters which needs to be thought of during catalyst engineering.

Changing the TiO₂-anatase morphology into nanotubes or nanowires resulted in enriching molybdenum's electron density. This increase is probably related to an enhanced charge transfer which is also reflected by the determined energy gaps for sulfided TiNT (2.37 eV) and TiNW (2.70 eV). The combination of S-doping and morphology change of bulk TiO₂ decreased significantly the energy gap. Consequently, by increasing charge transfer and the electron density of Mo, the metallic character of MoS₂ was efficiently enhanced allowing to improve the adsorption of protons due to stronger bonding between molybdenum and hydrogen. This increase in Mo electron density allowed to decrease Tafel slopes especially for MoS₂/TiNT-350°C with 69 mV/dec. In comparison, TiNW seems to have a more pronounced adhesion energy with MoS₂ leading to higher Tafel slopes.

We also observed that higher number of M-edge sites resulted in lower overpotentials meaning better activity rates. Herein, the synthesis method to introduce Mo plays a crucial role. It does not only affect the electron density of Mo which is more pronounced via incipient impregnation, but also the size of MoS₂ slabs and the concentration of M-edge sites. Indeed, dispersing Mo by incipient impregnation has resulted in the formation of small slabs with a size of 1.7 nm dispersed on (001) facets. But only by imbedding Mo into the nanotube wall, we were able under 10% H₂S/H₂ flow to obtain 1T-MoS₂ endowed with a large reactive basal plane under moderate sulfidation temperatures. Yet, imbedding Mo into the nanotube wall did not have any beneficial impact on HER kinetics as Tafel slopes demonstrates. Volmer step is still the rate determining step. Herein an overall conclusion can be made: In order to improve HER activity rates and kinetics (i.e. meaning low overpotential and Tafel slopes) incipient impregnation of Mo is favored on carriers with a tubular morphology. Thus, even the

poorest electrically conductive support allows to decrease overpotentials, decrease Tafel slopes and enhance electron transfer.

Consequently, we can establish a relation by connecting IR/CO results and HER activity tests. In order to increase the catalytic performance of MoS₂, two major parameters need to be considered: Tafel slope and overpotentials. Based on the obtained results in this work, just by changing the morphology of the carrier, we are impacting overpotentials by modulating the size of MoS₂ slabs, the concentration of M-edge sites, the electrical conductivity of the carrier. In contrast, Tafel slopes can be modulated by the electron density of Mo which reflects the affinity of Mo towards protons. Besides the interaction between MoS₂ and support seems to have also a huge impact on Tafel slope (Figure 34).

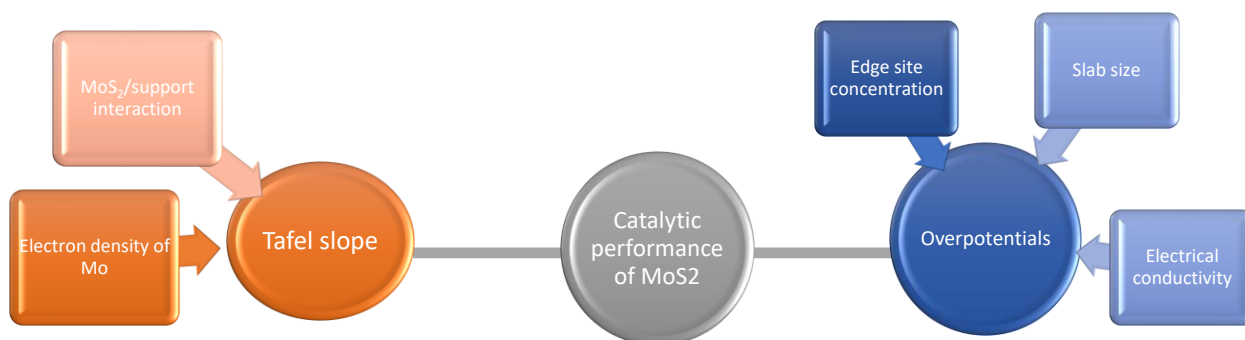


Figure 34: Parameters effecting the catalytic performance of MoS₂ based on obtained IR/CO and HER activity tests.

In regards to FTIR spectroscopy as surface characterization tool, we believe to have probed for the first time 1T-MoS₂ with CO. A downshifted absorption band was found at 2011 cm⁻¹. Its intensity increased with Mo-loading and sulfidation temperature (i.e. 320-335°C). Its possible detection by CO/IR after in-situ formation under H₂S/H₂ opens new opportunities to study 1T-MoS₂ under IR-spectroscopy and understand better its surface properties. Nevertheless, DFT calculations are needed to validate this absorption band which are to this point not have been reported about.

Reference

- (1) Earp, B.; Dunn, D.; Phillips, J.; Agrawal, R.; Ansell, T.; Aceves, P.; De Rosa, I.; Xin, W.; Luhrs, C. Enhancement of Electrical Conductivity of Carbon Nanotube Sheets through Copper Addition Using Reduction Expansion Synthesis. *Mater. Res. Bull.* **2020**, *131* (April), 110969.
- (2) Rendón-Rivera, A.; Toledo-Antonio, J. A.; Cortés-Jácome, M. A.; Angeles-Chávez, C. Generation of Highly Reactive OH Groups at the Surface of TiO₂ Nanotubes. *Catal. Today* **2011**, *166* (1), 18–24.
- (3) Choi, M. G.; Lee, Y. G.; Song, S. W.; Kim, K. M. Lithium-Ion Battery Anode Properties of TiO₂ Nanotubes Prepared by the Hydrothermal Synthesis of Mixed (Anatase and Rutile) Particles. *Electrochim. Acta* **2010**, *55* (20), 5975–5983.
- (4) Terracciano, M.; Galstyan, V.; Rea, I.; Casalino, M.; De Stefano, L.; Sberveglieri, G. Chemical Modification of TiO₂ Nanotube Arrays for Label-Free Optical Biosensing Applications. *Appl. Surf. Sci.* **2017**, *419*, 235–240.
- (5) Cao, Y.; Wu, Y.; Badie, C.; Cadot, S.; Camp, C.; Quadrelli, E. A.; Bachmann, J. Electrocatalytic Performance of Titania Nanotube Arrays Coated with MoS₂ by ALD toward the Hydrogen Evolution Reaction. *ACS Omega* **2019**, *4* (5), 8816–8823.
- (6) Lačnjevac, U.; Vasilić, R.; Dobrota, A.; Đurđić, S.; Tomanec, O.; Zbořil, R.; Mohajernia, S.; Nguyen, N. T.; Skorodumova, N.; Manojlović, D.; Elezović, N.; Pašti, I.; Schmuki, P. High-Performance Hydrogen Evolution Electrocatalysis Using Proton-Intercalated TiO₂nanotube Arrays as Interactive Supports for Ir Nanoparticles. *J. Mater. Chem. A* **2020**, *8* (43), 22773–22790.
- (7) Liu, Z.; Zhang, X.; Wang, B.; Xia, M.; Gao, S.; Liu, X.; Zavabeti, A.; Ou, J. Z.; Kalantar-Zadeh, K.; Wang, Y. Amorphous MoS_x-Coated TiO₂ Nanotube Arrays for Enhanced Electrocatalytic Hydrogen Evolution Reaction. *J. Phys. Chem. C* **2018**, *122* (24), 12589–12597.
- (8) AlAqad, K. M.; Kandiel, T. A.; Basheer, C. Synergy between In-Situ Immobilized MoS₂ Nanosheets and TiO₂ Nanotubes for Efficient Electrocatalytic Hydrogen Evolution. *Int. J. Hydrogen Energy* **2022**, *47* (4), 2366–2377.
- (9) Su, Z.; Zhu, Y.; Wu, Z.; Peng, X.; Gao, C.; Xi, K.; Lai, C.; Kumar, R. V. Introduction of “lattice-Voids” in High Tap Density TiO₂-B Nanowires for Enhanced High-Rate and High Volumetric Capacity Lithium Storage. *RSC Adv.* **2014**, *4* (44), 22989–22994.
- (10) Thommes, M. Physical Adsorption Characterization of Nanoporous Materials. *Chemie-Ingenieur-Technik* **2010**, *82* (7), 1059–1073.
- (11) Mino, L.; Ferrari, A. M.; Lacivita, V.; Spoto, G.; Bordiga, S.; Zecchina, A. CO Adsorption on Anatase Nanocrystals: A Combined Experimental and Periodic DFT Study. *J. Phys. Chem. C* **2011**, *115* (15), 7694–7700.
- (12) Travert, A.; Dujardin, C.; Maugé, F.; Cristol, S.; Paul, J. F.; Payen, E.; Bougeard, D. Parallel

- between Infrared Characterisation and Ab Initio Calculations of CO Adsorption on Sulphided Mo Catalysts. *Catal. Today* **2001**, *70* (1–3), 255–269.
- (13) Cordova, A.; Blanchard, P.; Lancelot, C.; Frémy, G.; Lamonier, C. Probing the Nature of the Active Phase of Molybdenum-Supported Catalysts for the Direct Synthesis of Methylmercaptan from Syngas and H₂S. *ACS Catal.* **2015**, *5* (5), 2966–2981.
- (14) Blanchard, P.; Lamonier, C.; Griboval, A.; Payen, E. New Insight in the Preparation of Alumina Supported Hydrotreatment Oxidic Precursors: A Molecular Approach. *Appl. Catal. A Gen.* **2007**, *322* (SUPPL.), 33–45.
- (15) Strachan, J.; Masters, A. F.; Maschmeyer, T. Critical Review: Hydrothermal Synthesis of 1T-MoS₂- an Important Route to a Promising Material. *J. Mater. Chem. A* **2021**, *9* (15), 9451–9461.
- (16) Zhang, Y.; Kuwahara, Y.; Mori, K.; Louis, C.; Yamashita, H. Hybrid Phase 1T/2H-MoS₂ with Controllable 1T Concentration and Its Promoted Hydrogen Evolution Reaction. *Nanoscale* **2020**, *12* (22), 11908–11915.
- (17) Er, E.; Hou, H. L.; Criado, A.; Langer, J.; Möller, M.; Erk, N.; Liz-Marzán, L. M.; Prato, M. High-Yield Preparation of Exfoliated 1T-MoS₂ with SERS Activity. *Chem. Mater.* **2019**, *31* (15), 5725–5734.
- (18) Plechinger, G.; Heydrich, S.; Eroms, J.; Weiss, D.; Schüller, C.; Korn, T. Raman Spectroscopy of the Interlayer Shear Mode in Few-Layer Flakes. *Appl. Phys. Lett.* **2018**, *101906* (May 2012), 99–102.
- (19) Arrouvel, C.; Breyse, M.; Toulhoat, H.; Raybaud, P. A Density Functional Theory Comparison of Anatase (TiO₂)- and γ -Al₂O₃-Supported MoS₂ Catalysts. *J. Catal.* **2005**, *232* (1), 161–178.
- (20) Søndergaard-Pedersen, F.; Broge, N. L. N.; Yu, J.; Roelsgaard, M.; Iversen, B. B. Maximizing the Catalytically Active {001} Facets on Anatase Nanoparticles. *Chem. Mater.* **2020**, *32* (12), 5134–5141.
- (21) Ong, W.; Tan, L.; Chai, S.; Yong, S. Highly Reactive {001} Facets of TiO₂-Based Composites: Synthesis, Formation Mechanism and Characterization. *Nanoscale* **2014**, *6*, 1946–2008.
- (22) Han, H.; Kim, M.; Lee, C.; Lee, C. S.; Pawar, R. C.; Jones, J. L.; Hong, Y.; Ryu, H. Few-Layered Metallic 1T-MoS₂/TiO₂ with Exposed (001) Facets: Two-Dimensional Nanocomposites for Enhanced Photocatalytic Activities. *R. Soc. Chem.* **2017**, 28207–28215. <https://doi.org/10.1039/c7cp05523d>.
- (23) Palencia-Ruiz, S.; Uzio, D.; Legens, C.; Laurenti, D.; Afanasiev, P. Stability and Catalytic Properties of 1T-MoS₂ Obtained via Solvothermal Synthesis. *Appl. Catal. A Gen.* **2021**, *626* (July).
- (24) Dominguez Garcia, E.; Chen, J.; Oliviero, E.; Oliviero, L.; Maugé, F. New Insight into the Support Effect on HDS Catalysts: Evidence for the Role of Mo-Support Interaction on the MoS₂ Slab Morphology. *Appl. Catal. B Environ.* **2020**, *260* (July 2019).
- (25) Arrouvel, C.; Digne, M.; Breyse, M.; Toulhoat, H.; Raybaud, P. Effects of Morphology

- on Surface Hydroxyl Concentration: A DFT Comparison of Anatase-TiO₂ and γ -Alumina Catalytic Supports. *J. Catal.* **2004**, 222 (1), 152–166.
- (26) Van Viet, P.; Huy, T. H.; Sang, N. X.; Thi, C. M.; Van Hieu, L. One-Step Hydrothermal Synthesis and Characterisation of SnO₂ Nanoparticle-Loaded TiO₂ Nanotubes with High Photocatalytic Performance under Sunlight. *J. Mater. Sci.* **2018**, 53 (5), 3364–3374.
- (27) Viet, P. Van; Huy, T. H.; You, S. J.; Hieu, L. Van; Thi, C. M. Hydrothermal Synthesis, Characterization, and Photocatalytic Activity of Silicon Doped TiO₂ Nanotubes. *Superlattices Microstruct.* **2018**, 123 (September), 447–455.
- (28) Zeng, T.; Wen, X.; Li, Y.; Jiao, H. Density Functional Theory Study of Triangular Molybdenum Sulfide Nanocluster and CO Adsorption on It. *Phys. Chem.* **2005**, 13704–13710.
- (29) Garcia, E. D. Effet Du Support Sur La Morphologie et l'activité Des Catalyseurs d'hydrodésulfuration. *PhD thesis Univ. Caen* **2017**.
- (30) Sharma, C. H.; Surendr, A. P.; Varghese, A.; Thalakulam, M. Stable and Scalable 1T MoS₂ with Low Temperature-Coefficient of Resistance. *Sci. Rep.* **2018**, No. August, 1–9.
- (31) Tsilomelekis, G.; Panagiotou, G. D.; Stathi, P.; Kalampounias, A. G.; Bourikas, K.; Kordulis, C.; Deligiannakis, Y.; Boghosian, S.; Lycourghiotis, A. Molybdena Deposited on Titania by Equilibrium Deposition Filtration: Structural Evolution of Oxo-Molybdenum(VI) Sites with Temperature. *Phys. Chem. Chem. Phys.* **2016**, 18 (34), 23980–23989.
- (32) Tian, H.; Roberts, C. A.; Wachs, I. E. Molecular Structural Determination of Molybdena in Different Environments: Aqueous Solutions, Bulk Mixed Oxides, and Supported MoO₃ Catalysts. *J. Phys. Chem. C* **2010**, 114 (33), 14110–14120.
- (33) Hu, H.; Wachs, I. E. Surface Structures of Supported Molybdenum Oxide Catalysts. Characterization by Raman and Mo L₃-Edge XANES. *J. Phys. Chem.* **1995**, 99 (27), 10897–10910. <https://doi.org/10.1021/j100027a034>.
- (34) Cordova, A. SUPPORTED MOLYBDENUM AND TUNGSTEN BASED CATALYSTS FOR THE DIRECT SYNTHESIS OF METHYLMERCAPTAN FROM SYNGAS, 2013.
- (35) Saber, M. R.; Khabiri, G.; Maarouf, A. A.; Ulbricht, M.; Khalil, A. S. G. A Comparative Study on the Photocatalytic Degradation of Organic Dyes Using Hybridized 1T/2H, 1T/3R and 2H MoS₂ Nano-Sheets. *RSC Adv.* **2018**, 8 (46), 26364–26370.
- (36) Details, E.; Characterization, F. O. R. Few Layered Metallic 1T-MoS₂ / TiO₂ with Exposed (001) Facets : Two-Dimensional Nanocomposites for Enhanced Photocatalytic Activities. **2017**, 699 (001), 1–9.
- (37) Tang, Q.; Jiang, D. E. Mechanism of Hydrogen Evolution Reaction on 1T-MoS₂ from First Principles. *ACS Catal.* **2016**, 6 (8), 4953–4961.
- (38) Putungan, D. B.; Lin, S. A Look into Atomic Carbon and Oxygen Adsorption on 1T'-MoS₂ Monolayer : Density Functional Theory A Look into Atomic Carbon and Oxygen Adsorption on 1T'-MoS₂ Monolayer : Density Functional Theory Calculations. *Mater. Res. Express* **2017**, No. 4, 125026.

- (39) Nanowires, T.; Armstrong, A. R.; Armstrong, G.; Canales, J.; Bruce, P. G. TiO₂ -B Nanowires. *Angew. Chemie - Int. Ed.* **2004**, *43*, 2286–2288.
- (40) Cristol, S.; Paul, J. F.; Payen, E.; Bougeard, D.; Clémendot, S.; Hutschka, F. Theoretical Study of the MoS₂ (100) Surface: A Chemical Potential Analysis of Sulfur and Hydrogen Coverage. 2. Effect of the Total Pressure on Surface Stability. *J. Phys. Chem. B* **2002**, *106* (22), 5659–5667.
- (41) Gumerova, N. I.; Rompel, A. Polyoxometalates in Solution: Speciation under Spotlight. *Chem. Soc. Rev.* **2020**, *49* (21), 7568–7601. <https://doi.org/10.1039/d0cs00392a>.
- (42) Benck, J. D.; Hellstern, T. R.; Kibsgaard, J.; Chakthranont, P.; Jaramillo, T. F. Catalyzing the Hydrogen Evolution Reaction (HER) with Molybdenum Sulfide Nanomaterials. *ACS Catal.* **2014**, *4* (11), 3957–3971.
- (43) Casalongue, H. G. S.; Benck, J. D.; Tsai, C.; Karlsson, R. K. B.; Kaya, S.; Ng, M. L.; Pettersson, L. G. M.; Abild-Pedersen, F.; Nørskov, J. K.; Ogasawara, H.; Jaramillo, T. F.; Nilsson, A. Operando Characterization of an Amorphous Molybdenum Sulfide Nanoparticle Catalyst during the Hydrogen Evolution Reaction. *J. Phys. Chem. C* **2014**, *118* (50), 29252–29259.
- (44) Li, L.; Wang, P.; Shao, Q.; Huang, X. Metallic Nanostructures with Low Dimensionality for Electrochemical Water Splitting. *Chem. Soc. Rev.* **2020**, *49* (10), 3072–3106.
- (45) Tsai, C.; Chan, K.; Nørskov, J. K.; Abild-Pedersen, F. Theoretical Insights into the Hydrogen Evolution Activity of Layered Transition Metal Dichalcogenides. *Surf. Sci.* **2015**, *640*, 133–140.
- (46) Kasztelan, S.; Toulhoat, H.; Grimblot, J.; Bonnelle, J. P. A Geometrical Model of the Active Phase of Hydrotreating Catalysts. *Appl. Catal.* **1984**, *13* (1), 127–159.

Annex

In the following the calculation of the theoretical amount of edge sites on TiNT is explained. For this calculation, the geometrical model of S. Kastzelan was used taking into account the Mo content of the catalyst and the proportion of Mo in sulfide phase from ICP-MS results.⁴⁶ Moreover, it was assumed that all formed slabs have a triangular shape (Figure A1).

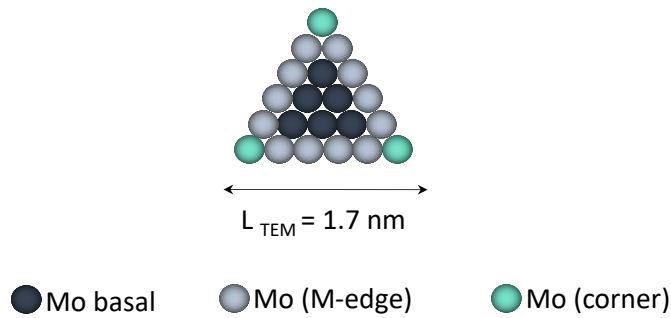


Figure A1: Schematic representation of MoS₂ slabs on TiNT having a triangular shape with only exposed M-edge sites.

As a reminder the total amount of Mo in MoS₂/TiNT is 1174 μmol/g and the average length of slabs was determined to be 1.7 nm. Besides only M-edges were formed as IR/CO results demonstrate. The number of Mo atoms on one side of the slab (noted: $n_{\text{Mo}/\text{side}}$) can be calculated using the equation (1):

$$\text{Equation (1)} \quad n_{\text{Mo}/\text{side}} = \frac{(10L)}{3.16} + 1 \quad (d_{\text{Mo-Mo}} = 3.16 \text{ \AA})$$

The total number of Mo atoms per slab ($n_{\text{Mo}/\text{slab}}$) was obtained using the equation (2):

$$\text{Equation (2)} \quad n_{\text{Mo}/\text{slab}} = [(n_{\text{Mo}/\text{side}}) * (n_{\text{Mo}/\text{side}} + 1)]/2$$

Herein, the number of Mo per slab in edge position (n_{Moe}) is determined from the equation (4):

$$\text{Equation (4):} \quad n_{\text{Moe}/\text{slab}} = 3 \left(\frac{n_{\text{Mo}}}{\text{side}} \right) - 3$$

The concentration of sulfide slabs per g of catalyst is determined by the equation (5):

$$\text{Equation (5):} \quad n_{\text{slab}} = \frac{n_{\text{Motot}}/10^{-6}}{n_{\text{Mo}/\text{slab}}/Na}$$

with n_{Motot} the molar concentration of Mo in MoS₂ per g of catalyst and Na equaling $6.02 \cdot 10^{23}$.

At last the concentration of M-edge sites ($\mu\text{mol/g}$) can be determined from the equation (7):

$$\text{Equation (7): } C_{Moe} = \frac{n_{slab} \cdot n_{Moe/slab} \cdot 10^6}{Na}$$

The determined values for each equation are summarized in the table below:

| Average slab length (nm) | $n_{Mo/side}$ | $n_{Mo/slab}$ | $n_{Moe/slab}$ | n_{Slab} | C_{Moe} ($\mu\text{mol/g}$) |
|---|---------------------------------|---------------------------------|----------------------------------|------------------------------|--|
| 1.7 | 6.4 | 23.5 | 16.1 | $3.0 \cdot 10^{19}$ | 805 |

Table of contents

| | |
|---|------------|
| General conclusion | 218 |
| 1. Main conclusion of the research work | 218 |
| 1.1. S-doping of bulk TiO ₂ | 218 |
| 1.2. Tubular morphology change of TiO ₂ | 219 |
| 1.3. Tubular morphology change: a key parameter in HER electrocatalyst engineering | 219 |
| 1.4. Introduction of Mo-precursor during preparation | 220 |
| 1.5. Insignificant impact of the addition of H ₃ PO ₄ and EDTA during preparation on HER activity | 221 |
| 1.6. Type of exposed facet | 222 |
| 1.7. Correlation between HDS and HER | 222 |
| 2. Future perspective | 223 |
| Reference | 226 |

General conclusion

1. Main conclusion of the research work

In this thesis, we tried to get a deep insight on the active phase MoS₂ for the electrocatalytic hydrogen evolution reaction by using different surface characterization methods. Especially by using IR/CO spectroscopy a profound understanding was gained about the effects of chelating agents, dopants and carrier's morphology on MoS₂ surface characteristics. The obtained results were correlated with HER activity tests in order to suggest synthesis strategies which will allow to reduce overpotentials and enhance kinetics.

In this work, the main analyzed HER catalyst was supported MoS₂ on TiO₂ (MoS₂/TiO₂). The semiconductor TiO₂ was used as a support due to its high BET surface, chemical stability in acidic media and importantly due its good IR transparency. Yet, TiO₂ electrical conductivity is a major drawback limiting HER activity. Herein two main strategies were applied to improve TiO₂ electrical conductivity: S-doping of bulk TiO₂ and tubular morphology change of TiO₂.

1.1. S-doping of bulk TiO₂

Doping bulk TiO₂ with sulfur through sulfidation (10% H₂S/H₂ flow at 400°C) allowed to introduce a sulfur concentration of 2%_{wt} in TiO₂ via an oxygen/sulfur exchange. This kind of method allowed parallely to form MoS₂ on molybdenum impregnated TiO₂ without losing the initial BET surface of the carrier. However, the amount of S-doping seems to be insufficient to improve significantly charge transfer based on determined energy gaps. Indeed the difference in energy gap between sulfided and non-sulfided TiO₂ is differing by 0.2 eV. This small difference explains the observed low HER activity and high Tafel slope indicating that the rate determining step is the Volmer step (i.e. adsorption of protons on edge sites).

1.2. Tubular morphology change of TiO₂

In contrary to the first described strategy, changing the morphology of bulk TiO₂ into a tubular one with the combining effect of S-doping has allowed to decrease significantly TiO₂ energy gap and improve charge transfer. The difference between the energy gap of TiO₂ and sulfided TiNW is 0.4 eV while compared to sulfided TiNT a significant difference of 0.7 eV was determined. This enhancement in charge transfer is also reflected by the higher electron density of Mo supported on TiNT and TiNW as demonstrated by IR/CO. This enrichment of Mo by electrons seems to have facilitated proton adsorption on M-edges leading to a decrease in Tafel slopes.

1.3. Tubular morphology change: a key parameter in HER electrocatalyst engineering

The tubular morphology change of TiO₂ did not only influence MoS₂ by increasing molybdenum's electron density. It also affected the creation of S-vacancies, Mo dispersion and the interaction between MoS₂ and the support.

The formation of S-vacancies on M-edges and corners were favored by changing bulk TiO₂ either into TiNT or TiNW. Yet based on the obtained results it is not possible to conclude whether they had a beneficial impact on HER or not.

In regards to the impact on Mo dispersion, TEM images provided evidence of the formation of small MoS₂ slabs with an average length of 1.7 ± 0.2 nm on TiNT which are perpendicular oriented to the support and form a striped pattern. Herein without using any chelating agents, the average slab size of MoS₂ was successfully reduced by a factor of four compared to the ones supported on bulk TiO₂ (i.e. 6.8 nm). This decrease in slab size can induce higher surface contact with reactants which could be beneficial for HER activity.

Besides, this decrease in slab size is indicating a strong weakening of MoS₂-support interaction. It is generally acknowledged that the existing strong Van der Waals interaction between MoS₂ and bulk TiO₂ is favoring the formation of large slabs. Subsequently by changing

TiO₂ into TiNT has favored a weakening of this interaction. However the average slab size of MoS₂ supported on TiNW was determined to be 6.1 ± 1.3 nm. Subsequently the interaction between MoS₂ and TiNW is comparable to the one of MoS₂/TiO₂. As a result, the “morphology type” of TiO₂ is of great importance for a good Mo dispersion and to modulate MoS₂-support interaction. The latter is of great importance for HER kinetics because a weak MoS₂-support interaction induces an increase in H-binding which is reflected by a strong decrease in Tafel slopes as observed for MoS₂/TiNT-350°C (Chapter 4).

1.4. Introduction of Mo-precursor during preparation

The morphology of the carrier is not the only parameter influencing MoS₂ surface characteristics. The way Mo-precursor is introduced during synthesis was demonstrated to be crucial in this work especially on MoS₂ phase nature. Indeed via incipient impregnation 2H-MoS₂ was formed on exposed (001) facets. However, when Mo was inserted into TiNT framework via one-pot hydrothermal synthesis, the phase nature of MoS₂ can be controlled based on two combined conditions: Mo-loading and sulfidation temperature. When Mo-loading is below 0.74 Mo/nm² and catalyst is sulfided at 350°C 2H-MoS₂ is formed. In contrary, when Mo-loading is equal to 0.74 Mo/nm² and sulfided at 335°C a mixt 1T/2H-phase is formed with a proportion of 1:2.5 respectively. The presence of the metallic phase was validated by XPS and seems also to be detected by IR/CO at 2011 cm⁻¹. For the latter DFT calculations should be performed in order to validate this contribution and clarify the CO adsorption site on 1T-MoS₂.

Despite the interesting surface characteristics of MoS₂ dispersed on TiNT either prepared by incipient impregnation or one-pot hydrothermal synthesis the low probed concentrations of M-edges are leading to high overpotentials and subsequently low HER activities. In the case of MoS₂ supported on TiNT the concentration of accessible M-edge sites is limited due the obstruction of nanotubes apparently by the formation of sodium molybdenum sulfide salt and MoS₂ slabs. On that account clogging of nanotubes needs to be resolved in order to increase the amount of exposed M-edges. One possible strategy could be enlarging the nanotubes' pore diameter by using for instance templates. Another possibility which was applied in this work, is to insert Mo into TiNT framework. This method permitted to overcome the issue of

clogging. Yet, M-edge sites concentration are limited by Mo-loading up to 0.74 Mo/nm² and sulfidation temperature up to 350°C because of stability issues.

Nevertheless the synthesis method of embedding Mo into TiNT framework remains interesting for the scaling-up production of 1T/2H-MoS₂ due to the reduced number of synthesis steps.

1.5. Insignificant impact of the addition of H₃PO₄ and EDTA during preparation on HER activity

Adding EDTA or H₃PO₄ at adequate amounts in the impregnation solution of MoS₂ supported on bulk TiO₂ did favor the creation of S-vacancies on M-edges and the increase in Mo dispersion. TEM images confirm the formation of monolayered MoS₂ slabs favored by the addition of EDTA during preparation with a molar ratio N/Mo of 0.5. Besides its slab size was reduced to 2.0 ± 0.1 nm. Based on the similar effect between EDTA and H₃PO₄ on Mo dispersion, slab sizes MoS₂/TiO₂ prepared with phosphoric acid might also have been reduced. However, H₃PO₄ favors the formation of mixt molybdenum oxysulfides with increasing P/Mo ratio. Consequently, it led to a strong decrease in probed M-edge sites concentration which was demonstrated by IR/CO.

Although these resulting impacts on MoS₂ have influenced HDS activity rates significantly, they did not have the same strong impact on HER activity. Using EDTA or H₃PO₄ did not allow to surpass the initial mechanism step (Volmer step) which consists in the adsorption of protons on M-edges. Tafel slopes remained high around 120 mV/dec.

The obtained results are not masked by the poor electrical conductivity of TiO₂ limiting HER activity. The same observations were made by HER activity tests performed on MoS₂ supported on carbon black which were prepared with EDTA. Certainly overpotentials have decreased slightly as well as Tafel slopes due to the enhanced electrical conductivity of carbon black. Nevertheless, they still remained constant for different N/Mo ratios ($x = \{0; 2\}$) and Tafel slopes are still indicating that the Volmer step is the rate determining step. A strong decrease in Tafel slope and overpotentials was only observed when H₃PO₄ was added into the preparation of molybdenum supported on carbon black. Yet, the obtained phase did not

include MoS₂ but an amorphous molybdenum sulfide phase which was probably doped with phosphorous and oxygen. Hence depending on the type of the support, the addition of H₃PO₄ during preparation seems to modify the formed molybdenum sulfide phase. Moreover, it concurs with the superior reported HER activities of amorphous molybdenum sulfide species.^{1,2} Unfortunately the analysis of MoS₂ supported on carbon by IR/CO resulted to be impossible even after trying to increase its transparency by coating MoS₂/C on sapphire substrates (Supplementary Chapter). The introduction of CO into the IR cell did not lead to any absorption band. The origin is not evident since the applied method allowed to successfully analyze MoS₂/TiO₂. It is clear that the possibility to characterize MoS₂ supported on carbon by IR/CO would provide more insight about the nature of edge sites and help to understand better their HER activity.

1.6. Type of exposed facet

The last parameter which seems to influence HER activity and needs to be underlined is the selective formation of exposed facets covered with MoS₂. In Chapter 3 we have noticed 0.5NMoS₂/TiO₂ to be the most active for HER and presenting the smallest Tafel slope (93 mV/dec) compared to the other analyzed catalysts which were prepared with or without EDTA and H₃PO₄. Based on IR/CO results, the molar ratio N/Mo equaling 0.5 favored the formation of small monolayered M-edge sites mostly on (001) facets. These facets are also found on MoS₂ supported on TiNT prepared via incipient impregnation. It presented also a low Tafel slope. It might be very possible, that those facets are having a particular interaction with MoS₂ compared to other TiO₂ facets due to their higher surface energy³ which might allow to enhance HER activity and decrease Tafel slopes. This point should be further analyzed in order to elucidate the impact of specific TiO₂ facets on MoS₂ properties and HER activity.

1.7. Correlation between HDS and HER

In this work we also tried to forecast the most active HER catalysts in a batch by using HDS activity tests. However this method resulted to be not always accurate. Often the trend of

activity observed in HDS activity tests did not fit with the one of HER. This observation can be explained by the fact that prepared catalysts are not solely containing MoS₂. IR/CO and Raman spectroscopy pointed out the formation of other species such as MoOxSy, amorphous molybdenum sulfide, phosphor derived sulfides or sodium molybdenum sulfide which might be inactive for HDS but act as additional HER active sites. Hence the strict comparison between HDS and HER activity by only considering MoS₂ on those prepared samples is misleading.

2. Future perspective

As expected and demonstrated in this work MoS₂/TiO₂ is not the most active catalyst for the electrocatalytic HER. However they might find a more appropriate application in photo(electro)catalysis. Indeed, MoS₂ and TiO₂ present complementary advantages. In one hand TiO₂ is endowed with strong optical adsorption capability and superior structural stability. On the other hand, MoS₂ is highly catalytically active and is endowed with unique layered structure. Based on this research work two interesting materials have been synthesized which might present promising activity rates especially for photo(electro)catalytic reactions.

MoS₂ supported on TiNT is characterized by small 2H-MoS₂ slabs dispersed on exposed (001) facets while molybdenum is enriched in electrons due to the enhanced charge transfer of sulfided TiNT. Since this catalyst presented already low Tafel slopes for the electrocatalytic HER we can expect to have lower overpotentials and possibly also Tafel slopes for the photoelectrocatalytic HER.⁴ Moreover titanium dioxides' (001) facets were reported to have a superior catalytic activity compared to the other facets because of its higher surface energy. Subsequently (001) facets are more efficient for dissociative adsorption of reactants and are endowed with higher energy conversion efficiency which is important for photocatalysis.³ These particular properties of (001) facets might have an influence on MoS₂ and improve its intrinsic activity. Moreover MoS₂/TiNT could also be used for photocatalytic degradation of pollutants and CO₂ reduction. For both applications MoS₂ supported on TiO₂ was reported to have promising results.⁵

TiNT(9%-MoS₂) characterized by a mixt 1T/2H phase might also find suitable applications in photoelectrocatalysis. Yet, the stability of the 1T-phase in the synthesized material is unclear for the moment. Moreover the amount of 1T-MoS₂ seems too small in order to induce a considerable improvement in activity as HER activity tests in Chapter 4 show. Herein, a strategy to increase the proportion of 1T-phase needs to be found. It may be possible to increase the proportion of 1T-phase by modifying sulfidation conditions (i.e. time, flow rate, H₂S concentration etc.). However, avoiding the agglomeration of TiNT(x-MoS₂) will present a big challenge.

In regards to the determined characteristics effecting the activity of MoS₂ for HER, we have demonstrated that the creation of S-vacancies, Mo dispersion, creation of specific facets, MoS₂ phase nature, Mo electron density and the interaction between Mo and the support are all parameters which needs to be considered during HER catalysts engineering in order to optimize overpotentials and Tafel slopes (i.e. summarized in Figure 1). Those key parameters can be modulated by using either additives such as EDTA and H₃PO₄ or more efficiently by changing the carrier's morphology. For the latter, even for the least active HER electrocatalyst, an enhancement in kinetics was observed. Hence, it is worth applying this strategy on other carrier's which are limited by their charge transfer and/or have a too strong MoS₂-support interaction leading to low Mo dispersions and high Tafel slopes.

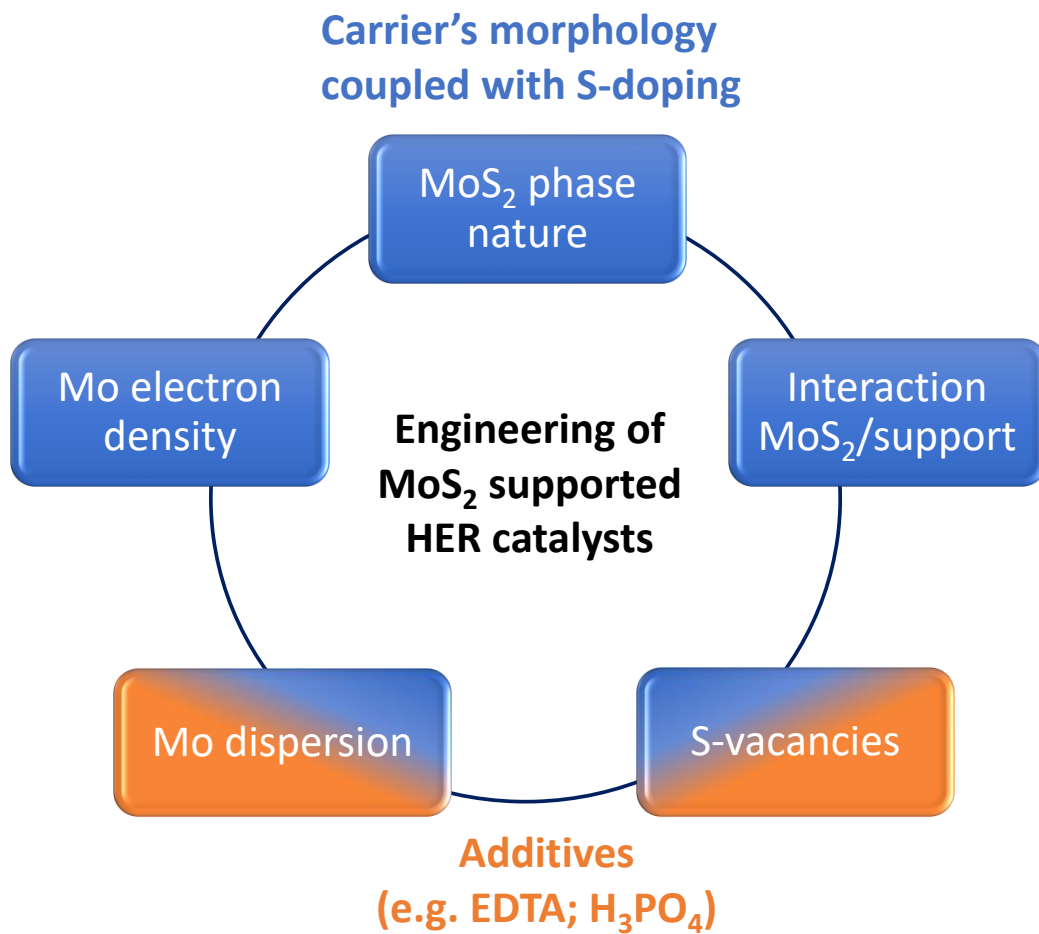


Figure 1: Overview on the key parameters which are important to be considered during MoS₂ supported HER catalysts engineering and are influenced by using additives such as EDTA and H₃PO₄ or by changing the carrier's morphology.

Reference

- (1) Benck, J. D.; Hellstern, T. R.; Kibsgaard, J.; Chakthranont, P.; Jaramillo, T. F. Catalyzing the Hydrogen Evolution Reaction (HER) with Molybdenum Sulfide Nanomaterials. *ACS Catal.* **2014**, *4* (11), 3957–3971. <https://doi.org/10.1021/cs500923c>.
- (2) Li, D. J.; Maiti, U. N.; Lim, J.; Choi, D. S.; Lee, W. J.; Oh, Y.; Lee, G. Y.; Kim, S. O. Molybdenum Sulfide/N-Doped CNT Forest Hybrid Catalysts for High-Performance Hydrogen Evolution Reaction. *Nano Lett.* **2014**, *14* (3), 1228–1233.
- (3) Ong, W.; Tan, L.; Chai, S.; Yong, S. Highly Reactive {001} Facets of TiO₂-Based Composites: Synthesis, Formation Mechanism and Characterization. *Nanoscale* **2014**, *6*, 1946–2008.
- (4) Paul, K. K.; Sreekanth, N.; Biroju, R. K.; Narayanan, T. N.; Giri, P. K. Solar Light Driven Photoelectrocatalytic Hydrogen Evolution and Dye Degradation by Metal-Free Few-Layer MoS₂ Nanoflower/TiO₂(B) Nanobelts Heterostructure. *Sol. Energy Mater. Sol. Cells* **2018**, *185* (April), 364–374.
- (5) Chen, B.; Meng, Y.; Sha, J.; Zhong, C.; Hu, W.; Zhao, N. Preparation of MoS₂/TiO₂ Based Nanocomposites for Photocatalysis and Rechargeable Batteries: Progress, Challenges, and Perspective. *Nanoscale* **2018**, *10* (1), 34–68.

Table of contents

| | |
|--|------------|
| Supplementary Chapter: Developing a new methodology to analyse carbon-based catalysts via IR-transmission | 228 |
| 1. Introduction | 228 |
| 2. Experimental part | 229 |
| 2.1. Dispersion preparation | 229 |
| 2.2. Characterization of samples | 229 |
| 3. Results and discussion | 230 |
| 4. Conclusion | 239 |
| Reference | 240 |

Supplementary Chapter: Developing a new methodology to analyse carbon-based catalysts via IR-transmission

1. Introduction

During analysis we encountered the issue to characterize dark, electrically conductive materials such as carbon derivatives and metals. Due to their either strong absorption capacity or their reflective behavior IR-transmission is impossible to perform. Yet, being able to characterize MoS₂/C with CO would be a step forward in comprehending the activity of these catalysts for HER. Indeed, there are existing other analysis tools based on IR-spectroscopy. For instance, ATR IR-spectroscopy could be promising for the characterization of carbon materials since it is based on the reflected emitted light by the sample after being hit by an IR-beam. But until today, the combination of ATR-IR spectroscopy with CO adsorption under vacuum was not developed. Hence, a new methodology allowing to perform CO adsorption via IR-transmission under vacuum was searched. For this methodology, sapphire substrates were used as IR support to analyze x-NMoS₂/C catalysts studied already in chapter 3.

Indeed, sapphire is a stable material in any acidic or basic media as well as under high temperature. Moreover, it is a hard material which is easy to manipulate and especially transparent for IR with an average transmission range of 1818.2- 58823.5 cm⁻¹. Hence, the characterization of MoS₂ by CO should be possible due to its frequency range around 2120 cm⁻¹. Hydroxyl groups of carbon should also be detectable at 3200-3500 cm⁻¹. However, vibrations of carbonyl groups as well as stretching vibrations of OH-groups won't be visible on IR-spectrum. The main idea of this method consists in depositing a thin coating layer on sapphire substrate. Due to the low thickness, the transmission of IR through the matter might be sufficiently enhanced to observe a certain signal. However, by depositing a thin layer, interference caused by internal reflections of IR-beam in the layer could deteriorate the signal making it impossible to analyze. Herein, the thickness of the layer must be controlled to minimize this phenomenon and in the same time be transmittable to IR. Moreover, the coating needs to be homogenous even after sulfidation at high temperature. Subsequently the preparation and deposition of coating was optimized. Additionally, since impregnated

catalysts should be sulfided in-situ, no additives should be mixed into the coating dispersion in order to avoid possible changes of surface properties (i.e. oxidation/ reduction of Mo, poisoning of active sites, coke formation etc.). Herein the ratio between sample and solvent is crucial in order to obtain the adequate viscosity.

2. Experimental part

2.1. Dispersion preparation

The mixture contained only the sample to analyze and a solvent. Herein the choice of solvent was based on its evaporation temperature and ability to disperse carbon. Propan-2-ol was chosen as solvent because of its evaporation temperature of 97°C. Due to this range of temperature, the solvent is not evaporating too fast and allows to avoid the coating's cracking. For all prepared samples the same method was used: 8 mg of sample grinded in 50 µL propan-2-ol and deposited via doctor blade method to obtain a homogenous coating. For the casting a mortar was used as blade. Afterwards a drying step was performed at 120°C for 1h with an increase of 0.5°C/min. Prior to deposition sapphire substrates were cleaned in acetone under sonication for 10 min and dried in oven.

2.2. Characterization of samples

2.2.1. IR/CO-analysis

CO adsorption were performed under liquid nitrogen (100 K) in an adapted quartz cell. Dried samples deposited on sapphire substrates (12.7x12.7x0.5 mm, Crystal GmbH) underwent sulfidation (10% H₂S/H₂, 30ml/min) at 350°C for 2h (3°C/min). Afterwards flushed with argon for 10 min and evacuated under vacuum (~10⁻⁶ Torr) for 2h until reaching room temperature.

After activation CO adsorption was performed under liquid nitrogen (256 scans; resolution is 4 cm^{-1}).

2.2.2. Raman analysis

A Raman analysis was conducted to verify the presence of MoS_2 . For this analysis a Jobin Yvon Labram 300 Raman spectrometer was used equipped with a confocal microscope, an Nd-YAG laser (frequency doubled, 532 nm) and a CCD detector.

3. Results and discussion

3.1. IR-transmission spectroscopy analysis of sapphire substrate

Sapphire wafers as received by Crystal GmbH were analyzed by IR-transmission spectroscopy. The obtained spectrum is shown in Figure 1. On the IR spectrum we observe the absence of interference fringes. Moreover, the sapphire wafer is absorbing up to 1700 cm^{-1} . Consequently, below this wavenumber spectra cannot be further interpreted as already expected. Only the region above can be used for analysis. Hence, samples which have vibration bands below 1700 cm^{-1} of major interests are not adequate for this kind of analysis. Since the sapphire substrate was not cleaned, several OH- and CH-groups are observed on the surface.

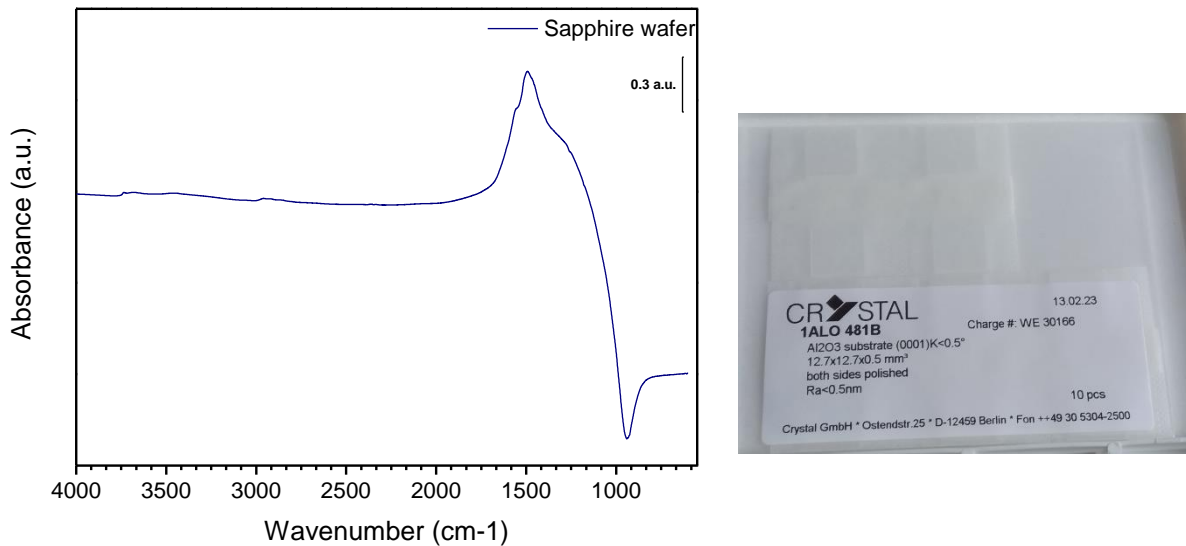


Figure 1: IR absorption spectrum of sapphire wafer and its appearance.

3.2. Initial step: confirming analysis methodology with TiO₂ and 1NMoS₂/TiO₂

To validate the method, two already analyzed samples via pellet conditioning, TiO₂ and 1-NMoS₂/TiO₂, were studied by casting a thin coating via Dr. Blade method on sapphire substrate as already explained in the experimental part.

On the obtained IR spectra, clear and well-defined absorption bands are visible (Figure 2). In the case of TiO₂@sapphire, we detect the same curve shape as on conditioned TiO₂ pellets. After annealing under vacuum at 300°C, the coating is still grafted to the substrate and after CO adsorption $\nu(\text{CO}/\text{Ti}^{4+})$ and $\nu(\text{CO}/\text{OH})$ appear as usual around 2180 and 2160 cm⁻¹.

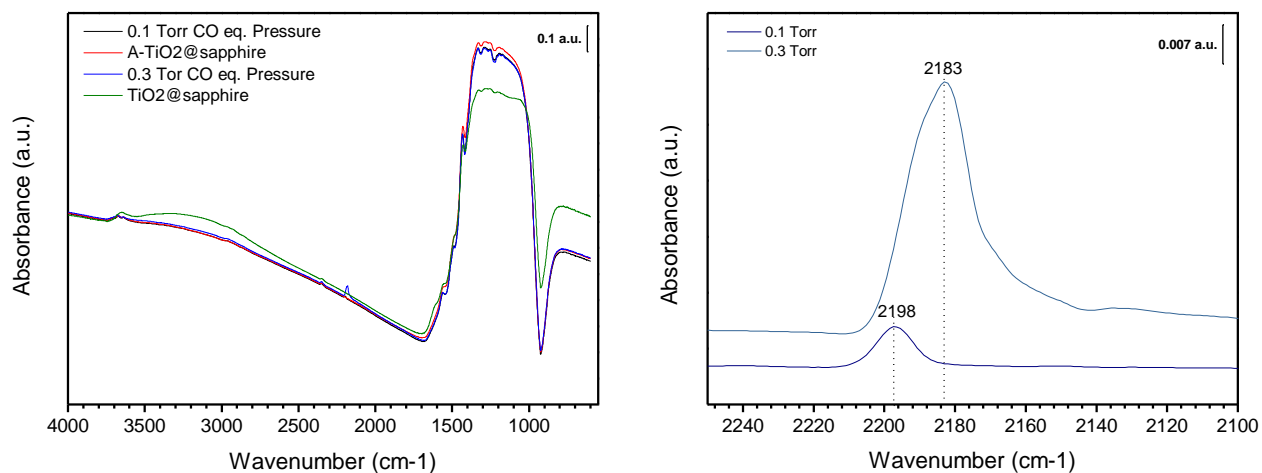


Figure 2: On the left, IR spectra of TiO₂@sapphire before and after annealing under vacuum at 300°C for 2h followed by CO adsorption. On the right, IR/CO spectra of TiO₂@sapphire at 0.1 and 0.3 Torr equilibrium pressure.

Likewise to TiO₂@sapphire, 1NMoS₂/TiO₂@sapphire presented a well-defined IR-spectrum (Figure3). Even after sulfidation under a flow of 30 ml/min, the coating was still grafted to the substrate without being damaged. After CO adsorption $\nu(\text{CO}/\text{Ti}^{4+})$ are found around 2184 cm⁻¹ as well as $\nu(\text{CO}/\text{OH})$ and $\nu(\text{CO}/\text{M-edge})$ at 2165 and 2119 cm⁻¹ respectively. No shift between the CO adsorption bands of pressed 1NMoS₂/TiO₂ described in Chapter 1 and coated sapphire were observed. Hence, the process is not affecting the surface properties of analyzed sample. Herein, we found the right methodology and coating procedure in which the examined sample stays homogeneously attached to the substrate without using any additives.

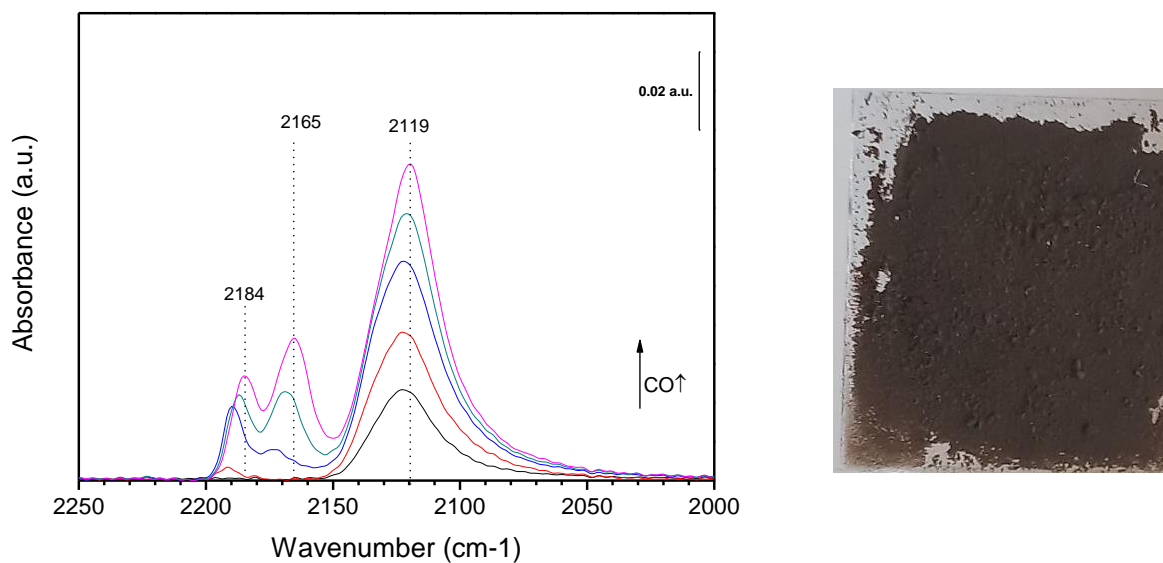


Figure 3: IR/CO spectra of 1NMoS₂/TiO₂@sapphire up to saturation and picture of 1NMo/TiO₂@sapphire coating after sulfidation. On the substrates border, sample detached itself after removing it from the sample holder.

3.3. Adapting methodology to x-NMoS₂/C

After sulfidation at 350°C for 2h (30 ml/min 10% H₂S/H₂), CO adsorption was carried out at 100K. Spectra before sulfidation and after sulfidation are shown in Figure 4.

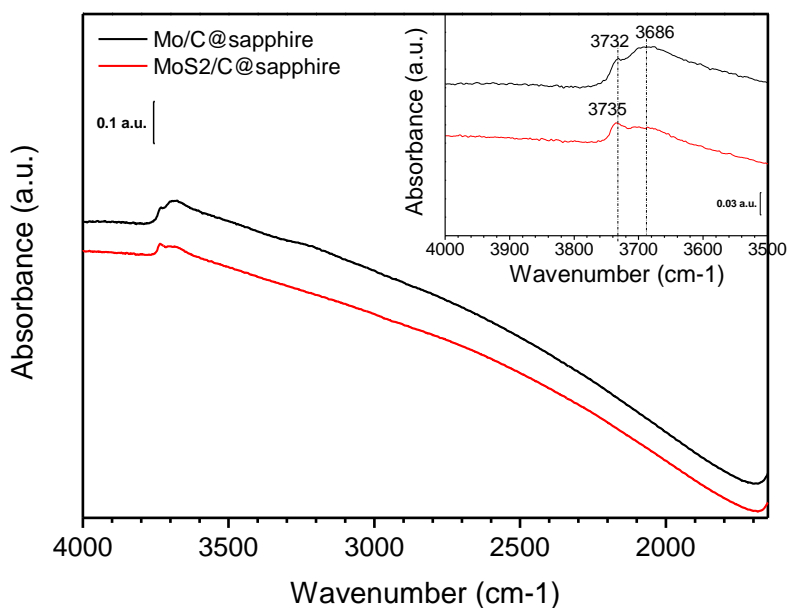


Figure 4: IR absorption spectra of Mo/C@sapphire and MoS₂/C@sapphire with a capture on OH-region.

On both spectra, only the vibration bands in the OH-region are visible. Before sulfidation the intensity of the OH bands at 3732 and 3686 cm⁻¹ are more intense than after sulfidation. Especially the intensity of $\nu(\text{OH})$ at 3686 cm⁻¹ is strongly decreasing. We detected also a slight upward shift of $\nu(\text{OH})$ from 3732 cm⁻¹ to 3735 cm⁻¹ translating a slight increase in basicity after sulfidation. Based on this spectrum we can observe a good transparency of MoS₂/C for IR-transmission.

Yet surprisingly when CO adsorption was performed, no adsorption bands in the region of $\nu(\text{CO}/\text{M-edge})$ around 2120 cm⁻¹ were observed (Figure 5). Only CO in gas phase was visible at 2143 cm⁻¹. Consequently, CO could not be adsorbed. Even by analyzing x-NMoS₂/C deposited on sapphire; no adsorption bands were visible.

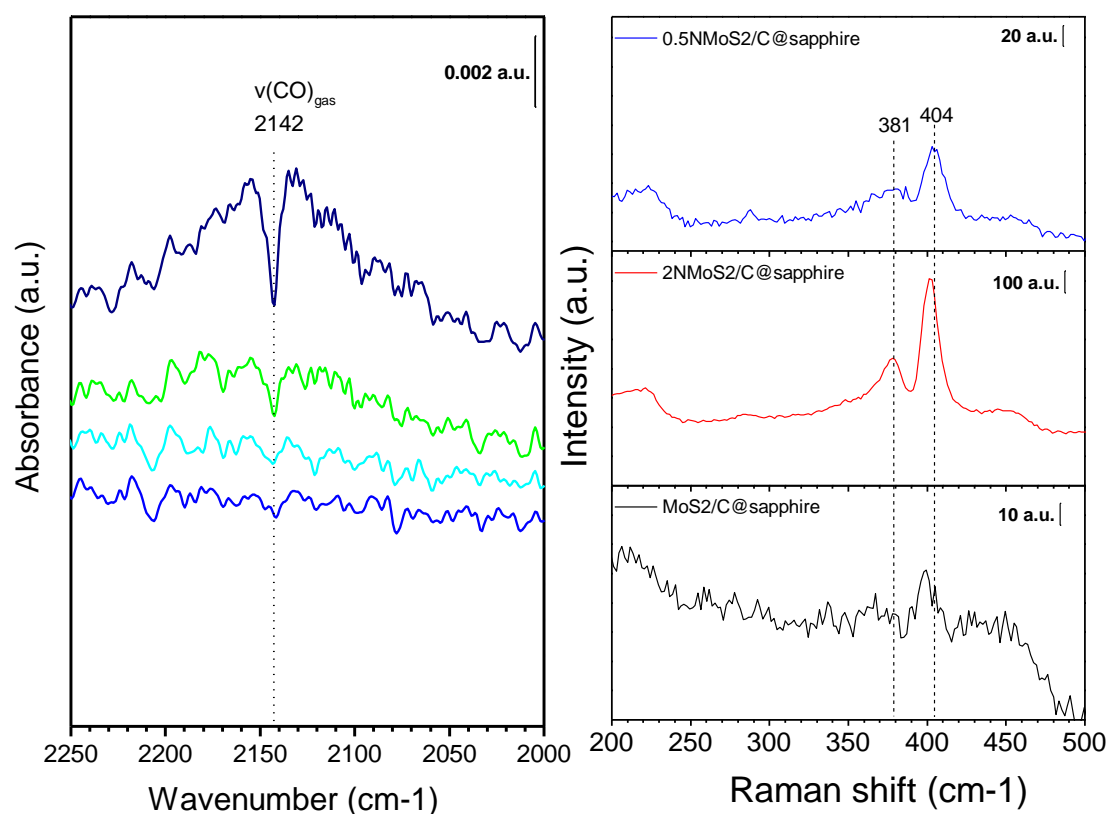


Figure 5: On the left, IR/CO spectra of MoS₂/C@sapphire up to 1 Torr equilibrium pressure. On the right, Raman spectra of MoS₂, 0.5NMoS₂, 2NMoS₂/C@sapphire after IR/CO adsorption.

Herein several possibilities may explain the presence of non-adsorbed CO:

- Absence of MoS₂
- Concentration of MoS₂ is below detection limit
- MoS₂ is not accessible due to coke formation
- Electrostatic phenomenon inhibiting CO adsorption

In order to answer those hypotheses several additional experiments were conducted.

- **Absence of MoS₂ and dilution of MoS₂ concentration:**

Raman was performed after analyzing x-NMoS₂/C@sapphire with IR/CO (Figure 5). The vibration bands E_{2g} and A_{1g} are visible around 381 and 404 cm⁻¹ respectively. Hence, MoS₂ presence is confirmed. We can also observe an increasing in intensity of E_{2g} when the molar ratio (N/Mo) is increasing. This observation is coherent with non-deposited samples as demonstrated in chapter 3. Based on these results, we can conclude that MoS₂ was present during CO adsorption. Yet, it could not be adsorbed. Herein, the hypothesis of non-accessible sites is reinforced.

- **Concentration of MoS₂ under detection limit**

MoS₂ should be observable even at small concentrations. Yet it may be possible that due to the low weight of sample, its concentration is not sufficient to observe a signal. Hence, the weight of deposited sample was doubled from 5 mg to 10 mg. Unfortunately, even though the transparency was good, no adsorption band was observed. As a result, the weight of deposited sample is not the issue.

- **Accessibility of MoS₂**

In chapter 4 we demonstrated that x-NMoS₂/C presented a certain activity in HDS of thiophen. Compared to CO, thiophen is a voluminous molecule and very sensitive to steric effects. Since a certain activity was observed, it means that MoS₂ on powder conditioned samples are accessible. Theoretically, MoS₂ deposited on sapphire should be accessible. Yet, it seems a plausible explanation why CO is not adsorbed. The main difference between the conducted catalytic tests on powder and IR/CO analysis is the presence of propanol. Propanol in the absence of oxygen and in the presence of water can polymerize and form coke at 350°C even at small doses.¹ The formed coke could block M-edge sites and inhibit CO adsorption. Hence, two strategies were followed: (i) Leave MoS₂/C@sapphire longer under vacuum to eliminate possible propanol traces. (ii) Change propanol with an alkane as a result avoiding coke formation.

(i) Longer drying of MoS₂/C@sapphire

In the IR cell analyzed sample was left under vacuum (10⁻⁶ Torr) at 100°C for 24h. No propanol traces were visible on taken IR-spectrum around 3300-3000 cm⁻¹. Consequently, coke cannot

be formed during sulfidation at 350°C. Yet, when CO adsorption at 100K was as usual performed, again CO adsorption bands were not observed even though MoS₂ was detected by Raman.

(ii) Change of solvent

Hexane and pentane were used as solvents for dispersions. They were chosen due to their low evaporation temperature which is 68.7°C and 36°C respectively. In short 10 mg of sample was grinded in 70 µL hexane or pentane. A too quick evaporation of pentane was observed during dispersion preparation leaving fractures in the coating (Figure 6). In the case of hexane the formation of granulates was observed. In between the granulated empty spaces were left.

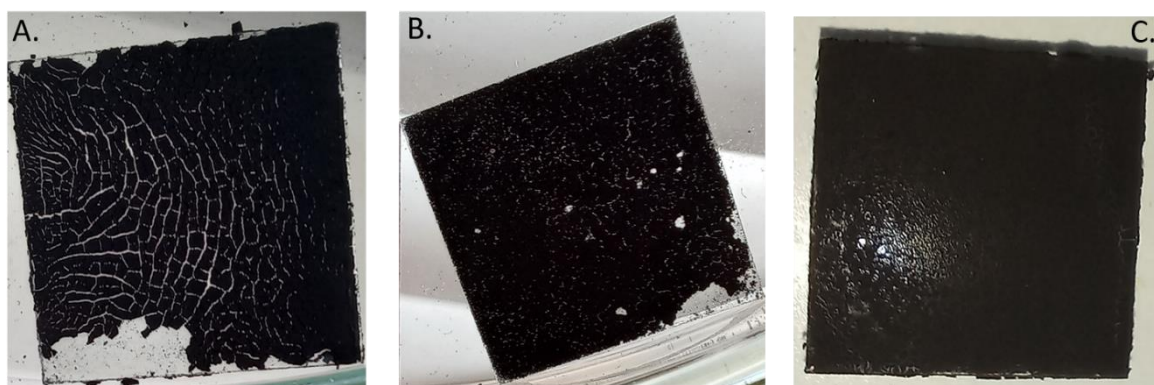


Figure 6: Appearance of obtained Mo/C deposited on sapphire via Dr. Blade method with A pentane.; B. hexane and C. propan-2-ol.

Other deposition technics such drop-casting was not feasible due to the immiscibility of these samples in alkanes. Consequently, the depositions prepared by pentane cannot be further used for IR/CO since the coating is not homogenous and cannot withstand strong gas flux. The deposition prepared by hexane was subject for IR/CO analysis. However, strong interference fringes were observed making the analysis of spectra impossible. They might be originated by the inhomogeneous coating resulting in internal diffraction phenomenon between small granulates. In contrary to the coatings prepared by propanol as shown in Figure 6C, a homogenous coating without any spaces in between the particles is visible avoiding those spectral interferences.

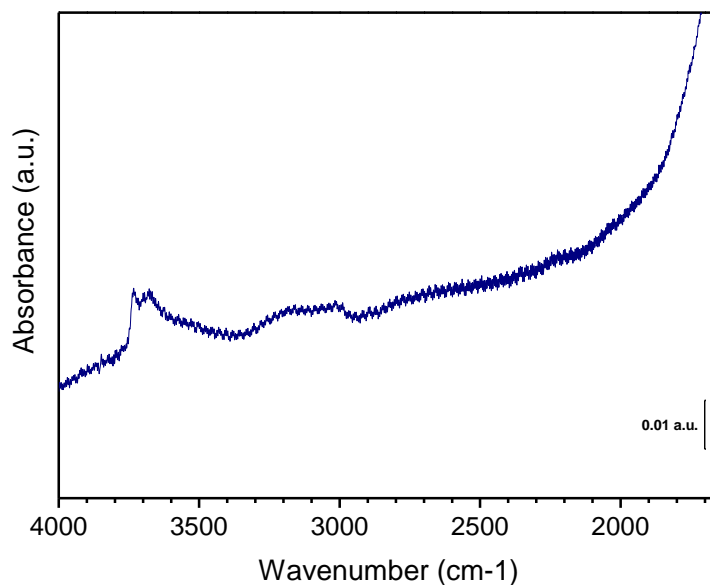


Figure 7: IR absorption spectrum of Mo/C@sapphire prepared with hexane.

Consequently, alkanes are not adequate for the deposition of Mo/C derived samples and the evaluation of possible coke formation cannot be further investigated.

- **CO not an adequate prob molecule?**

It may be possible due to the presence of carbon as carrier, the orbital properties of Mo have been modified limiting the interaction between Mo and CO. Hence, other prob molecules such as NO can be used (Figure 8). However, the adsorption band of NO on MoS₂ expected around 1800 cm⁻¹ is absent. Only NO in gas phase was observed.

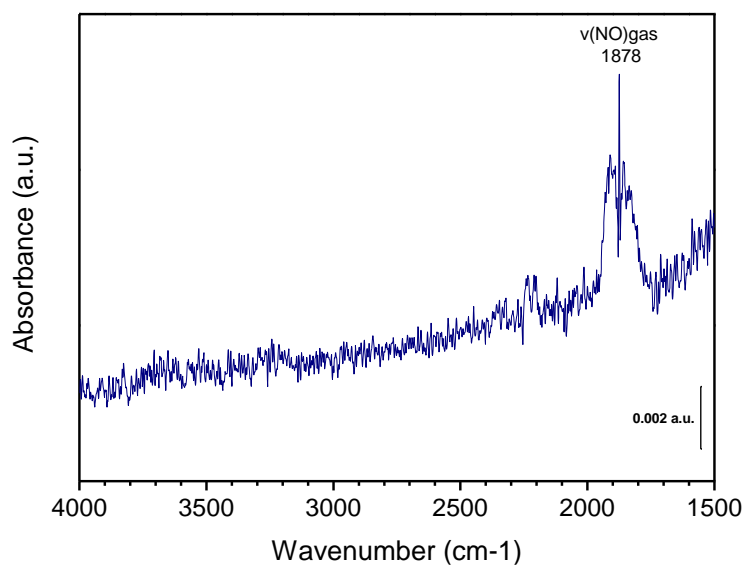


Figure 8: IR/NO spectra of MoS₂/C@sapphire at 1 Torr equilibrium pressure.

Other prob molecules as nitric acid and furan were also used. None of them allowed to observe an absorption band. Herein, this observation leads us to wonder why any prob molecule cannot be adsorbed? The only possible explanations which appear to be logical but cannot be proved experimentally are either a too weak interaction between Mo and CO even at 100K leading to an absence of absorption band or it exist an electrostatic repulsion on the carbon surface preventing the adsorption of CO.

The latter option seems to be more reasonable. During preparation we observed Mo/C particles to be loaded electrostatically due to the visible repulsion between particles. Herein, it may be possible that those electrostatic interactions are limiting the adsorption of carbon in absence of electrical current. It was demonstrated that electrostatic interaction can occur when carbon is layered thinly.² The used carbon has a more hydrophobic character. It was reported in the literature that hydrophobicity and electrostatic interactions are actually competing with each other. This competition can induce some perturbation during sorption.³ In order to investigate whether this physical parameter is the origin of CO adsorption issue, a hydrophilic carbon carrier was used. This hydrophilic carbon was provided by F. R. Sarria et al. which was rendered hydrophilic by CO₂ treatment of pyrolyzed olive branches. After deposition of Mo/bioC on sapphire and in-situ sulfidation followed by CO adsorption, no CO absorption bands were either observed (Figure 9). Herein we are blocked in our investigation and cannot comprehend why CO is not adsorbed although MoS₂ is formed.

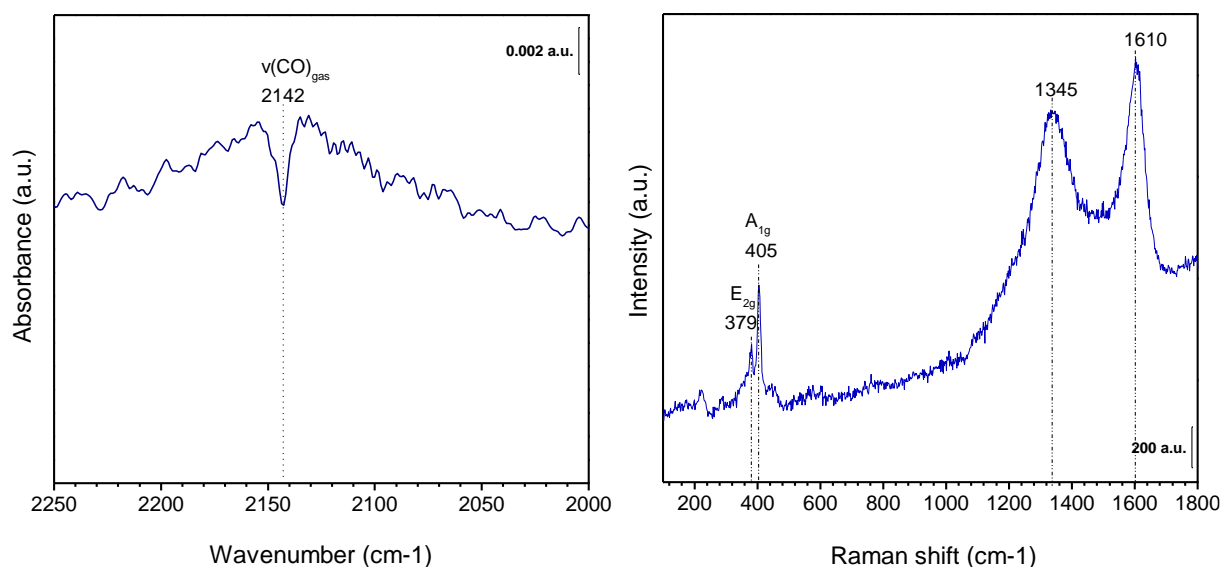


Figure 9: On the left IR/CO spectra at 1 Torr equilibrium pressure of MoS₂/bioC@sapphire and on the right its Raman spectrum.

4. Conclusion

In this work we tried to develop a new methodology for the analysis of carbon materials under IR-transmission. To overcome transparency issues, sapphire substrates were coated with a thin layer of Mo/C which was afterwards sulfided in-situ in the IR cell. Although clear spectra of analyzed samples were obtained, no adsorption bands of CO were observed. After changing several parameters which could be the origin of this issue, we still did not adsorb CO. Herein, it is impossible for us to explain why CO is not adsorbed on MoS₂ although its presence is confirmed by Raman. Yet, it is clear that carbon is the main origin, since we have confirmed this methodology on MoS₂/TiO₂ coated sapphire substrates and have observed CO adsorption bands. For some unclear physical reason, carbon is influencing the adsorption of CO on MoS₂ which cannot be elucidated at the moment.

Still this methodology is good replacement of Si-wafer, since they are stable in any pH-media, resistant to high temperature, easy to manipulate due to its hard texture and don't present interference fringes capable to limit spectrum analysis.

Reference

- (1) Wu, L. *et al.* Formation of coke during the esterification of pyrolysis bio-oil. *RSC Adv.* **6**, 86485–86493 (2016).
- (2) Stania, R. *et al.* Electrostatic Interaction across a Single-Layer Carbon Shell. *J. Phys. Chem. Lett.* **9**, 3586–3590 (2018).
- (3) Wang, L., Friesner, R. A. & Berne, B. J. Competition of electrostatic and hydrophobic interactions between small hydrophobes and model enclosures. *J. Phys. Chem. B* **114**, 7294–7301 (2010).

Spectroscopic study of supported MoS₂ catalysts for HER electrocatalysis in acidic media

Abstract:

The demand in new energy vectors as alternatives for fossil fuels with zero CO₂ emission is increasing. Hydrogen seems to be a good candidate since its production without any CO₂ emission is feasible through (photo)-electrocatalytic water splitting.

At the cathode, the state-of-the-art catalyst for the reduction of protons is Pt/C due to its oxygen resistance, long stability against corrosion, hydrogen adsorption affinity and good conductivity. However, platinum is expensive making scaling-up production of H₂ unaffordable. In order to generate low cost energy for man-kind, stable, highly active and efficient electrocatalysts need to be developed from non-precious and earth-abundant metals. In this purpose, MoS₂, a dichalcogenide which is abundant, stable, nontoxic and not expensive has received lot of attention. However, HER activity of MoS₂ is lower than the one for platinum. In this PhD thesis an effort in characterizing MoS₂ active sites for HER was made in order to reach a broader insight into the relation between surface characteristics of MoS₂ and HER activity. By conducting IR/CO spectroscopy studies of supported MoS₂ and by using different methods to increase MoS₂ edge site exposition and enhance the carrier's conductivity, several key parameters influencing HER activity were determined such as molybdenum's electron density, Mo dispersion and the morphology of the carrier. For the latter, a significant decrease in Tafel slope was demonstrated when bulk TiO₂ was replaced by TiO₂ nanotubes (TiNT). This enhancement in kinetics was related to the improved charge transfer of sulfided TiNT and the weakening of MoS₂/support interaction strengthening Mo-H-binding. Herein, the determined key parameters in this work give the opportunity to engineer HER electrocatalyst more efficiently and strategically.

Keywords: IR spectroscopy, HER, electrocatalysis, active sites, surface analysis, structure-activity relationships.

Résumé:

La demande de nouveaux vecteurs énergétiques ayant zéro émission de CO₂ est en pleine croissance notamment pour remplacer les combustibles fossiles. L'hydrogène semble être un bon candidat puisque sa production avec zéro émission de CO₂ est faisable par la photo(électro)-catalyse de l'eau.

A la cathode la réduction du proton en H₂ se réalise classiquement sur Pt/C. Celui-ci est considéré comme le catalyseur de référence en raison de sa résistance à l'oxydation, sa grande stabilité face à la corrosion, son affinité pour l'adsorption d'hydrogène et sa bonne conductivité. Cependant, le Pt est très onéreux empêchant la production économique de H₂ à grande échelle. Afin de rendre la production d'H₂ rentable, des électrocatalyseurs stables, non-toxique et efficaces doivent être développés à partir de métaux non rares et abondants. Dans ce contexte, le dichalcogenide MoS₂ qui répond à tous ces critères fait l'objet de beaucoup d'attention. Toutefois, l'activité en HER de MoS₂ est moins importante que celle du Pt. Lors de cette thèse un effort dans la caractérisation des sites actifs de MoS₂ pour l'HER a été réalisé afin d'obtenir un aperçu plus profond sur la relation entre les caractéristiques de surface de MoS₂ et l'activité HER. Ainsi MoS₂ supporté a été analysé par adsorption de CO suivi par spectroscopie IR. De plus, différentes méthodes ont été appliquées pour augmenter l'exposition des sites de bord M et pour améliorer la conductivité du support TiO₂. Lors de ces études plusieurs paramètres influençant l'activité HER ont été mis en évidence comme la densité électronique et la dispersion de Mo de même que la morphologie de support. Pour ce dernier, une diminution significative des pentes de Tafel a été démontrée lorsque le bulk-TiO₂ a été remplacé par des nanotubes de TiO₂ (TiNT). Cette amélioration du point de vue cinétique est reliée à l'augmentation de transfert de charge de TiNT sulfuré et la diminution de l'interaction MoS₂/support induisant un renforcement des liaisons Mo-H. Par conséquent les paramètres clés déterminés dans ce travail donnent l'opportunité de concevoir de manière plus efficace des électrocatalyseurs pour HER.

Mots clé : Spectroscopie IR, HER, électrocatalyse, sites actifs, analyse de surface, relation structure-activité.